



land

Special Issue Reprint

Recent Progress in Land Degradation Processes and Control

Edited by
Jianye Li, Xingyi Zhang, Weida Gao, Wei Hu and Qiang Chen

mdpi.com/journal/land



Recent Progress in Land Degradation Processes and Control

Recent Progress in Land Degradation Processes and Control

Guest Editors

Jianye Li

Xingyi Zhang

Weida Gao

Wei Hu

Qiang Chen



Basel • Beijing • Wuhan • Barcelona • Belgrade • Novi Sad • Cluj • Manchester

Guest Editors

Jianye Li

State Key Laboratory of Black
Soils Conservation and
Utilization

Northeast Institute of
Geography and Agroecology
Chinese Academy of Sciences
Harbin
China

Wei Hu

State Key Laboratory of Black
Soils Conservation and
Utilization

Northeast Institute of
Geography and Agroecology
Chinese Academy of Sciences
Harbin
China

Xingyi Zhang

State Key Laboratory of Black
Soils Conservation and
Utilization

Northeast Institute of
Geography and Agroecology
Chinese Academy of Sciences
Harbin
China

Qiang Chen

Heilongjiang Province Key
Laboratory of Geographical
Environment Monitoring and
Spatial Information Service in
Cold Regions

Harbin Normal University
Harbin
China

Weida Gao

College of Land Science and
Technology
China Agricultural University
Beijing
China

Editorial Office

MDPI AG

Grosspeteranlage 5

4052 Basel, Switzerland

This is a reprint of the Special Issue, published open access by the journal *Land* (ISSN 2073-445X), freely accessible at: https://www.mdpi.com/journal/land/special_issues/8894L53WJ5.

For citation purposes, cite each article independently as indicated on the article page online and as indicated below:

Lastname, A.A.; Lastname, B.B. Article Title. <i>Journal Name</i> Year , <i>Volume Number</i> , Page Range.
--

ISBN 978-3-7258-3847-9 (Hbk)

ISBN 978-3-7258-3848-6 (PDF)

<https://doi.org/10.3390/books978-3-7258-3848-6>

© 2025 by the authors. Articles in this book are Open Access and distributed under the Creative Commons Attribution (CC BY) license. The book as a whole is distributed by MDPI under the terms and conditions of the Creative Commons Attribution-NonCommercial-NoDerivs (CC BY-NC-ND) license (<https://creativecommons.org/licenses/by-nc-nd/4.0/>).

Contents

Qiannan Yang, Haidong Gao, Yong Han, Zhanbin Li and Kexin Lu Coupling Changes in Runoff and Sediment and Their Relationships with Erosion Energy and Underlying Surface in the Wuding River Basin, China Reprinted from: <i>Land</i> 2024 , <i>13</i> , 496, https://doi.org/10.3390/land13040496	1
Miklós Kázmér, Keyan Fang, Yunchao Zhou and Zoltán Kern Rapid Estimation of Soil Erosion Rate from Exhumed Roots (Xiaolong Mts, China) Reprinted from: <i>Land</i> 2024 , <i>13</i> , 771, https://doi.org/10.3390/land13060771	19
Jones Anschau Xavier de Oliveira, Frederico Terra de Almeida, Adilson Pacheco de Souza, Rhavel Salviano Dias Paulista, Cornélio Alberto Zolin and Aaron Kinyu Hoshide Determination of Soil Erodibility by Different Methodologies in the Renato and Caiabi River Sub-Basins in Brazil Reprinted from: <i>Land</i> 2024 , <i>13</i> , 1442, https://doi.org/10.3390/land13091442	33
Dovilė Gustienė and Iveta Varnagirytė-Kabašinskiėnė Changes in Ground Cover Layers, Biomass and Diversity of Vascular Plants/Mosses in the Clear-Cuts Followed by Reforested Scots Pine until Maturity Age Reprinted from: <i>Land</i> 2024 , <i>13</i> , 1477, https://doi.org/10.3390/land13091477	50
Jielin Liu, Yong Zhu, Jianye Li, Xiaolei Kong, Qiang Zhang, Xueshan Wang, et al. Short-Term Artificial Revegetation with Herbaceous Species Can Prevent Soil Degradation in a Black Soil Erosion Gully of Northeast China Reprinted from: <i>Land</i> 2024 , <i>13</i> , 1486, https://doi.org/10.3390/land13091486	67
Md Rezaul Karim, Md Abdul Halim, Imrul Kayes, Wenxi Liao, Sharif A. Mukul, H. M. Tuihedur Rahman and Sean C. Thomas Co-Management Effects on Forest Restoration in Protected Areas of Bangladesh: A Remote Sensing and GIS-Based Analysis Reprinted from: <i>Land</i> 2024 , <i>13</i> , 1709, https://doi.org/10.3390/land13101709	84
Beatrice Petti and Marco Ottaviano Identification of Agricultural Areas to Restore Through Nature-Based Solutions (NbS) Reprinted from: <i>Land</i> 2024 , <i>13</i> , 1954, https://doi.org/10.3390/land13111954	105
Qin Zhang, Chunfang Yue, Pujia Yu, Hailiang Xu, Kun Liu, Jie Wu and Fangyu Sheng Impacts of Different Vegetation Types on Soil Aggregate Stability in the Key Ecological Rehabilitation Area of the Tarim River Basin, Northwest China Reprinted from: <i>Land</i> 2024 , <i>13</i> , 2157, https://doi.org/10.3390/land13122157	126
Jana Podhrázská, Jan Szturc, Josef Kučera and Filip Chuchma Impact of Climate Change on Snowmelt Erosion Risk Reprinted from: <i>Land</i> 2025 , <i>14</i> , 55, https://doi.org/10.3390/land14010055	142
Admilson da Penha Pacheco, João Alexandre Silva do Nascimento, Antonio Miguel Ruiz-Armenteros, Ubiratan Joaquim da Silva Junior, Juarez Antonio da Silva Junior, Leidjane Maria Maciel de Oliveira, et al. Land Cover Transformations in Mining-Influenced Areas Using PlanetScope Imagery, Spectral Indices, and Machine Learning: A Case Study in the Hinterlands de Pernambuco, Brazil Reprinted from: <i>Land</i> 2025 , <i>14</i> , 325, https://doi.org/10.3390/land14020325	157

Article

Coupling Changes in Runoff and Sediment and Their Relationships with Erosion Energy and Underlying Surface in the Wuding River Basin, China

Qiannan Yang, Haidong Gao*, Yong Han, Zhanbin Li and Kexin Lu

State Key Laboratory of Eco-Hydraulics in Northwest Arid Region of China, Xi'an University of Technology, Xi'an 710048, China

* Correspondence: hdgao@xaut.edu.cn; Tel.: +86-29-8231-2658

Abstract: Investigating the changes in the runoff and sediment coupling relationship in the Middle Yellow River Basin of China can not only deepen the understanding of soil loss control in arid areas, but also help solve key issues of regional ecological protection. Since the 1960s, soil- and water-conservation projects have been implemented in the Middle Yellow River Basin, inducing a significant reduction in runoff and sediment and changes in the relationship between runoff and sediment. The study identified the change points of coupling relationship between runoff and sediment in the Wuding River Basin (WRB) by constructing a diagnostic method based on coupling coordination degree and the Pettitt test; the study validated this using the Copula function and analyzed the impacts of erosion energy and underlying surface factors. The results showed the following: (1) the method based on coupling coordination degree and the Pettitt test could accurately reflect the coupling relationship of runoff and sediment and identify two change points (1971 and 1996); (2) runoff and sediment in the WRB decreased gradually over three periods (P1, 1960–1970; P2, 1971–1995; P3, 1996–2020), with an average annual runoff of 15.34×10^8 , 10.72×10^8 , and 8.32×10^8 m³ and average annual sediment load of 1.84×10^8 , 0.82×10^8 , and 0.32×10^8 t, respectively; (3) the maximum possible joint design value of runoff and sediment under different return periods in P1 were all the highest, followed by P2 and P3, and the larger the return period, the higher the maximum possible joint design value; (4) runoff erosion power could promote runoff and sediment in PE (1960–2020), P1, P2 and P3 at a significant level, check dams and terrace could decrease runoff and sediment significantly in PE, and the highest contribution to runoff reduction was check dam (95.4%), while the highest contribution to sediment reduction was REP (93.8%). The study can provide a new way to analyze the changes in the runoff and sediment relationship and provide scientific support for runoff and sediment regulation in the Middle Yellow River Basin.

Keywords: runoff; sediment load; copula function; runoff erosion power; underlying surface

Citation: Yang, Q.; Gao, H.; Han, Y.; Li, Z.; Lu, K. Coupling Changes in Runoff and Sediment and Their Relationships with Erosion Energy and Underlying Surface in the Wuding River Basin, China. *Land* **2024**, *13*, 496.

<https://doi.org/10.3390/land13040496>

Academic Editor: Adrianos Retalis

Received: 13 March 2024

Revised: 6 April 2024

Accepted: 9 April 2024

Published: 11 April 2024



Copyright: © 2024 by the authors. Licensee MDPI, Basel, Switzerland. This article is an open access article distributed under the terms and conditions of the Creative Commons Attribution (CC BY) license (<https://creativecommons.org/licenses/by/4.0/>).

1. Introduction

A good runoff and sediment relationship is critical to the health of the river system and beneficial to regional ecosystem stability, economic prosperity, and human well-being [1–3]. Normally, runoff and sediment in the river system is mainly induced by rainfall and underlying surfaces, which dominate the amount of rainfall converted into runoff generated sediment yield [4,5]. As such indicating relationships among runoff, sediment and underlying surfaces can help to assess the effectiveness of conservation measures and improvements in river management [6,7].

As the primary source of sediment of the Yellow River, especially for the coarse sediment-producing area, to mitigate the severe soil loss in the Middle Yellow River Basin (MYRB) has always been a hot research topic [8]. After more than 60 years of comprehensive management, sediment in the MYRB during 2001 to 2018 decreased by 85% compared with that during 1919 to 1959 [9]. The major cause of this exciting result is the

many conservation measures that have been adopted in the MYRB since the 1960s. These measures mainly contain check dam construction, terracing, tree and grass planting, which were implemented rapidly in the 1970s, 1980s and 1990s, respectively [10]. Among them, check dams constructed in gullies decrease sediment of river outlets by trapping upstream sediment [11]. Terraces reduce sediment by absorbing slope rainwater and diminishing runoff energy [12]. Vegetation restoration can improve soil property and enhance soil anti-erodibility so as to control runoff and sediment entering gullies [13]. Therefore, check dams and terraces were the primary factors to reduce sediment during the 1970s to 1980s. Meanwhile, vegetation restoration plays a key role after 1999, especially the Grain for Green project, which was implemented on the Loess Plateau to combat soil and water loss into the Yellow River.

The runoff and sediment reduction in the MYRB mainly due to the decrease in runoff and sediment of sub-catchments in this region [14], especially for the Wuding River Basin (WRB), which was the most significant sediment reduction tributary [15]. Since the 1960s, the underlying surface of the WRB has been gradually changed for check dam and terrace construction to enhance grain production [16]. After the 1970s, runoff and sediment sharply decreased, mainly due to the impacts of the underlying surface, while precipitation and evapotranspiration had little influence [17]. By using elasticity coefficient method, Jin and Li calculated the contribution of underlying surfaces, such as check dams and vegetation restoration, for runoff reduction accounting for 78.75% and for sediment reduction accounting for 87.78% [18]. Shi et al. obtained similar results in that the contribution of underlying surfaces to runoff and sediment reduction in the WRB was 75% and 89%, respectively [19]. Of course, some researchers also proposed that the contribution of precipitation and underlying surfaces to runoff and sediment reduction was approximately equal [20].

The essence of soil erosion is the process of erosion energy dissipation, transmission and redistribution [21]. And the change processes of erosion energy mainly take runoff as medium [22]. Improved underlying surfaces can change the movement state of runoff on slope and then regulate erosion energy, which dominates sediment transportation [23]. However, few have attempted to investigate the coupling changes in runoff and sediment and the responses to runoff erosion energy. In this paper, we applied the entirety perspective to indicate the coupling change characteristics of runoff and sediment in the WRB and the impacts of erosion energy and the underlying surface. The specific objectives were as follows: (1) to reveal the coupling change characteristics of runoff and sediment in different periods by using the coupling coordination degree model; (2) to determine the responses of sediment to erosion energy; and (3) to compare the importance of impacting factors to runoff and sediment change.

2. Materials and Methods

2.1. Site Description

The WRB (37°02′–39°00′ N, 107°47′–110°34′ E) is the primary tributary of the Yellow River, which is located in the hinterland of the Loess Plateau (Figure 1). The whole area of the WRB is about 30,261 km², and the main channel length is 491 km. The elevation of the basin ranges from 600 to 1800 m and average slope of the riverbed is 1.8‰. The landform located in the south of main channel mainly belongs to the hilly–gully region, while the north of the main channel is situated in the wind–sandy region. The basin has a temperate continental monsoon climate. The average annual precipitation was 388 mm between 1960 and 2020, with 70% occurring from June to September. The average and maximum rainfall intensity is 5.4 mm h^{−1} and 51.2 mm h^{−1}, respectively. The annual temperature ranges from 7.9 °C to 11.2 °C. The loess soil and aeolian sandy soil are the most widely distributed in the basin. Limited by higher temperature and good soil permeability, snowmelt erosion does not occur. As precipitation decreases from southeast to northwest, vegetation types in the southeast of the basin are mainly composed of forest steppe, while the north is mainly composed of desert steppe. Soil erosion in the basin worsens from northwest to southeast. However, because soil- and water-conservation construction has gradually been carried

out since the 1960s, especially the implementation of the Returning Farmland to Forests and Grassland Project, soil and water loss in the whole basin has significantly improved.

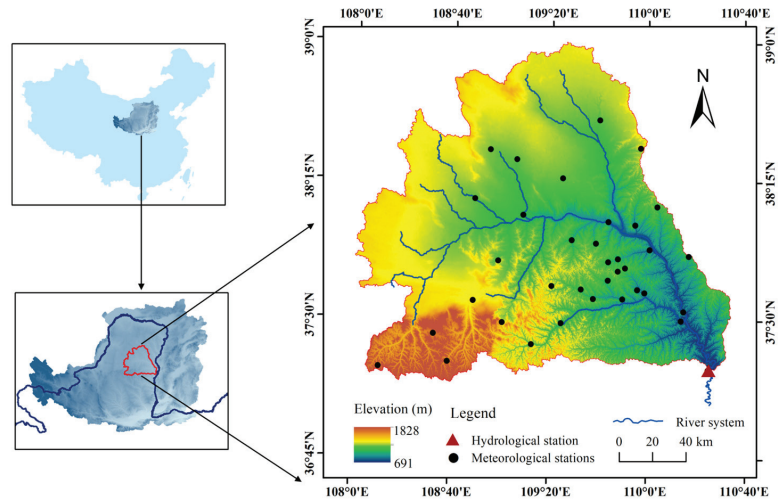


Figure 1. Location of the WRB.

2.2. Data Preparation

Precipitation and runoff data used in the study were all from the Yellow River Basin Hydrological Yearbook from 1960 to 2020. The average daily runoff data came from the control hydrological station, Baijiachuan. The areal precipitation of the WRB was calculated using the Tyson polygon based on daily average precipitation data, which came from 36 rain-gauge stations in the WRB, including Hanjiamao, Hengshan, Zhaoshiyao, Suide, etc.

Land-use data came from the V1.0 dataset, a fine classification product of 30 m global land cover developed by the Aerospace Information Research Institute, Chinese Academy of Sciences [24]. The study used two periods of land-use data from 1985 and 2019, and the main types of land use were arable land, forest land, grassland, water body, construction land, and unused land, respectively.

The NDVI came from two datasets: GIMMS NDVI and MODIS NDVI. The GIMMS NDVI dataset was sourced from the National Oceanic and Atmospheric Administration “<https://psl.noaa.gov> (accessed on 12 April 2016)”, with a time series from 1983 to 2015. The spatial resolution of GIMMS NDVI is 8 km with a temporal resolution of 15 days. The MODIS NDVI dataset was sourced from the National Aeronautics and Space Administration “<https://ladsweb.modaps.eosdis.nasa.gov/> (accessed on 4 July 2021)”, with a time series from 2000 to 2020. The spatial resolution of MODIS NDVI is 250 m and the temporal resolution is 16 days. According to the method proposed by Jia et al. [25], the study merged two time series together and extended the length of NDVI data from 1983 to 2020.

The information regarding check dams, especially large check dams, contained construction time, coordinates, controlled area, storage capacity and cumulative siltation capacity, which came from the 2011 National Water Resources Census. The information regarding terrace from 1960 to 2011 came from the 2011 National Water Resources Census, and others from 2011 to 2015 were extracted from the V1.0 dataset.

2.3. Methods

2.3.1. Coupling Coordination Degree Model

For a river system, the changes in runoff and its sediment are not independent [26]. Therefore, this study applied the coupling coordination degree to analyze the relationship

between runoff and sediment in order to explore the coupling changes in runoff and sediment in the WRB. The formula is as follows:

$$D = (C \cdot T)^{1/2} \quad (1)$$

$$T = au_1 + bu_2 \quad (2)$$

where D represents the coupling coordination degree; C represents the coupling degree; T represents the comprehensive harmonic index of runoff subsystem and sediment subsystem; u_1 and u_2 , respectively, represent contributions of the runoff subsystem and sediment subsystem to the overall river system; and a and b represent the undetermined coefficients, which often consider that the importance of two subsystems is equal, so $a = b = 0.5$.

The formula of C is as follows:

$$C = 2 \left\{ \frac{u_1 \cdot u_2}{(u_1 + u_2)^2} \right\}^{1/2} \quad (3)$$

In the study, indicators of the runoff subsystem and sediment subsystem corresponded to runoff and sediment of the WRB, respectively. The study assumed that the larger the value of D , the better the coupling relationship of runoff and sediment.

2.3.2. Pettitt Test

The Pettitt test is a nonparametric test method that was conducted by A. Pettitt, which is based on the Mann–Whitney statistical function and used to determine the change in time series [27]. Assuming time t is the most likely point in which change occurs, the time series can then be divided into two parts before and after it. The two samples are x_1, x_2, \dots, x_t , and $x_{t+1}, x_{t+2}, \dots, x_N$. The formula for $U_{t,N}$ is as follows:

$$U_{t,N} = \sum_{i=1}^t \sum_{j=i+1}^N \text{sgn}(x_i - x_j) \quad (4)$$

where if $(x_i - x_j) > 0$, $\text{sgn}(x_i - x_j) = 1$; if $(x_i - x_j) = 0$, $\text{sgn}(x_i - x_j) = 0$; if $(x_i - x_j) < 0$, $\text{sgn}(x_i - x_j) = -1$.

When $|U_{t,N}|$ reaches the maximum value, the corresponding x_t is considered the possible change point. The significance level (p) can be calculated by the following formula:

$$p = 2e^{-\frac{6U_{t,N}^2}{N^2 + N^3}} \quad (5)$$

When $p \leq 0.05$, the detected change point is just a significant change point.

2.3.3. Joint Distribution Function Fitting

The copula function is a linking function that can be used to describe the joint distribution of multiple variables and can connect any two marginal distribution functions [28]. As such, the calculation of marginal distribution model and joint distribution model are all based on it. When fitting marginal distribution of runoff and sediment, three popular probability distributions in hydrological analysis were used. They are Gamma distribution, Lognormal distribution and GEV (Generalized Extreme Value) distribution. Meanwhile, the K-S (Kolmogorov–Smirnov) test was used to examine the marginal distribution, and the AIC (Akaike information criterion) minimum criterion was used to determine the optimal marginal distribution [29]. The probability density functions of three marginal distributions are as follows:

(1) Gamma distribution

$$f(x|\alpha, \beta) = \frac{1}{\beta^\alpha \Gamma(\alpha)} x^{\alpha-1} e^{-\frac{x}{\beta}} \quad (6)$$

- where α represents shape parameters; β represents scale parameter.
 (2) Lognormal distribution

$$f(x|\mu, \sigma) = \frac{1}{x\sqrt{2\pi}\sigma} e^{-\frac{(\ln x - \mu)^2}{2\sigma^2}} \tag{7}$$

where μ represents the mean value of logarithm of variable; σ represents the standard deviation of logarithm of variable.

- (3) GEV distribution

$$f(x|k, \sigma, \mu) = \frac{1}{\sigma} \left[1 - k \left(\frac{x - \mu}{\sigma} \right)^{\frac{1}{k}-1} \right] e^{-[1 - k \left(\frac{x - \mu}{\sigma} \right)]^{\frac{1}{k}}} \tag{8}$$

where k represents shape parameters; σ represents scale parameter; μ represents position parameter.

When fitting the joint distribution of runoff and sediment, three popular copula functions of Archimedean type were selected. Detailed information is shown in Table 1.

Table 1. Three popular copula functions of Archimedean type.

Name	Function	Parameter Value	Relationship between τ and θ
Clayton Copula	$C(u, v) = (u^{-\theta} + v^{-\theta} - 1)^{-1/\theta}$	$\theta > 0$	$\tau = \frac{\theta}{2+\theta}$
Frank Copula	$C(u, v) = -\frac{1}{\theta} \left[1 + \frac{(e^{-\theta u} - 1)(e^{-\theta v} - 1)}{(e^{-\theta} - 1)} \right]$	$\theta \in R$	$\tau = 1 - \frac{4}{\theta} \left[-\frac{1}{\theta} \int_0^1 \frac{t}{\exp(t)^{\theta} - 1} dt - 1 \right]$
Gumbel-Hougaard Copula	$C(u, v) = \exp \left\{ - \left[(-\ln u)^{\theta} + (-\ln v)^{\theta} \right]^{1/\theta} \right\}$	$\theta \geq 1$	$\tau = 1 - \frac{1}{\theta}$

The parameter estimation of the joint distribution function was determined using the maximum likelihood method. By calculating R^2 of cumulative probabilities and empirical cumulative probabilities of three distribution functions, the optimal joint distribution function for runoff and sediment was selected.

2.3.4. Joint Return Period and Joint Design Value Calculating

The “OR” joint return period was used as the design control value for safety or risk to characterize the risk that runoff and sediment encounter [30]. For the risk, the occurring probability of unexpected events was considered, so we mainly considered the joint return period of runoff (X) and sediment (Y). The formula of the joint return period is as follows:

$$T_{OR} = \frac{1}{P(X > x \vee Y > y)} = \frac{1}{1 - C(F_X(x), F_Y(y))} = \frac{1}{1 - C(u, v)} \tag{9}$$

where T_{OR} represents the joint return period, which stands for the return period when the design value of any one of the two variables (X and Y) was exceeded. $C(u, v)$ represents the joint distribution function of the marginal distributions (u and v) for X and Y .

For any given joint return period, there are countless combinations of runoff (x) and sediment (y) theoretically that meet the design criteria. When the joint probability density function $f(x, y)$ reaches its maximum value, the joint design value combination (x, y) is just the maximum possible combination for that return period [31]. The formula is as follows:

$$\begin{cases} \max : f(x, y) = C(F_X(x), F_Y(y))f_X(x)f_Y(y) \\ C(F_X(x), F_Y(y)) = 1 - 1/T_{OR} \end{cases} \tag{10}$$

2.3.5. Cross-Wavelet Transform and Wavelet Coherence

Cross-wavelet transform is a signal analysis technique that combines wavelet transform with cross spectral analysis. This method can analyze the degree of mutual relationship between two time series in the time–frequency domain and identify the phase

relationship of the time series in time–frequency space. The main approach is to extract the cross-wavelet energy spectrum and the coherence spectrum. The energy spectrum can reflect the relationship between two time series in the high-energy region, while the coherence spectrum focuses on the relationship between the two time series in the low-energy region [32]. Assuming that the continuous transformation results of two time series $X(t)$ and $Y(t)$ are $W_n^x(t)$ and $W_n^y(t)$ respectively, then the cross-wavelet spectrum is as follows:

$$W_n^{xy}(t) = W_n^x(t) \cdot W_n^{y*}(t) \quad (11)$$

The wavelet coherence spectrum is as follows:

$$R_n^2(t) = \frac{\left| M(t^{-1}W_n^{xy}(t)) \right|^2}{M(t^{-1}|W_n^x(t)|^2) \cdot M(t^{-1}|W_n^y(t)|^2)} \quad (12)$$

where $W_n^{y*}(t)$ represents the complex conjugate of $W_n^y(t)$; M represents the Smoother; $|W_n^{xy}(t)|$ represents the cross-wavelet spectral density of $W_n^{xy}(t)$ and its value reflects the degree of significant correlation between the two time series in the high-energy region; $\left| M(t^{-1}W_n^{xy}(t)) \right|^2$ represents the cross-product of wave amplitude of two time series at a certain frequency; $M(t^{-1}|W_n^x(t)|^2)$ and $M(t^{-1}|W_n^y(t)|^2)$ represent the amplitude of two time series' vibration waves, respectively.

2.3.6. Runoff Erosion Power

In order to determine the annual runoff erosion power, we used the formula proposed by Cheng et al. [33], which is:

$$REP = Q'_m \cdot H_y \quad (13)$$

$$Q'_m = \frac{Q_m}{A} \quad (14)$$

$$H_y = \frac{Q_y \cdot \Delta t}{A} \quad (15)$$

where REP represents runoff erosion power, the unit is $m^4 s^{-1} km^{-2}$; Q'_m represents the maximum runoff modulus, the unit is $m^3 s^{-1} km^{-2}$, the value is the ratio of Q_m to A ; H_y represents average annual runoff depth, the unit is m; Q_m represents peak flow modulus, the unit is $m^3 s^{-1} km^{-2}$; A represents the area of the WRB, the unit is km^{-2} ; Q_y represents average annual runoff amount, the unit is $m^3 s^{-1}$, the value is equal to the sum of monthly runoff amount within the year divided by 12; Δt represents time interval, the value is $2592 \times 10^3 s$, which is calculated based on 30 days per month.

2.3.7. Elastic Coefficient

The elastic coefficient approach, which is based on the Budyko hypothesis, has been frequently used to quantify the key driving factors of runoff and sediment change [34]. Zhang recommended the concept of elasticity for evaluating the sensitivity of sediment to changes in impacting factors [35]. The impacting factors (REP , check dam, terrace and NDVI) elasticity of runoff, sediment (ε_{X-Y}) are as follows:

$$\varepsilon_{X-Y} = \frac{\Delta Y_a / \bar{Y}}{\Delta X_a / \bar{X}} = \frac{(Y_a - \bar{Y}) / \bar{Y}}{(X_a - \bar{X}) / \bar{X}} \quad (16)$$

where Y_a represents the annual value of runoff, sediment load; X_a represents the annual value of one of the four factors; ΔY_a represents the changes in Y_a induced by X_a ; ΔX_a represents changes in annual X ; \bar{Y} represents the average value of Y_a ; \bar{X} represents the

average value of X_a . The positive value of ε_{X-Y} means Y increased with X , while the negative value means Y decreased with X increased.

Based on ε_{X-Y} , the study estimated the contribution rate of four impacting factors to runoff and sediment changes. The contribution rate (C_X) was calculated by the following formula:

$$C_X = \varepsilon_{X-Y} \frac{\bar{Y}}{\bar{X}} \cdot \frac{\Delta X_p}{\Delta Y_p} \times 100\% \tag{17}$$

where ΔY_p represents the difference between the average value of Y_a in the change period and average value of Y_a in the reference period; ΔX_p represents the difference between the average value of X_a in the change period and the average value of X_a in the reference period.

3. Results

3.1. Runoff and Sediment Relationship and Change Diagnosis

3.1.1. Coupling Changes in Runoff and Sediment

Figure 2a shows the time series plot of the coupling coordination degree of runoff and sediment load in the WRB from 1960 to 2020. Except for the 1960s, the values of coupling coordination degree were generally kept above 0.8. The maximum value of coupling coordination degree was 0.96 in 2005, while the minimum value was 0.60 in 1964. The coupling relationship between runoff and sediment in the basin has always been at a high level. The change points of the coupling coordination degree of runoff and sediment load in the WRB were 1971 and 1996 (Figure 2b). The coupling relationship between runoff and sediment load changed significantly in 1971 and 1996. The two change points were consistent with the results that were calculated by Zhou et al., which were 1971 and 1997 in the WRB [17].

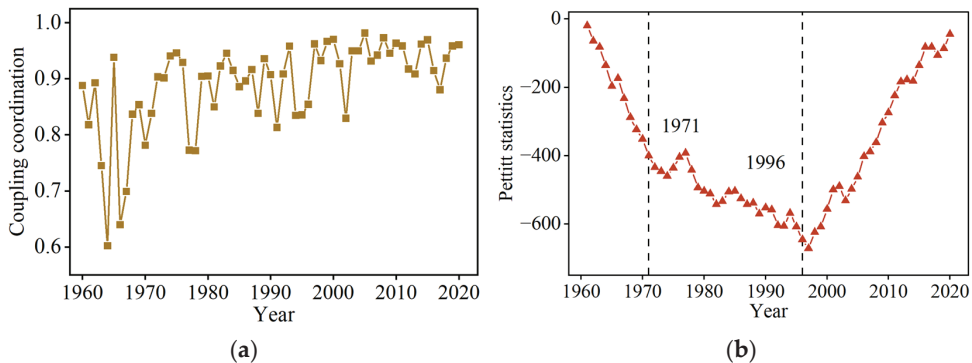


Figure 2. Coupling changes in runoff and sediment load and its change points in the WRB from 1960 to 2020. (a) The coupling coordination degree of runoff and sediment; (b) the Pettitt test result of coupling coordination degree.

3.1.2. Change Point Verification Based on Copula Function

By using the copula function, the study constructed the optimal joint distribution cumulative probability between runoff and sediment and validated the change points of the relationship between runoff and sediment (Figure 3). Due to the fact that all annual runoff and sediment loads have passed the K-S test, the four common theoretical distribution functions can be used to describe annual runoff and sediment load. On this basis, the linear moment method was used to estimate the parameters of four theoretical distribution functions, and the R^2 between the empirical cumulative probabilities of annual runoff and annual sediment load and the cumulative probabilities of the four theoretical distribution functions was calculated separately. According to the principle of R^2 maximum, the optimal

distribution functions for annual runoff and annual sediment load in the WRB from 1960 to 2020 were all GEV-type distribution (Figure 3a,b).

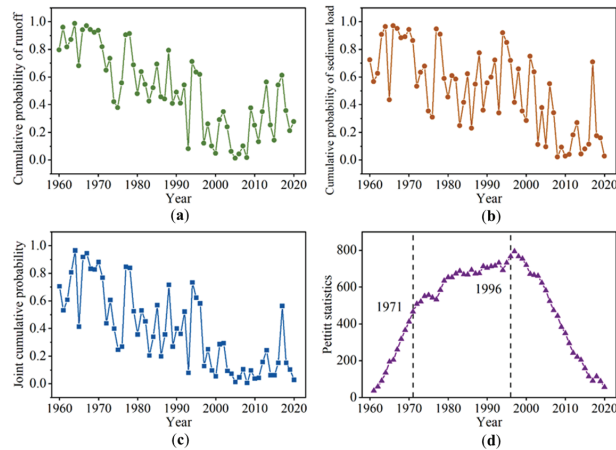


Figure 3. Cumulative probability of optimal copula joint distribution of runoff and sediment in the WRB from 1960 to 2020. (a) The cumulative probability of runoff; (b) the cumulative probability of sediment load; (c) the joint cumulative probability of runoff and sediment; (d) the Pettitt test result of joint cumulative probability.

Based on the AIC criterion, Gumbel Copula was selected as the optimal copula from three Archimedean copulas. Then, it was used to connect the optimal marginal distribution function of runoff and sediment and to calculate the cumulative probability of the joint distribution function of it in the WRB (Figure 3c). Furthermore, the Pettitt test was used once more to identify the cumulative probability of the joint distribution function of runoff and sediment. The results are shown in Figure 3d. The cumulative probability of the joint distribution function of runoff and sediment in the WRB also showed significant change in 1971 and 1996. Therefore, the change diagnosis method for runoff and sediment relationship based on the coupling coordination degree can accurately identify the change point.

3.2. Characteristics of Runoff and Sediment before and after Change Points

In Figure 4, runoff of the WRB increased in P1 and P3 and decreased in P2, while sediment load only increased in P1 (1960–1970) and decreased in P2 (1971–1995) and P3 (1996–2020). However, in fact, runoff and sediment load in the basin showed a downwards trend wholly from 1960 to 2020. Precipitation in the three periods was 209.3 mm, 353.5 mm and 425.6 mm, respectively. And precipitation in the WRB has increased significantly ($p < 0.01$) over the past 60 years. The statistical results indicate that average annual runoff of the WRB gradually decreased in the three periods, with values of $15.34 \times 10^8 \text{ m}^3$, $10.72 \times 10^8 \text{ m}^3$ and $8.32 \times 10^8 \text{ m}^3$, respectively. Average annual sediment load also gradually decreased in the three periods, with values of $1.84 \times 10^8 \text{ t}$, $0.82 \times 10^8 \text{ t}$ and $0.32 \times 10^8 \text{ t}$, respectively. Sediment load in three periods decreased more significantly than runoff.

Average annual runoff in P2 and P3 decreased by 30.1% and 47.8%, respectively, compared to P1. Meanwhile, average annual sediment load in P2 and P3 decreased by 55.4% and 82.6%, respectively, compared to P1. Moreover, the CV of runoff was 0.17 in P1 and 0.16 in P2 and P3. However, the CV of sediment load was 0.62 in P1, 0.76 in P2 and 0.89 in P3. The fluctuation of sediment load was more intense than runoff. It reflected that compared with runoff, sediment was more vulnerable to the impacting factors.

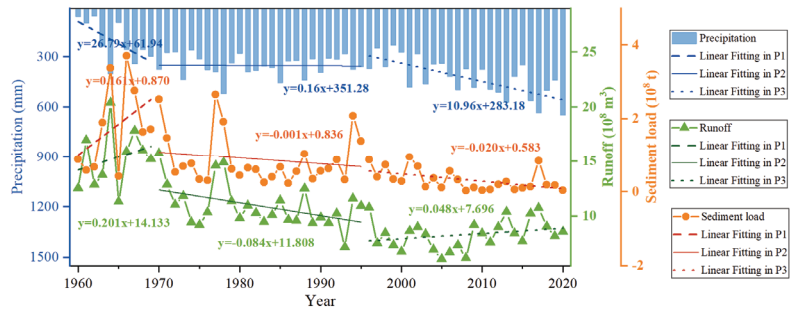


Figure 4. Changes in precipitation, runoff and sediment load in the WRB for three periods.

3.3. Joint Recurrence Characteristics of Runoff and Sediment

Analyzing the joint return period and joint design values of runoff and sediment can help indicate runoff and sediment change characteristics in the WRB and provide new management ideas for ecological construction in this basin. In Figure 5, it can be seen that under the same return period, the maximum possible joint design values of runoff and sediment load in the WRB were gradually decreased from P1 to P3. And with the return period increased, the maximum possible joint design value of runoff and sediment increased. However, under the return period of 200 years, the maximum possible joint design value of sediment in P2 was slightly smaller than that in P3. With soil and water conservation on the Loess Plateau promoted, the maximum possible joint design value of runoff and sediment in the WRB gradually decreased. However, there might appear a sharp increase in sediment due to extreme rainfall in some years.

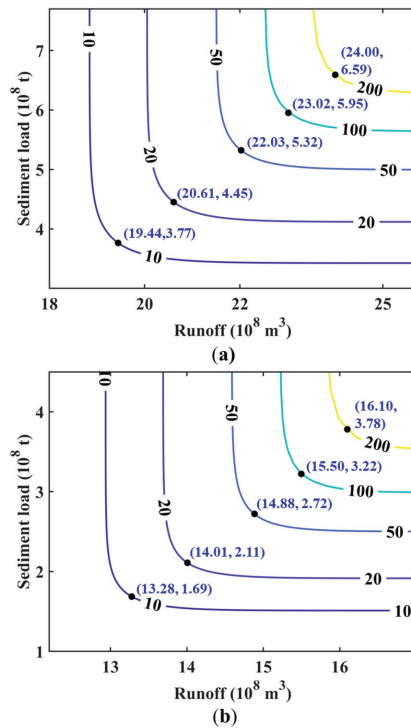


Figure 5. Cont.

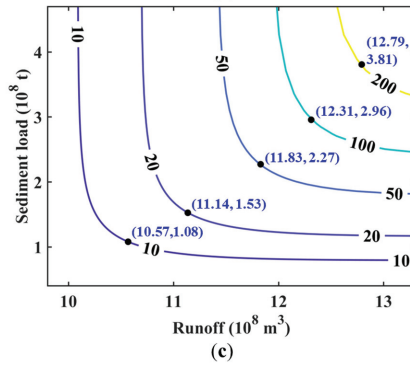


Figure 5. Joint return period of runoff and sediment and its maximum possible combined design value in the WRB for three periods. (a–c) is the maximum possible combined design value under different joint return periods in P1, P2 and P3, respectively.

In Table 2, the change rates of maximum possible joint design value of runoff in P2 and P3 were smaller than sediment load at five return periods. Compared with P1, the maximum possible joint design value of runoff decreased by about 32% in P2, while the maximum possible joint design value of sediment decreased by 42% to 56%; the maximum possible joint design value of runoff in the WRB in P3 decreased by about 46%, while the maximum possible joint design value of sediment decreased by 42% to 72%. Compared with P2, the maximum possible joint design value of runoff in P3 maintained the decrease rate at 20%, while the decrease rate of maximum possible joint design value of sediment displayed large differences that changed by −36% to 0%.

Table 2. Changing rates of maximum possible joint design value of runoff and sediment under different return periods in the WRB.

Joint Return Period	Period	Compared with P1	Compared with P2
10 years	P2	(−31.69, −55.17)	
	P3	(−45.63, −71.35)	(−20.41, −36.09)
20 years	P2	(−32.02, −52.58)	
	P3	(−45.95, −65.62)	(−20.49, −27.49)
50 years	P2	(−32.46, −48.87)	
	P3	(−46.30, −57.33)	(−20.50, −16.54)
100 years	P2	(−32.67, −45.88)	
	P3	(−46.52, −50.25)	(−20.58, −8.07)
200 years	P2	(−32.92, −42.64)	
	P3	(−46.71, −42.19)	(−20.56, 0.79)

Since the 1960s, human activities, such as the construction of check dams, returning farmland to forest and irrigation, have led to a significant decrease in runoff and sediment in the WRB. Among them, returning farmland to forests and irrigation played a dominant role in runoff changes, while the construction of check dams played a dominant role in sediment load changes [36]. Moreover, the lifespan of small- and medium-sized check dams, which were built in the 1970s and 1980s, are mostly less than 20 years. Most of them were silted up or even failed after the middle of the 1990s. This is also the main reason for the significant change rates in the maximum possible joint design value of sediment in P2 and P3.

4. Discussion

4.1. Impacts of Runoff Erosion Energy on Sediment

As the underlying surface continually changes, runoff and its erosion energy in the WRB also changes accordingly [37]. Therefore, analyzing the relationship between runoff erosion energy and sediment can effectively demonstrate the regulating effects of underlying surface on improving soil erosion. As such, REP was selected as the erosion dynamics index to reveal the impact of underlying surface on sediment load in the basin from the perspective of runoff erosion energy. In Figure 6, sediment load in the WRB increased linearly with the increase in REP for three periods. The linear fitting relationship between sediment and REP in P2 was the best, with R^2 of 0.88 (Figure 6b). The linear fitting relationship between sediment and REP in P3 was the worst, with R^2 of only 0.35 (Figure 6c). The slope of the linear fitting function between REP and sediment was $P1 > P2 > P3$, indicating that the erosion capacity of unit runoff was gradually decreasing. The continuous promotion of soil- and water-conservation measures in the basin over the past 60 years has profoundly changed the erosion features of runoff erosion energy, ultimately acting out a decrease in sediment.

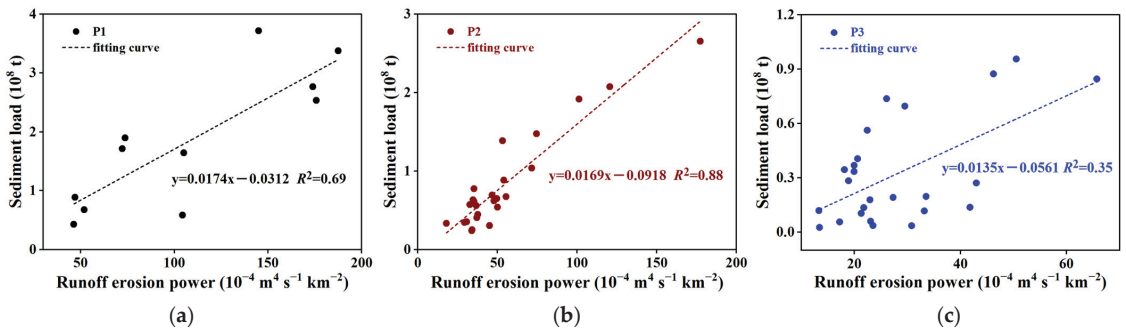


Figure 6. Relationships between REP and sediment load in the WRB under three periods. (a) The relationship in P1; (b) the relationship in P2; (c) the relationship in P3.

On the basis of previous results and experiments, Moore and Burch indicated that sediment load increased with unit runoff erosion power linearly, especially for sediment particles with sizes of 0.2 mm and 0.3 mm [38]. By using an indoor scouring experiment, Li et al. proposed that the greater the runoff erosion energy consumed, the more sediment particles were detached and transported; the relationship between them was logarithmic function [21]. Based on previous experiences and experiments, and by setting up five discharge intensities and ten slope gradients, Li et al. considered that runoff erosion power and sediment load existed in a linear relationship, and the higher the discharge intensity, the faster the speed that sediment load increased with runoff erosion power [23].

The study conducted cross-wavelet analysis on the relationship between REP and sediment load in order to support the periodic changes in sediment load and REP. Figure 7a showed the cross-wavelet energy spectrum of annual REP and annual sediment load in the WRB. There was a resonance period between annual REP and annual sediment load, which was about 0–4 years from 1962 to 1980. However, the change in annual REP lagged behind the change in annual sediment load from 1962 to 1970, while it stayed ahead in the opposite position from 1970 to 1980. Based on the wavelet coherence spectrum (Figure 7b), approximately 85% of the area was highly correlated between annual REP and annual sediment load in the entire time–frequency domain of the low-energy region. It indicated that REP was a representative factor affecting sediment load.

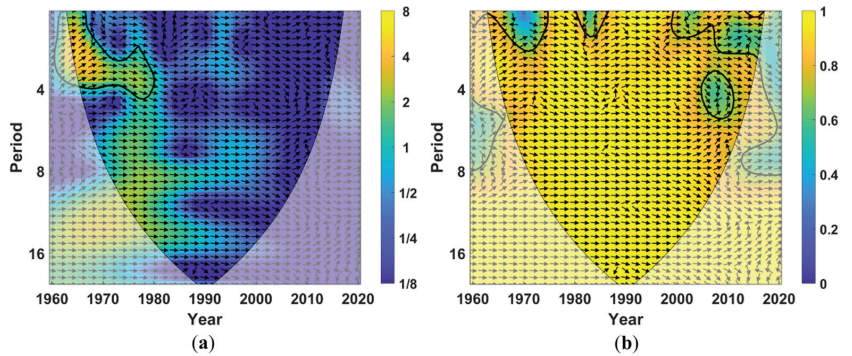


Figure 7. Cross-wavelet transform of annual sediment and annual REP in the WRB. (a) The cross-wavelet energy spectrum; (b) the wavelet coherence spectrum. Note: The black thin line vertebral body represents the effective spectral value area, and the black thick line within the area represents a confidence interval of significance level of 0.05. Arrows reflect phase difference: arrows pointing 0~90 degrees and 270~360 degrees indicate that the change phase of annual REP and annual sediment load is consistent; arrows pointing 90~270 degrees indicate that the change phase of annual REP and annual sediment load is opposite; arrows pointing 0~180 degrees indicate that annual REP change leads annual sediment transport change; and arrows pointing 180~360 degrees indicate that annual REP change lags behind annual sediment load change.

4.2. Impacts of Underlying Surface Change on Runoff and Sediment

4.2.1. Check Dam and Terrace Construction

Compared with other conservation measures, check dam has more obvious advantages in blocking sand, silting up the land and increasing grain yield, and it is widely promoted in the Loess Plateau. Since the 1960s, the WRB has gradually implemented soil- and water-conservation measures, including terrace and check dam. In Figure 8a, there are tremendous changes in cumulative number and cumulative siltation capacity (CSC) of large check dams in the WRB over the past 60 years. Up to 2008, there were 1184 large check dams in the WRB, with the CSC of $13.97 \times 10^8 \text{ m}^3$. It also can be seen that 1967–1975 was the first rapid construction period of check dams in the WRB, and the second peak appeared after 2000. Terrace was also widely constructed in the WRB and showed a continuous increase in cumulative area over the past 60 years, with a particularly fast growth rate from 1960 to 2000 (Figure 8b). After 2000, the construction speed of terrace in the WRB gradually slowed down. And until 2015, the cumulative area reached 1224.29 km². The terrace area (TA) in the watershed during 2001 to 2015 increased by 5.62 km² annually, which is much lower than that during 1960 to 2000 (increased by 27.78 km² annually).

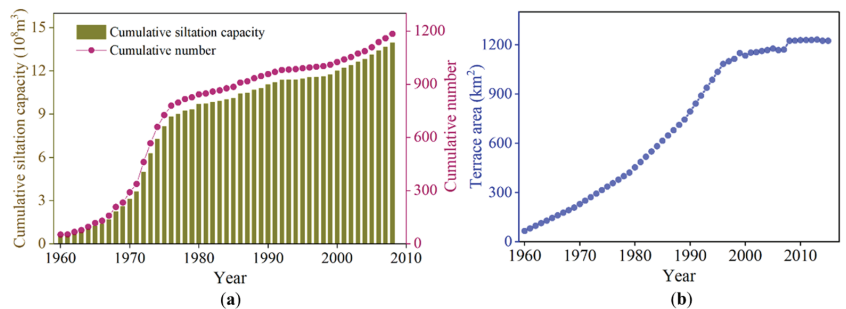


Figure 8. Change trend in large check dam and terrace in the WRB. (a) The variation curve of CSC and cumulative number of check dam; (b) the variation curve of TA.

Combined with Figure 4, large dam constructed in the 1970s significantly reduced runoff and sediment in the WRB during that period and became the main reason for change point of coupling coordination between runoff and sediment in 1971. In addition, with most of check dams constructed in the 1970s and 1980s gradually filled up, their retention effects decreased, which also led to the increase in runoff and sediment in the mid to late 1990s [39]. In the WRB, Xu et al. thought that with effective area of check dams reached its highest value in the 1980s and decreased after the 1990s, which led to the rebound of sediment load [40]. Unfortunately, the changes in TA did not coincide with runoff and sediment in the study period. It seems that the influence of check dam on changes in runoff and sediment in the WRB was more significant than that of terrace. On the time scale of single rainfall, the contribution of check dams to sediment reduction was higher than terraces. Taking the “7•26” rainstorm in 2017 as an example, sediment load reduced by conservation measures in the Chabagou watershed reached 79%, of which check dams contributed 58% and higher than terraces [41].

4.2.2. Vegetation Restoration

Affected by human activities and climate change, as well as the structure, process and pattern of land use, the Loess Plateau region has undergone significant changes, which has led to changes in surface ecological and hydrological processes [42]. From Figure 9, it can be seen that the overall change in land use in the WRB over the past 30 years was a decrease in the area of cropland and barren land and an increase in the area of shrubland, grassland, water body and construction land. The area of cropland and barren land decreased from 668.22 km² and 317.75 km² in 1985 to 510.31 km² and 95.33 km² in 2019, respectively. The corresponding decrease proportion was 5.6% and 9.8%. The area of shrubland, grassland, water area and construction land increased from 0.27 km², 1780.26 km², 6.03 km² and 6.30 km² in 1985 to 3.37 km², 2197.68 km², 7.51 km² and 18.65 km² in 2019, respectively. The corresponding increase proportion was 0.1%, 14.7%, 0.1% and 0.4%.

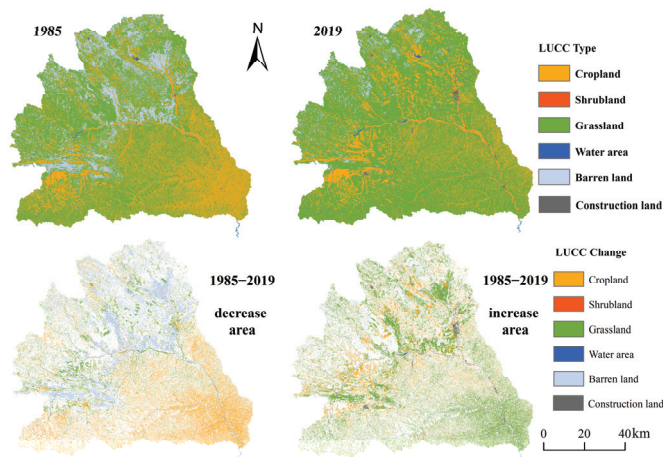


Figure 9. Land-use changes in the WRB.

The decrease in the cropland and barren land’s area, as well as the increase in shrubland and grassland’s area, induced a significant improvement in the vegetation conditions in the basin. By interpreting remote sensing images, the increased shrubland and grassland in the WRB mostly transformed from rehabilitated land or abandoned land [43,44]. Since the implementation of the “Returning Farmland to Forests and Grassland” project in 1999, vegetation restoration in the WRB has made remarkable achievements. After 2000, NDVI has increased at an average annual rate of 0.01 to 0.48 in 2020 (Figure 10).

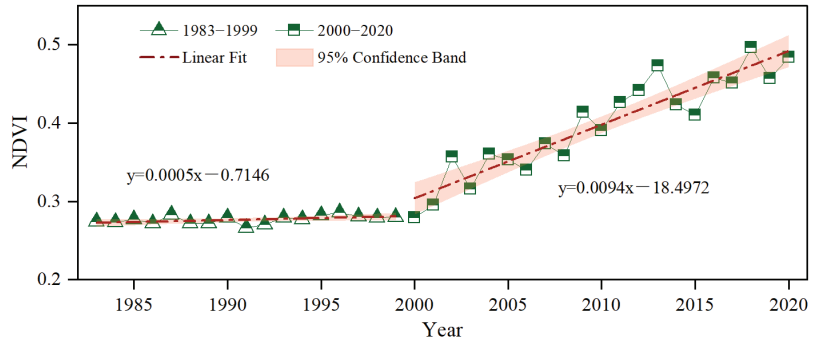


Figure 10. NDVI changes in the WRB from 1983 to 2020.

Because vegetation can intercept more runoff than barren land and construction land [45], the increase in shrubland and grassland could be the cause of runoff reduction. Most of all, the infiltration capacity of shrubland and grassland is stronger than other land use [46]. Therefore, it is likely that vegetation restoration in the WRB caused the decrease in runoff and sediment. The effects of land type change on runoff and sediment load has been investigated in several catchments. In the Cau River catchment, Phan et al. identified that if 11.07% of vegetation land converted to cropland, runoff and sediment load could increase by 3.93% and 8.94%, respectively [47]. In the Be River catchment, Khoi et al. reported that approximately 14.07% of shrubland converted to cropland during 1990 to 2001; thus, runoff and sediment load increased by 1.2% and 11.3%, respectively [48].

4.3. Relationships between Runoff, Sediment and Impacting Factors

The correlation analysis of Pr (precipitation), REP, CSC, TA, and NDVI with runoff and sediment load is shown in Table 3. The negative correlation relationships between Pr and runoff and sediment load were all poor in PE. It seems that precipitation did not promote runoff and sediment load throughout the entire study period on the surface. Actually, it was because the contributions of conservation measures to runoff and sediment reduction were too high (even over 100%), which hid the contribution of Pr. Similar results actually existed in the Zhifanggou watershed [49] and the Qingshui River Basin [50]. In addition, since precipitation, runoff and sediment load all increased in P1 (Figure 4), Pr and runoff, sediment load had a significant positive correlation relationships ($p < 0.01$).

Table 3. Relationships between runoff and sediment and impacting factors in the WRB.

Index	Period	Pr	REP	CSC	TA	NDVI
Runoff	PE	-0.216	0.892 ***	-0.809 ***	-0.779 ***	-0.152
	P1	0.778 **	0.859 ***	0.193	0.253	
	P2	0.558 **	0.825 ***	-0.328	-0.354	
	P3	0.547	0.852 ***	-0.596 *	-0.036	0.397 *
Sediment load	PE	-0.138	0.916 ***	-0.550 ***	-0.540 ***	-0.477 **
	P1	0.842 **	0.829 **	0.349	0.466	
	P2	0.345	0.938 ***	-0.071	0.028	
	P3	-0.093	0.590 **	-0.530	-0.737 ***	-0.455 *

Note: PE represents the entire research period from 1960 to 2020; *** represents significant at 0.001 level; ** represents significant at 0.01 level; * represents significant at 0.05 level; Pr represents precipitation.

The correlation coefficients between REP and runoff were all above 0.82 at four periods, which showed a highly significant correlation. The correlation relationship between REP and sediment load also reached a significant level ($p < 0.01$). CSC and TA all showed highly significant negative correlation with runoff and sediment load in PE, but CSC correlated with runoff ($p < 0.05$) and TA correlated with sediment load in P3 ($p < 0.001$). NDVI

had a significant negative correlation with sediment load in PE and P3 ($p < 0.05$), but showed a complex relationship with runoff. The correlation between NDVI and runoff was not significant in PE but significant in P3 ($p < 0.05$). Among three conservation measures, engineering measures represented by check dam showed the most significant sediment reduction function [41]. Moreover, when vegetation condition reached a good level, vegetation could significantly reduce sediment while increasing runoff to a certain degree [51,52]. The inner cause was vegetation, which led to a regional precipitation increase and ultimately produced more runoff [53,54].

The elastic coefficients' absolute value of REP, CSC, TA and NDVI to sediment was all higher than to runoff in Table 4. When REP increased by $1 \text{ m}^4 \text{ s}^{-1} \text{ km}^{-2}$, runoff and sediment increased by $0.32 \times 10^8 \text{ m}^3$ and $1.18 \times 10^8 \text{ t}$, respectively. When CSC increased by $1 \times 10^8 \text{ m}^3$, runoff and sediment decreased by $0.47 \times 10^8 \text{ m}^3$ and $0.98 \times 10^8 \text{ t}$, respectively. When TA increased by 1 km^2 , runoff and sediment decreased by $0.39 \times 10^8 \text{ m}^3$ and $0.92 \times 10^8 \text{ t}$, respectively. When NDVI increased by 1, runoff and sediment decreased by $0.12 \times 10^8 \text{ m}^3$ and $1.98 \times 10^8 \text{ t}$, respectively. As the same type of measure, the sediment retaining ability of check dam was better than terrace [55,56]. For runoff reduction, the contribution rate of CSC was the highest (95.4%), followed by REP (72.6%), TA (71.1%) and NDVI (25.4%). For sediment reduction, the contribution rate of REP was the highest (93.8%), followed by CSC (85.1%), NDVI (75.8%) and TA (63.0%). The contribution rate of CSC and TA to runoff change was higher than sediment. This was because check dam and terrace reduced sediment mainly by intercepting runoff [57]. The contribution rate of NDVI to sediment reduction was significantly higher than runoff. This is related to the property of vegetation with stronger sediment and weaker runoff controlling [58].

Table 4. Elastic coefficients and contribution rates of impacting factors to runoff and sediment.

Index	REP		CSC		TA		NDVI	
	Runoff	Sediment Load						
ϵ_{X-Y}	0.32	1.18	-0.47	-0.98	-0.39	-0.92	-0.12	-1.98
C_X	72.6%	93.8%	95.4%	85.1%	71.1%	63.0%	25.4%	75.8%

Note: The reference period of REP, CSC and TA are all 1960–1970, and the change period of them are 1970–2020, 1970–2008, 1970–2015, respectively; the reference period of NDVI is 1983–1999, and the change period is 2000–2020.

The contribution of underlying surface to runoff and sediment load in the MYRB has been calculated by several researchers. By comparing runoff and sediment change of two basins from 1956 to 2010, Sun et al. reported that contributions of underlying surface to runoff and sediment reduction in the Jialu River Basin were 97.3% and 95.8%, respectively, and in the Kuye River Basin, they were 86.1% and 80.5%, respectively [59]. Similar results were also obtained in the Lan River Basin. Ma et al. calculated that with underlying surface improved, the contribution of conservation measures to runoff and sediment reduction during 1999 to 2018 even reached 117.9% and 103.5%, respectively, which can be compared with the reference period (1955–1982) [60]. It could be said that changes in underlying surface caused by conservation measures are the main factor affecting runoff and sediment reduction in the WRB. However, with underlying surface improved, the hydrological connectivity of the WRB decreased continuously, leading to more runoff being intercepted and infiltrated [61]. Less runoff meant less sediment transportation, so the ultimate result was decreased sediment load in the WRB. Meanwhile, since REP was calculated based on runoff, the relationship between them was definitely very close, and so was the relationship between REP and sediment load (Table 3). But once runoff with low sediment concentration is generated, REP in the basin increases rapidly, inducing a large amount of sediment [62]. This may explain why the contribution of REP to sediment load was the highest compared with underlying surface.

5. Conclusions

Based on runoff and sediment data from 1960 to 2020, and supplemented with underlying surface information, this study evaluated the coupling relationship between runoff and sediment in the WRB and revealed the impacts of erosion energy and underlying surface. Finally, the study reached the following conclusions:

- (1) By constructing a diagnostic method based on coupling coordination degree for change point in runoff and sediment relationship, it was identified that there are two change points in the runoff and sediment coupling relationship in the WRB, which were 1971 and 1996. The copula joint distribution of runoff and sediment verified that there were indeed two change points. The diagnosis method for the runoff and sediment coupling relationship can be used to identify the change point. Runoff and sediment decreased gradually in three periods.
- (2) Under the same return period, the value of maximum possible joint design value of runoff and sediment in P1 were all the highest, followed by P2 and P3. The change trend in the return period was similar to the maximum possible joint design value. The change rates of the maximum possible joint design value of runoff in P2 and P3 were smaller than sediment under five return periods. With the underlying surface improved, the change rates of maximum possible joint design value decreased.
- (3) Although sediment increased with the increase in REP in three periods, the erosion capacity of unit runoff was gradually decreased. The resonance period between annual REP and annual sediment load was about 0–4 years from 1962 to 1980. Approximately 85% of the area was highly correlated between REP and sediment load. REP could significantly increase runoff and sediment in PE, P1, P2 and P3. The contribution rates of REP to runoff and sediment were 72.6% and 93.8%, respectively. Check dam and terrace could significantly decrease runoff and sediment in PE; the contribution rates of them to runoff reduction were 95.4% and 71.1%, respectively, and their contribution rates to sediment reduction were 85.1% and 63.0%, respectively. NDVI could decrease sediment in PE and increase runoff in P3.

Author Contributions: Conceptualization: Q.Y. and H.G.; methodology and software: K.L. and Y.H.; formal analysis: H.G.; resources and data curation: Y.H.; writing—original draft preparation and writing—review and editing: Q.Y.; visualization: Y.H. and Q.Y.; supervision: Z.L.; funding acquisition: H.G. All authors have read and agreed to the published version of the manuscript.

Funding: This research was funded by the National Key Research and Development Program of China (No. 2022YFF1300803).

Data Availability Statement: Original data is available from the Yellow River Basin Hydrological Yearbook.

Acknowledgments: We express our thanks to Yellow River Institute of Hydraulic Research (YRIHR) for providing data, as well as the anonymous reviewers and editors for providing constructive suggestions that improved the manuscript greatly.

Conflicts of Interest: The authors declare no conflicts of interest.

References

1. Douglas, I. Man, vegetation and the sediment yields of rivers. *Nature* **1967**, *215*, 925–928. [CrossRef]
2. Best, J. Anthropogenic stresses on the world's big rivers. *Nat. Geosci.* **2018**, *12*, 7–21. [CrossRef]
3. Miao, C.Y.; Gou, J.J.; Fu, B.J.; Tang, Q.H.; Duan, Q.Y.; Chen, Z.S.; Lei, H.M.; Chen, J.; Guo, J.L.; Borthwick Alistair, G.L.; et al. High-quality reconstruction of China's natural streamflow. *Sci. Bull.* **2022**, *67*, 547–556. [CrossRef] [PubMed]
4. Jansen, I.M.L.; Painter, R.B. Predicting sediment yield from climate and topography. *J. Hydrol.* **1974**, *21*, 371–380. [CrossRef]
5. Khoi, D.N.; Suetsugi, T. The responses of hydrological processes and sediment yield to land-use and climate change in the Be River Catchment, Vietnam. *Hydrol. Process.* **2014**, *28*, 640–652. [CrossRef]
6. Yan, Q.H.; Lei, T.W.; Yuan, C.P.; Lei, Q.X.; Yang, X.Y.; Zhang, M.L.; Su, G.X.; An, L.P. Effects of watershed management practices on the relationships among rainfall, runoff, and sediment delivery in the hilly-gully region of the Loess Plateau in China. *Geomorphology* **2015**, *228*, 735–745. [CrossRef]

7. Taye, T.; Moges, A. Implication of long-term watershed development on land use/land cover change and sediment loss in Maybar Sub-Watershed, South Wello Zone, Ethiopia. *Cogent Food Agric.* **2020**, *7*, 1863596. [CrossRef]
8. Gao, P.; Mu, X.M.; Wang, F.; Li, R. Changes in streamflow and sediment discharge and the response to human activities in the middle reaches of the Yellow River. *Hydrol. Earth Syst. Sci.* **2011**, *15*, 1–10. [CrossRef]
9. Zhao, Y.; Hu, C.H.; Zhang, X.M.; Lv, X.Z.; Yin, X.L.; Wang, Z.Y. Response of sediment discharge to soil erosion control in the middle reaches of the Yellow River. *Catena* **2021**, *203*, 105330. [CrossRef]
10. Tang, K.L. *Soil and Water Conservation in China*; Science Press: Beijing, China, 2004.
11. Jin, Z.; Cui, B.L.; Song, Y.; Shi, W.Y.; Wang, K.B.; Wang, Y.; Liang, J. How many check dams do we need to build on the Loess Plateau? *Environ. Sci. Technol.* **2012**, *46*, 8527–8528. [CrossRef]
12. Wei, W.; Chen, D.; Wang, L.X.; Daryanto, S.; Chen, L.D.; Yu, Y.; Lu, Y.L.; Sun, G.; Feng, T.J. Global synthesis of the classifications, distributions, benefits and issues of terracing. *Earth Sci. Rev.* **2016**, *159*, 388–403. [CrossRef]
13. Mohammad, A.G.; Adam, M.A. The impact of vegetative cover type on runoff and soil erosion under different land uses. *Catena* **2010**, *81*, 97–103. [CrossRef]
14. Li, M.; Zhang, C.Y.; Wang, H.Y.; Wang, S. Influence of ecological technology measures on the annual sediment load of the Wuding River. *J. Resour. Ecol.* **2017**, *8*, 385–391.
15. Wang, W.Z.; Jiao, J.Y. Temporal and spatial variation characteristics of erosion and sediment yield in the Loess Plateau. *Acta Geogr. Sin.* **2002**, *57*, 210–217.
16. Cai, Q.G. Soil erosion and management on the Loess Plateau. *J. Geogr. Sci.* **2001**, *11*, 53–70.
17. Zhou, Y.Y.; Shi, C.X.; Du, J.; Fan, X.L. Characteristics and causes of changes in annual runoff of the Wuding River in 1956–2009. *Environ. Earth Sci.* **2013**, *69*, 225–234. [CrossRef]
18. Jin, Z.; Li, J.Y. Analysis of driving factors for runoff and sediment variations during 1961 to 2012 in Wuding River Basin. *Acta Agric. Jiangxi* **2016**, *28*, 79–84.
19. Shi, P.; Zhang, Y.; Ren, Z.P.; Li, P.; Gong, J.F. Land-use changes and check dams reducing runoff and sediment yield on the Loess Plateau of China. *Sci. Total Environ.* **2019**, *664*, 984–994. [CrossRef]
20. Xu, J.; Wang, H. Influence of soil and water conservation measures on reducing in frequency of hyperconcentrated flows in the Wudinghe River basin. *Environ. Earth Sci.* **2011**, *62*, 1513–1520. [CrossRef]
21. Li, Z.B.; Lu, K.X.; Ding, W.F. Study on the dynamic process of rill erosion of loess slope surface. *Int. J. Sediment Res.* **2001**, *2*, 308–314.
22. Ellison, W.D. Soil erosion studies, part I. *Agric. Eng.* **1947**, *28*, 145–146.
23. Li, P.; Zhang, L.H.; Li, Z.B.; Zheng, L.Y. Dynamic Mechanics of Soil Erosion by Runoff on Loess Slope. *Nat. Environ. Pollut. Technol.* **2013**, *12*, 297–301.
24. Zhang, X.; Liu, L.Y.; Chen, X.D.; Gao, Y.; Xie, S.; Mi, J. GLC_FCS30: Global land-cover product with fine classification system at 30 m using time-series Landsat imagery. *Earth Syst. Sci. Data* **2021**, *13*, 2753–2776. [CrossRef]
25. Jia, S.F.; Zhu, W.; Lv, A.F.; Yan, T. A statistical downscaling algorithm of TRMM precipitation based on NDVI and DEM in the Qaidam Basin of China. *Remote Sens. Environ.* **2011**, *115*, 3069–3079. [CrossRef]
26. Carriaga, C.C.; Mays, L.W. Optimal control approach for sedimentation control in alluvial rivers. *J. Water Res. Plan. Manag.* **1995**, *121*, 408–417. [CrossRef]
27. Pettitt, A.N. A non-parametric approach to the change-point problem. *Appl. Stat.* **1979**, *28*, 126–135. [CrossRef]
28. Yu, K.X.; Xiong, L.H.; Gottschalk, L. Derivation of low flow distribution functions using copulas. *J. Hydrol.* **2014**, *508*, 273–288. [CrossRef]
29. Bozdogan, H. Model selection and Akaike's information criteri on (AIC): The general theory and its analytical extension. *Psychometrika* **1987**, *52*, 345–570. [CrossRef]
30. Salvadori, G.; De Michele, C.D. Frequency analysis via copulas: Theoretical aspects and applications to hydrological events. *Water Resour. Res.* **2004**, *40*, W12511. [CrossRef]
31. Salvadori, G.; De Michele, C.; Durante, F. On the return period and design in a multivariate framework. *Hydrol. Earth Syst. Sci.* **2011**, *15*, 3293–3305. [CrossRef]
32. Labat, D. Cross wavelet analysis of annual continental freshwater discharge and selected climate indices. *J. Hydrol.* **2020**, *385*, 269–278. [CrossRef]
33. Cheng, S.D. The Effects of Vegetation Pattern on Erosion and Sediment Yield of Slope-Gully System-Watershed. Ph.D. Thesis, Xi'an University of Technology, Xi'an, China, 2016.
34. Sankarasubramanian, A.; Limbrunner, J.F.; Vogel, R.M. Climate elasticity of streamflow in the United States. *Water Resour. Res.* **2001**, *37*, 1771–1781. [CrossRef]
35. Zhang, J.J.; Gao, G.Y.; Fu, B.J.; Gupta, H.V. Formulating an elasticity approach to quantify the effects of climate variability and ecological restoration on sediment discharge change in the Loess Plateau, China. *Water Resour. Res.* **2019**, *55*, 9604–9622. [CrossRef]
36. Bai, L.C.; Wang, N.; Jiao, J.Y.; Chen, Y.X.; Tang, B.Z.; Wang, H.L.; Chen, Y.L.; Yan, X.Q.; Wang, Z.J. Soil erosion and sediment interception by check dams in a watershed for an extreme rainstorm on the Loess Plateau, China. *Int. J. Sediment Res.* **2020**, *35*, 408–416. [CrossRef]

37. Han, Y.; Yang, Q.N.; Gao, H.D.; Xu, H. Runoff and sediment characteristics of flood event in typical watershed on the Loess Plateau based on vegetation restoration. *J. Soil Water Conserv.* **2023**, *37*, 278–283.
38. Moore, I.D.; Burch, G.J. Sediment transport capacity of shear and rill flow: Application of unit stream power theory. *Water Resour. Res.* **1986**, *22*, 1350–1360. [CrossRef]
39. Liu, X.Y.; Yang, S.T.; Li, X.Y.; Zhou, X.; Luo, Y.; Dang, S.Z. The current vegetation restoration effect and its influence mechanism on the sediment and runoff yield in severe erosion area of Yellow River Basin. *Sci. Sin. (Technol.)* **2015**, *45*, 1052–1059.
40. Xu, J.X.; Sun, J. Study of temporal variation of check dam construction in Wuding River Basin and some suggestion for some countermeasure. *J. Soil Water Conserv.* **2006**, *2*, 26–30.
41. Xiao, P.Q.; Wang, L.L.; Yang, Z.S.; Jiao, P.; Wang, Z.H. Study on sediment benefits of soil and water conservation measures in typical watershed in the Loess Plateau under the heavy rainfall. *J. Hydraul. Eng.* **2020**, *51*, 1149–1156.
42. Fu, B.J.; Wang, S.; Liu, Y.; Liu, J.B.; Liang, W.; Miao, C.Y. Hydrogeomorphic ecosystem responses to natural and anthropogenic changes in the Loess Plateau of China. *Annu. Rev. Earth Planet. Sci.* **2017**, *45*, 223–243. [CrossRef]
43. Zhang, X.P.; Zhang, L.; Zhao, J.; Rustomji, P.; Hairsine, P. Responses of streamflow to changes in climate and land use /cover in the Loess Plateau, China. *Water Resour. Res.* **2008**, *44*, W00A07. [CrossRef]
44. Feng, X.M.; Wang, Y.F.; Chen, L.D.; Fu, B.J.; Bai, G.S. Modeling soil erosion and its response to land-use change in hilly catchments of the Chinese Loess Plateau. *Geomorphology* **2010**, *118*, 239–248. [CrossRef]
45. Ma, X.; Xu, J.C.; Luo, Y.; Aggarwal, S.P.; Li, J.T. Response of hydrological processes to landcover and climate changes in Kejie watershed, South-West China. *Hydrol. Process.* **2009**, *23*, 1179–1191. [CrossRef]
46. Bai, P.; Liu, X.M.; Zhang, Y.Q.; Liu, C.M. Assessing the impacts of vegetation greenness change on evapotranspiration and water yield in China. *Water Resour. Res.* **2020**, *56*, e2019WR027019. [CrossRef]
47. Phan, D.B.; Wu, C.C.; Hsieh, S.C. Impact of climate change on stream discharge and sediment yield in northern Vietnam. *Water Resour.* **2011**, *38*, 827–836. [CrossRef]
48. Khoi, D.N.; Suetsugi, T. Impact of climate and land-use changes on hydrological processes and sediment yield—a case study of the Be River catchment, Vietnam. *Hydrol. Sci. J.* **2014**, *59*, 1095–1108. [CrossRef]
49. Yu, R.H.; Wang, G.L.; Yang, Y.F. Attribution analysis of water and sediment changes based on Budyko Hypothesis—Taking the small watershed of Zhifanggou in Ansai as an example. *Res. Soil Water Conserv.* **2023**, *30*, 86–92.
50. Huang, K.; Lu, K.X.; Shen, Z.Z.; Zhang, G.J.; Ren, Z.P.; Li, P. Attribution analysis of runoff and sediment changes at different scales in the Qingshui River Basin. *J. Irrig. Drain.* **2023**, *42*, 93–98.
51. Zhang, B.Q.; Tian, L.; Yang, Y.T.; He, X.G. Revegetation does not decrease water yield in the loess plateau of China. *Geophys. Res. Lett.* **2022**, *49*, e2022GL098025. [CrossRef]
52. Wang, H.; Sun, F.B.; Xia, J.; Liu, W.B. Impact of LUCC on streamflow based on the SWAT model over the Wei River basin on the Loess Plateau in China. *Hydrol. Earth Syst. Sci.* **2017**, *21*, 1929–1945. [CrossRef]
53. Liu, Y.; Ge, J.; Guo, W.D.; Cao, Y.P.; Chen, C.R.; Luo, X.; Yang, L.M.; Wang, S.Y. Revisiting biophysical impacts of greening on precipitation over the loess plateau of China using WRF with water vapor tracers. *Geophys. Res. Lett.* **2023**, *50*, e2023GL102809. [CrossRef]
54. Lü, M.X.; Ma, Z.G.; Lü, M.Z. Effects of climate/land surface changes on streamflow with consideration of precipitation intensity and catchment characteristics in the Yellow River Basin. *J. Geophys. Res. Atmos.* **2018**, *123*, 1942–1958.
55. Yuan, S.L.; Li, Z.B.; Chen, L.; Li, P.; Zhang, Z.Y. Influence of check dams on flood hydrology across varying stages of their lifespan in a highly erodible catchment, Loess Plateau of China. *Catena* **2022**, *210*, 105864. [CrossRef]
56. Ran, Q.H.; Tang, H.L.; Wang, F.; Gao, J.H. Numerical modelling shows an old check-dam still attenuates flooding and sediment transport. *Earth Surf. Proc. Land.* **2021**, *46*, 1549–1567. [CrossRef]
57. Wang, Z.Y.; Chen, Z.Y.; Yu, S.; Zhang, Q.; Wang, Y.; Hao, J.W. Erosion-control mechanism of sediment check dams on the Loess Plateau. *Int. J. Sediment Res.* **2021**, *36*, 668–677. [CrossRef]
58. Braud, I.; Vich, A.I.J.; Zuluaga, J.; Fornero, L.; Pedrani, A. Vegetation influence on runoff and sediment yield in the Andes region: Observation and modelling. *J. Hydrol.* **2001**, *254*, 124–144. [CrossRef]
59. Sun, Q.; Yu, K.X.; Li, Z.B.; Li, P.; Zhang, X.M.; Gong, J.F. The trends of streamflow and sediment and their driving factors in the middle reaches of the Yellow River. *Acta Geogr. Sinica* **2018**, *73*, 945–956.
60. Ma, Y.X.; Xia, L.; Fan, Y.; Gao, Y.Y. Effects of land use and climate change on runoff and sediment variation in typical watershed of the Loess Plateau. *J. Soil Water Conserv.* **2021**, *35*, 38–45.
61. Appels, W.M.; Bogaart, P.W.; van der Zee, S.E.A.T.M. Surface runoff in flat terrain: How field topography and runoff generating processes control hydrological connectivity. *J. Hydrol.* **2016**, *534*, 493–504. [CrossRef]
62. Zhang, G.H.; Liu, Y.M.; Han, Y.F.; Zhang, X.C. Sediment Transport and Soil Detachment on Steep Slopes: I. Transport Capacity Estimation. *Soil Sci. Soc. Am. J.* **2009**, *73*, 1291–1297. [CrossRef]

Disclaimer/Publisher’s Note: The statements, opinions and data contained in all publications are solely those of the individual author(s) and contributor(s) and not of MDPI and/or the editor(s). MDPI and/or the editor(s) disclaim responsibility for any injury to people or property resulting from any ideas, methods, instructions or products referred to in the content.

Article

Rapid Estimation of Soil Erosion Rate from Exhumed Roots (Xiaolong Mts, China)

Miklós Kázmér¹, Keyan Fang², Yunchao Zhou³ and Zoltán Kern^{4,5,*}

¹ Department of Palaeontology, Eötvös University, Pázmány Sétány 1/c, H-1117 Budapest, Hungary; mkazmer@gmail.com

² Key Laboratory of Humid Subtropical Eco-Geographical Process (Ministry of Education), College of Geographical Sciences, Fujian Normal University, Fuzhou 350007, China; kfang@fjnu.edu.cn

³ Department of Soil and Water Conservation, Forest College, Guizhou University, Huaxi, Guiyang 550025, China; yczhou@gzu.edu.cn

⁴ Institute for Geological and Geochemical Research, HUN-REN Research Centre for Astronomy and Earth Sciences, Budaörsi út 45, H-1122 Budapest, Hungary; zoltan.kern@csfk.hun-ren.hu

⁵ CSFK, MTA Centre of Excellence, Konkoly Thege Miklós út 15-17, H-1121 Budapest, Hungary

* Correspondence: kern@geochem.hu or kern.zoltan@csfk.hun-ren.hu

Abstract: Soil erosion is a challenge worldwide, including in China. The dendrogeomorphic method was applied, for the first time, at Xiaolong Mts in Gansu Province to obtain a quantitative estimate of the soil erosion rate. The dataset built in this pilot study allowed the identification of exhumation texture in exposed roots between 1967 and 2002. The calculated mean erosion rate estimates (E_r) ranged from 2.6 to 16.5 mm yr⁻¹ and showed an increase with the slope steepness (s). The best fitting linear model ($E_r = 0.043(\pm 0.017) \times s + 3.09(\pm 1.04)$; $R^2 = 0.20$; $R^2_{adj} = 0.16$; $F = 6.18$; $p = 0.02$) could be used in future research to determine and to map soil denudation in this part of the Xiaolong Mts. Notable associations were found between erosive rainfalls and root exhumation events. Daily (R_{x1day}) and 5-day (R_{x5day}) precipitation totals of 56 and 73 mm, respectively, seem to be critical thresholds which if exceeded will always induce root exhumation in the same year or in the consecutive season in the forest of the Xiaolong Mts in the studied period.

Keywords: dendrogeomorphology; erosion rate; tree roots; wood anatomy; China

Citation: Kázmér, M.; Fang, K.; Zhou, Y.; Kern, Z. Rapid Estimation of Soil Erosion Rate from Exhumed Roots (Xiaolong Mts, China). *Land* **2024**, *13*, 771. <https://doi.org/10.3390/land13060771>

Academic Editors: Jianye Li, Xingyi Zhang, Weida Gao, Wei Hu and Qiang Chen

Received: 12 April 2024
Revised: 21 May 2024
Accepted: 23 May 2024
Published: 29 May 2024



Copyright: © 2024 by the authors. Licensee MDPI, Basel, Switzerland. This article is an open access article distributed under the terms and conditions of the Creative Commons Attribution (CC BY) license (<https://creativecommons.org/licenses/by/4.0/>).

1. Introduction

Soil erosion is a primary driver of land degradation worldwide [1]. Reduction in land degradation caused by soil erosion is one of the main issues among the United Nations' adopted Sustainable Development Goals [2]. China, in particular, faces a substantial soil erosion challenge. According to the national soil erosion survey conducted by the Ministry of Water Resources of the People's Republic of China in 2011, the total soil loss area was approximately 1.29 million km², meaning 13.5% of the land area of the country [3]. China's Loess Plateau has long been one of the most severely eroded areas not only within the country but on Earth [4].

The rainfall–runoff process is primarily responsible for causing soil erosion and transporting soil [5,6], driving the detachment of soil particles by rain splash [7–10] and the downslope transport of soil particles by runoff [11]. Extreme weather events, especially heavy rainfall [12], remove an increasing amount of soil from unprotected surfaces. A recent assessment project found an increase in rainfall erosivity for most regions in China. Under the SSP1-RCP2.6 and SSP5-RCP8.5 scenarios, the rainfall erosivity factor is expected to rise by 18.9 and 19.8% for the near-term and 26.0 and 46.5% for the long-term, respectively [13], underlining the importance of improved understanding of the generation, impacts, and future trends of extreme rainfall erosivity [12].

There are a multitude of studies describing and measuring the pattern and rate of soil erosion, ranging from the simple pin method up to high-resolution terrestrial laser

scanning [14,15]. However, time series longer than a couple of years are rare, and decadal-scale measurements—mostly represented by fallout radionuclides—lack annual temporal resolution [16–18].

Estimation and modelling of soil erosion are important issues in environmental assessment in Asian mountains as well [19–21]. Numerous soil erosion studies are related to arable soils [5,22], while forested regions are much more neglected in this respect [23]. This dichotomy is likely explained by the fact that soil loss and runoff rates on land covered by grass and trees are one to three orders of magnitude lower than rates on cropland [6].

Plant growth and vegetational succession can be hindered by erosion to varying degrees [24–26]. Root exhumation is the process where roots growing underground appear at the soil surface due to natural or human-made causes. As the erosion process progresses, exposed roots start to appear [24].

Schulman's [27] seminal paper started the 'career' of root-based soil erosion studies. The recognition that tree roots are suitable for dating [28] was also a key step in the development of root-ring-based erosion rate quantification. First, the age of exposed roots was determined [29], and then the starting asymmetry of buttress roots was dated [30], and dating cambium damage was the method used [31] later. When cambium is damaged, it dies back, and growth is discontinued along certain sectors of the root circumference. However, segments that are diametrically opposed, usually in lower parts, continue growing. It was a 'revolutionary' new method in assessing erosion rates over millennia [30]. A further step in methodological development was recognizing that growth rings, which are mostly concentric in underground settings, tend to change to elliptical cross-section of various eccentricities when exposed [32]. Dating the initiation of reaction wood formation in exposed roots, in combination with scar-induced cambium dieback, became a further indicator of initial root exposure [31]. Owing to the experience gained during the past decades, dendrogeomorphological analysis of exposed tree roots has evolved into an established method capable of dating soil erosion with annual accuracy on a decadal to centennial temporal scale [33]. Both sheet erosion of slopes and linear erosion of gullies can be quantified by dendrogeomorphological analysis of exposed tree roots yielding medium-term erosion rates [33]. Theoretically, roots of all tree and shrub species can be used for the determination of erosion rates [34], although anatomical ambiguities could make the application of the method impossible in certain cases.

Great dendrogeomorphological studies were carried out in subregions of the USA, the Mediterranean area, and in the Alps (see Stoffel, Corona, Ballesteros-Cánovas, and Bodoque [33], for an exhaustive list). However, we are aware only four studies in China, one on hillslopes in the temperate north [23] and few more on karsts in the subtropical south [35–37]. Inland continental regions, such as Gansu Province, are neglected in this respect. The total soil loss area makes up 76,112 km² in Gansu Province out of which ~18% is forest and shrub according to the interpolated maps of the national soil erosion survey of China completed in 2011 [3]. In the light of this, the dendrogeomorphological method offers itself to be applied for soil erosion estimation in the forested areas of Gansu Province. In the present paper, we illustrate selected root cross-sections from Gansu Province, People's Republic of China, and apply these features to quantify root exhumation caused by soil erosion for the first time in this region.

2. Materials and Methods

2.1. Site

The Xiaolong Mts are located in the West Qinling Mountain Range near Tianshui city and located in Tianshui area (34°26'27" N, 106°07'29" E, and 2085 m above sea level) in eastern Gansu Province (Figure 1). Gansu Province is locating in the southwestern sector of the erosion hotspot of China's Loess Plateau [4].

Abundant forest coverage is maintained by orographic precipitation. Natural mixed pine–oak forests dominated by Chinese pine (*Pinus tabulaeformis*) and Liaotung oak (*Quercus wutaishanica* Mayr) occur also relatively frequently at certain places in this region [38]. The

mountain has steep ridges, where many roots are conveniently exposed. The bedrock is coarse granite bearing thin soil cover classified as Leptic Cambisol, characterized by an organic matter content of 15 g kg^{-1} and a high content of sand and silt. The coarse soil structure is prone to water erosion. Gullies or small debris cones were not observed on the studied slopes so sheet erosion can be assumed to be the dominant type of soil erosion.

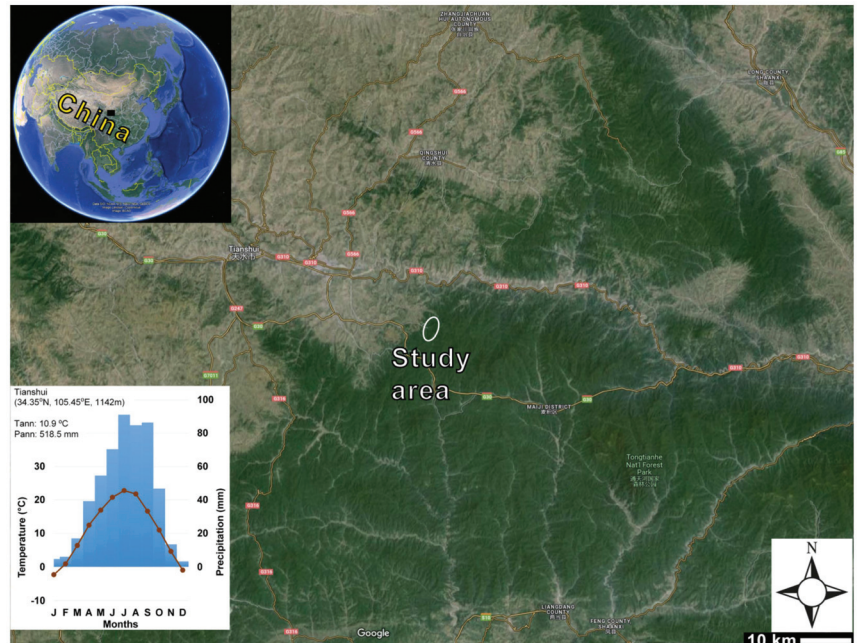


Figure 1. Location of Xiaolong Mts near Tianshui city. The study area is indicated in the main map (white ellipse), while the enlarged region is indicated by the black square to show the wider geographical context in the inset globe. Map source: GoogleEarth 2024. Inset graph: climate diagram for the Tianshui meteorological station showing the monthly mean temperature (solid line) and monthly precipitation (bar).

The region is at the marginal area of the Asian summer monsoon. Mean annual temperature is $10.9 \text{ }^{\circ}\text{C}$ and annual precipitation total is 520 mm at the nearby meteorological station (Tianshui). Annual rainfall is clearly concentrated in a wet season centered on July to September, registering $\sim 51\%$ of the annual precipitation total during these three months (Figure 1). The long-term average rainfall erosivity factor, the so-called R-factor, is moderate (~ 900 to $1000 \text{ MJ mm ha}^{-1} \text{ h}^{-1} \text{ a}^{-1}$) in this region [39]. The soil erosion rate at the study site is around $10 \text{ t ha}^{-1} \text{ a}^{-1}$, but there are also areas with higher annual rates in the surroundings [3].

2.2. Sampling and Measurements

Procedures involved in the root-based reconstruction of soil erosion processes followed standard working steps [33]. Thirty root disk samples were taken (coded from SMM101 to SMM130) using a hand-saw in May 2010 (Table 1 and Table S1). The exhumed roots were collected during a survey of several hectares of slopes (Figure 2). In the vicinity of the exhumed roots, trees were spaced 1 to 4 m apart. Roots extend up to several meters from the trees, so unfortunately, for roots exhumed further away from the trunk, it was not possible to clearly identify which root belonged to which tree (Figure 2A). Therefore, we cannot say that each sample belongs to a different tree, but it is very likely. A single disc sample was taken from a root.

Table 1. Exhumed root samples with the inferred basic input parameters and estimated average soil erosion rate taken from Xiaolong Mts, Gansu, China. Variable codes in the topmost row refer to Equation (1). Estimated uncertainty of E_{ra} is presented in brackets.

Variable in Equation (1)	-	C	D	NR_{ex}	E_{ra}
Sample Code	Slope Steepness	Average Exposure ¹	Exposure to Root Top	Years Elapsed Since First Exposure	Average Erosion Rate
	%	mm	mm	yr	mm yr ⁻¹
SMM101	36.4	89	0	42	3.3 (0.1)
SMM102	17.6	13.5	0	14	4.5 (0.2)
SMM103	17.6	12	2	21	2.9 (0.1)
SMM104	46.6	20	9	8	7.6 (0.4)
SMM105	46.6	40	2	19	4.6 (0.2)
SMM106	57.7	47	1.7	21	4.5 (0.1)
SMM107	57.7	28.5	1.5	15	5.1 (0.2)
SMM108	57.7	7	0	9	6.3 (0.3)
SMM109	17.6	40	4.5	16	5.3 (0.2)
SMM110	36.4	17	7.5	11	5.4 (0.3)
SMM111	17.6	128	5	37	4.7 (0.1)
SMM112	17.6	25	5	11	6.4 (0.3)
SMM113	36.4	63	2	24	4.6 (0.1)
SMM114	36.4	32	4	27	2.9 (0.1)
SMM115	70.0	87	6	29	4.5 (0.1)
SMM116	36.4	51	10	21	4.3 (0.1)
SMM117	46.6	117	0	27	6.2 (0.1)
SMM118	70.0	51	5	34	2.8 (0.1)
SMM119	57.7	68	15	40	2.6 (0.1)
SMM123	57.7	210	0	28	9.3 (0.1)
SMM124	119.2	345	0	24	16.5 (0.1)
SMM125	83.9	83	1.5	35	3.8 (0.1)
SMM126	83.9	175	0	40	5.6 (0.1)
SMM127	83.9	110	14	43	3.4 (0.1)
SMM128	83.9	140	0.5	27	7.0 (0.1)
SMM129	119.2	128	5.5	27	6.4 (0.1)
SMM130	46.6	108	0	30	5.3 (0.1)

¹ Mean of field measurements at both sides of the exposed root section. For the original field measurements see Table S1.



Figure 2. Field photos of exhumed roots. (A) A network of exhumed roots probably belonging to multiple trees. The position of sample SMM109 is shown. (B) Exhumed roots parallel to the slope. The position of sample SMM118 is shown.

Needed parameters to quantify the erosion rate are the thickness of the eroded soil layer since exposure and the number of rings grown since exposure. Data for the first are

measured both in the field (see Section 2.2.1) and in the laboratory (Figure 3); for the second, they are measured exclusively in the lab (see Section 2.2.2).

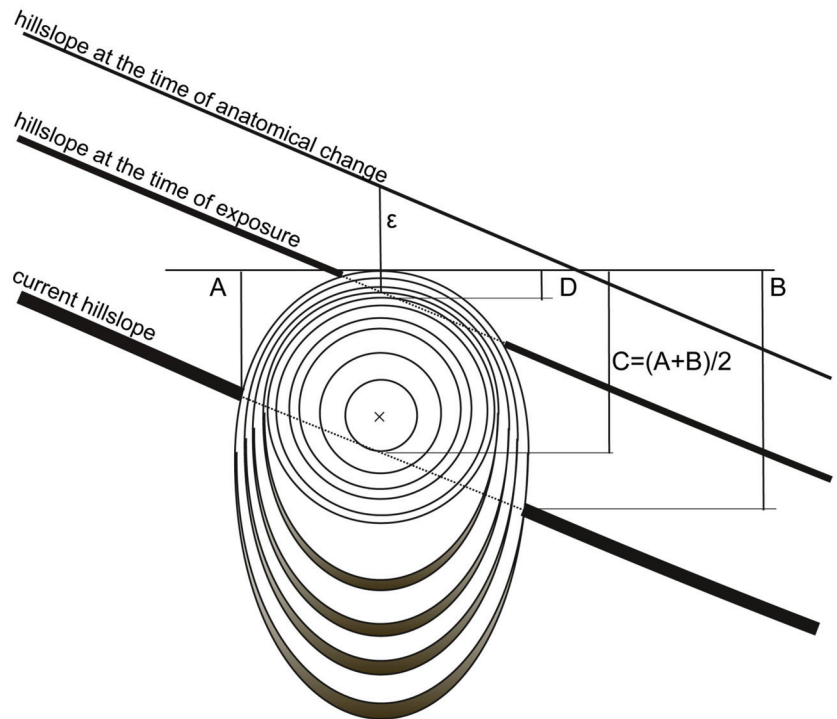


Figure 3. The scheme of measurements on exhumed roots. Soil-covered root: circular annual rings. Exhumed root: elliptical rings. To be measured in the field: A and B are the exhumation data of the top of the root above the soil surface on opposing sides of the root. C is the average of A and B. To be measured in the laboratory: D is the distance of the (first) exhumation marker from top of the root. ϵ is the thickness of the soil cover above the root at the appearance of the first exhumation marker. $C - D + \epsilon$ is the estimated total eroded thickness of soil since the first exhumation marker.

2.2.1. Field Methods

The following data were recorded for each sample: angle and aspect of slope and whether the root is parallel, perpendicular, or oblique to the slope. A detailed methodological description is provided in a separate paper [40]; only the key steps are listed below.

- Roots overgrowing stones in the soil were not sampled: these cannot grow downwards, i.e., their pith possibly moves upwards due to growth in diameter [41].
- Roots at least a meter away from stems were selected to avoid reaction wood potentially grown by the stress of the moving stem or erosion being overestimated due to the pull of the stem [42–44].
- Ground surface was carefully cleared of leaf litter, taking care not to remove any soil.
- A cross was marked on the topmost portion of the root with indelible ink.
- A photo was taken for documentation (Figure 2).
- Azimuth and tilt of the slope were measured by a geological compass or by a simple compass and tiltmeter and rounded to the nearest 5° .
- Direction of the root was recorded relative to the dip of the slope (parallel, perpendicular, or oblique). We note that we found that exposed roots in all directions were useful in the soil erosion reconstruction despite the recommendation of [33], in the caption to his Figure 10).

- Height of the cross-marked top portion of the root above the homogeneous slope was measured on both sides [33] to the closest millimeter with the help of ruler and level or with a caliper; this measurement was always made in vertical direction (i.e., not perpendicularly to the slope, see Figure 3) and the average of the two values was used in calculations (see Section 2.3).
- Soil was removed from both sides and from below the root for easy access for sawing.
- A disk of ~20 to 50 mm thickness was sawed from the root (thickness was determined so as to allow the sample to be held easily by fingers during grinding and polishing, see Section 2.2.2).

2.2.2. Laboratory Methods

Specimens of sawn disks were left to dry as necessary (often for weeks) before grinding and polishing by a belt sander using the facilities of the Budapest Tree-Ring Laboratory [45]. Particular care was taken to preserve the cross marking on the top of the sample.

- Direction of the top marker (drawn in the field) was marked again on at least one face of the disk.
- Both faces were grinded on a belt sander using progressively finer grit sizes [46] beginning with P120 (~125 μm) and ultimately finishing with P400 (33.5–36.5 μm), which is usually enough for an almost polishing-level quality of the sanded face. Occasionally, in the case of very fine rings, we hand-sanded portions of the disk with a P800 (20.8–22.8 μm) sandpaper.
- Exhumation markers, both geometrical and textural [40], were identified (see Section 2.2.3) under the microscope and marked with pencil.
- The number of rings was counted from the outermost ring grown during the year of sampling towards the pith and calendar years were assigned. The outermost ring in this case was incomplete since sampling was carried out in the growing season. The rings were checked over the entire transect to also account for the frequently observed wedging rings.
- Calendar years were assigned to exhumation markers.
- Distance between pith and the top of the sample was measured to the nearest 0.5 mm using a ruler or a caliper (Figure 3). Independent measurements of this parameter were performed to characterize the uncertainty of the laboratory measurements (see Appendix A).
- Distance between the first exhumation marker and the top of the sample was similarly measured to the nearest 0.5 mm using a ruler or a caliper (Figure 3).

2.2.3. Exhumation Markers in Conifers

Roots, when exhumed above ground, display various features in their altered tissue. A detailed treatment is provided and anatomical exposure markers are discussed in a separate paper [40]. Here, we briefly discuss only the markers used in the present study, recognizable without specialist equipment. Recognition of these features allows us to date the exhumation and decide whether it was slow or fast [40]. Features are grouped as (1) change from root texture to stem texture (gradual or sudden), (2) formation of reaction wood of increased ring width and lignin content, (3) injuries causing wounds and their overgrowth ring patterns, and (4) phenolic staining.

1. Change from root texture to stem texture (Figure 4A). Soil-covered roots are largely protected from frost and drought. The reduced environmental signals mostly yield uniformly sized cell lumina and thin walls in the earlywood of conifer roots. Latewood is often a single row of cells only. Exposure to aboveground conditions usually yields smaller cell lumina and thicker cell walls, both in the earlywood and in the latewood. In macroscopic view, this change is displayed as lighter belowground and darker aboveground rings. Latewood is particularly affected by aboveground conditions: it is significantly thicker than the underground latewood. In short: roots produce xylem similar to that of stems after exposure to aboveground conditions [47].

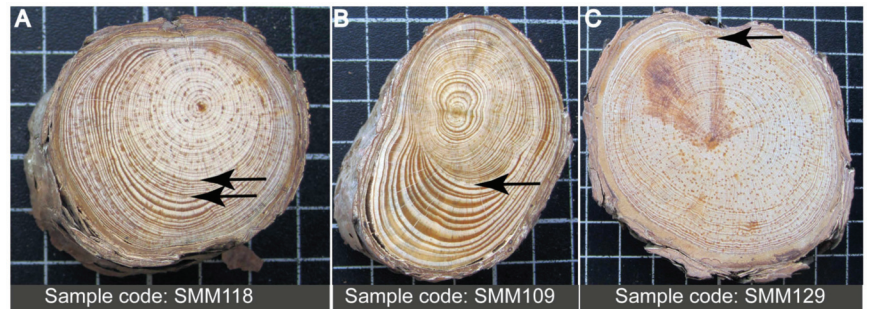


Figure 4. Examples of exhumation markers in exposed conifer roots. (A) Stepwise change from root texture to stem texture. Light, concentric rings with narrow latewood were substituted by increasingly elliptical rings with wide latewood (thin arrow) in the year of rapid exhumation. Later, irregular rings of reaction wood (thick arrow) mark the effect of mechanical stress. Resin ducts visible throughout. (B) Distorted symmetry. Narrow rings with thin latewood belong to underground roots. Rapid exhumation yielded reaction wood of wide rings and thick latewood (arrow). (C) Wound. Gradual change from root texture (narrow rings with barely visible latewood) in the center to stem texture along the margins is observed. It is evidence for gradual exhumation. There is a wound on top (arrow) overgrown by subsequent rings and covered by bark. Brownish phenolic compounds indicate the presence of another wound, out of the plane of the section. Resin ducts visible throughout. Scale: 10×10 mm grid pattern in black background.

2. Reaction wood is formed in the wood under mechanical stress. Conifers' reaction wood has wider rings than normal. The first ring with reaction wood dates the exhumation of the root. Multiple tilting events in the same stem may be recognized by changes in—among others—orientation of compression wood [33].
3. Distorted symmetry (Figure 4B). The growth of rings with eccentric symmetry and of reaction wood goes hand-in-hand [31]. Root exhumation, mass movement, or tilting of the plant can disturb this symmetry.
4. Wounds (Figure 4C) are caused by injury to the root by mechanical means, mostly above ground, rarely below ground. If the cambium is damaged and suffers dieback, growth is stopped at that place, bark falls off, and an open wound is formed.
5. Phenolic staining (by dark, reddish-brown compounds) adjacent to the wound (Figure 4C). These precipitates isolate the open wound from infection by bacteria and fungi. External surface of the stain is parallel with a ring—this is the year when the injury occurred.

2.3. Calculations and Evaluation

Unclearly discernible ring boundaries accompanied with dense/narrow tree-ring structure were observed in three semi-ring porous samples, presumably derived from *Quercus wutaishanica* roots, which could not be used for further evaluation. However, all the conifer samples ($n = 27$) were suitable for erosion dating.

Values of field-measured exhumation on both sides of the root (A and B) are averaged (C) since most roots enclosed an angle with the dip of the slope and were exhumed asymmetrically (Figure 3). Since roots overgrowing stones were not sampled, we assumed stability of the root axis through time. In this case, only the subsequent growth of the upper part of the root (D) since exposure must be subtracted from the field-measured exhumation of the root section [41]. It was demonstrated that anatomical changes associated with root exposure can occur already when the soil cover is reduced below a critical thickness [36,41], resulting in a bias. A species-specific estimate of this bias was not determined for the study area, but the mean value ($\varepsilon \cong 50$ mm) reported for roots of *Pinus* genera in previous studies [36,41] was taken. Exhumation rate—interpreted as mean annual erosion rate (Er_a)—was calculated since first exhumation as follows:

$$Er_a = (C - D + \epsilon) / NR_{ex} \quad (1)$$

where NR_{ex} stands for the number of growth rings counted following the oldest exhumation mark, with consideration of incomplete rings grown only in a portion of circumference. It practically equals the years elapsed since the exposure of the root. The measurement unit of C , D , and ϵ parameters is mm.

Measurement uncertainty of the field measurements (A and B) can be assigned to ± 2 mm, which corresponds to the reading uncertainty of the millimeter-scaled ruler based on our own long field experience. Measurement uncertainty of the lab measurements (D) was assigned to ± 1.2 mm if $D > 0$, since standard deviation of the lab measurement was overwhelmingly found below this value (Appendix A) while measurement uncertainty was assigned to 0 when $D = 0$. Individual uncertainties of the components were combined following the Gaussian error propagation approach [48].

Monthly precipitation totals and the monthly maximum daily precipitation sum (R_{x1day}) corresponding to the study site were retrieved from CRU TS4.07 [49] and HadEX2 [50] datasets, respectively, and combined to estimate monthly rainfall erosivity factor (R) following the Monthly III model of [51] as follows:

$$R_{month} = 0.077 \times P_{month} \times R_{x1day}_{month} \quad (2)$$

Monthly estimates of the rainfall erosivity factor were aggregated for each year to approximate the yearly erosivity factor (R), since better prediction capabilities resulted from using the finer resolution rainfall data as inputs at a given erosivity timescale and by summing results for coarser erosivity timescales [51].

Most soil erosion is induced by a small number of intense rainstorms with short duration and high rainfall intensity [12]. To account for the rainfall events or series of events within a year, annual R_{x1day} and maximum consecutive 5-day precipitation amount (R_{x5day}) were considered as indicators of short-period erosional activity for each year, retrieved again from HadEX2 [50]. The time series were screened to find the highest index values below which a root exhumation event did not occur and the lowest index in which exceedance was always accompanied by a root exhumation event. These index values could serve as empirical thresholds to define calm and intense conditions for soil erosional activity.

3. Results and Discussion

3.1. Rate and Time of Erosion

The first appearance of exhumation texture in the studied root sections appeared in 19 years between 1967 and 2002 (Table S1). More than one root exhumation appearance was dated to five years, and the most represented year is 1983 with four initiations; however, there is no obvious temporal clustering in the occurrence of the root exhumation events. We tend to interpret this as suggesting that the detected erosion events cannot be dominated anthropogenic causes, but this allows us to infer the evolution of erosion processes caused by natural factors over time.

The calculated erosion rate estimates ranged from 2.6 to 16.5 mm yr⁻¹ (Table 1). These values fit well to the published dendrogeomorphic reconstructions of erosion rates [33]. The limited data at hand is obviously insufficient to evaluate any potential difference related to slope facing. However, the expected positive association between slope steepness and erosion rate [20,52,53] is well reflected in the dataset (Figure 5). It is in agreement with the findings of other dendrogeomorphic studies detecting a positive relation between slope angle and erosion rates robustly at different timescales [36,41]. These observations further strengthen the credibility of root exhumation-based erosion rate estimates, which is worth emphasis since a recent analysis of erosion and runoff measurements on erosion plots in non-crop land use types in China did not find a systematic association with slope gradient either with the soil losses or with the runoff rates [6]. The presented regression model between slope steepness as an independent variable and erosion rate as a dependent

variable (Figure 5) could be used in future research to determine and to map soil denudation in this part of the Xiaolong Mts without the need for expensive instrumentation.

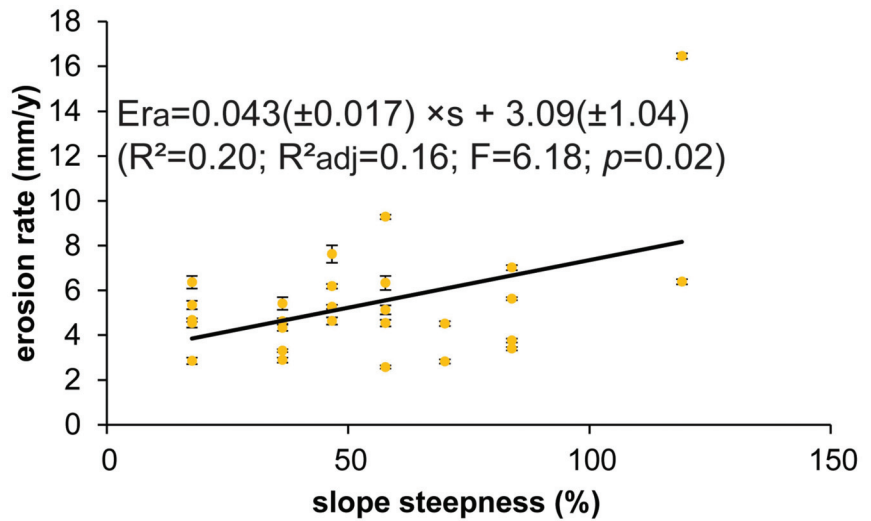


Figure 5. Estimated soil erosion rate (E_{ra}) and slope steepness (s) in the Xiaolong Mts (Gansu Province, China) and the derived linear regression model.

3.2. Coincidence between Wet Summers and Root-Based Erosion Events in the Xiaolong Mts between 1967 and 2002

Dendrogeomorphic evidence of root exhumation was lacking in each year when the sum of the estimated yearly erosivity factor did not reach $822 \text{ MJ mm ha}^{-1} \text{ h}^{-1} \text{ a}^{-1}$, while $R > 1448 \text{ MJ mm ha}^{-1} \text{ h}^{-1} \text{ a}^{-1}$ was always accompanied by root exposure evidence either in the same year or in the consecutive season (Figure 6). Considering the current estimate of the average R-factor ($\sim 1000 \text{ MJ mm ha}^{-1} \text{ h}^{-1} \text{ a}^{-1}$) in this region [39], this suggests that a yearly R-factor exceeding by $\sim 45\%$ the long-term average always induces major erosion in the pine forest of the Xiaolong Mts. The projected average R-factor increase ranges from 26 up to 46.5% for the long-term (2076–2100) in mainland China depending on the considered climate change scenario [13]. Taking this range of increase, the average erosivity factor might become the norm for inducing root exhumation in the Xiaolong Mts by the end of the 21st century. The match between the longest period continuously recording root exhumation (1980–1983) and the time interval (1978–1983) experiencing an estimated yearly R-factor $> 1365 \text{ MJ mm ha}^{-1} \text{ h}^{-1} \text{ a}^{-1}$ in all but one year (Figure 6) strengthens the view that an increase $> 40\%$ in the R-factor is surely a critical forecast for the soil erosion in this region.

Since the projected R-factor increase is primarily attributed to the elevated probability of extreme precipitation events [13], the temporal correspondence between extreme rainfall events and soil erosion events deserves scrutiny considering their strong coupling [12]. A simple visual inspection revealed notable associations between erosive rainfalls and root exhumation events. A root exhumation event was not documented in the Xiaolong Mts between 1965 and 2010 if the maximum daily precipitation sum ($R_{x1\text{day}}$) was below 30 mm. If an $R_{x1\text{day}}$ exceeding 56 mm appeared in a year, then it was always accompanied by root exposure evidence either in the same year or in the consecutive season. This empirical threshold is close to, although slightly above, the erosive rainstorm criterion for daily rainfall durations in the Loess Plateau [54]. Similar correspondence was observed with the maximum consecutive 5-day precipitation amount ($R_{x5\text{day}}$), as well. A root exhumation event did not occur in the Xiaolong Mts between 1965 and 2010 if the $R_{x5\text{day}}$ was below 45 mm in two consecutive years. However, if the $R_{x5\text{day}}$ exceeded 73 mm in a year then

it was always accompanied by root exposure evidence either in the same year or in the consecutive season (Figure 6). These empirically identified thresholds of extreme rainfall events can contribute practical clues considering the impact of extreme rainfall erosivity on soil erosion, and improving rainfall erosivity estimation [12] in the forest environments of the Xiaolong Mts, or maybe even for the wider Gansu region.

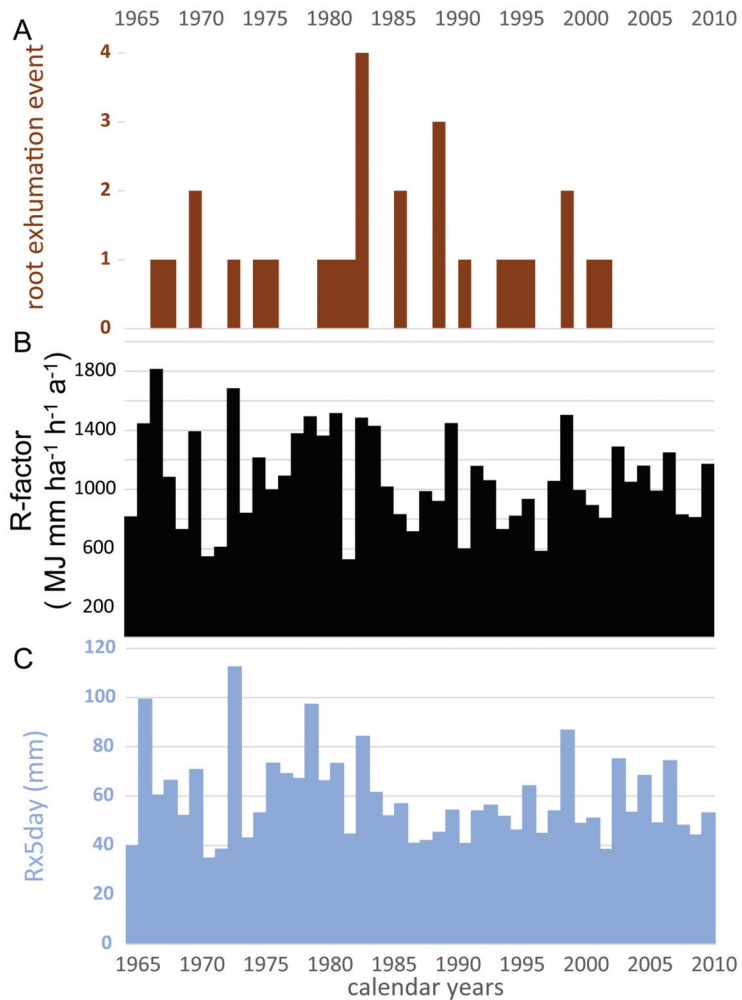


Figure 6. Root exhumation events documented in the Xiaolong Mts (Gansu Province, China) and annual rainfall erosivity indicators between 1965 and 2010. (A) Annual sum of detected root exhumation markers; (B) annual sum of monthly estimates of rainfall erosivity factor (Equation (2) and Section 2.3); (C) yearly maximum consecutive 5-day precipitation amount (Rx5day) retrieved from HadEX2 [50] corresponding to the study site.

The lack of identified exposure events after 2002 (Figure 6), or even any exposure scar after 2005 (Table S1), is tempting to link to the documented decrease in soil erosion in the Loess Plateau region between 2000 and 2008 [4], leading to praise for the efficacy of the great efforts targeting soil and water conservation, such as Grain for Green across China's Loess Plateau. However, we are afraid that this pattern instead points to a methodological limitation which needs improvement in future applications. Smaller root(let)s potentially

experience and are capable of documenting the most recent exposure events, and could be too small to attract attention in the field. In this dataset, for instance, the smallest sampled roots were ~1 cm wide. A general methodological suggestion can be to also pay special attention to the strings of small exposed root(let)s.

3.3. Microscopic versus Macroscopic Analysis

Recently, there has been a shift in studies of root-based erosion measurements from ring width variations and textural changes towards microscopic analysis and dating of exposure [24,33,55]. While the latter method is certainly more sensitive to oncoming exhumation and can sense the approach of soil surface even a few years before it reaches the root [41], it needs special wood anatomical equipment and is time-consuming. Despite all above-mentioned limitations, the presented results argue that the ‘old-fashioned’ identification of tree ring pattern features is capable of promoting further studies in this field by those who have no access to a specialized laboratory.

4. Conclusions

Based upon the anatomical changes of exposed tree roots of Chinese pine (*Pinus tabulaeformis*) from the Xiaolong Mts near Tianshui city, Gansu, China, we reconstructed a soil erosion history dating back to the late 1960s and quantitative estimates of soil erosion rate were developed for the first time. A linear regression model between slope steepness as an independent variable and erosion rate was established and could be used in future research to determine soil denudation in this part of the Xiaolong Mts.

The correspondence between an erosivity factor exceeding $1448 \text{ MJ mm ha}^{-1} \text{ h}^{-1} \text{ a}^{-1}$ in the year or in the preceding year of a root exhumation event indicates a threshold of soil erosion in the studied pine forest environment. Furthermore, daily and 5-day precipitation totals of 56 and 73 mm, respectively, seem to be critical thresholds which if exceeded it will always induce root exhumation in the same year or in the consecutive season. The projected increase of the R-factor is primarily attributed to the elevated probability of extreme precipitation events [13], and together with the documented strong coupling between heavy rainfall extremes and soil erosion [12] highlights the need for enhanced soil and water conservation measures in Gansu Province to mitigate the challenges posed by ongoing climate change. The lack of reconstructed data after 2002 in this dataset might be due to a sampling bias as the strings of the smallest exposed root(let)s can be unrecognized and unintentionally avoided in the field.

Supplementary Materials: The following supporting information can be downloaded at: <https://www.mdpi.com/article/10.3390/land13060771/s1>, Table S1: Complementary data for the exhumed root samples collected in Xiaolong Mts near Tianshui city (Gansu, China) in May 2010 for dendrogeomorphological analysis.

Author Contributions: Conceptualization, M.K., K.F., Y.Z. and Z.K.; methodology, M.K. and Z.K.; formal analysis, Z.K.; investigation, M.K., K.F., Y.Z. and Z.K.; writing—original draft preparation, M.K. and Z.K.; writing—review and editing, M.K., K.F., Y.Z. and Z.K.; visualization, M.K. and Z.K.; supervision, M.K., K.F. and Y.Z.; funding acquisition, M.K., K.F. and Y.Z. All authors have read and agreed to the published version of the manuscript.

Funding: This research was funded by Chinese–Hungarian scientist exchange program, grant number CN-48/2007.

Data Availability Statement: Data are contained within the article or Supplementary Materials.

Acknowledgments: This is contribution No. 90 of ‘2ka Palaeoclimatology’ Research Group and No. 41 of Budapest Tree-Ring Laboratory.

Conflicts of Interest: The authors declare no conflicts of interest.

Appendix A

In order to characterize the uncertainty of the laboratory measurements, pith-to-top distances were measured by two analysts (A, B) independently on each of the 30 sampled root discs. B researcher performed two measurements, and in some cases repeated the measurement another time. So finally, at least three measurements were available on the same parameter and the subjectivity bias could be also evaluated comparing the data obtained from A and B researchers' measurements.

Measurement results of the two independent analysts show excellent agreement (Figure A1A); the difference between the measured data is ≤ 1 mm in 70% of the cases (Figure A1B). The negative intercept of the regression slope (Figure A1A), and the slightly skewed histogram of the inset chart showing the distribution of the difference between measured values of A researcher and the mean of the measurements of B researcher (Figure A1B) suggest that A researcher tended to measure slightly larger distances.

The histogram showing the distribution of the standard deviation of the pith-to-top distance recorded for all root discs shows that overwhelmingly (>90%) it was below 1.2 mm. To provide a quantitative estimate on the uncertainty of the laboratory distance measurements, we adopted this value which includes both the uncertainty of the repeated measurements and the subjectivity error of independent analysts.

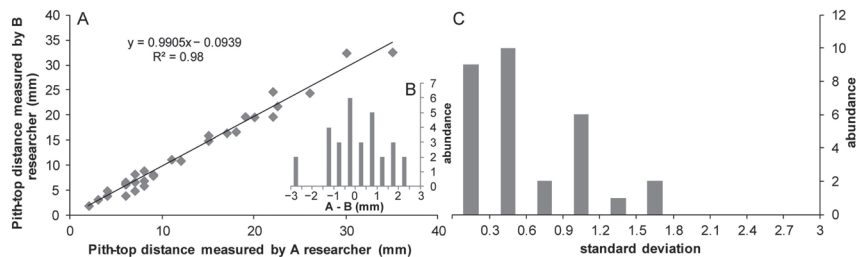


Figure A1. Assessing uncertainty of the laboratory distance measurements of the study. (A) Cross-plot between pit-to-top distance measured on the 30 studied root discs by A and B researcher; (B) histogram of the difference between the measurements of A and B researcher; (C) distribution of the standard deviation of the pith-to-top distance records for all root discs calculated from the merged dataset.

References

1. Verheijen, F.G.A.; Jones, R.J.A.; Rickson, R.J.; Smith, C.J. Tolerable versus actual soil erosion rates in Europe. *Earth-Sci. Rev.* **2009**, *94*, 23–38. [CrossRef]
2. Keesstra, S.; Mol, G.; De Leeuw, J.; Okx, J.; Molenaar, C.; De Cleen, M.; Visser, S. Soil-Related Sustainable Development Goals: Four Concepts to Make Land Degradation Neutrality and Restoration Work. *Land* **2018**, *7*, 133. [CrossRef]
3. Liu, B.; Xie, Y.; Li, Z.; Liang, Y.; Zhang, W.; Fu, S.; Yin, S.; Wei, X.; Zhang, K.; Wang, Z.; et al. The assessment of soil loss by water erosion in China. *Int. Soil Water Conserv. Res.* **2020**, *8*, 430–439. [CrossRef]
4. Fu, B.; Wang, S.; Liu, Y.; Liu, J.; Liang, W.; Miao, C. Hydrogeomorphic Ecosystem Responses to Natural and Anthropogenic Changes in the Loess Plateau of China. *Annu. Rev. Earth Planet. Sci.* **2017**, *45*, 223–243. [CrossRef]
5. Sun, J.; Zhang, N.; Shi, M.; Zhai, Y.; Wu, F. The effects of tillage induced surface roughness, slope and discharge rate on soil detachment by concentrated flow: An experimental study. *Hydrol. Process.* **2021**, *35*, e14261. [CrossRef]
6. Zhao, J.; Wang, Z.; Dong, Y.; Yang, Z.; Govers, G. How soil erosion and runoff are related to land use, topography and annual precipitation: Insights from a meta-analysis of erosion plots in China. *Sci. Total Environ.* **2022**, *802*, 149665. [CrossRef] [PubMed]
7. Nearing, M.A.; Bradford, J.M. Single Waterdrop Splash Detachment and Mechanical Properties of Soils. *Soil Sci. Soc. Am. J.* **1985**, *49*, 547–552. [CrossRef]
8. Van Dijk, A.I.J.M.; Bruijnzeel, L.A.; Eisma, E.H. A methodology to study rain splash and wash processes under natural rainfall. *Hydrol. Process.* **2003**, *17*, 153–167. [CrossRef]
9. Nanko, K.; Mizugaki, S.; Onda, Y. Estimation of soil splash detachment rates on the forest floor of an unmanaged Japanese cypress plantation based on field measurements of throughfall drop sizes and velocities. *CATENA* **2008**, *72*, 348–361. [CrossRef]
10. Szabó, J.A.; Centeri, C.; Keller, B.; Hatvani, I.G.; Szalai, Z.; Dobos, E.; Jakab, G. The Use of Various Rainfall Simulators in the Determination of the Driving Forces of Changes in Sediment Concentration and Clay Enrichment. *Water* **2020**, *12*, 2856. [CrossRef]

11. Szabó, J.A.; Keller, B.; Centeri, C.; Hatvani, I.G.; Kovács, J.; Szalai, Z.; Jakab, G. Varying particle size selectivity of soil erosion along a cultivated catena. *Open Geosci.* **2023**, *15*, 20220585. [CrossRef]
12. Zhao, Y.; Zhu, D.; Wu, Z.; Cao, Z. Extreme rainfall erosivity: Research advances and future perspectives. *Sci. Total Environ.* **2024**, *917*, 170425. [CrossRef]
13. Wang, W.; Yin, S.; He, Z.; Chen, D.; Wang, H.; Klik, A. Projections of rainfall erosivity in climate change scenarios for mainland China. *CATENA* **2023**, *232*, 107391. [CrossRef]
14. Godfrey, A.E.; Everitt, B.L.; Duque, J.F.M. Episodic sediment delivery and landscape connectivity in the Mancos Shale badlands and Fremont River system, Utah, USA. *Geomorphology* **2008**, *102*, 242–251. [CrossRef]
15. Lucia, A.; Laronne, J.B.; Martín-Duque, J.F. Geodynamic processes on sandy slope gullies in central Spain field observations, methods and measurements in a singular system. *Geodin. Acta* **2011**, *24*, 61–79. [CrossRef]
16. Mabit, L.; Benmansour, M.; Walling, D.E. Comparative advantages and limitations of the fallout radionuclides ¹³⁷Cs, ²¹⁰Pb_{ex} and ⁷Be for assessing soil erosion and sedimentation. *J. Environ. Radioact.* **2008**, *99*, 1799–1807. [CrossRef] [PubMed]
17. Kalkan, K.S.; Forkapić, S.; Marković, S.B.; Bikit, K.; Gavrilov, M.B.; Tošić, R.; Mrđa, D.; Lakatoš, R. The application of ¹³⁷Cs and ²¹⁰Pb_{ex} methods in soil erosion research of Titel loess plateau, Vojvodina, Northern Serbia. *Open Geosci.* **2020**, *12*, 11–24. [CrossRef]
18. Šamonil, P.; Jaroš, J.; Daněk, P.; Tikhomirov, D.; Novotný, V.; Weiblen, G.; Christl, M.; Egli, M. Soil erosion affected by trees in a tropical primary rain forest, Papua New Guinea. *Geomorphology* **2023**, *425*, 108589. [CrossRef]
19. Markose, V.J.; Jayappa, K.S. Soil loss estimation and prioritization of sub-watersheds of Kali River basin, Karnataka, India, using RUSLE and GIS. *Environ. Monit. Assess.* **2016**, *188*, 225. [CrossRef] [PubMed]
20. Koirala, P.; Thakuri, S.; Joshi, S.; Chauhan, R. Estimation of Soil Erosion in Nepal Using a RUSLE Modeling and Geospatial Tool. *Geosciences* **2019**, *9*, 147. [CrossRef]
21. Chen, P.; Czymzik, M.; Yu, Z.; Aldahan, A.; Wang, J.; Yi, P.; Hou, X.; Guo, S.; Zheng, M. Tendency of soil erosion dynamics by coupling radioisotopes and RUSLE model on the Southeastern Tibetan Plateau in response to climate warming and human activity. *CATENA* **2023**, *223*, 106954. [CrossRef]
22. Zheng, F.-L. Effect of Vegetation Changes on Soil Erosion on the Loess Plateau 1 | Project supported by the Chinese Academy of Sciences (No. KZCX3-SW-422) and the National Natural Science Foundation of China (Nos. 9032001 and 40335050). *Pedosphere* **2006**, *16*, 420–427. [CrossRef]
23. Zhou, F.; Gou, X.; Zhang, J.; Zhao, Z.; Chen, Q.; Cao, Z. Application of *Picea wilsonii* roots to determine erosion rates in eastern Qilian Mountains, Northwest China. *Trees* **2013**, *27*, 371–378. [CrossRef]
24. Bodoque, J.M.; Lucía, A.; Ballesteros, J.A.; Martín-Duque, J.F.; Rubiales, J.M.; Genova, M. Measuring medium-term sheet erosion in gullies from trees: A case study using dendrogeomorphological analysis of exposed pine roots in central Iberia. *Geomorphology* **2011**, *134*, 417–425. [CrossRef]
25. Hao, H.; Cheng, L.; Guo, Z.; Wang, L.; Shi, Z. Plant community characteristics and functional traits as drivers of soil erodibility mitigation along a land degradation gradient. *Land Degrad. Dev.* **2020**, *31*, 1851–1863. [CrossRef]
26. Kou, M.; Jiao, J.; Yin, Q.; Wang, N.; Wang, Z.; Li, Y.; Yu, W.; Wei, Y.; Yan, F.; Cao, B. Successional Trajectory Over 10 Years of Vegetation Restoration of Abandoned Slope Croplands in the Hill-Gully Region of the Loess Plateau. *Land Degrad. Dev.* **2016**, *27*, 919–932. [CrossRef]
27. Schulman, E. Root Growth-Rings and Chronology. *Tree-Ring Bull.* **1945**, *12*, 2–5.
28. Krause, C.; Eckstein, D. Dendrochronology of roots. *Dendrochronologia* **1993**, *11*, 9–23.
29. Hueck, K. Eine biologische Methode zum Messen der erodierten Tätigkeit des Windes und des Wassers. *Berichte Dtsch. Bot. Ges.* **1951**, *64*, 53–56.
30. LaMarche, V. Rate of slope erosion in the white mountains, California. *GSA Bull.* **1961**, *72*, 1579. [CrossRef]
31. Carrara, P.E.; Carroll, T.R. The determination of erosion rates from exposed tree roots in the Piceance Basin, Colorado. *Earth Surf. Process.* **1979**, *4*, 307–317. [CrossRef]
32. McCord, V.A.S. Late Holocene sediment yield and transport in a northern Arizona drainage basin reconstructed by tree-ring analysis. In Proceedings of the International Symposium on Ecological Aspects of Tree-ring Analysis, Tarrytown, NY, USA, 17–21 August 1986; pp. 213–223.
33. Stoffel, M.; Corona, C.; Ballesteros-Cánovas, J.A.; Bodoque, J.M. Dating and quantification of erosion processes based on exposed roots. *Earth-Sci. Rev.* **2014**, *123*, 18–34. [CrossRef]
34. Gärtner, H. Tree roots—Methodological review and new development in dating and quantifying erosive processes. *Geomorphology* **2007**, *86*, 243–251. [CrossRef]
35. Luo, M.; Zhou, Y.; Wang, K. Soil Erosion Characteristics According to Tree-rings in a Karst Area. *J. Resour. Ecol.* **2015**, *6*, 257–262. [CrossRef]
36. Zhang, D.; Zhou, F.; Fang, K.; Davi, N.; Chen, Z.; Wang, F.; Chen, Y. Quantification of soil erosion dynamics in the hilly red soil region of Southeast China based on exposed roots. *CATENA* **2023**, *232*, 107386. [CrossRef]
37. Zhang, Y.; Fang, K.; Zhou, F.; Dong, Z.; Li, Y.; Zhang, P. Reconstruction of soil erosion rates from exposed roots in southeast China. *Asian Geogr.* **2017**, *34*, 91–105. [CrossRef]
38. Fang, K.; Gou, X.; Chen, F.; Frank, D.; Liu, C.; Li, J.; Kazmer, M. Precipitation variability during the past 400 years in the Xiaolong Mountain (central China) inferred from tree rings. *Clim. Dyn.* **2012**, *39*, 1697–1707. [CrossRef]

39. Yue, T.; Yin, S.; Xie, Y.; Yu, B.; Liu, B. Rainfall erosivity mapping over mainland China based on high-density hourly rainfall records. *Earth Syst. Sci. Data* **2022**, *14*, 665–682. [CrossRef]
40. Kázmér, M.; Kern, Z.; Fang, K.; Zhou, Y.-c. Tree ring pattern of roots exhumed by soil erosion. *Hantkeniana* **2014**, *9*, 133–167.
41. Corona, C.; Lopez Saez, J.; Rovéra, G.; Stoffel, M.; Astrade, L.; Berger, F. High resolution, quantitative reconstruction of erosion rates based on anatomical changes in exposed roots at Draix, Alpes de Haute-Provence—Critical review of existing approaches and independent quality control of results. *Geomorphology* **2011**, *125*, 433–444. [CrossRef]
42. Mattheck, C.; Breloer, H. *The Body Language of Trees: A Handbook for Failure Analysis*; HMSO Publications Centre: London, UK, 1994.
43. Stokes, M.A.; Smiley, T.L. *An Introduction to Tree-Ring Dating*; University of Chicago Press: Chicago, IL, USA, 1968.
44. Watson, A. Wind-induced forces in the near-surface lateral roots of radiata pine. *For. Ecol. Manag.* **2000**, *135*, 133–142. [CrossRef]
45. Kern, Z.; Árvai, M.; Kázmér, M. The Budapest Tree-Ring Laboratory—Status report after 20 years of activity. *Cent. Eur. Geol.* **2023**, *66*, in press.
46. Orvis, K.H.; Grissino-Mayer, H.D. Standardizing the reporting of abrasive papers used to surface tree-ring samples. *Tree-Ring Res.* **2002**, *58*, 47–50.
47. Patel, R. A comparison of the anatomy of the secondary xylem in roots and stems. *Holzforschung* **1965**, *19*, 72–79. [CrossRef]
48. Clifford, A.A. *Multivariate Error Analysis*; Applied Science Publishers: Essex, UK, 1973.
49. Harris, I.; Osborn, T.J.; Jones, P.; Lister, D. Version 4 of the CRU TS monthly high-resolution gridded multivariate climate dataset. *Sci. Data* **2020**, *7*, 109. [CrossRef] [PubMed]
50. Donat, M.G.; Alexander, L.V.; Yang, H.; Durre, I.; Vose, R.; Dunn, R.J.H.; Willett, K.M.; Aguilar, E.; Brunet, M.; Caesar, J.; et al. Updated analyses of temperature and precipitation extreme indices since the beginning of the twentieth century: The HadEX2 dataset. *J. Geophys. Res. Atmos.* **2013**, *118*, 2098–2118. [CrossRef]
51. Yin, S.; Xie, Y.; Liu, B.; Nearing, M.A. Rainfall erosivity estimation based on rainfall data collected over a range of temporal resolutions. *Hydrol. Earth Syst. Sci.* **2015**, *19*, 4113–4126. [CrossRef]
52. Zingg, A.W. Degree and length of land slope as it affects soil loss in run-off. *Agric. Eng.* **1940**, *21*, 59–64.
53. Assouline, S.; Ben-Hur, M. Effects of rainfall intensity and slope gradient on the dynamics of interrill erosion during soil surface sealing. *CATENA* **2006**, *66*, 211–220. [CrossRef]
54. Wang, W.Z.; Jiao, J.Y. *Rainfall and Erosion Sediment Yield and Sediment Reduction of Soil and Water Conservation in the Loess Plateau*; Science China Press: Beijing, China, 2018. (In Chinese)
55. Gärtner, H.; Schweingruber, F.H.; Dikau, R. Determination of erosion rates by analyzing structural changes in the growth pattern of exposed roots. *Dendrochronologia* **2001**, *19*, 81–91.

Disclaimer/Publisher’s Note: The statements, opinions and data contained in all publications are solely those of the individual author(s) and contributor(s) and not of MDPI and/or the editor(s). MDPI and/or the editor(s) disclaim responsibility for any injury to people or property resulting from any ideas, methods, instructions or products referred to in the content.

Article

Determination of Soil Erodibility by Different Methodologies in the Renato and Caiabi River Sub-Basins in Brazil

Jones Anschau Xavier de Oliveira ¹, Frederico Terra de Almeida ^{2,*}, Adilson Pacheco de Souza ², Rhavel Salviano Dias Paulista ³, Cornélio Alberto Zolin ⁴ and Aaron Kinyu Hoshide ^{5,6}

¹ Environmental Sciences, Federal University of Mato Grosso, Sinop 78550-728, MT, Brazil; jonesbr14@gmail.com

² Institute of Agrarian and Environmental Sciences, Federal University of Mato Grosso, Sinop 78550-728, MT, Brazil; pachecoufnt@gmail.com

³ Postgraduate Program in Environmental Physics, Institute of Physics, Federal University of Mato Grosso, 2367, Av. Fernando Corrêa da Costa, Cuiabá 78060-900, MT, Brazil; rhavel.paulista@sou.ufmt.br

⁴ EMBRAPA Agrossilvipastoril, Brazilian Agricultural Research Corporation, Sinop 78550-970, MT, Brazil; cornelio.zolin@embrapa.br

⁵ College of Earth, Life, and Health Sciences, The University of Maine, Orono, ME 04469, USA; aaron.hoshide@maine.edu

⁶ AgriSciences, Federal University of Mato Grosso, Sinop 78555-267, MT, Brazil

* Correspondence: frederico.almeida@ufmt.br or fredterr@gmail.com; Tel.: +55-(66)-99995-1315

Abstract: Mitigating soil erosion's effects have been prioritized since the early 20th century. Rainfall simulators and analytical prediction models are used to determine soil erosion susceptibility. This study used different methodologies to measure soil erodibility in two hydrographic sub-basins, the Renato and Caiabi, in the Middle and Upper Teles Pires River in Mato Grosso state, Brazil. The rainfall simulator showed a higher range of K-factor values for the Renato sub-basin of 0.0009 to $0.0086 \text{ Mg} \times \text{h} \times (\text{MJ} \times \text{mm})^{-1}$ and a lower range of K-factor values for the Caiabi sub-basin of 0.0014 to $0.0031 \text{ Mg} \times \text{h} \times (\text{MJ} \times \text{mm})^{-1}$. Soil loss equations similarly estimated a higher range of K-factor values for the Renato of 0.0008 to $0.0990 \text{ Mg} \times \text{h} \times (\text{MJ} \times \text{mm})^{-1}$ and a lower range of K-factor values for the Caiabi of 0.0014 to $0.0846 \text{ Mg} \times \text{h} \times (\text{MJ} \times \text{mm})^{-1}$. There was no significant difference at the 5% level for the K factor determined by the rainfall simulator for both sub-basins. Equations specified in Bouyoucos (1935) and Lombardi Neto and Bertoni (1975) showed significant correlation (5%) for farming systems in the Caiabi sub-basin. Indirect methodologies that performed well for correlation were equations 2 and 3 from Roloff and Denardin (1994), which use iron and aluminum as parameters. Soil erosion was most influenced by physical texture parameters of the region's soil.

Citation: Oliveira, J.A.X.d.; Almeida, F.T.d.; Souza, A.P.d.; Paulista, R.S.D.; Zolin, C.A.; Hoshide, A.K. Determination of Soil Erodibility by Different Methodologies in the Renato and Caiabi River Sub-Basins in Brazil. *Land* **2024**, *13*, 1442. <https://doi.org/10.3390/land13091442>

Academic Editors: Jianye Li, Xingyi Zhang, Weida Gao, Wei Hu, Qiang Chen and Nick B. Comerford

Received: 29 June 2024

Revised: 8 August 2024

Accepted: 3 September 2024

Published: 5 September 2024



Copyright: © 2024 by the authors. Licensee MDPI, Basel, Switzerland. This article is an open access article distributed under the terms and conditions of the Creative Commons Attribution (CC BY) license (<https://creativecommons.org/licenses/by/4.0/>).

Keywords: analytical methods; erodibility; soil erosion; rainfall simulator; Universal Soil Loss Equation

1. Introduction

Soil erosion can reflect problems of an economic, social, and mainly environmental nature [1]. Soil erosion is also considered to be a factor that triggers concern worldwide due to the historical prevalence of crop production involving plowing, harrowing, cultivation, and other forms of soil disturbance from repeated tillage [2]. Excessive tillage can result in poor agro-environmental management, which can result in greater soil degradation and degeneration [3]. In Latin America, deforestation of native habitats for agriculture and livestock, such as in the Brazilian Amazon, results in high soil erosion due to direct exposure of the soil [4]. In Sub-Saharan Africa, subsistence farming and expansion into pastures also cause severe soil degradation [5,6]. In Europe, the outcomes vary with agricultural practices and soil conservation regulations [7].

Globally, soil erosion rates are variable, ranging from 17 to 40 metric tons (t) hectare (ha)⁻¹ year (yr)⁻¹ [8]. Similarly in Brazil for plot-scale surface runoff studies involving natural precipitation, soil loss for major annual commodity crop sequences (e.g., cultivated crop, fallow, etc.) ranges from 5 t ha⁻¹ yr⁻¹ for sugarcane (*Saccharum officinarum*) to 26.7 t ha⁻¹ yr⁻¹ for peanut (*Arachis hypogaea*) to 50.3 t ha⁻¹ yr⁻¹ for bare fallow [9]. Undisturbed land cover, such as forests, can have erosion rates below 0.5 t ha⁻¹ yr⁻¹ [8]. Perennial crops such as pasture in Brazil also have lower erosion rates averaging 6.5 t ha⁻¹ yr⁻¹ of soil loss measured in plot-scale surface runoff studies [9].

The Universal Soil Loss Equation developed by Wischmeier and Smith [10] became widespread throughout the world. It is an empirical model that seeks to estimate soil loss through mathematical equations. The Universal Soil Loss Equation (USLE) models erosion through explanatory variables of rainfall erosivity (R), erodibility (K), length of slope (L), slope (S), management (C), and conservation practices (P) [11,12].

Erosion models are widely used to estimate soil loss [13]. The assessment of soil erosion in various countries around the world is based on the Universal Soil Loss Equation (USLE), which is widely accepted [14]. For example, the USLE was applied in studies, such as that by Mahamud et al. (2021) [13], to predict soil loss in the Cameron Highlands, Malaysia. It was also used to estimate soil erosion in Tzicatlacoyan, Puebla, Mexico [15], to analyze soil erosion in the Nan River basin, Thailand [16], and for the integrated use of GIS models and USLE in the Hulan River basin, Northeast China [17].

The erodibility (K factor) is complex since it requires the determination of factors such as physical and chemical soil parameters [18] and the configuration of the aptitude that the soil has in tolerating erosive processes [11]. This erodibility can be determined directly or indirectly. To determine the K factor, Marques et al. [4] and Denardin [19] explain that there are three known methodologies: natural rainfall, rainfall simulators, and erodibility estimates through the verification of physical and chemical attributes using prediction equations related to soil variables.

To provide examples of the applicability of the K factor according to the USLE standard worldwide, several studies can be cited. Gupta et al. (2024) [20] conducted a comprehensive analysis of soil erodibility, considering the effects of saturated hydraulic conductivity. Marques et al. (2019) [4] estimated the K factor to assess the average annual soil erosion and sediment production in the Córrego Água Azul basin, located in the central-west region of Brazil. Addis et al. (2015) [5] aimed to estimate the soil erodibility factor (K) using the USLE nomogram and analyze the spatial distribution of the K factor in a watershed in Ethiopia. Additionally, Ojo et al. (2023) [6] investigated the impacts of soil conservation practices on erodibility, with the goal of improving erosion management and agricultural productivity in Ido, Oyo State, southwestern Nigeria.

The use of rainfall simulators is an important tool for obtaining data on erodibility in relatively short periods. It is also a piece of equipment that is commonly used in cultivated areas in order to evaluate the infiltration of water into the soil [21]. Rainfall simulators allow for more rapid data collection of simulated rainfall conditions, which can contribute to more dynamic understanding of elements such as surface runoff, water infiltration, and soil loss [22]. In the Renato and Caiabi River sub-basins in the state of Mato Grosso, Brazil where this study was conducted, rainfall simulation indicates soil erosion is more dependent on the degree of soil disturbance in commodity cropping systems rather than geographic location in the watershed [23].

This region of Mato Grosso state, Brazil is characterized by high to very high rates of soil erosion [24]. The Renato and Caiabi sub-basins, as with other areas in Mato Grosso, saw a shift from native forest and savannah to cultivated crops and extensive pasture over the past 35 years [25]. Compared to native forest/habitat, commodity cropping resulted in physical soil degradation in the Renato sub-basin and crops/pasture reduced soil water conductivity in the Caiabi sub-basin [26]. Both the Renato and Caiabi River sub-basins feed into the Teles Pires River, which eventually feeds into the Amazon River. Increased soil

erosion from crops/pasture can contribute to higher sediment loads in the Teles Pires River, particularly during the rainy season from October to March [27].

In Brazil, information about the K factor is considered scarce due to the presence of different types of Brazilian soils. These different types of soils can represent a range of distinct values even within a single soil class [28]. In this context, when dealing with regional/tropical watersheds, the choice of the best model for studying the K factor could lead to consistent results for soil loss prevention [4].

The importance of this research is reflected in the determination of the K factor indirectly for soils in the region, which is crucial for understanding the erosion process and enabling the mitigation of erosive effects for different land uses. This will allow for more effective soil conservation. Additionally, this approach will stimulate reflection on the necessary care in soil management, especially in the context of agribusiness. It will also promote scientific debate and may encourage the development of new studies on other perspectives regarding soil erodibility.

Given the environmental importance of reducing soil erosion in Brazil, it is critical to better validate soil loss equations such as the Universal Soil Loss Equation (USLE) with real-world data. The USLE is best calibrated to region-specific areas [29]. The objectives of this study were to (1) distinguish differences in soil characteristics and to (2) determine the soil erodibility or K factor part of the USLE equation in both cultivated farmland and pasture in two sub-basins located in the Middle and Upper Teles Pires River region, in the northern part of Mato Grosso state, Brazil. Soil erosion data were obtained through direct field observations using a rainfall simulator. Empirical equations were also used to model soil erosion, and these were compared to observed soil erosion during rainfall simulation.

2. Materials and Methods

2.1. Study Area

The study area corresponds to the sub-basins of the Renato River and Caiabi River, which are both sub-basins of the Renato River positioned between the geographic coordinates, longitudes $55^{\circ}11'47.333''$ W and $55^{\circ}11'31''$ W and latitudes $11^{\circ}3'52.609''$ S and $11^{\circ}22'40.65''$ S. The Caiabi River sub-basin is positioned between the coordinates of longitudes $55^{\circ}27'3.909''$ W and $55^{\circ}20'30.97''$ W and latitudes $12^{\circ}9'2.976''$ S and $12^{\circ}17'55.006''$ S. Located between the municipalities of Itaúba and Cláudia is the sub-basin of the Renato River, which is approximately 65 kilometers (km) to the south of the Caiabi River sub-basin, located between the municipalities of Sinop and Vera, Mato Grosso state, Brazil. Figure 1 shows the areas of both sub-basins.

The Renato and Caiabi River sub-basins have areas of 1341 km² and 519 km², respectively. The Renato sub-basin has soils such as Dystrophic Red Oxisol and Red–Yellow Oxisol Dystrophic. The Caiabi sub-basin is dominated by Dystrophic Red–Yellow Oxisol. These classifications were identified according to the Brazilian Soil Classification System [30]. The experiment was conducted in plots (0.70 m²) in three areas of both sub-basins: the source, the middle of the basin, and the mouth of the river basin. There were four replicates for each treatment.

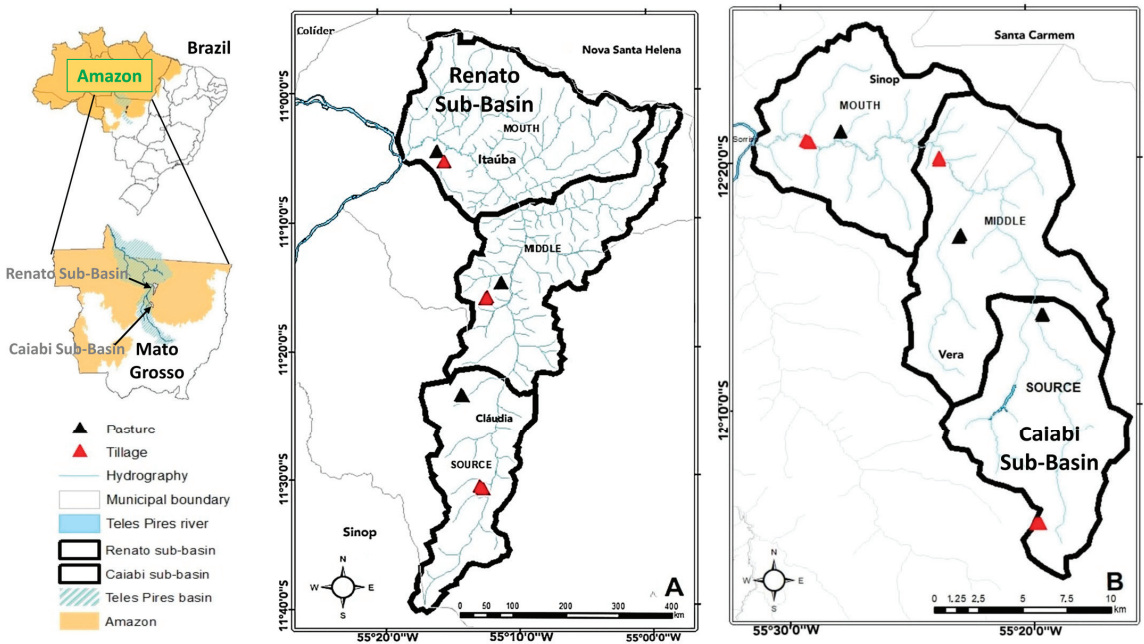


Figure 1. Location of the (A) Renato sub-basin, and the (B) Caiabi sub-basin in the state of Mato Grosso, Brazil. Sub-basin divisions are by geography (source, middle, and mouth), soil collection points, and the areas under tillage and in pasture. Source: the authors.

2.2. Rainfall Simulation to Measure Soil Erosion

Following methods described in detail in Alves et al. [23], the rainfall simulation was conducted under two agricultural systems, one grain crop and the other pasture. Agricultural systems in the Renato River and Caiabi River basins commonly involve soybean (*Glycine max*) followed by corn (*Zea mays*) throughout the year, starting with soybean in October and ending with the corn harvest in June. The pasture evaluated occurs year-round, and the predominant grass cultivated is *Brachiaria brizantha* spp. Because the study took place in a single harvest, the treatments used were soybean (*Glycine max*) and *Brachiaria brizantha* spp. for the Caiabi River basin and corn (*Zea mays*) and *Brachiaria brizantha* spp. for the Renato River basin.

The plots studied were 0.70 meter (m) wide and 1.0 m long (area of 0.70 m²), and were evaluated at a depth of 0 to 10 centimeters. When bare soil was encountered, the plot was prepared with rakes. The ramps had average slopes in both experimental areas between 3 and 5 degrees. The InfiAsper rainfall simulator used was developed by Sobrinho et al. (2008) [31]. Before the application of the simulated rainfall, all plots received pre-wetting using standard drippers. The device was calibrated before each simulated rainfall in order to maintain constant rainfall, according to the methodology described by Sobrinho et al. in (2003) [32]. The equipment was calibrated to produce rainfall with an intensity of 75 millimeters hour⁻¹ (mm h⁻¹), a characteristic of designated precipitation observed over a 10-year period in the region [33].

2.3. Soil Sampling

Deformed and undeformed soil samples were collected in order to measure the following components: soil density (Sd), macroporosity (Ma), microporosity (Mi), total porosity (Tp), hydraulic conductivity through constant load permeameter, particle size analysis, organic matter (Om), particle density (Pd), chemical analysis of iron (Fe), aluminum (Al),

and sand sieving. Particle size analysis was conducted by the pipette method with dispersion in water and 1 mol L⁻¹ of NaOH. The particle density was determined by the volumetric flask method. All these analyses strictly followed the methodology described by Teixeira et al. [34].

2.4. Calculation of Rainfall Kinetic Energy

To calculate the kinetic energy of simulated rainfall, the methodology adapted from Foster et al. [35] was used. This is described in Equation (1):

$$EC = 0.119 + 0.0873 \log I \quad (1)$$

where EC = the kinetic energy, in megajoules (MJ) \times (hectare)⁻¹ and I = the rainfall intensity in mm h⁻¹.

2.5. Calculation of Soil Components

2.5.1. Soil Erosivity Index and Soil Erodibility

To determine the erosivity index ($EI30$) expressed in MJ \times mm \times (ha \times h)⁻¹, the maximum water depth that occurred in 30 min was identified. Next, the maximum precipitation intensity was calculated using the equation proposed by Wischmeier in 1959 [36], represented by Equation (2):

$$EI30 = EC \times I30 \quad (2)$$

where $EI30$ = soil erosivity, in MJ mm \times (hectare h)⁻¹; EC = the kinetic energy in MJ \times (hectare)⁻¹, and $I30$ = the maximum rainfall intensity that occurred in 30 min, measured in mm h⁻¹.

The material containing water and sediment was taken for weighing and dried in an oven at 221 °F for an average period of 24 h to determine the runoff volume and the soil mass.

Soil erodibility can be estimated using Equation (3), using the elements soil loss (A) and the soil erosivity index ($EI30$). The C factors of soil management and P factors of conservation practices were a value of 1, considering the standard plot conditions established by Wischmeier and Smith in 1978 [10]:

$$K = \frac{A}{R} \quad (3)$$

where K is soil erodibility measured in Mg (1 Mg = 1 million grams = 1 metric ton) \times h \times (MJ \times mm)⁻¹. A is soil loss in Mg \times (ha \times h)⁻¹ and R is rainfall erosivity in MJ \times mm \times (hectare \times h)⁻¹.

2.5.2. Equation for Soil Loss

Universal Soil Loss Equation (USLE) standard values for slope length and slope gradient were considered and Equation (4) was used to adjust these to research plots. This adjustment used the equation proposed by Wischmeier and Smith [10]:

$$LS = \left(\frac{L}{22.1} \right) m \times (0.065 + 0.0454 + 0.0065 \times S^2) \quad (4)$$

where S = land slope in %; L = land length in meters; $m = 0.2$ for $S \leq 1\%$; $m = 0.3$ for $3\% \geq S > 1\%$; $m = 0.4$ for $5\% \geq S > 3\%$; and $m = 0.5$ for $S > 5\%$. Empirical equations for evaluating the soil erodibility (K) factor of the USLE, expressed as Mg \times h \times (MJ \times mm)⁻¹, were tested and the equations used are presented as follows.

2.5.3. Equations Used to Estimate Soil Erodibility

The K factor in the USLE can be calculated using numerous equations. One of these equations is the Bouyoucos 1935 [37] method and is specified as Equation (5):

$$K = \frac{\% \text{ of sand} + \% \text{ of silt}}{\% \text{ of clay}} \times \frac{1}{100} \quad (5)$$

where soil composition is specified as percentages of sand, clay, and silt. The Lima et al. [38] method adapted for Brazilian Latosols by Marques et al. [39] is summarized in Equation (6):

$$K = [1.451 \times 10^{-10} \times (120 - Om) \times Ma^{1.14}] + [0.0043(S - 2)] + [0.0033(P - 2)] \quad (6)$$

where Ma represents the soil texture and expresses the sum of the silt in grams kilogram⁻¹ (g kg⁻¹) and very fine sand (g kg⁻¹) contents multiplied by 1000 minus the clay content (g kg⁻¹), where dispersion was conducted in water. Om expresses the organic matter content (g kg⁻¹), S represents the soil structure class, and P expresses the hydraulic permeability. Here S and P are dimensionless factors. The morphological description of the soil was evaluated through field observations and also according to that described by the Office of Planning of the State of Mato Grosso [40]. For the study of the Renato and Caiabi River sub-basins, the soil structure was defined as fine granular assuming use of their code 2.

The Wischmeier et al. 1978 [10] method for soils of the United States of America estimate soil erodibility (K) specified in Equation (7):

$$K = 1.451 \times 10^{-10} \times (120 - Om) \times M^{1.14} + 0.0043(S - 2) + 0.0033(P - 2). \quad (7)$$

This equation has the same parameters as Equation (6); however, M represents the soil texture and expresses the sum of the silt (g kg⁻¹) and very fine sand (g kg⁻¹) contents multiplied by 1000 minus the clay content (g kg⁻¹). Here, dispersion was conducted in sodium hydroxide (NaOH at 1 mol L⁻¹). Structure (S) and permeability (P) were coded as described in Wischmeier et al. in 1971 [41], where S is coded as: very fine granular = 1; fine granular = 2; medium/coarse granular and subangular blocks = 3; and massive laminar = 4. The P is coded as: fast = 1; moderate to fast = 2; moderate = 3; moderate to slow = 4; and slow = 5; and very slow = 6.

Lombardi Neto and Bertoni (1975) [42] outline another method for estimating K based on Middleton 1930 [43] outlined in Equation (8):

$$K = \frac{\% \text{ clay dispersed in water} / \% \text{ total clay}}{\% \text{ clay total} / \% \text{ moisture equivalent}}. \quad (8)$$

Roloff and Denardin 1994 [44] proposed another method for estimating K specified in Equation (9) as:

$$K = (0.0049 \times P) + (3.31 \times 10^{-5} \times Mm^{0.5}) \quad (9)$$

where Mm is the silt content (g kg⁻¹) multiplied by the sum of silt and fine sand (g kg⁻¹) and the particle size analysis disposing of 1 mol L⁻¹ of NaOH. Roloff and Denardin [44] used another method for estimating K which requires iron extraction and was developed for soils in the Paraná region shown in Equation (10):

$$K = (9.17 \times 10^{-5} \times Mm^{0.5}) - (5.26 \times 10^{-5} \times Fe) + (1.76 \times 10^{-5} \times FS) \quad (10)$$

where iron (Fe) is related to the Fe₂O₃ content of air-dried fine soil fraction (ADFS) extracted by sulfuric attack, where fine soil (FS) is related to the fine sand content (g kg⁻¹) using 1 mol L⁻¹ of NaOH as a dispersant. Finally, Roloff and Denardin [44] use another equation for estimating K which requires aluminum extraction:

$$K = (1.038 \times 10^{-4} \times Mm^{0.5}) - (4.54 \times 10^{-5} \times Al) \quad (11)$$

where Mm refers to the silt content (g kg^{-1}) multiplied by the sum of silt and fine sand (g kg^{-1}); Al is related to the aluminum oxide (Al_2O_3) content of the ADFS fraction extracted by sulfuric acid with particle size analysis using 1 mol L^{-1} of NaOH as a dispersant.

2.6. Soil Erodibility by Soil Textural Class and Soil Organic Matter Content

Soil erodibility (K) can also vary by the soil type and soil organic matter content. Table 1 presents estimates for K developed by McKague 2023 [45]. Average values of K are specified by different soil texture (e.g., sand, silt, and clay) as well as organic matter content both below and above 2%. These estimates of K were adapted by Lima et al., 2007 [46].

Table 1. Distribution of the predefined values of erodibility in relation to soil textural class and organic matter content based on McKague 2023 [45].

Soil Textural Class	Soil Erodibility (K) in $\text{Mg} \times \text{h} \times (\text{MJ} \times \text{mm})^{-1}$		
	Mean	Organic Matter (<2%)	Organic Matter (>2%)
Very clayey	0.022	0.025	0.020
Clayey	0.029	0.032	0.028
Clay loam	0.040	0.043	0.037
Loam	0.040	0.045	0.034
Sandy loam	0.005	0.007	0.005
Sandy	0.003	0.004	0.001
Sandy clay loam	0.026	-	0.026
Sandy loam	0.017	0.018	0.016
Silty loam	0.050	0.054	0.049
Silty clay	0.034	0.036	0.034
Silty clay loam	0.042	0.046	0.040

3. Results

The data were submitted to the non-parametric Kruskal–Wallis 5% probability test and Dwass–Steel–Chritchlow–Fligner post HOC test ($p < 0.05$). These tests were used to verify the differences between sub-basin positions and treatments. Averages were evaluated at the 5% significance level ($p < 0.05$).

We paid attention to possible differences that could be found in both the Renato and Caiabi River basins because they present different land use and occupation times for each sub-basin. These two sub-basins also differ from each other chronologically, as can be observed through satellite images over the years, starting in the 1970s [47]. Table 2 shows the values of the particle size analysis and Table 3 shows the values determined for sand fractionation.

Table 2. Particle size distribution in different treatments of the soils studied along the sub-basins of the Renato and Caiabi rivers, Mato Grosso state, Brazil.

Land Use	Dispersant	Sub-Basin Region	Renato Sub-Basin (%) ¹			Caiabi Sub-Basin (%) ¹		
			Total Sand	Silt	Clay	Total Sand	Silt	Clay
Cultivated	NaOH	Source	75.20 A	8.62 A	16.20 A	42.50 A	29.60 A	27.90 A
		Middle	82.90 B	4.23 A	12.90 A	76.60 B	5.64 B	17.80 B
		Mouth	73.90 A	6.70 A	19.40 B	78.50 B	5.90 B	15.60 B
		CV%	7	56	22	27	87	33
	Water	Source	82.00 A	10.30 A	7.69 A	59.90 A	27.40 A	12.60 A
		Middle	85.80 B	8.52 B	5.70 B	81.30 B	11.60 B	7.15 B
		Mouth	80.70 A	12.60 A	6.70 A	85.00 C	6.84 C	8.14 B
		CV%	3	20	16	15	61	33

Table 2. Cont.

Land Use	Dispersant	Sub-Basin	Renato Sub-Basin (%) ¹			Caiabi Sub-Basin (%) ¹		
		Region	Total Sand	Silt	Clay	Total Sand	Silt	Clay
Pasture	NaOH	Source	80.40 A	3.67 A	15.90 A	49.20 A	14.70 A	36.10 A
		Middle	83.20 A	3.94 A	12.90 A	49.20 A	16.20 A	34.60 A
		Mouth	81.90 A	3.36 A	14.70 A	84.40 B	4.63 B	11.00 B
		CV%	2	29	14	29	51	45
	Water	Source	87.10 A	7.32 A	5.58 A	66.90 A	17.30 A	15.80 A
		Middle	86.60 A	6.93 A	6.43 A	65.40 A	15.90 A	18.70 A
		Mouth	88.40 A	8.02 A	3.57 B	88.40 B	5.94 B	5.66 B
		CV%	2	13	28	15	43	45

¹ Equal capital letters in the column do not differ significantly from each other by the non-parametric Kruskal–Wallis test ($p < 0.05$). CV% = coefficient of variation percentage.

Table 3. Distribution of sand fractionation of the soils studied along the sub-basins of the Renato and Caiabi rivers, Mato Grosso state, Brazil.

Land Use	Disper-sant	Sub-Basin Region	Renato Sub-Basin (%) ¹					Caiabi Sub-Basin (%) ¹				
			Very Coarse Sand	Coarse Sand	Med. Sand	Fine Sand	Very Fine Sand	Very Coarse Sand	Coarse Sand	Med. Sand	Fine Sand	Very Fine Sand
Cultivated	NaOH	Source	0.10 A	0.15 A	9.55 A	7.39 A	1.33 A	0.30 A	0.32 A	9.73 A	2.49 A	1.40 A
		Middle	0.13 A	0.16 A	10.80 A	7.67 A	1.73 A	0.07 B	0.12 B	15.14 B	3.90 B	0.97 A
		Mouth	0.14 A	0.13 A	5.92 B	11.31 B	0.61 B	0.08 B	0.15 B	17.93 C	2.37 A	0.61 B
		CV%	71	52	28	28	45	69	62	40	51	45
	Water	Source	0.03 A	0.19 A	8.60 A	9.67 A	1.79 A	0.27 A	0.78 A	7.73 A	3.77 A	2.37 A
		Middle	0.04 A	0.16 A	10.40 A	8.07 A	1.73 A	0.03 B	0.13 B	12.78 A	5.55 B	1.75 A
		Mouth	0.20 B	0.22 A	9.58 A	7.87 A	2.22 A	0.04 B	0.16 B	14.10 C	5.08 B	1.67 A
		CV%	84	55	15	13	17	107	89	25	18	18
Pasture	NaOH	Source	0.03 A	0.08 A	11.99 A	6.31 A	1.65 A	0.08 A	0.24 A	6.95 A	4.47 A	0.79 A
		Middle	0.10 B	0.14 A	11.31 A	7.04 A	1.83 A	0.45 B	0.26 A	8.15 A	3.11 A	0.67 A
		Mouth	0.14 B	0.07 A	16.93 B	2.31 B	0.79 B	0.04 A	0.08 B	19.33 B	1.98 B	0.63 A
		CV%	74	52	21	51	48	104	47	49	69	22
	Water	Source	0.01 A	0.12 A	10.60 A	8.63 A	2.24 A	0.04 A	0.43 A	9.20 A	5.11 A	1.89 A
		Middle	0.03 A	0.10 A	12.90 A	6.94 A	1.67 B	0.09 A	0.61 B	9.25 A	4.83 A	1.41 A
		Mouth	0.16 B	0.07 A	17.80 B	2.98 B	1.05 C	0.10 A	0.16 C	13.10 B	6.53 A	2.20 A
		CV%	103	24	24	40	39	72	56	21	22	25

¹ Equal capital letters in the column do not differ significantly from each other by Kruskal–Wallis non-parametric test ($p < 0.05$). Particle size range (millimeter(s) or mm) for very coarse sand (1 mm), coarse sand (1 to 0.50 mm), medium sand (0.49 to 0.25 mm), fine sand (0.24 to 0.13 mm), and very fine sand (0.12 to 0.06 mm). CV% = coefficient of variation.

The granulometric analysis for the Renato sub-basin (Table 2) demonstrated a higher concentration of sand in the middle of the sub-basin, followed by the source. The same did not occur for the Caiabi sub-basin, where the sand fraction made up a higher proportion of granular composition in the mouth region, followed by the middle part of the sub-basin. The fine sand (FS) and very fine sand (VFS) averaged 7.17 and 4.10 g kg⁻¹ and 1.55 and 1.36 g kg⁻¹ for Renato and Caiabi, respectively.

Table 4 shows the averages for permeability (cm h⁻¹), particle density (Mg m⁻³), as well as unitless parameters M (dispersed in NaOH), Ma (dispersed in water), permeability code (P), and structure code. The permeability for Renato and Caiabi averaged 5.41 and 4.41 cm h⁻¹, respectively. The average particle density remained at 2.5 Mg m⁻³ for both pasture and tillage in both sub-basins. Regarding the Ma parameter, there was an increase in its value with the dispersion processed in water. The increase in the Ma parameter in this study confirms the observations made by Lima et al. in 1990 [38] that attribute such an increase to the dispersion conducted in water.

Table 4. Distribution of mean values for permeability, particle density, the M parameter (dispersed in NaOH), the Ma parameter (dispersed in water), permeability code (P), and structure code in the sub-basins of the Renato and Caiabi Rivers, Mato Grosso state, Brazil.

Land Use	Sub-Basin Region	Renato Sub-Basin (%) ¹						Caiabi Sub-Basin (%) ¹					
		Permeability (cm h ⁻¹)	Particle Density (Mg m ⁻³)	M Parameter	Ma Parameter	P Code	Structure Code	Permeability (cm h ⁻¹)	Particle Density (Mg m ⁻³)	M Parameter	Ma Parameter	P Code	Structure Code
Cultivated	Source	4.49 A	2.60 A	854.2	1121.3	4	2	5.60 A	2.09 A	2258.9	2604.9	3	2
	Middle	7.01 A	2.67 A	518.4	979.5	3	2	5.26 A	2.47 B	557.0	1244.5	4	2
	Mouth	3.91 A	2.57 A	588.0	1384.5	4	2	6.08 A	2.52 B	550.3	791.6	3	2
	CV%	65	4					19	9				
Pasture	Source	8.56 A	2.58 A	449.7	899.2	3	2	1.55 A	2.42 A	989.3	1618.2	5	2
	Middle	3.25 A	2.55 A	481.6	803.8	4	2	3.16 B	2.31 A	1105.4	1409.8	4	2
	Mouth	5.21 A	2.62 B	354.8	859.3	3	2	4.84 B	2.61 B	467.0	773.9	4	2
	CV%	66	4					13	6				

¹ Equal capital letters in the column do not differ significantly by the non-parametric Kruskal–Wallis test ($p < 0.05$); permeability values obtained through constant load permeameter and P = hydraulic permeability code. CV% = coefficient of variation.

According to Table 5, it was observed that organic matter varied for the two sub-basins. However, the Caiabi sub-basin has a higher percentage of land area devoted to cultivated crops (59.24%) compared to the Renato sub-basin (13.41%), while for a perennial pasture, this was the opposite at 6.26% versus 15.94% [26]. For this scenario, organic matter content is considered one of the main soil stabilization agents [48].

Table 5. Distribution of the average values of the chemical analysis of organic matter, iron, and aluminum of soils sampled in the Renato and Caiabi River sub-basins, Mato Grosso state, Brazil.

Land Use	Sub-Basin Region	Renato Sub-Basin (%) ¹			Caiabi Sub-Basin (%) ¹		
		Organic Matter (dag kg ⁻¹)	Fe ₂ O ₃ (mg dm ⁻³)	Al ₂ O ₃ (cmolc dm ⁻³)	Organic Matter (dag kg ⁻¹)	Fe ₂ O ₃ (mg dm ⁻³)	Al ₂ O ₃ (cmolc dm ⁻³)
Cultivated	Source	2.76 A	47.0 A	0.06 A	5.14 A	26.5 A	0.04 A
	Middle	2.59 A	44.5 A	0.04 B	3.32 B	28.0 A	0.03 A
	Mouth	3.46 A	36.5 B	0.03 B	3.07 B	20.5 A	0.05 A
	CV%	25	16	49	31	22	30
Pasture	Source	1.64 A	63.5 A	0.36 A	3.80 A	75.5 A	0.05 A
	Middle	1.92 A	67.0 A	0.11 A	4.87 B	50.0 B	0.04 A
	Mouth	1.94 A	92.0 A	0.36 A	1.89 C	42.5 B	0.07 A
	CV%	19	25	82	38	26	27

¹ Equal capital letters in the column do not differ significantly from each other by the non-parametric Kruskal–Wallis test ($p < 0.05$). Fe₂O₃ = iron oxide, and Al₂O₃ = aluminum-derived oxide. CV% = coefficient of variation.

Chemical evaluation showed that areas under agricultural cultivation had the lowest levels of iron (Fe) and aluminum (Al). Additionally, a decrease in Fe and Al can contribute to the soil leaching process, which can be accelerated by the intensive tillage used in these farming areas. The importance of Fe and Al oxides is linked to their cohesive ability to act as cementing agents, which intensely favors agglutination. These elements are present mainly in soils in tropical climates such as those found in Brazil [49]. Fe and Al oxides are associated with chemical weathering [28], primarily in Oxisols. Such agglutination can reduce the impact of raindrops, hindering the disaggregation of particles through surface runoff [50]. Table 5 presents the chemical values of soil evaluated from both the Renato and Caiabi sub-basins.

The kinetic energy produced for the events ranged from 0.278 to 0.287 MJ hectare⁻¹. The erosivity among all rainfall events obtained minimum of 1065.73 and maximum of 1214.36 MJ × mm × (hectare × h)⁻¹ for both sub-basins. Soil loss ranged from 0.178 to 0.813 Mg hectare⁻¹ h⁻¹, specifically for the Renato sub-basin and 0.205 to 0.359 Mg

$\text{ha}^{-1} \text{h}^{-1}$ for the Caiabi sub-basin. Table 6 presents other values observed by the rainfall simulator.

Table 6. Distribution of mean values of soil loss, precipitation intensity, length and slope, and erodibility factor (K) in the Renato and Caiabi River sub-basins, Mato Grosso state, Brazil.

Land Use	Sub-Basin Region	Renato Sub-Basin (%) ¹				Caiabi Sub-Basin (%) ¹			
		Soil Loss (Mg ha ⁻¹ h ⁻¹)	Precipitation Intensity (MJ × mm × (h × ha × year) ⁻¹)	Length and Slope (m)	K (Mg × h × (MJ × mm) ⁻¹)	Soil Loss (Mg ha ⁻¹ h ⁻¹)	Precipitation Intensity (MJ × mm × (h × ha × year) ⁻¹)	Length and Slope (m)	K (Mg × h × (MJ × mm) ⁻¹)
Cultivated	Source	0.676 A	1174.38 A	0.114 A	0.0052 A	0.306 A	1206.26 A	0.082 A	0.0031 A
	Middle	0.813 A	1137.88 A	0.102 A	0.0086 A	0.275 A	1120.75 A	0.134 B	0.0020 A
	Mouth	0.622 A	1065.73 A	0.102 A	0.0058 A	0.205 A	1145.15 A	0.143 B	0.0012 A
	CV%	63	8	8	76	43	5	29	52
Pasture	Source	0.431 A	1157.06 A	0.143 A	0.0025 A	0.359 A	1141.41 A	0.204 A	0.0017 A
	Middle	0.505 A	1214.36 A	0.163 A	0.0026 A	0.327 A	1154.30 A	0.156 B	0.0016 A
	Mouth	0.178 B	1150.50 A	0.177 A	0.0009 B	0.205 A	1126.98 A	0.137 B	0.0014 A
	CV%	88	4	17	96	63	6	20	57

¹ Equal capital letters in the column do not differ significantly from each other by the non-parametric Kruskal–Wallis test ($p < 0.05$). CV% = coefficient of variation.

The K values ranged from 0.0009 to 0.0086 $\text{Mg} \times \text{h} \times (\text{MJ} \times \text{mm})^{-1}$ for SBR (higher intensity) and 0.0014 to 0.0031 $\text{Mg} \times \text{h} \times (\text{MJ} \times \text{mm})^{-1}$ (lower intensity), the middle of the Renato River sub-basin and the source of the Caiabi River sub-basin being the most susceptible areas. However, the results of the statistical test indicate that there was no significant difference at 5% probability for the analysis of factor K tied to the positions of the sub-basins.

It can be seen that the tillage and pasture systems did not interfere with erodibility. This suggests that the K factor is not altered through the use and management of the soil, but rather with the physical–chemical characteristics of the land. The observed field data using the rainfall simulator and estimated soil erodibility using indirect methodologies such as equations for K factor from the literature were not linked to sediment transfer along the sub-basins. However, these results appear to be connected to the intrinsic characteristics of the soil.

Related to anthropic actions, the factors that draw greater attention to the characteristics of these results may be linked to the intense interventions and movement of agricultural machinery [51], as well as the intense use of tillage in agricultural areas [52]. This includes exposure of soil without vegetation and pastures that were intensely trampled by animals. Both intensive tillage and animal traffic in pastures can accelerate soil erosion and degradation. It is worth noting that erodibility does not depend only on the textural relationship and cohesion between particles, but also on parameters such as soil structure and chemistry [49]. These elements may have influenced the erodibility characteristics in both the Renato and Caiabi River sub-basins.

The Caiabi River sub-basin source showed the lowest density value (1.03 kg dm^{-3}) among both sub-basins, and the highest value of microporosity followed by total porosity were observed for this region of spring whose granulometric condition was classified as clayey. Macroporosity ranged from 0.02 kg dm^{-3} to 0.12 kg dm^{-3} for the Renato sub-basin and 0.02 kg dm^{-3} to 0.14 kg dm^{-3} for the Caiabi sub-basin. Table 7 shows the values for the attributes macroporosity, microporosity, total porosity, soil density, and organic matter throughout both sub-basins.

Table 7. Distribution of mean values for the attributes macroporosity, microporosity, total porosity, and soil density in the Renato and Caiabi River sub-basins, Mato Grosso state, Brazil.

Land Use	Sub-Basin Region	Renato Sub-Basin (%) ¹				Caiabi Sub-Basin (%) ¹			
		Micro-Porosity (m ³ m ⁻³)	Macro-Porosity (m ³ m ⁻³)	Total Porosity (m ³ m ⁻³)	Soil Density (kg dm ⁻³)	Micro-Porosity (m ³ m ⁻³)	Macro-Porosity (m ³ m ⁻³)	Total Porosity (m ³ m ⁻³)	Soil Density (kg dm ⁻³)
Cultivated	Source	0.27 A	0.09 A	0.36 A	1.57 A	0.43 A	0.08 A	0.52 A	1.03 A
	Middle	0.27 A	0.10 A	0.37 A	1.51 A	0.29 B	0.07 A	0.36 B	1.48 B
	Mouth	0.36 B	0.08 A	0.44 B	1.57 A	0.28 B	0.10 A	0.38 B	1.51 B
	CV%	15	28	10	4	24	47	19	18
Pasture	Source	0.27 A	0.11 A	0.38 A	1.52 A	0.40 A	0.02 A	0.45 A	1.41 A
	Middle	0.35 A	0.02 B	0.37 A	1.59 A	0.37 A	0.05 B	0.48 A	1.30 B
	Mouth	0.26 A	0.12 A	0.38 A	1.74 B	0.24 B	0.14 B	0.50 B	1.59 C
	CV%	17	73	6	8	24	70	9	9

¹ Equal capital letters in the column do not differ significantly by the non-parametric Kruskal–Wallis test ($p < 0.05$). CV% = coefficient of variation.

Table 8 presents the erodibility results and Table 9 presents the values of the correlation performed through the items observed by the use of the rain simulator and estimated through the indirect methodologies. Regarding the estimation models, the results point to intensity in the distribution of K values. For RSB the indirect models presented range from 0.0008 to 0.0990 Mg × h × (MJ × mm)⁻¹ (greater intensity) and for SBC ranges from 0.0014 to 0.0846 Mg × h × (MJ × mm)⁻¹ (less intensity). Although this range was considered small. In general, the equations that presented alpha (0.05) significance level were the equations of Bouyoucos [37] and Lombardi Neto and Bertoni [42]. However, these correlations presented were negative, leading values in opposite directions for cultivated areas in the Caiabi sub-basin. Moderate and positive correlation was observed with values between 0.469 and 0.660, where the pasture of the Renato sub-basin presented the greatest number of contrasts with moderate correlation.

Table 8. Distribution of erodibility values (K factor) estimated by indirect methodologies along the Renato and Caiabi River sub-basins, Mato Grosso state, Brazil.

Land Use	Source Used for Soil Erodibility Value (K Factor)	Renato Sub-Basin (Mg × h × (MJ × mm) ⁻¹) ¹				Caiabi Sub-Basin (Mg × h × (MJ × mm) ⁻¹) ¹			
		Source	Middle	Mouth	CV%	Source	Middle	Mouth	CV%
Cultivated	Boyocous (1935) [37]	0.0528 Aa	0.0681 Aa	0.0427 Ba	25	0.0282 Aa	0.0464 Ba	0.0541 Bb	31
	Lima et al. (1990) [38]	0.0102 Ab	0.0076 Ab	0.0122 Ab	32	0.0173 Aa	0.0088 Ab	0.0067 Ab	50
	Lombardi Neto and Bertoni (1975) [42]	0.0811 Aa	0.0942 Aa	0.0480 Ba	38	0.0381 Aa	0.0574 Ba	0.0846 Ba	39
	Roloff and Denardin (1994) [44]	0.0188 Ab	0.0162 Ab	0.0199 Ab	21	0.0194 Aa	0.0162 Ab	0.0174 Ab	19
	Roloff and Denardin (1994) [44]	0.0073 Ab	0.0024 Ab	0.0056 Bb	85	0.0436 Ab	0.0029 Bb	0.0023 Bb	126
	Roloff and Denardin (1994) [44]	0.0083 Ab	0.0027 Bb	0.0063 Ab	85	0.0493 Ab	0.0033 Bb	0.0026 Bb	126
	McKague (2023) [45]	0.0160 Ab	0.0110 Ab	0.0210 Ab	38	0.0355 Aa	0.0160 Ab	0.0165 Bb	42
	Wischmeier and Smith (1978) [10]	0.0083 Ab	0.0041 Ab	0.0077 Ab	48	0.0150 Aa	0.0040 Bb	0.0050 Bb	68
	Boyocous (1935) [37]	0.0539 Aa	0.0679 Aa	0.0587 Aa	16	0.0178 Aa	0.0190 Aa	0.0835 Ba	84
	Lima et al. (1990) [38]	0.0083 Ab	0.0090 Ab	0.0086 Ab	24	0.0154 Aa	0.0111 Ba	0.0080 Cb	29
Pasture	Lombardi Neto and Bertoni (1975) [42]	0.0573 Aa	0.0990 Ba	0.0449 Aa	40	0.0294 Aa	0.0365 Bb	0.1260 Ca	76
	Roloff and Denardin (1994) [44]	0.0174 Ab	0.0198 Ab	0.0185 Ab	16	0.0226 Aa	0.0202 Aa	0.0186 Ba	13
	Roloff and Denardin (1994) [44]	0.0019 Ab	0.0017 Ab	0.0008 Ab	52	0.0137 Aa	0.0158 Aa	0.0014 Bb	79

Table 8. Cont.

Land Use	Source Used for Soil Erodibility Value	Renato Sub-Basin (Mg × h × (MJ × mm) ⁻¹) ¹				Caiabi Sub-Basin (Mg × h × (MJ × mm) ⁻¹) ¹			
	(K Factor)	Source	Middle	Mouth	CV%	Source	Middle	Mouth	CV%
	Roloff and Denardin (1994) [44]	0.0021 Ab	0.0020 Ab	0.0009 Ab	52	0.0155 Aa	0.0179 Aa	0.0016 Bb	79
	McKague (2023) [45]	0.0175 Ab	0.0083 Bb	0.0143 Ab	41	0.0287 Aa	0.0260 Aa	0.0093 Bb	46
	Wischmeier and Smith (1978) [10]	0.0046 Ab	0.0065 Ab	0.0047 Ab	40	0.0109 Aa	0.0092 Aa	0.0056 Bb	32

¹ Same capital letters in the row do not differ significantly from each other by the non-parametric Kruskal–Wallis test ($p < 0.05$). Same lower-case letters in the column do not differ significantly from each other by the non-parametric Kruskal–Wallis test ($p < 0.05$). CV% = coefficient of variation.

Table 9. Correlation between direct soil erodibility values measured using a rainfall simulator and indirect values estimated from K factor equations from the literature in the Renato and Caiabi River sub-basins, Mato Grosso state, Brazil.

Source Used for Soil Erodibility Value (K Factor)	Correlation Coefficients			
	Renato Sub-Basin ¹		Caiabi Sub-Basin ¹	
	Cultivated	Pasture	Cultivated	Pasture
Boyoucos (1935) [37]	0.245	0.322	−0.660 *	0.042
Lima et al. (1990) [38]	−0.126	0.322	0.497	0.154
Lombardi Neto and Bertoni (1975) [42]	0.210	0.483	−0.587 *	0.147
Roloff and Denardin (1994) [44]	−0.126	0.559	0.021	0.147
Roloff and Denardin (1994) [44]	−0.469	0.510	0.287	0.231
Roloff and Denardin (1994) [44]	−0.469	0.510	0.287	0.231
McKague (2023) [45]	−0.484	−0.451	0.486	0.165
Wischmeier and Smith (1978) [10]	−0.035	0.441	0.217	0.224

¹ Values in bold and asterisk * are different from 0 at a significance level of alpha = 0.05 (5%). Significantly higher averages were identified at the source of the Caiabi River sub-basin compared to other regions, especially in cultivated and pasture areas. Overall, for the Renato sub-basin, there were little statistically significant differences in the averages from one area of the sub-basin compared to another. These statistically significant differences can be found in cultivated areas at the mouth of the sub-basin.

4. Discussion

4.1. Comparisons and Contrasts to Prior Studies

When evaluating the equation of Bouyoucos 1935 [37], it was found that this model presented a significant difference (5%) in relation to the other indirect methodologies evaluated for most of the cultivated and pasture areas in both the Renato and Caiabi River sub-basins. High values were also observed by da Rocha Lima et al., 2021 [53] who detected erodibility for a dark red Oxisol at $0.0790 \text{ Mg} \times \text{h} \times (\text{MJ} \times \text{mm})^{-1}$ and for a dystrophic purple Oxisol at $0.0290 \text{ Mg} \times \text{h} \times (\text{MJ} \times \text{mm})^{-1}$. The same can be verified in the model proposed by Lombardi Neto and Bertoni 1975 [42], which also presented a significant difference (5%) and the explanation may be related to the smaller number of parameters associated with this model.

Analyzing the other equations, there was no significant difference in the means between the methodologies evaluated. The model adapted by Lima et al. in 1990 [38] pointed to an increase in erodibility values compared to the Wischmeier and Smith 1978 [10] method. The interpretation for this can be addressed by Lima et al. [38], who discuss that the clay element when flocculated resembles the performance of silt and very fine sand for Latosols. The Wischmeier and Smith [10] model had higher values for the K factor observed in the source region in the Caiabi sub-basin. However, the highest susceptibility in the Renato sub-basin occurred in the source area of the sub-basin for cultivated areas and in the middle part of the sub-basin for pasture.

Generally, Oxisols are known for having low silt contents and structurally have granular characteristics. This contributes to a greater flow of hydraulic conductivity in

the soil. Therefore, the estimation of erodibility through methodologies that focus on parameters such as conductivity and percentages of silt in its composition can reduce the values of K factor when analyzed in Oxisols [38].

Godoi et al. [18] explain an analysis for results with low values estimated by the Wischmeier and Smith [10] model. This can be explained as a function of fixed values in the structure code because indexed values can contribute to uncertainties in the erodibility results. On the other hand, there is insufficient measurable data for this attribute, which contributes to assumptions of soil structure.

The model developed by McKague 2023 [45] obtained moderate correlation for most of the systems with the exception of the pastureland of the Caiabi sub-basin. Here, there was weak correlation (0.165). The models proposed by Roloff and Denardin [44] had one of the best correlations among all the methodologies, especially for models 2 and 3, which had iron and aluminum being intrinsically linked to weathered Oxisols [54]. Methodologies 2 and 3 from Roloff and Denardin [44] had moderate correlation for most of the systems of the sub-basins.

According to Godoi et al. [18], Oxisols present less susceptibility to erosion than other soils. However, this soil type becomes much more susceptible when exposed to intensive agricultural land use. The same observation applies in the context of both sub-basins of the study, especially in relation to the soil in the Caiabi River sub-basin. The Caiabi has areas that were deforested much longer ago for agricultural production compared to the Renato sub-basin.

From the perspective of the correlation between direct and indirect methods, Silva et al. [55] concluded that when determining the erodibility of latosols in the Cerrado, indirect methods may not provide statistically accurate estimates when compared to the direct method to calculate the absolute value of the erodibility factor. However, in the study of the Renato and Caiabi Rivers sub-basin, equations 2 and 3 by Roloff and Denardin [44], which use elements such as iron and aluminum as parameters, showed reasonable to moderate correlations, especially as they are latosols.

Di Raimo et al. (2019) [50] studied various soils from the state of Mato Grosso using indirect methodologies for determining erodibility. The authors employed the equations of Wischmeier and Smith (1978) [10] and Denardin (1990) [19]. They determined an erodibility range for the oxisols in the region from 0.0019 to 0.0340 $\text{Mg} \times \text{h} \times \text{MJ}^{-1} \times \text{mm}^{-1}$.

Marques et al. [4], using indirect methodologies, determined erodibility values of 0.0080 and 0.0060 $\text{Mg} \times \text{h} \times \text{MJ}^{-1} \times \text{mm}^{-1}$ for Typic Eutrophic Red Latosol (LVe) and Typic Dystrophic Red Latosol (LVd), respectively. Using a rainfall simulator, they found concentrations of 0.0030 and 0.0020 $\text{Mg} \times \text{h} \times \text{MJ}^{-1} \times \text{mm}^{-1}$ for LVe and LVd, respectively. These values are similar to the results we obtained using a rainfall simulator for the Renato and Caiabi river sub-basins.

4.2. Implications of Research

The identification of soil erodibility in cultivated and pasture areas in the Renato and Caiabi Rivers sub-basins contributes to a better understanding of the factors that influence erosion in these specific ecosystems. Understanding the mechanisms related to erodibility makes it possible to mitigate the complex effects of erosion [24]. In the most varied uses and occupations, soil management policies can promote the effective use of new conservation mechanisms. In this sense, the analysis of erodibility in different scenarios aims to detect characteristics intrinsic to the soil, which may vary over time or due to agricultural activities, without forgetting that the soil can be modified mainly by compaction processes, agricultural mechanization, and trampling by cattle.

The research conducted in this study has substantial social implications, especially for rural communities. Preventing soil degradation allows communities to maintain the productivity of their land, supporting livelihoods and preventing potential risks of economic losses due to poor soil health. In addition, effective land management is critical

for environmental sustainability, which results in benefits for society at large in terms of preserving ecosystems and natural resources.

Frequently tested methodologies can provide improvements in the phases of soil erodibility determination. This can lead to better soil management practices, increasing crop yields, and ensuring food security. Another important point is that the correct adjustment of parameters for specific soil prediction models directly results in adequate performance of the tested model and the reliability of the data obtained. Magalhães et al. [56], used a soil and water prediction model (GeoWEPP) to evaluate sediment production in different land uses and considered it extremely important to observe the geographic conditions of the environment to be tested. This study emphasized that it is essential to correctly insert data according to geographic and environmental characteristics [56]. Our results can be used to update 14 other erosion/sediment transport models in addition to USLE and GeoWEPP [57]. Our results can also help validate machine learning techniques that were developed to globally map the K factor for soils [58].

The appropriate selection of techniques compatible with soil availability and variability in specific environmental conditions not only refines existing theoretical frameworks on the topic, but also suggests a more focused approach to modeling soil erosion, emphasizing the need for adaptable and sensitive methodologies to the environment. Throughout our study, however, it was observed that the models proposed by Lombardi Neto and Bertoni [42], in addition to geographic information and inclusion of a smaller number of parameters could result in significantly different erodibility estimates if a smaller number of parameters is included. This suggests the need to generate new models that integrate a greater number of appropriate criteria. Composing mixed models that combine multiple approaches can provide a more accurate and comprehensive assessment of soil erodibility.

5. Conclusions

Experiments with a rainfall simulator indicated higher values and also variation in the K factor for the Renato sub-basin ranging from 0.0009 to 0.0086 $\text{Mg} \times \text{h} \times (\text{MJ} \times \text{mm})^{-1}$ and lower values and also variation for the Caiabi sub-basin at 0.0014 to 0.0031 $\text{Mg} \times \text{h} \times (\text{MJ} \times \text{mm})^{-1}$. Indirect methodologies also estimated a higher K factor for the Renato River sub-basin at 0.0008 to 0.0990 $\text{Mg} \times \text{h} \times (\text{MJ} \times \text{mm})^{-1}$ and lower for the Caiabi River sub-basin at 0.0014 to 0.0846 $\text{Mg} \times \text{h} \times (\text{MJ} \times \text{mm})^{-1}$. There was no significant difference at the 5% level of the K factor determined by the rainfall simulator for both sub-basins. The equations of Bouyoucos (1935) [37] and Lombardi Neto and Bertoni (1975) [42] presented significant (5%) correlation for cultivated soils surveyed in the Caiabi River sub-basin. The indirect methodologies that obtained reasonable correlation and that showed the best performance were equations 2 and 3 from Rolloff and Denardin (1994) [44] that use iron and aluminum as parameters. The elements that most influenced soil erodibility were the physical textures of the soil. This study aims to open new studies for future investigations on the subject, keeping in mind the focus on new methods of corroboration in various scenarios, such as different soil categories, different climatic conditions, and the most varied use and occupation of land. Furthermore, the insertion of improved technologies, such as remote sensing and geoprocessing, could increase the precision of erosion and erodibility estimates and become more developed, reliable, and applicable anywhere.

Author Contributions: Conceptualization, J.A.X.d.O. and F.T.d.A.; methodology, J.A.X.d.O., C.A.Z., A.P.d.S. and F.T.d.A.; software, J.A.X.d.O.; validation, J.A.X.d.O., F.T.d.A., A.P.d.S. and C.A.Z.; formal analysis, J.A.X.d.O.; investigation, J.A.X.d.O.; resources, A.K.H.; data curation, J.A.X.d.O.; writing—original draft preparation, J.A.X.d.O., F.T.d.A., R.S.D.P. and A.P.d.S.; writing—review and editing, A.K.H.; visualization, J.A.X.d.O.; supervision, F.T.d.A. and A.P.d.S.; project administration, F.T.d.A. and A.P.d.S.; funding acquisition, A.P.d.S. All authors have read and agreed to the published version of the manuscript.

Funding: To the Federal University of Mato Grosso (UFMT) and the Coordination for the Improvement of Higher Education Personnel (CAPES) for granting a scholarship and the National Water Agency (ANA)—research funding (Process: 88887.144957/2017-00—CAPES-ANA-DPB).

Data Availability Statement: The data presented in this study are available on request from the corresponding author.

Conflicts of Interest: Author Cornélio Alberto Zolin was employed by the company Brazilian Agricultural Research Corporation. The remaining authors declare that the research was conducted in the absence of any commercial or financial relationships that could be construed as a potential conflict of interest.

References

1. Wang, B.; Zheng, F.; Römken, M.J.M. Comparison of soil erodibility factors in USLE, RUSLE, EPIC and Dg models based on a Chinese soil erodibility database. *Acta Agric. Scand. B* **2013**, *63*, 69–79. [CrossRef]
2. Shojaei, S.; Kalantari, Z.; Rodrigo-Comino, J. Prediction of factors affecting activation of soil erosion by mathematical modeling at pedon scale under laboratory conditions. *Sci. Rep.* **2020**, *10*, 20163. [CrossRef] [PubMed]
3. Hateffard, F.; Mohammed, S.; Alsafadi, K.; Enaruvbe, G.O.; Heidari, A.; Abdo, H.G.; Rodrigo-Comino, J. CMIP5 climate projections and RUSLE-based soil erosion assessment in the central part of Iran. *Sci. Rep.* **2021**, *11*, 7273. [CrossRef] [PubMed]
4. Marques, V.S.; Ceddia, M.B.; Antunes, M.A.H.; Carvalho, D.F.; Anache, J.A.A.; Rodrigues, D.B.B.; Oliveira, P.T.S. USLE K-Factor Method Selection for a Tropical Catchment. *Sustainability* **2019**, *11*, 1840. [CrossRef]
5. Addis, H.K.; Klik, A. Predicting the spatial distribution of soil erodibility factor using USLE nomograph in an agricultural watershed, Ethiopia. *Int. Soil Water Conserv. Res.* **2015**, *3*, 282–290. [CrossRef]
6. Ojo, A.O.; Nwosu, N.J.; Oshunsanya, S.O.; Ayantayo-Ojo, V.I.; Aladele, S.E. Impacts of soil conservation techniques on soil erodibility on an Alfisol. *Heliyon* **2023**, *9*, E13768. [CrossRef] [PubMed]
7. Panagos, P.; Meusburger, K.; Ballabio, C.; Borrelli, P.; Alewell, C. Soil erodibility in Europe: A high-resolution dataset based on LUCAS. *Sci. Total Environ.* **2014**, *479–480*, 189–200. [CrossRef] [PubMed]
8. Pimentel, D.; Harvey, C.; Resosudarmo, P.; Sinclair, K.; Kurz, D.; McNair, M.; Crist, S.; Shpritz, L.; Fitton, L.; Saffouri, R.; et al. Environmental and Economic Costs of Soil Erosion and Conservation Benefits. *Science* **1995**, *267*, 1117–1123. [CrossRef]
9. Anache, J.A.A.; Wendland, E.C.; Oliveira, P.T.S.; Flanagan, D.C.; Nearing, M.A. Runoff and soil erosion plot-scale studies under natural rainfall: A meta-analysis of the Brazilian experience. *Catena* **2017**, *152*, 29–39. [CrossRef]
10. Wischmeier, W.H.; Smith, D.D. *Predicting Rainfall Erosion Losses: A Guide to Conservation Planning*; Agricultural Handbook 537; Science and Education Administration, U.S. Department of Agriculture: Washington, DC, USA, 1978. Available online: <https://www.govinfo.gov/app/details/GOVPUB-A-PURL-gpo31516> (accessed on 4 June 2024).
11. Renard, K.G.; Foster, G.R.; Weesies, G.A.; McCool, D.K.; Yoder, D.C. *Predicting Soil Erosion by Water: A Guide to Conservation Planning with the Revised Universal Soil Loss Equation (RUSLE)*; Agricultural Handbook Number 703; Agricultural Research Service, U.S. Department of Agriculture: Washington, DC, USA, 1997; pp. 1–64. Available online: <https://www3.epa.gov/npdes/pubs/ruslech2.pdf> (accessed on 4 June 2024).
12. Benavidez, R.; Jackson, B.; Maxwell, D.; Norton, K. A review of the (Revised) Universal Soil Loss Equation ((R)USLE): With a view to increasing its global applicability and improving soil loss estimates. *Hydrol. Earth Syst. Sci.* **2018**, *22*, 6059–6086. [CrossRef]
13. Mahamud, M.A.; Saad, N.A.; Zainal Abidin, R.; Yusof, M.F.; Zakaria, N.A.; Arumugam, M.A.R.M.A.; Desa, S.M.; Noh, M.M.N. Determination of Cover and Land Management Factors for Soil Loss Prediction in Cameron Highlands, Malaysia. *Agriculture* **2021**, *12*, 16. [CrossRef]
14. Lin, B.S.; Chen, C.K.; Thomas, K.; Hsu, C.K.; Ho, H.-C. Improvement of the K-factor of USLE and soil erosion estimation in Shihmen Reservoir Watershed. *Sustainability* **2019**, *11*, 355. [CrossRef]
15. López-García, E.; Torres-Trejo, E.; López-Reyes, L.; Flores-Domínguez, Á.D.; Peña-Moreno, R.D.; López-Olguín, J.F. Estimation of soil erosion using USLE and GIS in the locality of Tzicatlacoyan, Puebla, México. *Soil Water Res.* **2020**, *15*, 9–17. [CrossRef]
16. Pakoksung, K. Assessment of Soil Loss from Land Cover Changes in the Nan River Basin, Thailand. *GeoHazards* **2024**, *5*, 1–21. [CrossRef]
17. Cheng, J.; Zhang, X.; Jia, M.; Su, Q.; Kong, D.; Zhang, Y. Integrated Use of GIS and USLE Models for LULC Change Analysis and Soil Erosion Risk Assessment in the Hulan River Basin, Northeastern China. *Water* **2024**, *16*, 241. [CrossRef]
18. Godoi, R.d.F.; Rodrigues, D.B.B.; Borrelli, P.; Oliveira, P.T.S. High-resolution soil erodibility map of Brazil. *Sci. Total Environ.* **2021**, *781*, 146673. [CrossRef]
19. Denardin, J.E. Erodibilidade do Solo Estimada por Meio de Parâmetros Físicos e Químicos. Ph.D. Thesis, Universidade de São Paulo, Escola Superior de Agricultura Luiz de Queiroz, Piracicaba, São Paulo, Brazil, 1990. [CrossRef]
20. Gupta, S.; Borrelli, P.; Panagos, P.; Alewell, C. An advanced global soil erodibility (K) assessment including the effects of saturated hydraulic conductivity. *Sci. Total Environ.* **2024**, *908*, 168249. [CrossRef]
21. Ngezahayo, E.; Burrow, M.; Ghataora, G. Calibration of the Simple Rainfall Simulator for Investigating Soil Erodibility in Unpaved Roads. *Int. J. Civ. Infrastruct.* **2021**, *4*, 144–156. [CrossRef]
22. Silva, J.R.I.; de Souza, E.S.; Souza, R.; dos Santos, E.S.; Antonino, A.C.D. Effect of different land uses on water erosion in a semi-arid region. *Rev. Eng. Agric.* **2019**, *27*, 272–283. [CrossRef]

23. Alves, M.A.B.; de Souza, A.P.; de Almeida, F.T.; Hoshide, A.K.; Araújo, H.B.; da Silva, A.F.; de Carvalho, D.F. Effects of Land Use and Cropping on Soil Erosion in Agricultural Frontier Areas in the Cerrado-Amazon Ecotone, Brazil, Using a Rainfall Simulator Experiment. *Sustainability* **2023**, *15*, 4954. [CrossRef]
24. Guerra, A.J.T.; Fullen, M.A.; do Carmo Oliveira Jorge, M.; Alexandre, S.T. Soil Erosion and Conservation in Brazil. *Anu. Inst. Geociênc.* **2014**, *37*, 81–91. [CrossRef]
25. Kraeski, A.; de Almeida, F.T.; de Souza, A.P.; de Carvalho, T.M.; de Abreu, D.C.; Hoshide, A.K.; Zolin, C.A. Land Use Changes in the Teles Pires River Basin's Amazon and Cerrado Biomes, Brazil, 1986–2020. *Sustainability* **2023**, *15*, 4611. [CrossRef]
26. Moratelli, F.A.; Alves, M.A.B.; Borella, D.R.; Kraeski, A.; de Almeida, F.T.; Zolin, C.A.; Hoshide, A.K.; de Souza, A.P. Effects of Land Use on Soil Physical-Hydric Attributes in Two Watersheds in the Southern Amazon, Brazil. *Soil Syst.* **2023**, *7*, 103. [CrossRef]
27. Borella, D.R.; de Souza, A.P.; de Almeida, F.T.; de Abreu, D.C.; Hoshide, A.K.; Carvalho, G.A.; Pereira, R.R.; da Silva, A.F. Dynamics of Sediment Transport in the Teles Pires River Basin in the Cerrado-Amazon, Brazil. *Sustainability* **2022**, *14*, 16050. [CrossRef]
28. Nunes, M.C.M.; Cassol, E.A. Estimation of erodibility in inter-ridge of latosols in Rio Grande do Sul. *Rev. Bras. Ciênc. Solo* **2008**, *32*, 2839–2845. [CrossRef]
29. Batista, P.V.G.; Davies, J.; Silva, M.L.N.; Quinton, J.N. On the evaluation of soil erosion models: Are we doing enough? *Earth Sci. Rev.* **2019**, *197*, 102898. [CrossRef]
30. dos Santos, H.G.; Jacomine, P.K.T.; dos Anjos, L.H.C.; de Oliveira, V.A.; Lumbrreras, J.F.; Coelho, M.R.; de Almeida, J.A.; de Araújo Filho, J.C.; de Oliveira, J.B.; Cunha, T.J.F. *Sistema Brasileiro de Classificação de Solos*, 5th ed.; Embrapa Informação Tecnológica: Brasília, DF, Brazil, 2018; pp. 1–590, ISBN 978-85-7035-800-4.
31. Sobrinho, T.A.; Gómez-Macpherson, H.; Gómez, J.A. A portable integrated rainfall and overland flow simulator. *Soil Use Manag.* **2008**, *24*, 163–170. [CrossRef]
32. Nephew, T.A.; Vitorino, A.C.T.; de Souza, L.C.F.; Gonçalves, M.C.; de Carvalho, D.F. Water infiltration into the soil in direct and conventional planting systems. *Rev. Bras. Eng. Agrícola e Ambient.* **2003**, *7*, 191–196. [CrossRef]
33. Sabino, M.; de Souza, A.P.; Uliana, E.M.; de Almeida, F.T.; Lisboa, L.; Zolin, C.A. Probability distributions for maximum rainfall in the state of Mato Grosso. *Rev. Bras. Climatol.* **2021**, *29*, 321–340.
34. Teixeira, P.C.; Donagemma, G.K.; Fontana, A.; Teixeira, W.G. *Manual de Métodos de Análise de Solo*, 3rd ed.; Embrapa Informação Tecnológica: Brasília, DF, Brazil, 2017; pp. 1–573, ISBN 978-85-7035-771-7. Available online: <https://www.embrapa.br/en/busca-de-publicacoes/-/publicacao/1085209/manual-de-metodos-de-analise-de-solo> (accessed on 4 June 2024).
35. Foster, G.R.; McCool, D.K.; Renard, K.G.; Moldenhauer, W.C. Conversion of the universal soil loss equation to SI metric units. *J. Soil Water Conserv.* **1981**, *36*, 355–359. Available online: https://www.engr.colostate.edu/~pierre/ce_old/Projects/linkfiles/USLE%20Unit%20conversions.pdf (accessed on 4 June 2024).
36. Wischmeier, W.H. A Rainfall Erosion Index for a Universal Soil-Loss Equation. *Soil Sci. Soc. Am. J.* **1959**, *23*, 246–249. [CrossRef]
37. Bouyoucos, G.J. The Clay Ratio as a Criterion of Susceptibility of Soils to Erosion. *Agronomy J.* **1935**, *27*, 738–741. [CrossRef]
38. Lima, J.M.; Curi, N.; Resende, M.; Santana, D.P. Dispersion of soil material in water for indirect evaluation of latosol erodibility. *Rev. Bras. Ciênc. Solo* **1990**, *14*, 85–90. Available online: <https://www.alice.cnptia.embrapa.br/alice/bitstream/doc/489138/1/Dispersaomaterial.pdf> (accessed on 4 June 2024).
39. Marques, J.J.G.S.M.; Curi, N.; de Lima, J.M.; Ferreira, M.M.; Silva, M.L.N.; Ferreira, D.F. Estimation of erodibility from attributes of soils with argillic horizon in Brazil. *Rev. Bras. Ciênc. Solo* **1997**, *21*, 457–465. [CrossRef]
40. Secretaria de Planejamento do Estado de Mato Grosso (SEPLAN). *Classificação dos solos-Pedologia; Socioeconomic and Ecological Zoning of the State of Mato Grosso (ZSEE): Mato Grosso, Brazil, 1997*. Available online: <https://geo.mt.gov.br/zsee2018/> (accessed on 4 June 2024).
41. Wischmeier, W.H.; Johnson, C.B.; Cross, B.V. Soil erodibility nomograph for farmland and construction sites. *J. Soil Water Conserv.* **1971**, *26*, 189–193.
42. Lombardi Neto, F.; Bertoni, J. *Erodibilidade de Solos Paulistas*. Boletim técnico, Instituto Agronômico: Campinas, Brazil, 1975; Volume 27, pp. 1–12.
43. Middleton, H.E. Properties of Soils Which Influence Soil Erosion. *Soil Sci. Soc. Am. J.* **1930**, *B11*, 1–16. [CrossRef]
44. Roloff, G.; Denardin, J.E. Estimativa simplificada da erodibilidade do solo. In *Reunião Brasileira de Manejo e Conservação do Solo e da Água, Resumos*, 10; SBCS: Florianópolis Santa Catarina, Brazil, 1994; pp. 150–151.
45. McKague, K. *Universal Soil Loss Equation (USLE)*; Ontario Ministry of Agriculture and Food (OMAFRA): Ontario, Canada, 2023; Available online: <https://files.ontario.ca/omafra-universal-soil-loss-equation-23-005-en-2023-03-02.pdf> (accessed on 4 June 2024).
46. Lima, J.E.F.W.; da Silva, E.M.; Eid, N.J.; de Souza Martins, E.; Koide, S.; Reatto, A. Development and verification of indirect methods for estimating the Erodibility of Soils in the Alto Rio Jardim Experimental Basin—DF. *Rev. Bras. Geomorfol.* **2007**, *8*, 23–36. [CrossRef]
47. Paulista, R.S.D.; de Almeida, F.T.; de Souza, A.P.; Hoshide, A.K.; de Abreu, D.C.; da Silva Araújo, J.W.; Martim, C.C. Estimating Suspended Sediment Concentration using Remote Sensing for the Teles Pires River, Brazil. *Sustainability* **2023**, *15*, 7049. [CrossRef]
48. Soares, M.D.R.; Campos, M.C.C.; da Cunha, J.M.; Mantovanelli, B.C.; de Oliveira, I.A.; de Brito Filho, E.G.; Leite, A.F.L. Spatial variability of aggregate stability and soil organic matter in archaeological terra preta under pasture. *Gaia Sci.* **2018**, *12*, 125–133. [CrossRef]

49. Pruski, F.F. *Soil and Water Conservation: Mechanical Practices for Water Erosion Control*, 2nd ed.; Universidade Federal Viçosa: Viçosa, MG, Brazil, 2009; pp. 1–279, ISBN 9788572693646.
50. Di Raimo, L.A.d.L.; Amorim, R.S.S.; Torres, G.N.; Bocuti, E.D.; Couto, E.G. Spatial variability of erodibility in the state of Mato Grosso, Brazil. *Rev. Ciênc. Agrár.* **2019**, *42*, 55–67. [CrossRef]
51. Girardello, V.C.; Amando, T.J.C.; Santi, A.L.; LanzaNova, M.E.; Tasca, A. Soil penetration resistance and soybean root growth under no till with controlled traffic farming. *Rev. Sci. Agrar.* **2017**, *18*, 86–96. Available online: <https://www.redalyc.org/pdf/995/99551919009.pdf> (accessed on 4 June 2024).
52. Freitas, L.; de Oliveira, I.A.; Silva, L.S.; Frare, J.C.V.; Filla, V.A.; Gomes, R.P. Indicators of soil chemical and physical quality under different management systems. *Rev. Unimar Ciênc.* **2017**, *26*, 8–25. Available online: <http://ojs.unimar.br/index.php/ciencias/article/view/511/278> (accessed on 10 May 2024).
53. da Rocha Lima, C.G.; Bacani, V.M.; Montanari, R.; Vick, E.P.; Ferreira, C.C.; dos Santos da Silva, E.R. Indirect methodologies for measurement of soil erodibility and characterization of spatial variability. *Mercator* **2021**, *20*, 1–15. Available online: <https://www.redalyc.org/journal/2736/273667617013/> (accessed on 4 June 2024).
54. Bócoli, F.A.; dos Santos, W.J.R.; Silva, S.H.G.; dos Santos Teixeira, A.F.; Mancini, M.; Curi, N. Study of an abnormal occurrence of Oxisols in strongly undulated relief in the south of Minas Gerais. Brazil. with support of pXRF and geomorphology. *Ciênc. e Agrotecnologia* **2021**, *45*, 1–13. [CrossRef]
55. Silva, M.L.N.; Curi, N.; de Oliveira, M.S.; Ferreira, M.M.; Neto, F.L. Comparison between direct and indirect methods for determining erodibility in latosols under cerrado. *Pesqui. Agropecu. Bras.* **1994**, *29*, 1751–1761. Available online: <https://seer.sct.embrapa.br/index.php/pab/article/view/4231> (accessed on 4 June 2024).
56. Magalhães, W.d.A.; Amorim, R.S.S.; Hunter, M.O.; Bocuti, E.D.; Di Raimo, L.A.D.L.; da Silva, W.M.; Hoshide, A.K.; de Abreu, D.C. Using the GeoWEPP Model to Predict Water Erosion in Micro-Watersheds in the Brazilian Cerrado. *Sustainability* **2023**, *15*, 4711. [CrossRef]
57. Igwe, P.U.; Onuigbo, A.A.; Chinedu, O.C.; Ezeaku, I.I.; Muoneke, M.M. Soil Erosion: A Review of Models and Applications. *Int. J. Adv. Eng. Res. Sci.* **2017**, *4*, 138–150. [CrossRef]
58. Yang, M.; Yang, Q.; Zhang, K.; Pang, G.; Huang, C. Global soil erodibility factor (K) mapping and algorithm applicability analysis. *Catena* **2024**, *239*, 107943. [CrossRef]

Disclaimer/Publisher’s Note: The statements, opinions and data contained in all publications are solely those of the individual author(s) and contributor(s) and not of MDPI and/or the editor(s). MDPI and/or the editor(s) disclaim responsibility for any injury to people or property resulting from any ideas, methods, instructions or products referred to in the content.

Article

Changes in Ground Cover Layers, Biomass and Diversity of Vascular Plants/Mosses in the Clear-Cuts Followed by Reforested Scots Pine until Maturity Age

Dovilė Gustienė^{1,2} and Iveta Varnagirytė-Kabašinskiene^{1,*}

¹ Lithuanian Research Centre for Agriculture and Forestry, Silviculture and Ecology Department, Liepų Str. 1, Kaunas District, 53101 Girionys, Lithuania

² Landscape Engineering and Forestry Department, Lithuanian Engineering University of Applied Engineering Sciences, Liepų Str. 1, Kaunas District, 53101 Girionys, Lithuania

* Correspondence: iveta.kabasinskiene@lammc.lt

Abstract: The distribution of Scots pine (*Pinus sylvestris* L.) forests, particularly the *Vaccinio myrtillo-Pinetum* type, is determined by edaphic conditions, and although clear-cutting is used to promote regeneration, it remains controversial. This study evaluated the changes in non-living (forest floor and dead wood) and living (mosses, herbs, and dwarf shrubs) ground cover in clear-cut areas and reforested Scots pine stands. Continuous ground cover studies were conducted in clear-cuts, with samples collected over three years after clear-cutting, while data from 8–80-year-old and mature Scots pine stands were collected using the chronological series method with a consistent methodology in temporary plots. The research has shown that, as ecosystem recovery progresses, similarity to the mature forest increases, and a threshold stand age has been identified, beyond which the ecological changes induced by clear-cutting diminish. The study findings demonstrated that clear-cutting in *Pinetum vaccinio-myrtillosum*-type forest stands lead to a rapid increase in herb and dwarf shrub cover due to reduced competition for light and nutrients. However, clear-cutting caused a significant decline in forest-specific species and a drastic reduction in forest floor and dead wood mass, with a gradual recovery of moss cover over 10–30 years. These findings highlight the importance of managing clear-cutting practices to balance immediate vegetative responses with long-term ecosystem stability and biodiversity conservation.

Keywords: *Pinus sylvestris*; clear-cutting; ground vegetation; forest floor; biomass

Citation: Gustienė, D.; Varnagirytė-Kabašinskiene, I. Changes in Ground Cover Layers, Biomass and Diversity of Vascular Plants/Mosses in the Clear-Cuts Followed by Reforested Scots Pine until Maturity Age. *Land* **2024**, *13*, 1477. <https://doi.org/10.3390/land13091477>

Academic Editors: Jianye Li, Xingyi Zhang, Weida Gao, Wei Hu and Qiang Chen

Received: 7 August 2024

Revised: 2 September 2024

Accepted: 11 September 2024

Published: 12 September 2024



Copyright: © 2024 by the authors. Licensee MDPI, Basel, Switzerland. This article is an open access article distributed under the terms and conditions of the Creative Commons Attribution (CC BY) license (<https://creativecommons.org/licenses/by/4.0/>).

1. Introduction

Understanding the dynamics of Scots pine (*Pinus sylvestris* L.) forests in recovering ground cover following clear-cutting is essential for sustainable forest management and biodiversity conservation. Clear-cutting, a common forestry practice, significantly impacts forest ecosystems, particularly on the forest floor and mineral soil [1–3]. Numerous studies have investigated the short-term effects of clear-cutting on chemical indices of forest ecosystems, emphasizing significant effects on the soil structure, nutrient dynamics, and microbial activity. Post-harvest changes in soil moisture and elemental composition, important for nutrient fluxes and retention, have been observed [4,5]. Clear-cutting significantly affects nitrogen (N) and C cycling, critical to maintaining soil fertility and overall forest health [6,7]. Clear-cutting has also affected the soil water chemistry, increasing soil nutrient leaching and acidification [8,9]. In addition, dissolved organic carbon (DOC) concentrations increased significantly in boreal forest waters after logging, affecting water quality and nutrient dynamics [9]. Previous studies reported a direct biochemical response of soil organisms to forest cover removal with significant changes in soil respiration and microbial activity [10].

More specifically, research focusing on the changes in different vegetation groups after clear-cutting primarily concentrated on the initial years post-harvesting [4,7,11–15]. Much

of the research focuses on the impact of a single forestry activity, leading to sparse and highly specific data that can lead to conflicting results [16]. Few studies have assessed changes in both living and dead ground cover in Scots pine forests after clear-cutting or during the age of stand rotation in Europe [17].

Previous studies have shown that both edaphic and climatic conditions are critical factors that alter land cover ecological responses to clear-cutting, influencing nutrient cycling, biomass production, and overall vegetation dynamics. The effects of various soil types and climatic conditions on vegetation recovery and soil nutrient cycling after clear-cutting have been previously emphasized [18,19]. Similarly, the role of soil properties and climate in influencing changes in plant biomass and nutrient pools in boreal forests has been analyzed, demonstrating that soil moisture and temperature regimes are crucial factors in altering plant community composition and biomass recovery [5,20].

Earlier, it was found that living and non-living ground cover elements in the forest ecosystem closely interact with each other [21]. The living ground vegetation was identified as a key element for a successful process after clear-cutting. The importance of ground cover in early forest succession and its influence on ecosystem functions was widely discussed [22–25]. The effects of clear-cutting on plant community composition and succession have been studied, revealing how early successional species establish and influence the development of subsequent stands [26,27]. Similarly, the early stages of forest stand formation have been investigated, highlighting the crucial role of ground cover vegetation in these processes [28,29]. Vegetation plays a critical role in nutrient cycling in clear-cutting areas and throughout the stand rotation, as well as in maintaining soil fertility and facilitating the recovery of forest ecosystems after clear-cutting [12,25,29–31].

In Lithuania, the distribution of Scots pine forests, particularly of *Vaccinio myrtillo-Pinetum* forest type, is largely determined by edaphic conditions. These forests typically grow on low-fertility sandy soils with a normal moisture regime dominating the region among other forest types. Despite the most suitable soil type for Scots pine, the natural transition from Scots pine to Norway spruce (*Picea abies* (L.) H. Karst.) is common in this forest type [23]. Norway spruce has been observed to grow more successfully under Scots pine canopies due to the optimal light regime, while Scots pine understory regeneration is often limited [32]. To ensure the dominance of Scots pine in the next forest generation, clear-cutting is purposefully applied in mature Scots pine forests to create favorable conditions. Furthermore, clear-cutting practices continue to raise environmental and biodiversity debates, highlighting the need for a better understanding of the processes involved and for detailed research to find optimal solutions.

One of the indicator layers of Scots pine forest—living and non-living ground cover—is crucial for assessing the changes after clear-cutting, and it could be assumed that the recovery of this layer is essential for the overall dynamics of a stable ecosystem. This study aimed to evaluate changes in the ground cover layers in clear-cuts followed by reforested Scots pine stands over their development until maturity age. This study defined ground cover as the layer covering the mineral soil, including forest floor and dead wood, as the non-living ground cover layer, and ground vegetation, including mosses, herbs, and dwarf shrubs, as the living ground cover layer. For this study, we hypothesized that (1) clear-cutting in *Pinetum vaccinio-myrtillosum*-type Scots pine stands initially reduces forest-specific species and forest floor mass but increases herb and dwarf shrub cover within 2–3 years, and (2) the moss cover and mass characteristics for mature stands, influenced by canopy density changes, gradually recovers over 15–20 years after clear-cutting, playing a crucial role in stabilizing ground cover.

2. Materials and Methods

2.1. Study Design and Characteristics

The study on the threshold age of Scots pine forests for the recovery of ground cover following clear-cuttings was performed at the three Regional Divisions of State Forest Enterprise in the middle, south, and southeastern parts of Lithuania (Figure 1).

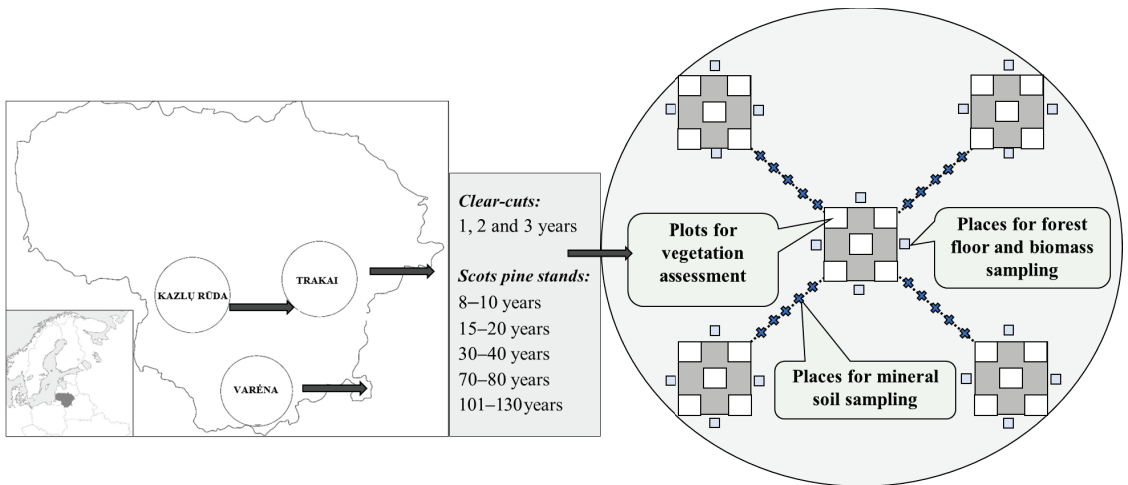


Figure 1. Research scheme: three research objects (Trakai, Varėna, and Kazlų Rūda), each included study sites of selected 1–3-year-old clear-cuts and 8–10-, 15–20-, 30–40-, 70–80-, and 110–130-year-old Scots pine stands.

Study sites included at least 90% Scots pine trees, which, as far as is historically known, were reforested after clear-cutting (Table 1). The study was carried out from 2020 to 2023. Permanent study plots of approximately 2000 m² (2001.38 m²) with a radius of 25.24 m were established in clear-cuts to continuously conduct the ground cover evaluation for three years (Figure 1), i.e., in clear-cuts that were 1, 2, and 3 years old. To establish fresh clear-cuts, the mature Scots pine forest was harvested through clear-cutting, with the stems and logging residues, except stumps and roots, removed from the cutting site. The 2- and 3-year-old clear-cuts were reforested with artificially planted Scots pine trees. The study plots in the clear-cuts, designated for continuous vegetation assessment, were carefully replanted with Scots pine trees, ensuring that the vegetation layer and forest floor remained undisturbed. The chronosequence method was applied to explore changes in ground cover in the stands of different ages over stand rotation. The age of available stands varied insignificantly in objects. Therefore, the 8–10-, 15–20-, 30–40-, 70–80-, and 110–130-year-old stands were selected for the study. In the stands of different ages, temporary study plots of the same size as in clear-cuts were established (Figure 1). Altogether, seven study plots, including two plots in 1- 2-, and 3-year-old clear-cut sites and one site in each 8–10-, 15–20-, 30–40-, 70–80-, and 110–130-year-old Scots pine stands were selected in each of three research objects. The sites were chosen at close distances—up to 2 km—from each other within each object. All study sites represented comparable meteorological and soil conditions. According to the 1991–2020 normal climate, in Lithuania, the mean annual temperature was 7.4 °C, and the mean annual precipitation was 695 mm. The soil was characterized by low fertility with coarse sand, low (<5%) clay and silt content, and normal moisture [33]. The soil was classified as Albic Arenosol [34], and the forest vegetation type was classified as *Vaccinio-myrtilliosa*. The dominant ground vegetation species were *Pleurozium schreberi* (Brid.) Mitt., *Hylocomium splendens* (Hedw.) Schimp., *Ptilium crista-castrensis* (Hedw.) De Not., *Vaccinium myrtillus* L., and *V. vitis-idaea* L [21,23,33,35]. These

characteristics well represented the *Vaccinio myrtillo-Pinetum* forest type in Lithuania, which was classified according to the Lithuanian Forest Site Type classification in [35].

Table 1. The characteristics of the Scots pine stands are derived from the State Forest Cadastre (Lithuania) and tree height measurements of planted Scots pine stands collected during this study in 2020–2023.

Object	Stand Composition *	Stand Age (Years)	DBH (cm)	Height (m)	Stocking Level ***	Volume (m ³ ha ⁻¹)
Trakai 54°44' N, 24°80' E	90P10E	2 **	-	-	6000 trees ha ⁻¹	-
	90P10E	2 **	-	-	6000 trees ha ⁻¹	-
	100P	10	5	4.5	0.9	20
	100P	15	9	7	0.8	60
	90P10E	30	14	15	0.8	160
	100P	70	25	26	0.7	280
Varėna 54°26' N, 24°53' E	100P	135	46	30	0.7	415
	90P10B	2 **	-	-	6000 trees ha ⁻¹	-
	100P	2 **	-	-	6000 trees ha ⁻¹	-
	90P10B	8	3	2.5	0.9	14
	90P10B	15	5	6	1.0	50
	100P	39	13	16	0.8	120
Kazlų Rūda 54°76' N, 23°40' E	100P	70	21	24	0.9	300
	100P	110	34	27	0.8	360
	100P	2 **	-	-	7000 trees ha ⁻¹	-
	100P	2 **	-	-	5000 trees ha ⁻¹	-
54°73' N, 23°47' E	90P10B	8	4	3.1	0.9	19
	90P10B	15	8	4.8	0.9	70
	90P10B	30	14	15	0.9	150
	100P	77	29	28	0.9	400
90P10E	117	38	31	0.7	320	

* Stand composition shown in % of each species totaling 100%: P—Scots pine (*Pinus sylvestris*), E—Norway spruce (*Picea abies*), and B—birch (*Betula* sp.). ** Scots pine seedlings for reforestation were grown in the forest nursery for two years before planting, as is the standard practice. *** Stocking level, available from the State Forest Cadastre (Lithuania), describes the ratio of the sums of diameters of the measured and normal stands when the normal stand is equated to 1 and indicates a stand in which the tree crowns are completely closed. As the State Forest Cadastre does not provide data on the stocking level in reforested clear-cuts, tree density was evaluated specially for this study and shown as the number of trees per 1 ha.

2.2. Assessment of Ground Vegetation Cover

As previously mentioned, the ground cover, which lay on the mineral soil, included ground vegetation, including mosses, herbs, and dwarf shrubs (living layer), as well as forest floor and dead wood (non-living/dead layer) [36]. In ground cover, the following parameters were assessed: (1) ground vegetation species composition and percentage cover, (2) forest floor and ground vegetation biomass, and (3) dead wood accumulation.

Vegetation coverage was assessed each July from 2020 to 2023, during the peak growth period for herbaceous plants in the climatic region. Vegetation was observed within systematically arranged one-square-meter (1 m²) quadrats. A special frame marked with a one-square-decimeter (1 dm²) grid was used to estimate each vegetation quadrat species' percentage cover visually. A total of 25 m² per study site was assessed.

The ground vegetation species were categorized into four vertical strata: moss layer, herbs (non-woody and woody plants up to 0.5 m), shrubs (woody vegetation from 0.5 to 5.0 m), and trees (woody vegetation exceeding 5.0 m in height). The mean value of each species cover was calculated per site.

To evaluate the importance of vegetation species within an ecosystem, the prominence value (*PV*) was calculated using Formula (1):

$$PV = \sqrt{D} \times P \quad (1)$$

where P is the mean cover, %, and D is the frequency, determined as the number of subplots in which the species was detected divided by the total number of subplots [37].

To quantify the compositional dissimilarity between two different sites, the Bray–Curtis coefficient was calculated using Formula (2):

$$BC_{jk} = 1 - \frac{2\sum_{i=1}^p \min(N_{ik}, N_{ik'})}{\sum_{i=1}^p (N_{ij} + N_{ik})} \quad (2)$$

where N_{ij} is the cover (%) of species i at site j , N_{ik} is the cover (%) of species i at site k , and p is the total number of species in the samples.

2.3. Assessment of Forest Floor, Ground Vegetation Mass, and Dead Wood Accumulation

The mass of the forest floor and aboveground vegetation (mosses, herbs, and dwarf shrubs) was determined using physical sampling within a 25×25 cm metallic frame. The forest floor was defined as all dead organic material on the surface of the mineral soil. It included recognizable material, such as annual litter composed of dead needles, twigs and small branches, dead herbs, and also fragmented and humified layers composed of unidentifiable decomposed fragments of organic material. All the mosses and herbs inside the area of the frame were clipped and placed in a paper bag. If no vegetation was within the frame area, its biomass was zero. The removed vegetation was thoroughly grouped into individual species, placing them in separate bags. For mass determination, composite samples of the forest floor and aboveground parts of vegetation were obtained from 5 subsamples ($n = 5$) oven-dried at 105°C to a constant mass and weighed.

Dead wood accumulation in clear-cut sites and Scots pine stands of different ages were assessed using a methodology adapted to Lithuanian conditions [38]. Four systematically selected 100 m^2 (10×10 m) plots within a 2000 m^2 area were used. All dead wood elements were recorded within the plots, including standing dead trees, logs, lying dead trunks, fallen branches, and stumps larger than or equal to 5 cm in diameter. The decomposition stages of dead wood were categorized into five classes: 1st class, described as recently dead or fresh wood; 2nd class, slightly dead or fairly hard wood without bark, not yet rotted; 3rd class, medium decayed or fairly soft wood; 4th class, very decayed, soft and fragmented wood; and 5th class, almost decomposed, soft and rotten wood [38].

2.4. Canopy Density Assessment

A spherical crown densiometer was used to measure stand canopy density in 8–10-, 15–20-, 30–40-, 70–80-, and 110–130-year-old Scots pine. Measurements were taken at the center of each 10×10 m plot (Figure 1), with five measurement locations per plot.

2.5. Calculations and Statistical Analysis

To find the significant differences between the sites, ANOVA followed by a post hoc LSD test was used. Data are presented as the means \pm standard error (SE). Different letters next to the mean values show statistically significant differences at $p < 0.05$ between the sites. Statistical analyses were conducted using STATISTICA 12.0 (StatSoft. Inc. 2007, Tulsa, OK, USA) software. Using R statistical software (Version 4.4.0), we visualized the Bray–Curtis dissimilarity index, clearly comparing species compositions in different sites.

3. Results

3.1. Change of Living Ground Cover at Different Forest Succession Stages

Similar trends in the mean coverage of mosses and herbaceous plants along the stand age groups were determined in the research objects of Trakai, Varėna, and Kazlų Rūda. The moss coverage dominated the living ground cover of the *Vaccinio myrtillo-Pinetum* forest type (Table 2 and Figure 2A). The mean cover (Table 2) and the proportion (Figure 2A) of mosses in the 1-year-old clear-cuts were lower than that in the Scots pine stand. However,

the lowest cover was found in the 3-year-old clear-cuts, which decreased by approximately 3 times in Kazlų Rūda and 17 times in Trakai compared to the 1-year-old clear-cut.

Table 2. Mean cover ± SE (%) of the forest floor, mosses, and vascular plants in the 1–3-year-old clear-cuts and 8–130-year-old Scots pine stands in Trakai, Varėna, and Kazlų Rūda objects. Different letters indicate statistically significant differences between the stands of different ages at $p < 0.05$.

Object	Ground Cover Layer	Clear-Cut (Years)			Scots Pine Stands (Years)					
		1	2	3	8–10	15–20	30–40	70–80	110–130	
		Cover (%)								
Trakai	Mosses	56.2 ± 4.2 ^c	18.1 ± 3.3 ^b	6.5 ± 1.2 ^a	53.0 ± 4.4 ^c	59.8 ± 6.3 ^c	92.5 ± 1.3 ^d	96.0 ± 2.4 ^d	88.9 ± 3.5 ^d	
	Vascular plants	14.5 ± 2.1 ^a	23.2 ± 2.3 ^b	52.2 ± 2.2 ^d	59.0 ± 4.4 ^d	34.6 ± 1.4 ^c	24.1 ± 7.1 ^b	39.6 ± 3.1 ^c	16.6 ± 3.1 ^a	
	Forest floor	95.8 ± 1.7 ^{cd}	39.6 ± 4.7 ^a	56.2 ± 5.3 ^b	80.1 ± 4.8 ^c	99.8 ± 0.1 ^d	100.0 ± 0.0 ^d	100.0 ± 0.0 ^d	100.0 ± 0.0 ^d	
Varėna	Mosses	44.0 ± 5.7 ^c	12.0 ± 3.2 ^b	2.6 ± 0.5 ^a	43.0 ± 4.5 ^c	64.9 ± 4.2 ^d	96.0 ± 2.6 ^e	92.6 ± 1.5 ^e	90.3 ± 3.5 ^e	
	Vascular plants	15.2 ± 1.7 ^a	16.7 ± 1.7 ^a	40.7 ± 3.2 ^c	28.6 ± 3.8 ^b	23.8 ± 2.7 ^b	12.4 ± 3.0 ^a	21.3 ± 3.6 ^b	23.3 ± 4.6 ^b	
	Forest floor	65.8 ± 5.2 ^b	35.7 ± 5.2 ^a	35.9 ± 4.7 ^a	34.6 ± 7.7 ^a	86.3 ± 3.3 ^c	100.0 ± 0.0 ^d	100.0 ± 0.0 ^d	99.9 ± 0.2 ^d	
Kazlų Rūda	Mosses	18.8 ± 2.0 ^c	10.9 ± 0.8 ^b	6.5 ± 0.5 ^a	27.8 ± 1.7 ^d	77.8 ± 4.3 ^e	87.4 ± 6.8 ^e	97.9 ± 11.9 ^f	93.3 ± 9.8 ^f	
	Vascular plants	33.6 ± 0.7 ^c	29.6 ± 0.8 ^b	66.9 ± 1.1 ^d	53.2 ± 2.4 ^d	28.2 ± 0.8 ^b	21.5 ± 0.6 ^a	34.9 ± 1.6 ^c	26.7 ± 1.5 ^b	
	Forest floor	68.2 ± 4.1 ^a	56.2 ± 3.9 ^a	79.8 ± 4.2 ^b	92.2 ± 5.5 ^c	99.2 ± 0.6 ^c	99.5 ± 0.5 ^c	94.8 ± 5.0 ^c	99.9 ± 0.2 ^c	

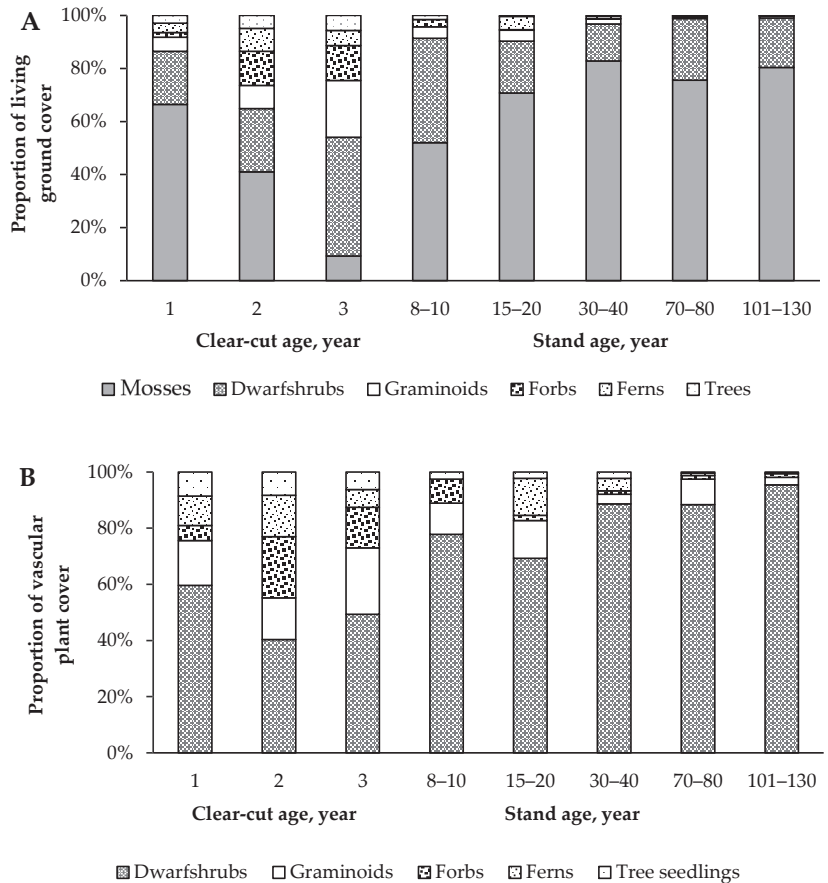


Figure 2. The percentage distribution (%) of living ground cover (A) and vascular plant cover (B), each calculated from the total living ground cover (100%) and total vascular plant cover (100%), respectively, in the 1–3-year-old clear-cuts and 8–130-year-old Scots pine stands (aggregated data from three sites).

The moss cover started to recover in the 10-year-old stands, and the mosses became dominant in the living ground cover in the 15-year-old stands. Contrary to the vascular plants, the highest mean moss cover was found in the 30–70-year-old stands. Vascular plants showed a quick response and ability to exploit the conditions created after clear-cutting in all research objects. The mean coverage of the vascular plants was slightly higher in the 1-year-old clear-cuts in the Trakai object and 25.6% higher in Kazlų Rūda. However, in the Varėna object, 34.7% lower mean coverage of the vascular plants was found in the 1-year-old clear-cuts. Higher vascular plant coverage was found in the 3-year-old clear-cuts: their coverage was 1.7–3.1 times higher than in the mature stand (Table 2). The mean vascular plant cover peak was fixed until the stands reached 8–10 years of age. The lowest mean coverage of dwarf shrubs and herbs was observed in the 30-year-old forest, except for the Trakai object.

During stand rotation, dwarf shrubs prevailed in the vascular plant coverage of all objects (Figure 2B). The second prevailing growth form was graminoids, followed by forbs. The latter were predominant only in the 2- and 3-year-old clear-cuts. In the stands of the 70–80 age group, the moss cover reached its maximum, and so did the dwarf shrubs. However, in the mature stand, a smaller percentage of dwarf shrubs was assessed.

The Bray–Curtis coefficients were calculated for Varėna, Trakai, and Kazlų Rūda (Figure 3). The analysis focused on the dissimilarity between different pairs of time points within each object. In the Trakai object, significant dissimilarities of 0.675 to 0.782 were found between 1- and 2-year-old clear-cuts, 3-year-old clear-cuts and 15-year-old stands, and 3-year-old clear-cuts and 70-year-old stands. Moderate dissimilarities of 0.668 to 0.675 were identified between 2-year-old clear-cuts and 10-year-old stands, 2-year-old clear-cuts and 15-year-old stands, and 15- and 30-year-old stands. The lowest Bray–Curtis coefficients, 0.260 and 0.566, were found between the 30- and 70-year-old stands and between 1-year-old clear-cuts and 110-year-old stands, respectively. In the Varėna object, the highest dissimilarities—the Bray–Curtis coefficients were from 0.856 to 0.895—were observed between the 3-year-old clear-cuts and 15-year-old stands, 3-year-old clear-cuts and 70-year-old stands, and 3-year-old clear-cuts and 110-year-old stands (Figure 3B). The 1- and 2-year-old clear-cuts, 2- and 3-year-old clear-cuts, and 1-year-old clear-cuts and 70-year-old stands showed moderate similarity (0.441–0.549). Lower dissimilarities from 0.327 to 0.383 were identified between the 1-year-old clear-cuts and 110-year-old stands and between the 15-year-old and 30-year-old stands. In the Kazlų Rūda object, the indicated dissimilarities in pairs were as follows: the highest from 0.826 to 0.833 between 2- and 3-year-old clear-cuts, 2-year-old clear-cuts and 30-year-old stands, and 3-year-old clear-cuts and 70-year-old stands; the moderate—from 0.512 to 0.755—between 1- and 2-year-old clear-cuts, 2-year-old clear-cuts and 10-year-old stands, and 3-year-old clear-cuts and 30-year-old stands; and the lowest Bray–Curtis coefficient of 0.126 was between 70- and 110-year-old stands (Figure 3C).

The Bray–Curtis coefficient revealed that the species composition and mean ground coverage of 2–3-year-old clear-cuts differed the most from those of mature stands (Figure 3). Starting from the thirties, the species composition becomes closer to that of mature stands as they age.

Being sensitive to edaphic, relief, and climatic conditions and their changes, the living ground cover showed variations in species composition among the research objects in the stands of the same age group. This range led to a relatively large variation in species composition, especially in the initial age of stand formation (Table 3). However, *Vaccinium myrtillus* L. and *Vaccinium vitis-idaea* L. were found to be the most significant species among the vascular plants in all the studied objects. Clear-cuttings decreased *Vaccinium myrtillus* cover in the clear-cuts, but it still retained dominant in the coverage of vascular plants with a PV 54.30 (Table 3). The highest coverage and frequency of *Vaccinium myrtillus* was found in the pre-mature stands, and the highest prominence value (PV) of 205.2 was estimated. In the mature stands, the PV of *Vaccinium myrtillus* was also high, amounting to 148.8. The dominance of the *Vaccinium vitis-idea* was different: the highest PV (174.1) was in the

8–10-year-old stands and lasted for 30–40 years with a PV of 122.3. *Calluna vulgaris* L. (Hull) also had comparatively high PV at the 8–10-year-old stand, except for the Varėna object. Site-specific variations were found in the Trakai and Kazlų Rūda objects. *Rubus idaeus* L. and *Pteridium aquilinum* (L.) were frequent and had significant cover in the clear-cuts and young stands [36]. In contrast, *Festuca rubra* (Hack. ex Celak.) Fritsch dominated the living ground cover in the clear-cuts of the Varėna object.

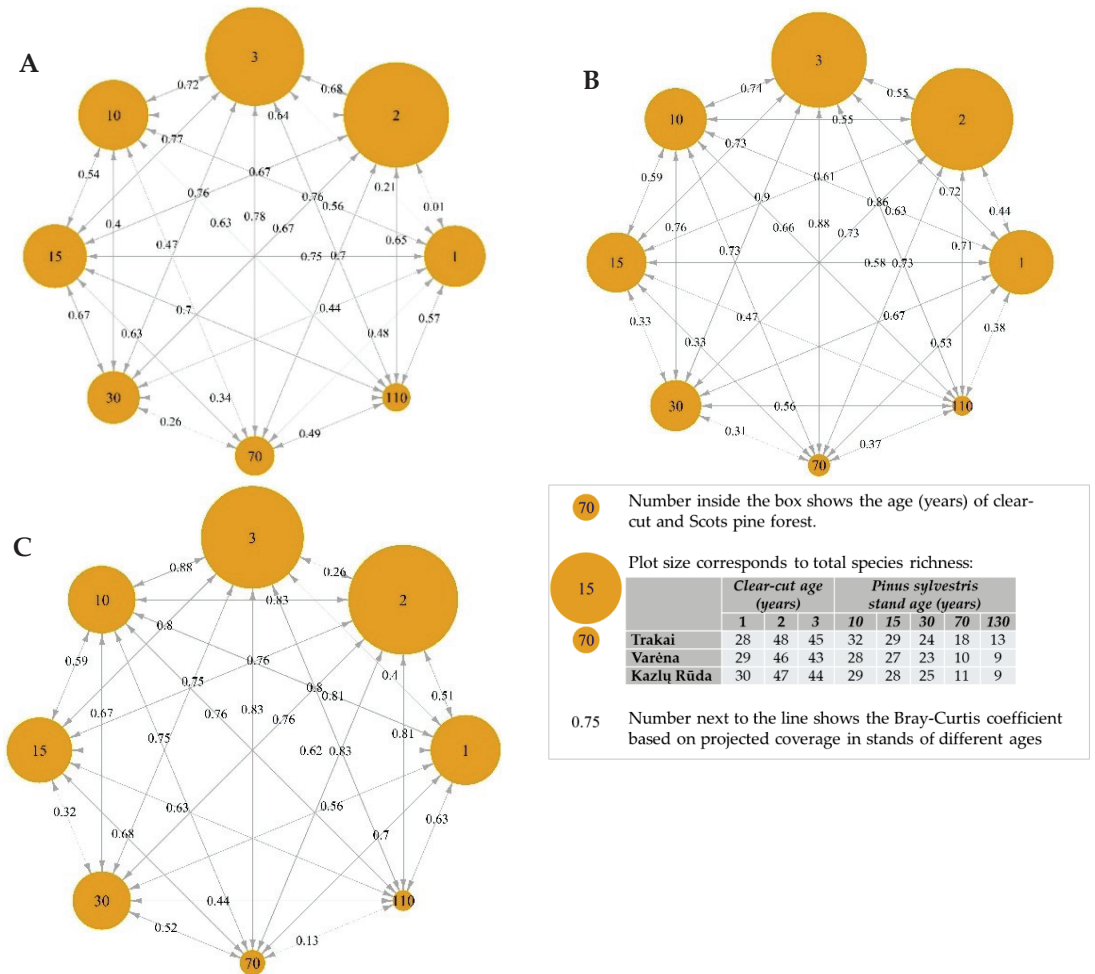


Figure 3. Pair distances between the 1–3-year-old clear-cuts and 8–130-year-old Scots pine stands, illustrated for three sites: Trakai (A), Varėna (B), and Kazlų Rūda (C).

Data analysis from three research objects showed that mosses had the highest prominence value in the living ground cover in this forest type. For example, the prominence value of *Pleurozium schreberi* (Brid.) Mitt. in the 30–80-year-old stands varied within the range of 478.7–499.7. It was 2.4 times higher than *Vaccinium myrtillus* PV during its dominance period. *Hylocomium splendens* (Hedw.) Scimp. and *Dicranum* sp. were characterized by those with the highest coverage and frequency after *Pleurozium schreberi*, emphasizing those species with the highest PV in *Vaccinio myrtillo-Pinetum* forests. However, it should be noted that *Hylocomium splendens* had the highest PV of 552.38 in the mature stands, exceeding the PV of *Pleurozium schreberi* (Table 3). *Dicranum* sp. was most significant in

the 15–40-year-old stands. In addition, a decrease in the PV of *Hylocomium splendens* in clear-cuts described this species as the most sensitive to clear-cutting in this forest type. The individuals of *Hylocomium splendens* had diminished viability in the 1-year-old clear-cuts. Later, their coverage drastically decreased by 98.2% in the 3-year-old clear-cuts compared to those found in the mature stands. In 8–10-year-old stands, after clear-cutting, *Polytrichum* sp. and *Pohlia nutans* (Hedw.) Lindb. become more abundant and frequent at the living cover for a short period of stand cover formation.

Table 3. Prominence value of vascular plants and moss species in the 1–3-year-old clear-cuts and 8–130-year-old Scots pine stands (aggregated data from three sites).

Species of Vascular Plants/Mosses	Clear-Cuts (Years)			Scots Pine Stands (Years)					
	1	2	3	8–10	15–20	30–40	70–80	110–130	
	Prominence Value								
<i>Vaccinium myrtillus</i> L.	76.81 ± 31.57	46.38 ± 15.71	54.30 ± 19.07	25.81 ± 21.03	19.85 ± 9.42	88.02 ± 32.30	205.20 ± 64.96	148.82 ± 58.96	
<i>Vaccinium vitis-idaea</i> L.	17.08 ± 7.53	16.43 ± 8.27	32.02 ± 15.25	174.07 ± 53.06	122.32 ± 64.94	44.28 ± 11.64	85.43 ± 37.94	44.37 ± 24.73	
<i>Calluna vulgaris</i> L. (Hull)	12.24 ± 12.07	2.17 ± 1.96	3.55 ± 1.79	159.68 ± 73.25	20.63 ± 12.22	0.00 ± 0.00	0.00 ± 0.00	0.00 ± 0.00	
<i>Rubus idaeus</i> L.	6.35 ± 6.07	27.71 ± 25.30	111.35 ± 81.78	15.34 ± 15.10	0.00 ± 0.00	0.00 ± 0.00	0.00 ± 0.00	0.00 ± 0.00	
<i>Festuca</i> sp.	20.92 ± 20.56	19.29 ± 19.28	84.48 ± 82.18	16.88 ± 16.81	34.40 ± 34.40	11.46 ± 11.46	3.69 ± 3.69	6.33 ± 6.33	
<i>Pteridium aquilinum</i> (L.)	10.14 ± 0.34	17.81 ± 2.16	23.23 ± 9.02	0.00 ± 0.00	47.48 ± 47.48	4.85 ± 4.85	0.00 ± 0.00	0.00 ± 0.00	
<i>Pleurozium schreberi</i> (Brid.) Mitt.	200.71 ± 65.92	75.01 ± 29.23	12.58 ± 4.92	164.89 ± 76.84	323.01 ± 109.80	499.69 ± 15.99	478.67 ± 198.73	207.64 ± 42.94	
<i>Hylocomium splendens</i> (Hedw.) Scimp.	85.96 ± 49.44	5.34 ± 4.37	1.29 ± 0.16	31.10 ± 26.79	33.84 ± 31.12	167.31 ± 84.32	323.81 ± 219.68	552.38 ± 77.06	
<i>Dicranum</i> sp.	24.43 ± 11.83	11.97 ± 7.35	7.48 ± 6.26	20.68 ± 4.57	126.16 ± 13.03	157.36 ± 119.17	42.96 ± 36.84	20.68 ± 13.27	
<i>Ptilium crista-castrensis</i> (Hedw.) De Not	4.98 ± 4.54	6.47 ± 6.46	5.09 ± 5.09	10.20 ± 10.20	9.88 ± 8.13	11.66 ± 11.03	50.17 ± 25.03	31.60 ± 28.85	
<i>Cirriphyllum piliferum</i> (Hed.) Grout	00.00 ± 0.00	00.00 ± 0.00	00.00 ± 0.00	7.30 ± 7.30	83.64 ± 83.64	4.64 ± 4.64	00.00 ± 0.00	00.00 ± 0.00	
<i>Polytrichum</i> sp.	00.00 ± 0.00	0.41 ± 0.36	0.47 ± 0.47	67.82 ± 44.00	12.83 ± 11.49	2.28 ± 2.16	6.91 ± 6.91	00.00 ± 0.00	

3.2. Ground Cover Layer Mass Dynamics and Relationships

Changes in the stand cover affected the mass of typical forest vascular plants and mosses. For vascular plants, there was an initial increase in mass, rising from 0.6 t ha⁻¹ in the 1-year-old clear-cut to a peak of 2.5 t ha⁻¹ in 8–10-year-old Scots pine stands (Figure 4A). After this peak, a decline was found, with the mass decreasing to 1.8 t ha⁻¹ in 15–20-year-old stands and further decreasing to 0.3 t ha⁻¹ in 30–40-year-old stands. A partial recovery occurred in 80-year-old stands, where the mass reached 1.1 t ha⁻¹ and slightly declined again to 0.8 t ha⁻¹ in the mature stands. In contrast, mosses showed an initial decline in mass, decreasing from 1 t ha⁻¹ in the 1-year-old clear-cut to a low of 0.1 t ha⁻¹ in the 3-year-old clear-cut (Figure 4A). Also, it was two times smaller in the fresh clear-cuts than in mature stands. A steady recovery was found from the third year after clear-cutting, with the mass of the mosses increasing to 2.1 t ha⁻¹ in the 15–20-year-old Scots pine stands. Already, in the 8–10-year-old stand, the mass of the mosses was about seven times higher than in the 2–3-year-old clear-cut sites. This upward trend continued, stabilizing around 2.3–2.4 t ha⁻¹ when the stands reached 40 years. The mosses generally dominated the living ground cover and comprised about 52% of the mass in 15–20-year-old stands. Furthermore, in 30–40-year-old stands, mosses comprised about 90% of the total living ground cover; in 70–130-year-old stands, mosses accounted for 64–70% of the total biomass.

The loss of stand cover due to clear-cutting has a drastic negative effect on the forest floor, as the annual litterfall is significantly reduced. The loss of tree cover leads to changes in the microclimate, contributing to more intensive microbial activity and forest floor decomposition. The dynamics of the forest floor and dead wood mass over time are shown in Figure 4B. Initially, the forest floor mass declined significantly, decreasing from approximately 32 t ha⁻¹ in the 1-year-old clear-cuts to nearly 6 t ha⁻¹ in the 8–10-year-old

Scots pine stands. After this period, the forest floor mass gradually recovered, increasing to 14 t ha^{-1} in 40-year-old stands. Notably, this upward trend continued, and the forest floor mass reached 38.5 t ha^{-1} in the mature stand. Overall, in 2–3-year-old clear-cuts and 8–10-year-old stands, the forest floor mass was 75–85% lower than in mature stands. In contrast, the dead wood mass showed different dynamics. It remained stable at 6 t ha^{-1} during the first three years after clear-cutting. However, a notable decline occurred in 10-year-old stands, with the mass decreasing to 2.8 t ha^{-1} . After this period, the dead wood mass partially recovered, reaching 4 t ha^{-1} in the 20-year-old stands. When the stand reached 40 years, the dead wood mass stabilized at approximately 3.3 t ha^{-1} , showing little to no change until the stand reached 130 years.

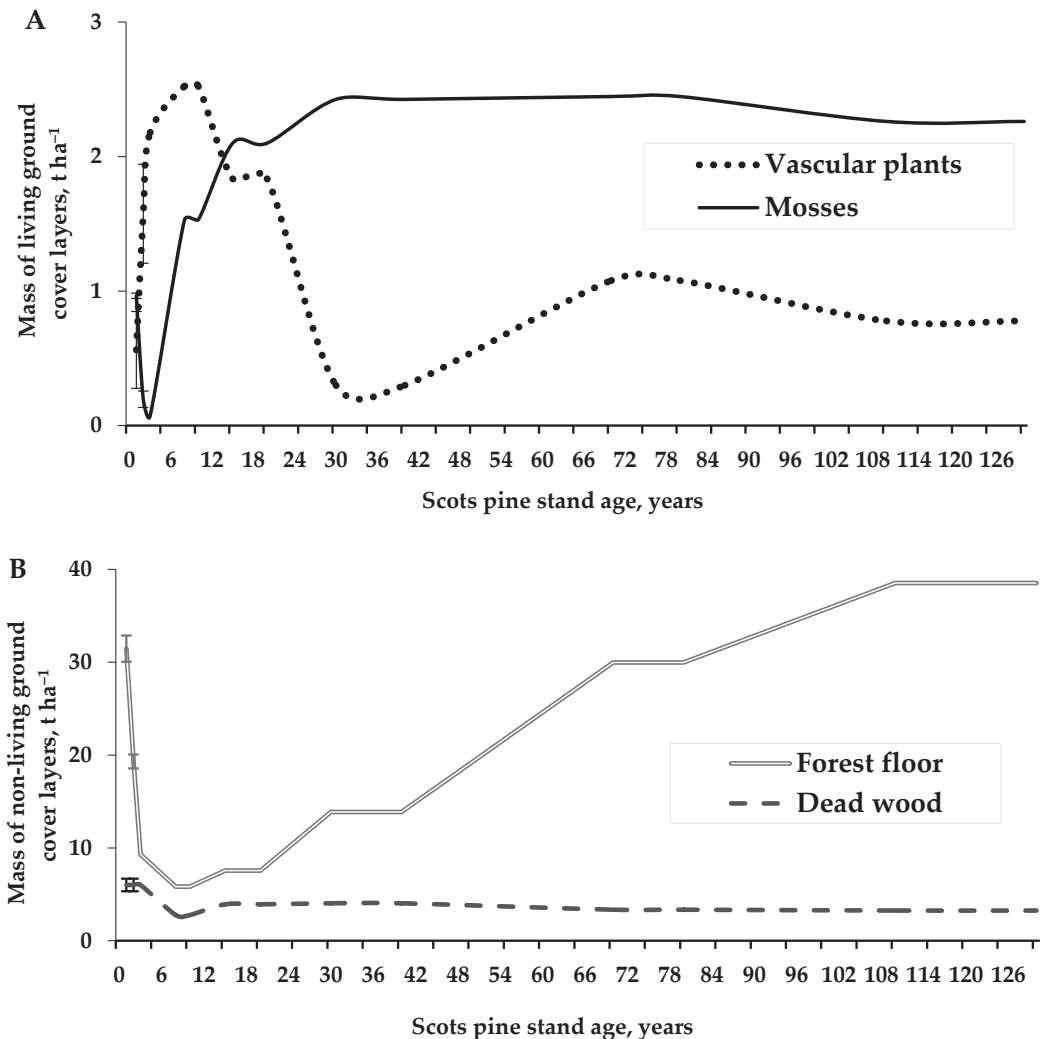


Figure 4. The trend of living (A) and non-living (B) ground cover mass in Scots pine stands of *Pinetum vaccinio-myrtillosum* type throughout the rotation period following clear-cutting (aggregated data from three sites).

A positive correlation of moss mass with the average density of the tree canopy ($R^2 = 0.629$) was found (Figure 5). The biomass of herbaceous plants and dwarf shrubs at

different stand ages differed significantly. Changes in microclimatic conditions, reduced competition with tree cover, and ongoing changes in soil chemical indicators positively influenced the aboveground biomass of vascular plants [39]. The biomass of vascular plants in 2–3-year-old clear-cuts was 2.8–3.9 times higher than in 1-year-old clear-cuts and 2.0–2.8 times higher than in the mature stands. The biomass of herbs and dwarf shrubs showed an increasing trend until the stands reached 15–20 years old. The predominant part of the biomass of the vascular plants in the total biomass of the living ground cover was found in 2–3-year-old clear-cuts, where it accounted for 86.8–90.5% of the total living biomass, and in 8-year-old stands, where it accounted for 60.8%.

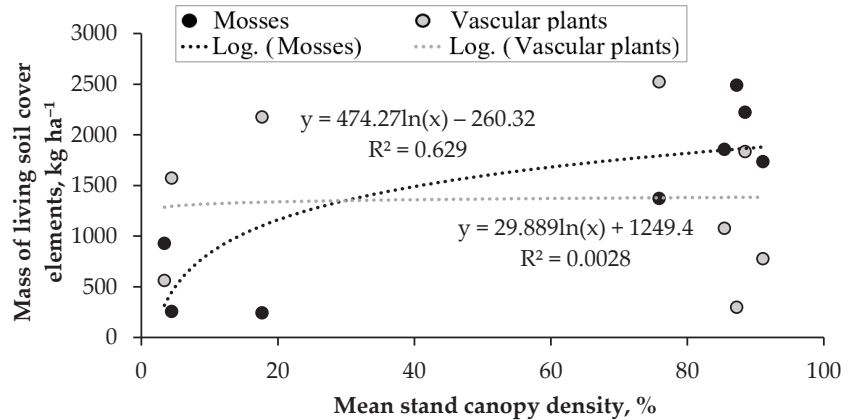


Figure 5. Relations between the mean aboveground mass of vascular plants and mosses (kg ha^{-1}) with the mean stand canopy density in the 1–3-year-old clear-cuts and 8–130-year-old Scots pine stands (aggregated data from three sites).

In the total moss biomass, the largest biomass shares of *Pleurozium schreberi*, *Hylocomium splendens*, and *Dicranum sp.* were found (Figure 6A). *Pleurozium schreberi* biomass in the 8–10-year-old stand was comparable to that in the mature stands. In the 15–20-year-old stands, this mass exceeded the mass assessed in mature stands by 2.2 times. In the later age groups of the stand, the biomass of *Pleurozium schreberi* slightly decreased, and *Hylocomium splendens* started prevailing. *Dicranum sp.* seem to be prevailing in the young stands. The 8–10-year-old stands were characterized by twice as much biomass as the mature stands. Its biomass consistently increased with the stand age until the stand reached 30–40 years, and here, the *Dicranum sp.* mass was 7.1 times higher than in the mature stands. Meanwhile, the biomass of *Hylocomium splendens* has recovered the mature stand level in 70–80-year-old Scots pine forests.

The aboveground biomass of herbs and dwarf shrubs consisted of similar species in all stands. *Vaccinium myrtillus* and *Vaccinium vitis-idaea* comprised a major biomass proportion of vascular plants (Figure 6B). As shown above, a decrease in the total biomass of vascular plants was observed in 30–40-year-old pine forests (See Figure 4). However, starting from 30–40-year-old pine forests, the biomass of *Vaccinium myrtillus* comprised 32% of the total plant biomass and showed an increasing trend with the increasing stand age (Figure 6B). The highest biomass of *Vaccinium myrtillus* was found in 70–130-year-old stands. Meanwhile, the biomass of *Vaccinium vitis-idaea* accounted for 11–16% of the total vascular plant biomass in clear-cuts and varied between 39.2 and 47.9% of the total vascular plant biomass of the living ground cover in 8–80-year-old stands. The biomass of *Vaccinium vitis-idaea* in 8–20-year-old pine forests was 3.7 times higher than in mature stands. However, the variable mass of other species more common in these stands, such as *Calluna vulgaris* and *Festuca sp.*, was fixed until the stand reached about 20–30 years of age.

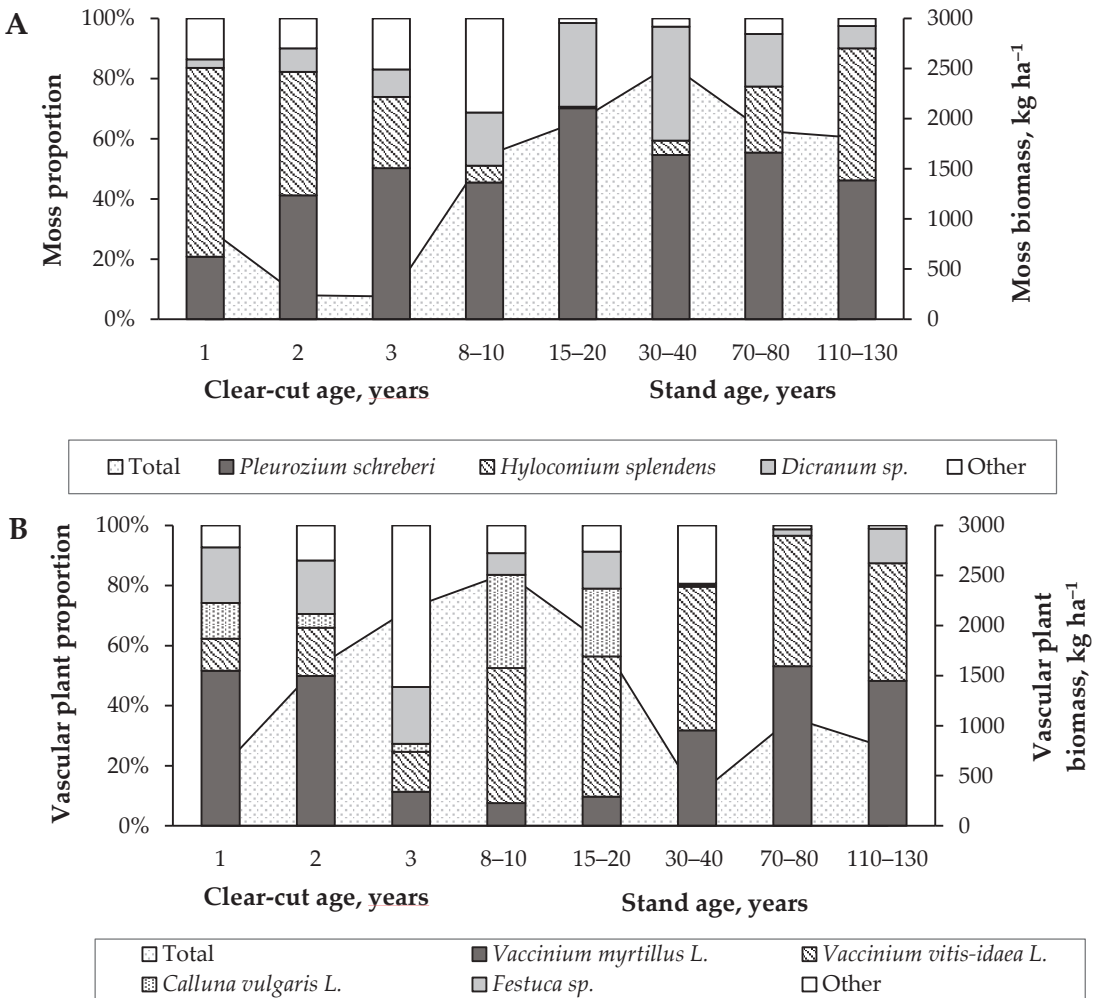


Figure 6. The percentage of vascular plant (key species of herbs and dwarf shrubs) mass (A) and moss species mass (B) of the total vascular plant and moss mass, respectively, and aboveground biomass (kg ha⁻¹) of the living ground cover (Total) in 1–3-year-old clear-cuts and 8–130-year-old Scots pine stands (aggregated data from three sites).

A moderately strong negative correlation between the mass of vascular plants and the mass of the forest floor was determined ($R^2 = 0.570$) (Figure 7). Still, no correlations were found between the biomass of moss and the mass of the forest floor.

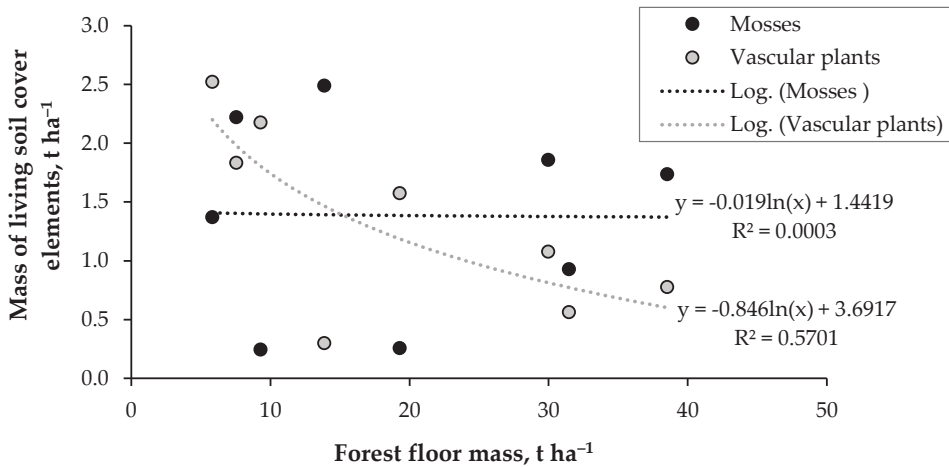


Figure 7. Relations between the biomass of living soil cover elements (t ha^{-1}) and the mean forest floor mass (t ha^{-1}) in the 1–3-year-old clear-cuts and 8–130-year-old Scots pine stands (aggregated data from three sites).

4. Discussion

Reduced competition with the main stand layers due to light and nutrients after the clear-cutting and soil scarification for the reforestation preparation positively affected the abundance of vascular plant mean coverage [24,25,40]. Like previous studies [5,15], our results indicated a slight reduction in vascular plant cover in the 1-year-old clear-cuts. Herbs and dwarf shrub cover increased in the 2–3-year-old clear-cuts, exceeding the cover found in mature stands. Previous studies also confirmed this trend, which observed an increased herbaceous plant cover after logging [26,27,29,30,41]. These changes often occur at the expense of forest-related families such as *Ericaceae* ([5,15]). Although *Ericaceae* remained dominant in clear-cut areas, their projective cover was significantly reduced. Forest-specific vascular species, such as *Goodyera repens* (L.) R. Br., *Lycopodium clavatum* L., and *Chimaphila umbellata* (L.), W. P. C. Barton also showed similar trends [26,29]. On the other hand, newcomer herbaceous plants and dwarf shrubs play an important role in reducing the leaching of soil nutrients [12,25,29]. Tall herbs create more favorable conditions for the survival of forest-related species that avoid sunlight [29]. As an example from the present study, in the 2–3-year-old clear-cuts, more *Pleurozium schreberi* was found under taller plants than under direct sunlight. Meanwhile, in the later stages of stand formation, light transmission becomes one of the limiting factors, because the parameters of the trees increase, and the canopy layer develops. As a result, the amount of nutrients consumed by the trees also increases, leading to the disappearance of plant species that require more nitrogen and light at this stage [42,43]. The amount of light and nutrients available to the living ground cover significantly influence the distribution of vascular plants under the canopy [44,45]. This study also showed a decrease in the mean coverage of vascular plants in 30–40 years (see Figure 4). However, an increase in the moss cover was observed. The stability of the species composition in the living ground cover of *Pinetum vaccinio-myrtillosum* pine stands was achieved in the middle-aged stands, mostly 30–70 years old, after clear-cutting. For 15–20 years after clear-cutting, moss cover has become prevalent, covering 67.5%. After 30 years, it covered more than 90%. During this study, it was found that mosses were the dominant vegetation, covering more than 90.8–95.5% of the total ground cover in stands older than 30 years, among which, *Pleurozium schreberi*, *Hylocomium splendens*, *Dicranum polysetum*, and *Ptilium crista-castrensis* prevailed. According to Kumar et al. [30], mosses tend to have lower requirements for light and soil fertility, leading to their dominance in conifer stands on oligotrophic mineral soil

of normal moisture. However, continuous sunlight, increased wind speed, and reduced relative humidity caused by clear-cutting, create unfavorable conditions for moss survival in clear-cuts [12]. Therefore, the mean moss cover in 3-year-old clear-cuts decreased more than 17 times, and the biomass was almost 8 times lower than in mature stands. This distinguishes mosses as having a rapid response to the changed environment after clear-cutting and with higher intensity than other ground layer components [27].

The emergence of new species, such as *Pohlia nutans*, *Polytrichum commune* L., and *Polytrichum juniperinum* Hedw, characterized clear-cut sites. The most affected moss species after clear-cutting was *Hylocomium splendens*; it recovered up to the mature stand level only in the premature stands in the 70–80-year-old stands. *Pleurozium schreberi* and *Dicranum polysetum*, after significant reduction in the cover and biomass in clear-cuts, reached pre-clear-cutting coverage and biomass in 10–30-year-old stands. While Palviainen et al. [12] noticed that this time interval was seven years. Palviainen et al. [12] also discussed that *Hylocomium splendens* react more negatively to logging than other species due to slower reproduction and colonization processes, higher moisture requirements, and sensitivity to sunlight. Meanwhile, Kelly & Connolly [46] observed that *Hylocomium splendens* is intolerant to calcium-rich soils. Previous research found a negative correlation between the projection cover of *Hylocomium splendens* and the total calcium concentration in the forest floor and mineral soil [21].

The obtained species composition and mean coverage of mosses during this research corresponded to the previously determined trends and represented the moss species characteristic of the *Pinetum vaccinio-myrttilosum* forest type [21,23,35]. Overall, 15–20 years after clear-cutting could be considered the threshold for successful restoration of mean moss cover in the *Pinetum vaccinio-myrttilosum* forest type, as the mean moss cover projection reached 67.5% of the ground cover. Additionally, moss biomass comprised 51.0% of the living ground cover biomass in this restoration period. According to the results of previous studies, in mature *Pinetum vaccinio-myrttilosum* pine forests, the cover of vascular plants was 14–40%, and the moss cover was 80–85% [47,48].

In total ground cover biomass, which consisted of living ground cover (moss, herbaceous plants, and dwarf shrubs) and non-living ground cover (forest floor and dead trees) biomass, the highest mass was found on the forest floor. In the first year after clear-cutting, the biomass of the forest floor started to decrease due to the higher activity of microorganisms [49,50]. However, the larger than usual amounts of fresh dead wood left after felling compensated for the loss of biomass in the non-living ground cover. Therefore, in clear-cuts, the biomass of the non-living ground cover remained like that in the mature stands (see Figure 4). In older clear-cuts and stands, despite the decline in forest floor biomass compared to the biomass of mature forests, the largest proportion of biomass in the non-living cover remained in the forest floor.

The biomass peak of the living ground cover in *Pinetum vaccinio-myrttilosum* pine forests, both mosses and herbaceous plants with dwarf shrubs, was found in the 8–20-year-old stands. The biomass of herbaceous and dwarf shrub cover increased rapidly at the stand initiation stage and significantly decreased in the 30-year-old stand, i.e., at the highest stocking level of the stands. Later, due to forestry activities, an increase in the dwarf shrub biomass was observed in thinned stands, while the biomass of the mosses remained dominant. Similar patterns have been recorded in other studies [42,51]. According to Kumar et al. [30], the cover of conifer stands favors the growth of mosses due to the formation of coarse litter, C:N ratio and acidic pH medium, and relatively low nutrient content. Additionally, *Pleurozium schreberi* is known to have a relationship with cyanobacteria responsible for N fixation. Increasing competition with the canopy for light and nutrients results in a struggle for N, so the ability to fix N improves N availability to mosses [52].

Even though living ground cover biomass averaged just between 3.8 and 32.6% of the total ground cover biomass per rotation, living ground cover plays a significant role in CO₂ absorption [30]. Already in the early stages of tree succession, the living ground cover can

enrich the soil with organic matter, absorbing excess nutrients in the clear-cut sites and relatively quickly returning them to the soil, thereby contributing to retaining soil nutrients and reducing their leaching.

5. Conclusions

This study showed the ecological impact of clear-cutting on *Pinetum vaccinio-myrtillosum* pine stands. The study observed that reduced the competition for light and nutrients positively affected vascular plant abundance, with a significant increase in herb and dwarf shrub cover within 2–3 years after clear-cutting compared to mature Scots pine stands. The results indicated a substantial decline in forest-specific species immediately following clear-cutting, with a gradual recovery of moss cover, particularly *Pleurozium schreberi* and *Dicranum polysetum*, to pre-clear-cutting levels within 10–30 years. The mosses showed a restoration threshold around 15–20 years post-clear-cutting, achieving 67.5% ground cover and contributing 51.0% of the living ground cover biomass during this period. Clear-cutting drastically reduced the forest floor and dead wood mass, decreasing forest floor mass by 75–85% in 2–3-year-old and 8–10-year-old stands compared to mature stands due to reduced litterfall and increased nutrient leaching. Moss mass showed the most significant decline in 2–3-year-old clear-cuts compared to mature stands but started to recover in the 8–10-year-old stands, comprising a major portion of the living ground cover in older stands. These findings emphasize the critical role of mosses in stabilizing ground cover. Lastly, the study highlighted the importance of managing clear-cutting practices to balance immediate vegetative responses with long-term ecosystem stability and biodiversity conservation. The rapid recovery of herbaceous plants and dwarf shrubs aids in nutrient retention and reduces leaching. Furthermore, the slower restoration of moss cover plays a crucial role in maintaining forest floor stability and ecological functions.

Author Contributions: Conceptualization, D.G. and I.V.-K.; Data curation, D.G. and I.V.-K.; Formal analysis, D.G. and I.V.-K.; Investigation, D.G.; Methodology, D.G.; Software, D.G. and I.V.-K.; Visualization, D.G. and I.V.-K.; Writing—original draft, D.G. and I.V.-K.; Writing—review and editing, I.V.-K. All authors have read and agreed to the published version of the manuscript.

Funding: This research received no external funding.

Data Availability Statement: The original contributions presented in the study are included in the article, further inquiries can be directed to the corresponding author.

Acknowledgments: This study presents findings from Task 1 on patterns of forest ecosystem changes caused by human activities, conducted by the Silviculture and Ecology Department as part of the Long-term Research Program, “Sustainable Forestry and Global Changes,” at the Lithuanian Research Center for Agriculture and Forestry. The authors thank Audrius Kabasinskas (Kaunas University of Technology) for his assistance with the statistical analysis.

Conflicts of Interest: The authors declare no conflicts of interest.

References

1. Clarke, N.; Gundersen, P.; Jönsson-Belyazid, U.; Kjonaas, O.J.; Persson, T.; Sigurdsson, B.D.; Stupak, I.; Vesterdal, L. Influence of different tree-harvesting intensities on forest soil carbon stocks in boreal and northern temperate forest ecosystems. *For. Ecol. Manag.* **2015**, *351*, 9–19. [CrossRef]
2. Česonienė, L.; Daubaras, R.; Bimbiraitė-Survilienė, K.; Kaškonienė, V.; Kaškonas, P.; Tiso, N.; Maruška, A.; Zych, M. Effects of clear-cuts in Scots pine-dominated forests on *Vaccinium myrtillus* and *Vaccinium vitis-idaea* vegetative characteristics, and accumulation of phenolic compounds. *Balt. For.* **2019**, *24*, 278–286.
3. Mayer, M.; Prescott, C.E.; Abaker, W.E.A.; Augusto, L.; Cécillon, L.; Ferreira, G.W.D.; James, J.; Jandl, R.; Katzensteiner, K.; Laclau, J.-P.; et al. Tamm Review: Influence of forest management activities on soil organic carbon stocks: A knowledge synthesis. *For. Ecol. Manag.* **2020**, *466*, 118127. [CrossRef]
4. Finér, L.; Mannerkoski, H.; Piirainen, S.; Starr, M. Carbon and nitrogen pools in an old-growth, Norway spruce mixed forest in eastern Finland and changes associated with clear-cutting. *For. Ecol. Manag.* **2003**, *174*, 51–63. [CrossRef]
5. Palviainen, M. Logging residues and ground vegetation in nutrient dynamics of a clear-cut boreal forest. *Diss. For.* **2005**, *12*, 38. [CrossRef]

6. Gundersen, P.; Schmidt, I.K.; Raulund-Rasmussen, K. Leaching of nitrate from temperate forests-effects of air pollution and forest management. *Environ. Rev.* **2006**, *14*, 1–57. [CrossRef]
7. Hedwall, P.-O.; Grip, H.; Linder, S.; Lövdahl, L.; Nilsson, U.; Bergh, J. Effects of clear-cutting and slash removal on soil water chemistry and forest-floor vegetation in a nutrient optimised Norway spruce stand. *Silva Fenn.* **2013**, *47*, 933. [CrossRef]
8. Häkkinen, M.; Heikkinen, J.; Mäkipää, R. Soil carbon stock increases in the organic layer of boreal middle-aged stands. *Biogeosciences* **2011**, *8*, 1279–1289. [CrossRef]
9. Schelker, J.; Eklof, K.; Bishop, K.; Laudon, H. Effects of forestry operations on dissolved organic carbon concentrations and export in boreal first-order streams. *J. Geophys. Res. Biogeosci.* **2012**, *117*, G1. [CrossRef]
10. Zhu, X.; Zhang, W.; Chen, H.; Mo, J. Impacts of nitrogen deposition on soil nitrogen cycle in forest ecosystems: A review. *Acta Ecol. Sin.* **2015**, *35*, 35–43. [CrossRef]
11. Balandier, P.; Collet, C.; Miller, J.H.; Reynolds, P.E.; Zedaker, S.M. Designing forest vegetation management strategies based on the mechanisms and dynamics of crop tree competition by neighbouring vegetation. *Forestry* **2005**, *79*, 3–27. [CrossRef]
12. Palviainen, M.; Finér, L.; Mannerkoski, H.; Piirainen, S.; Starr, M. Responses of ground vegetation species to clear-cutting in a boreal forest: Aboveground biomass and nutrient contents during the first 7 years. *Ecol. Res.* **2005**, *20*, 652–660. [CrossRef]
13. Parker, W.C.; Pitt, D.G.; Morneau, A.E. Influence of woody and herbaceous competition on microclimate and growth of eastern white pine (*Pinus strobus* L.) seedlings planted in a central Ontario clearcut. *For. Ecol. Manag.* **2009**, *258*, 2013–2025. [CrossRef]
14. Vanha-Majamaa, I.; Shorohova, E.; Kushnevskaya, H.; Jalonen, J. Resilience of understory vegetation after variable retention felling in boreal Norway spruce forests—A ten-year perspective. *For. Ecol. Manag.* **2017**, *393*, 12–28. [CrossRef]
15. Česonienė, L.; Daubaras, R.; Kaškonas, P.; Kaškonienė, V.; Maruška, A.S.; Tiso, N.; Zych, M. Initial impact of clear-cut logging on dynamics of understory vascular plants and pollinators in Scots pine-dominated forests in Lithuania. *Turkish JAF Sci. Tech.* **2018**, *42*, 433–443. [CrossRef]
16. Moreaux, C.; Martin, P.; Hereş, A.-M.; Yuste, J.C. Effects of forestry practices on the conservation of soil and forest ecosystem health and functioning: An umbrella review protocol. *OSFPreprints* **2022**, 1–44. [CrossRef]
17. Stefańska-Krzaczek, E.; Szymura, T.H. Species diversity of forest floor vegetation in age gradient of managed Scots pine stands. *Balt. For.* **2015**, *21*, 233–243.
18. Chen, J.; Saunders, S.C.; Crow, T.R.; Naiman, R.J.; Brosofske, K.D.; Mroz, G.D.; Brookshire, B.L.; Franklin, J.F. Microclimate in forest ecosystem and landscape ecology. *BioScience* **1999**, *49*, 288–297. [CrossRef]
19. Nave, L.E.; Vance, E.D.; Swanston, C.W.; Curtis, P.S. Harvest impacts on soil carbon storage in temperate forests. *For. Ecol. Manag.* **2010**, *259*, 857–866. [CrossRef]
20. Tonteri, T.; Salemaa, M.; Rautio, P.; Hallikainen, V.; Korpela, L.; Merilä, P. Forest management regulates temporal change in the cover of boreal plant species. *For. Ecol. Manag.* **2016**, *381*, 115–124. [CrossRef]
21. Gustienė, D.; Varnagirytė-Kabašinskienė, I.; Stakėnas, V. Ground Vegetation in *Pinus sylvestris* Forests at different successional stages following clear cuttings: A case study. *Plants* **2022**, *11*, 2651. [CrossRef] [PubMed]
22. Keenan, R.J.; Kimmins, J.P. The ecological effects of clear-cutting. *Environ. Rev.* **1993**, *1*, 121–144. [CrossRef]
23. Karazija, S. Age-related dynamics of pine forest communities in Lithuania. *Balt. For.* **2002**, *9*, 50–62.
24. Hart, S.A.; Chen, H.Y.H. Fire, logging, and overstorey affect understory abundance, diversity, and composition in boreal forest. *Ecol. Monogr.* **2008**, *78*, 123–140. [CrossRef]
25. Kumar, P.; Chen, H.Y.H.; Thomas, S.C.; Shahi, C. Linking resource availability and heterogeneity to understorey species diversity through succession in the boreal forest of Canada. *J. Ecol.* **2017**, *106*, 1266–1276. [CrossRef]
26. Boch, S.; Prati, D.; Müller, J.; Socher, S.; Baumbach, H.; Buscot, F.; Gockel, S.; Hemp, A.; Hessenmöller, D.; Kalko, E.K.V.; et al. High plant species richness indicates management-related disturbances rather than the conservation status of forests. *Basic Appl. Ecol.* **2013**, *14*, 496–505. [CrossRef]
27. Liu, X.; Bao, W.K. Understorey plant assemblages present distinct short-term responses to the clear-cutting of an old-growth spruce forest near an alpine timberline. *Can. J. For. Res.* **2014**, *44*, 562–571. [CrossRef]
28. Bačkaitis, J. Paprastosis Pušies (*Pinus sylvestris* L.) Žėlimui Įtaką Darantys Aplinkos Veiksniai: Daktaro disertacija [Environmental Factors Influencing Scots Pine (*Pinus sylvestris* L.) Renovation]. Ph.D. Thesis, Lithuanian University of Agriculture, Akademija, Lithuania, 2005. (In Lithuanian).
29. Heinrichs, S.; Schmidt, W. Short-term effects of selection and clear-cutting on the shrub and herb layer vegetation during the conversion of even-aged Norway spruce stands into mixed stands. *For. Ecol. Manag.* **2009**, *258*, 667–678. [CrossRef]
30. Kumar, P.; Chen, H.Y.H.; Searle, E.B.; Shahi, C. Dynamics of understorey biomass, production and turnover associated with long-term overstorey succession in Boreal forest of Canada. *For. Ecol. Manag.* **2018**, *427*, 152–161. [CrossRef]
31. Petersson, L.; Holmström, E.; Lindblad, M.; Felton, A. Tree species impact on understory vegetation: Vascular plant communities of Scots pine and Norway spruce managed stands in northern Europe. *For. Ecol. Manag.* **2019**, *448*, 330–345. [CrossRef]
32. Juodvalkis, A.; Kairiūkštis, L. *Medynų Formavimas ir Kirtimai [Stand Forming and Felling]*; Lututė: Kaunas, Lithuania, 2009. (In Lithuanian)
33. Vaičys, M.; Karazija, S.; Kuliešis, A.; Rutkauskas, A. *Miškų Augavietės. Miško Augaviečių Tipai [Forest Sites. Forest Site Types]*; Lututė: Kaunas, Lithuania, 2006; p. 95. (In Lithuanian)
34. IUSS Working Group WRB. *World Reference Base for Soil Resources 2014; International Soil Classification System for Naming 615 Soils and Creating Legends for Soil Maps*; World Soil Resources Reports No. 106; FAO: Rome, Italy, 2015; p. 192.

35. Karazija, S. *Lietuvos Miškų Tipai [Lithuanian Forest Types]*; Mokslas: Vilnius, Lithuania, 1988. (In Lithuanian)
36. Gustienė, D. Dirvožemio Dangos Dinamika Paprastosios Pušies Medynuose po Plynųjų Kirtimų [Dynamics of Ground Cover in Scots Pine Stands after Clear Cuttings]. Ph.D. Thesis, Vytautas Magnus University, Kaunas, Lithuania, 2024. (In Lithuanian with English Summary).
37. Ehlers, T.; Berch, S.; Mackinnon, A. Inventory of non-timber forest product plant and fungal species in the Robson Valley. *BC J. Ecosyst. Manag.* **2003**, *4*, 1–15. [CrossRef]
38. Stakėnas, V.; Varnagirytė-Kabašinskiėnė, I.; Sirgedaitė-Šežienė, V.; Armolaitis, K.; Araminienė, V.; Muraškienė, M.; Žemaitis, P. Dead wood density and carbon estimates for the main tree species in the Lithuanian hemiboreal forest. *Eur. J. For. Res.* **2020**, *139*, 1045–1055. [CrossRef]
39. Gustienė, D.; Varnagirytė-Kabašinskiėnė, I.; Stakėnas, V. Ground vegetation, forest floor and mineral topsoil in a clear-cutting and reforested Scots pine stands of different ages: A case study. *J. For. Res.* **2022**, *33*, 1247–1257. [CrossRef]
40. Hart, S.A.; Chen, H.Y.H. Understorey vegetation dynamics of North American boreal forests. *Crit. Rev. Plant Sci.* **2006**, *25*, 381–397. [CrossRef]
41. Arduini, I.; Ercoli, L. Recovery of understorey vegetation in clear-cut stone pine (*Pinus pinea* L.) plantations. *Plant Biosyst.* **2012**, *146*, 244–258. [CrossRef]
42. Reich, P.B.; Frelich, L.E.; Voldseth, R.A.; Bakken, P.; Adair, E.C. Understorey diversity in southern boreal forests is regulated by productivity and its indirect impacts on resource availability and heterogeneity. *J. Ecol.* **2011**, *100*, 539–545. [CrossRef]
43. Halpern, C.B.; Lutz, J.A. Canopy closure exerts weak controls on understorey dynamics: A 30-year study of overstorey–understorey interactions. *Ecol. Monogr.* **2013**, *83*, 221–237. [CrossRef]
44. Pykälä, J. Immediate increase in plant species richness after clear-cutting of boreal herb-rich forests. *Appl. Veg. Sci.* **2004**, *7*, 29–34. [CrossRef]
45. Bainbridge, E.L.; Strong, W.L. *Pinus contorta* understorey vegetation dynamics following clearcutting in west-central Alberta, Canada. *For. Ecol. Manag.* **2005**, *213*, 133–150. [CrossRef]
46. Kelly, D.L.; Connolly, A. A review of the plant communities associated with Scots pine (*Pinus sylvestris* L.) in Europe, and an evaluation of putative indicator/specialist species. *For. Syst.* **2000**, *9*, 15–39. [CrossRef]
47. Navasaitis, M.; Ozolinčius, R.; Smaliukas, D.; Balevičienė, J. *Lietuvos Dendroflora [Dendroflora of Lithuania]*; Lututė: Kaunas, Lithuania, 2003. (In Lithuanian)
48. Česonienė, L.; Daubaras, R.; Tamutis, V.; Kaškonienė, V.; Kaškonas, P.; Stakėnas, V.; Zych, M. Effect of clear-cutting on the understorey vegetation, soil and diversity of litter beetles in Scots pine-dominated forest. *J. Sustain. For.* **2019**, *38*, 791–808. [CrossRef]
49. Fierer, N.; Strickland, M.S.; Liptzin, D.; Bradford, M.A.; Cleveland, C.C. Global patterns in belowground communities. *Ecol. Lett.* **2009**, *12*, 1238–1249. [CrossRef] [PubMed]
50. Waring, B.; Neumann, M.; Prentice, I.C.; Adams, M.; Smith, P.; Siegert, M. Forests and decarbonization—Roles of natural and planted forests. *Front. For. Glob. Chang.* **2020**, *3*, 534891. [CrossRef]
51. Bartels, S.F.; Chen, H.Y.H. Is understorey plant species diversity driven by resource quantity or resource heterogeneity? *Ecology* **2010**, *91*, 1931–1938. [CrossRef]
52. Arróniz-Crespo, M.; Bougoure, J.; Murphy, D.V.; Cutler, N.A.; Souza-Egipsy, V.; Chaput, D.L.; Jones, D.L.; Ostle, N.; Wade, S.C.; Clode, P.L.; et al. Revealing the transfer pathways of cyanobacterial-fixed N into the boreal forest through the feather-moss microbiome. *Front. Plant Sci.* **2022**, *13*, 1036258. [CrossRef]

Disclaimer/Publisher’s Note: The statements, opinions and data contained in all publications are solely those of the individual author(s) and contributor(s) and not of MDPI and/or the editor(s). MDPI and/or the editor(s) disclaim responsibility for any injury to people or property resulting from any ideas, methods, instructions or products referred to in the content.

Article

Short-Term Artificial Revegetation with Herbaceous Species Can Prevent Soil Degradation in a Black Soil Erosion Gully of Northeast China

Jielin Liu¹, Yong Zhu², Jianye Li^{2,*}, Xiaolei Kong¹, Qiang Zhang¹, Xueshan Wang¹, Daqing Peng¹ and Xingyi Zhang²

- ¹ Department of Herbage Breeding, Prataculture Research Institute, Heilongjiang Academy of Agricultural Sciences, Harbin 150081, China; liujielin7857@163.com (J.L.); cysbgs@126.com (X.K.); zhangqiang_aa@163.com (Q.Z.); wangxueshan1013@163.com (X.W.); bofskey@foxmail.com (D.P.)
- ² State Key Laboratory of Black Soils Conservation and Utilization, Northeast Institute of Geography and Agroecology, Chinese Academy of Sciences, Harbin 150081, China; 17662459550@163.com (Y.Z.); zhangxy@iga.ac.cn (X.Z.)
- * Correspondence: lijianye@iga.ac.cn

Abstract: Understanding the effects of short-term artificial revegetation on preventing soil degradation in erosion gullies of black soil areas is essential to choosing the most suitable species of vegetation for controlling the development of erosion gullies. A field experiment with short-term artificial revegetation with herbaceous species (*Medicago sativa* L., *Glycyrrhiza pallidiflora* Maxim., *Elytrigia repens* (L.) Desv. ex Nevski, *Rheum palmatum* L., *Asparagus officinalis* L., *Trifolium repens* L., *Bromus inermis* Leyss., *Elymus dahuricus* Turcz.) and a runoff scouring test were conducted in a typical erosion gully in a black soil area. Soil erosion, physicochemical characteristics, and shoot/root characteristics were measured to evaluate the effects of short-term artificial revegetation. Short-term artificial revegetation significantly decreased ($p < 0.05$) sediment yield by $91.1\% \pm 7.2\%$ compared with that of bare soil. Soil total nitrogen (TN), total potassium (TP), available phosphorus (AP), cation exchange capacity (CEC), water-stable aggregates > 0.25 mm ($WR_{0.25}$), and aggregate mean weight diameter (MWD) and mean geometric diameter (GWD) were significantly correlated with vegetated treatments, indicating they were factors sensitive to short-term artificial revegetation. Except for total potassium (TK), the other soil characteristics decreased in vegetated treatments. In addition to increasing TK, vegetated treatments also increased soil available nitrogen (AN)/TN ratios in the short term. The overall effects of different herbaceous species on soil and water conservation, soil quality, and vegetation growth were evaluated, and *Trifolium repens* L. is the most suitable for preventing soil degradation in an erosion gully. The results of this study will provide a reference for the restoration and protection of the ecological environment in black soil areas with gully erosion.

Citation: Liu, J.; Zhu, Y.; Li, J.; Kong, X.; Zhang, Q.; Wang, X.; Peng, D.; Zhang, X. Short-Term Artificial Revegetation with Herbaceous Species Can Prevent Soil Degradation in a Black Soil Erosion Gully of Northeast China. *Land* **2024**, *13*, 1486. <https://doi.org/10.3390/land13091486>

Academic Editor: Adrianos Retalis

Received: 2 August 2024

Revised: 4 September 2024

Accepted: 10 September 2024

Published: 13 September 2024



Copyright: © 2024 by the authors. Licensee MDPI, Basel, Switzerland. This article is an open access article distributed under the terms and conditions of the Creative Commons Attribution (CC BY) license (<https://creativecommons.org/licenses/by/4.0/>).

Keywords: vegetation restoration; soil aggregate size fractions; sediment yield; root characteristics; soil physicochemical characteristics

1. Introduction

Soil erosion is a global phenomenon that is becoming increasingly important, especially in the context of climate change. Gully erosion occurs across a wide range of environments as a sign of land degradation. Agricultural fields are damaged by gully erosion, sediments are lost, and surface soil quality is compromised [1,2]. In Northeast China, the mainly black and fertile soils are essential for grain production, and therefore play a crucial role in national food security. However, as of 2020, 666.7 thousand gullies were reported in the region (Songliao River Water Resources Commission of the Ministry of Water Resources, <http://www.slwr.gov.cn/>, accessed on 1 May 2024). As erosion gullies expand annually, they encroach on arable land by $7.39 \text{ km}^2 \text{ y}^{-1}$ [3]. The annual loss in grain yields due to

gully erosion is approximately 36.2×10^8 kg, which represents 10% of the country's total grain supply (National Earth System Science Data Center, <http://northeast.geodata.cn>, accessed on 1 May 2024).

Combating the gully erosion is very necessary to prevent land degradation in black soil. Erosion gullies develop by headcuts and expanding gully slopes. Trees and shrubs are commonly used types of vegetation to prevent gully wall expansion and effectively control gully erosion [4]. Although the mechanisms by which vegetation conserves water and soil are well understood [5,6], planting trees or shrubs to control gully erosion has some drawbacks. First, the trees planted may not be suitable for the environment. It is generally true that native forest trees retain soil and water better than shrubs and grasslands, but when planted, the effects can be very different [7]. Second, the effects of trees and shrubs are slow to develop because of the long growing periods. Third, in contrast to nonintercepted drops, those intercepted by tall trees without an understory can be larger and have greater kinetic energy, which can lead to soil crusting, surface runoff generation, and gully formation [8,9]. Last, shrubland is hydraulically more efficient than grassland, leading to higher runoff and erosion rates [10].

Herbaceous revegetation can effectively reduce soil and water loss [11,12], and it conserves more soil and water compared with trees and shrubs on gully slopes [7,13]. On gully slopes, herbaceous canopies, roots, and litter all play a role in controlling soil erosion [14]. In addition to intercepting and diverting rainwater, herbaceous vegetation canopies provide physical protection to soils by reducing the impact of raindrops and reducing "splash" effects [15]. As with the canopy, litter can serve as a protective barrier, while roots can hold soil in place, trap sediment, and add organic substances to soil, thus improving soil structure [16]. The infiltrability and structural stability of soil are improved by plant roots and reduce gully erosion [4]. Roots play a major role in soil resistance to concentrated flow erosion by virtue of the characteristics of their fibrils (fibrils < 1.0 mm in diameter), which are distributed densely at a depth of 0–30 cm [17]. It may be helpful to use herbaceous revegetation studies to understand the relationships between herbaceous species and soil characteristics, and to select the species that are most suitable for restoration [18,19]. Several soil quality characteristics are commonly evaluated under different vegetation treatments, including total phosphorus, bulk density, aggregate stability, saturated hydraulic conductivity, and macroporosity [20,21]. It is crucial to fully understand how to restore degraded soils, determining the responses of soil nutrients and structure to revegetation.

Compared with trees and shrubs, herbaceous vegetation has the advantages of low cost, efficiency, and multiple roles. According to Wang et al. [22], grassland has important effects on erosion control. In addition, the cost of controlling gully erosion by herbaceous vegetation is expected to be only a third of that by trees or shrubs. Last, planted forage grass has a short growing period, and the effects are apparent in one year. Yan et al. [23] also found that herbaceous vegetation on gully slopes decreased runoff and soil loss by 19–30% and 78–97%, respectively. However, few managers use herbaceous vegetation to measure whether it can control the active degrading soil quality in gullies. Whether short-term artificial herbaceous revegetation is suitable for controlling erosion gullies and preventing soil degradation on gully slopes in black soil regions remains uncertain. In addition, little is known about which herbaceous species are suitable for preventing soil degradation in gully slopes.

To examine the effects of different species of short-term herbaceous vegetation on the soil quality in gully slopes and then select the species best suited for controlling soil degradation in an erosion gully of a black soil region, we conducted a field artificial revegetation experiment and a runoff scouring experiment with eight species of herbs. Study objectives included determining (1) the role of herbaceous vegetation in preventing soil and water loss on gully slopes; (2) the effects of short-term artificial herbaceous vegetation restoration on soil physicochemical properties; and (3) the suitable herbaceous species to combat soil degradation in an erosion gully. The hypotheses are as follows: (1) herbaceous revegetation

can reduce soil erosion on gully slopes; (2) short-term artificial herbaceous revegetation will improve the soil quality.

2. Materials and Methods

2.1. Study Area

The erosion gully was in Zhaoguojun Village of Baiquan County in Heilongjiang Province ($47^{\circ}23'45.23''$ – $47^{\circ}23'54.18''$ N, $126^{\circ}16'21.03''$ – $126^{\circ}16'25.52''$ E; Figure 1), China. The length of the erosion gully was 789 m, and the area of the gully was 1.1 ha. The mean depth of the erosion gully was 5 m. The longitudinal gradient of the gully was 61.3‰. The average annual temperature in the region is 1.5 °C, and the average annual rainfall is 530 mm. The soil is a silt loam soil and classified as Mollisol (also called black soil), with a soil depth of 30–50 cm. Soils and their parent materials are generally acidic to alkaline, with varying textures ranging from loam to clay loam, with most soils consisting mainly of clay loam. The land use types are forests and sloped croplands (3° to 5°).

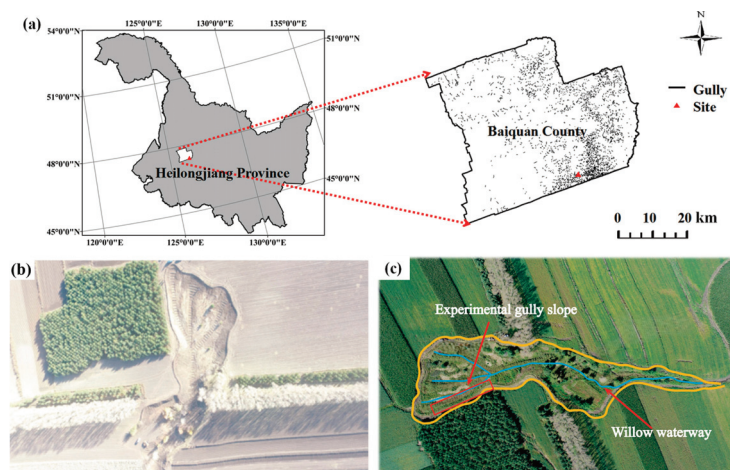


Figure 1. Location of the study site in Baiquan County, Heilongjiang Province, China, with the color image showing the erosion gully examined in the study. Note: (a) is the location of the study site, (b) is the aerial view of the experimental gully slope before artificial revegetation, and (c) is the aerial view of the experimental gully slope after artificial revegetation.

2.2. Experimental Setup

In May 2018, eight species of perennial herbaceous plants were planted on the gully slope (Table S1), and bare soil was used for the control (BARE). *Rheum palmatum* L. (RH) is a perennial herb in the Caryophyllales, Polygonaceae, and *Rheum* L. *Asparagus officinalis* L. (AS) is a perennial herb in the Asparagales, Liliaceae, and *Asparagus* L. *Elymus dahuricus* Turcz. (ET) is a perennial herb in the Gramineae, and *Elymus* Linn. *Medicago sativa* L. (ME) is a perennial herb in the Rosaceae, Leguminosae, and *Medicago* L. *Glycyrrhiza pallidiflora* Maxim. (GL) is a perennial herb in the Rosaceae, Leguminosae, and *Glycyrrhiza* L. *Elytrigia repens* (L.) Desv.ex Nevski. (EN) is a perennial herb in the Gramineae, and *Elytrigia* Desv. *Trifolium repens* L. (TR) is a perennial herb in the Fabales Bromhead, Leguminosae, and *Trifolium* L. *Bromus inermis* Leyss. (BR) is a perennial herb in the Gramineae, and *Bromus* L. Fabaceae can fix nitrogen (N), a potentially important contribution in degraded soils. The Fabaceae and Gramineae plants were achieved by strip sowing with a 30 cm row spacing and 2–3 cm depth. AS was also sown using strip sowing with a row spacing of 30 cm and a sowing depth of 4–6 cm. RH was transplanted with a 30 cm row spacing with 1–2 plants per hole, growing to 15 cm, and a plant spacing of 50 cm. The germination rate and clarity were obtained (GB 6141 seed quality grading of *Leguminosae* and GB 6142 seed quality

grading of *Gramineae*). Six replicate photos of each plot were taken at a height of 1.5 m, and PCOVER software (Version 3.00) was used to obtain the vegetation coverage (VC, %).

2.3. Runoff Scouring Experiment

Sixteen months after sowing, we conducted a field runoff scouring experiment, in September 2019. Three months before the runoff scouring experiment, each species of herbaceous plant was surrounded in three replicate runoff plots (2 m × 1 m). To isolate treatments, a steel sheet was embedded to a soil depth of 0.1 m around each runoff plot. Plastic pipes, valves, a buffer tank, and a water supply tank were used to supply water to the runoff plot [23]. An attachment was designed to connect the buffer tank to the water supply tank at its bottom. Until the runoff plot was filled with water, water from the water supply tank spilled into the buffer tank, ensuring uniform water flow that was stable and nonpressurized. In order to ensure adequate water supplementation during the experiment, two trucks supplied filtered water. The flow discharge was controlled using an adjusting valve and measured three times before and after each experiment. First, the soil of a runoff plot was saturated with water with a watering can to prevent the water from infiltrating into it. According to the maximum rainfall intensity (75 mm h⁻¹) in the area (China Meteorological Data Service Centre, <https://data.cma.cn/>, accessed on 1 May 2024), the flow discharge was set at 0.24 L s⁻¹, which was controlled by a switch. Runoff velocity was measured with a staining method. Each runoff scouring experiment was conducted three times. After the start and at the end of the experiment, three 5 s runoff samples were collected. Sediment yield was collected for 5 s every 15 s. As a measure of sediment concentration, samples were dried at 105 °C until a constant weight was reached (SC, g cm⁻³).

Surface runoff (SR, mm), sediment yield (SY, g m⁻²), and soil erosion rate (ER, g m⁻² s⁻¹) during the observation time (t, s) were calculated using Equations (1)–(4), respectively, as follows:

$$SR = V/LW \times 10^3 \quad (1)$$

$$SY = M/LW \quad (2)$$

$$M = V \times SC \times 1000 \quad (3)$$

$$ER = SY/t \quad (4)$$

where V is the runoff volume (m³); L and W are the length (m) and width (m) of the plot, respectively; and M is the amount of soil loss (g).

The mean flow velocity (u, m s⁻¹) was calculated as the product between surface flow velocity (u_s, m s⁻¹) and the correction factor (α = 0.67). We measured the u_s every 2 min at a marked 1 m distance with five replications using the KMnO₄ coloration technique. An accurate 1.0 mm steel rule was used to measure flow width (w, m) at three runoff observation sections. The flow hydraulic parameter unit flow discharge (q, m² s⁻¹), flow depth (h, m), flow shear stress (τ, Pa), stream power (ω, W m⁻²), Reynolds number (Re), and Froude number (Fr) were calculated using Equations (5)–(10), respectively, as follows:

$$q = Q/w \quad (5)$$

$$h = q/u \quad (6)$$

$$\tau = \rho gRJ \quad (7)$$

$$\omega = u\tau \quad (8)$$

$$Re = uR/\nu_0 \quad (9)$$

$$Fr = u/\sqrt{gh} \quad (10)$$

where Q is flow discharge ($\text{m}^3 \text{s}^{-1}$); ρ is the water density (kg m^{-3}); g is the constant of gravity (m s^{-2}); R is the hydraulic radius (m), which is equal to the mean flow depth; J is the hydraulic gradient, which is equal to the sine of the soil surface slope angle; and ν_0 is the kinematical viscosity ($\text{m}^2 \text{s}^{-1}$).

2.4. Soil Sampling and Laboratory Analysis

Before Frost's Descent in 2018, a 1 m long sample section was randomly selected within the plant row of each plot. Three replications were carried out. We recorded the number of plants in each sample area. In the following year, the number of surviving plants was investigated after the plants in the sample area had resumed growth to calculate the resume growth rate of the plant. The resume growth rate = N (number of surviving plants before winter)/ $N1$ (number of surviving plants after winter) $\times 100\%$.

Soil samples were collected outside the runoff plot with shovels before runoff scouring experiments at depths of 0–5 and 5–10 cm. Three samples were collected from the top to bottom of the gully slope and then composited as one soil sample. The sampling process was repeated three times per vegetated treatment and the bare soil. Drying was allowed to take place naturally by storing soil samples in well-ventilated conditions. Dried soils were sieved through a 200 μm mesh. Sieved soils were analyzed for physical and chemical properties.

The aggregate size distribution was measured by a slow-wetting method, with 50 g of air-dried soil that passed through a 10 mm sieve placed on the top of three nested sieves (2.0, 0.25, and 0.053 mm mesh) and submerged in tap water for 10 min. For 2 min, the wet sieve apparatus (DIK-2001, Daiki Rika Kogyo Co., Ltd., Saitama, Japan) was oscillated 3 cm up and down at a rate of 30 cycles per minute. Using the resistant soil materials on top of each sieve and the remaining unstable aggregates (<0.25 mm), all materials were oven-dried at 50 °C for 48 h. The wet aggregate stability (WAS) of the soil aggregates that remained above the sieves was calculated by weighing them after oven-drying:

$$WAS = (\text{weight of aggregates on sieves}/50 \text{ g}) \times 100\% \quad (11)$$

The bulk density (BD) of the undisturbed soil was determined using a cutting ring (volume = 100 cm^3) and oven-dried at 105 °C to a constant weight. By analyzing soil particle size distribution with a Mastersizer 2000 laser sizer (Malvern Instruments Ltd., Malvern, UK), soils were divided into sand, silt, and clay fractions. Soil BD, field capacity (FC), water content (SWC), and porosity (P) were measured separately by steel ring (volume = 100 cm^3) and gravimetric methods. Soil aeration porosity was calculated as the difference between P and FC.

Soil organic carbon (SOC) and total nitrogen (TN) contents were determined by a Euro single elemental analyzer (Euro Vector, Milan, Italy). We measured soil total potassium (TK) using flame photometry, and soil nitrogen (AN) using Kang Hui dishes [24]. Soil available phosphorus (AP) was measured using a molybdenum–antimony resistance colorimetric method [25]. The soil cation exchange capacity (CEC) was determined by the $\text{CH}_3\text{COONH}_4$ exchange method, while the soil pH level was measured using a pH meter (S20P-K; Mettler-Toledo, Greifensee, Switzerland) in suspension with a 1:2.5 soil-to-water ratio.

After runoff scouring experiments, plants were clipped above the soil surface, sorted by species, and oven-dried for 48 h at 65 °C to a constant mass, then weighed to calculate shoot dry weight (SDW, kg ha^{-1}). Topsoil root samples were collected by digging a randomly selected soil block of 20 cm (width) \times 20 cm (length) \times 30 cm (depth). After immersing a soil block in water for 12 h, intact and clean roots were collected by washing three times in water. Specific root length (SRL, m g^{-1}), root/shoot ratio (RSR), root length

density (RLD, cm cm^{-3}), root surface area density (RSD, $\text{cm}^2 \text{cm}^{-3}$), and root volume (RV, cm^3) were analyzed by a scanner (Expression 1640XL, Epson, Nagano-ken, Japan) and the WinRHIZO 2004a root analysis system (Regent Instrument Inc., Quebec, QC, Canada). RLD and RSD are the ratios of root length and surface area, respectively, and soil volume. Root biomass was determined by oven-drying at 65 °C for 48 h to a constant mass.

2.5. Statistical Analyses

The soil properties of eight species were compared with analysis of variance (ANOVA; *t*-test) and least significant difference (LSD), both at significance level $p < 0.05$. The coefficients of correlation between soil clay content, root characteristics, and aggregate characteristics were determined using Pearson correlation analysis with $p < 0.05$. Analysis of the data and data processing were performed using SPSS 22 (SPSS Inc., Chicago, IL, USA) and Origin 2021 (Origin Lab Corp., Northampton, MA, USA). ArcGIS 10.6 (Esri Inc., Redlands, CA, USA) was used to generate the study area map. Principal component analysis was performed with SPSSAU (<https://spssau.com/>, accessed on 1 May 2024) to obtain scores to evaluate the effects of short-term artificial revegetation.

3. Results

3.1. Adaptability of Artificial Revegetation

Differences in the timing of growth stages demonstrated the adaptability of artificial revegetation on the gully slope (Tables S1 and S2). Resume growth is an important indicator in evaluating vegetation adaptability. BR and RH were the first species to resume growth on 3 May. Most of the species returned to green during the first 10 d period of May. The last species to resume growth was GL on June 10. The resume growth ratio varied from 60% to 92% and was greater than 90% for ME, GL, and TR.

There were large differences in shoot and root characteristics among treatments with different herbaceous species. GL had the largest shoot dry weight ($34,817 \pm 12,106 \text{ kg ha}^{-1}$, $p < 0.05$), whereas AS had the smallest ($425 \pm 150 \text{ kg ha}^{-1}$, $p > 0.05$, Figure 2A). EN had the largest specific root length ($1.094 \pm 0.240 \text{ m g}^{-1}$, $p > 0.05$), whereas RH had the smallest ($0.004 \pm 0.004 \text{ m g}^{-1}$, $p > 0.05$, Figure 2B). RH had the largest root/shoot ratio (2.93 ± 0.76 , $p < 0.05$), whereas EN had the smallest (0.36 ± 0.06 , $p > 0.05$, Figure 2C). As shown in Figure 2D, BR had the largest root length density ($0.94 \pm 0.10 \text{ cm cm}^{-3}$, $p < 0.05$), whereas GL had the smallest ($0.03 \pm 0.01 \text{ cm cm}^{-3}$, $p > 0.05$). BR had the largest root surface area density ($0.06 \pm 0.00 \text{ cm}^2 \text{cm}^{-3}$, $p > 0.05$), whereas GL had the smallest ($0.01 \pm 0.00 \text{ cm}^2 \text{cm}^{-3}$, $p > 0.05$, Figure 2E). As shown in Figure 2F, RH had the largest root volume ($135.2 \pm 68.1 \text{ cm}^3$, $p < 0.05$), whereas ET had the smallest ($8.1 \pm 0.2 \text{ cm}^3$, $p > 0.05$).

3.2. Factors Sensitive to Short-Term Artificial Revegetation

According to the correlation matrix shown in Figure 3, the factors SY, ER, TN, TK, AP, CEC, water-stable aggregates ($>0.25 \text{ mm}$) ($\text{WR}_{0.25}$), aggregate mean weight diameter (MWD), and aggregate geometric mean diameter (GWD) were significantly correlated with vegetated treatments ($p < 0.05$). Thus, those factors were sensitive to short-term artificial revegetation. The factors are analyzed in detail in the following paragraphs.

3.3. Effects of Artificial Revegetation on Reducing Soil and Water Loss

An important function of herbaceous vegetation in controlling gully wall expansion is to reduce surface runoff and sediment loss. Compared with bare soil without vegetation coverage (BARE), vegetated treatments reduced average sediment yield by $91.1\% \pm 7.2\%$ during runoff scouring (Figure 4). Among the herbaceous species, sediment yield was most reduced with TR ($p > 0.05$). By contrast, the highest sediment yield was with AS. Vegetation coverage of RH, AS, and ET was lower than that of ME, GL, EN, TR, and BR. Surface runoff was not significantly different between vegetated treatments and BARE ($p > 0.05$). Among the herbaceous species (Table S3), flow hydraulic parameters varied with species. AS had

the largest q and RH had the smallest q . AS had the largest Re and RH had the smallest Re . BR had the largest Fr and GL had the smallest Fr .

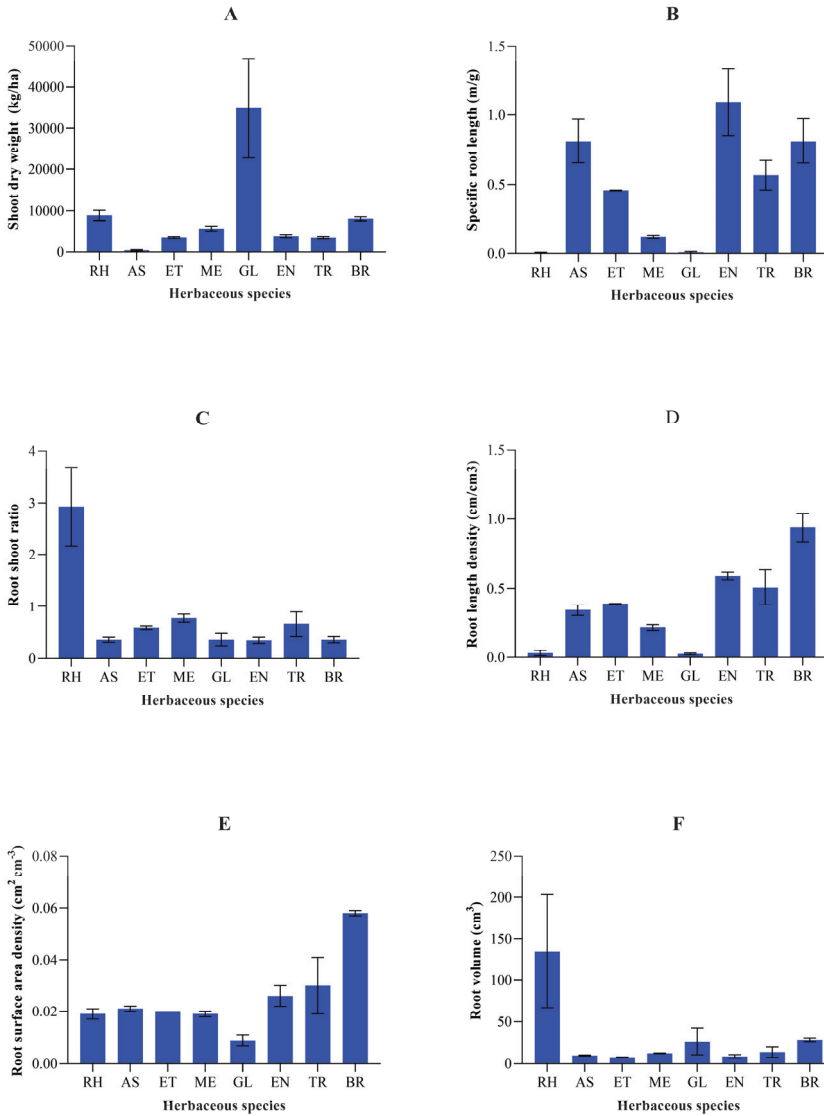


Figure 2. Shoot and root characteristics ((A) shoot dry weight; (B) specific root length; (C) root shoot ratio; (D) root length density; (E) root surface area density; (F) root volume) of eight herbaceous species used in vegetation restoration of a gully slope. Values are mean \pm SE ($n = 3$).

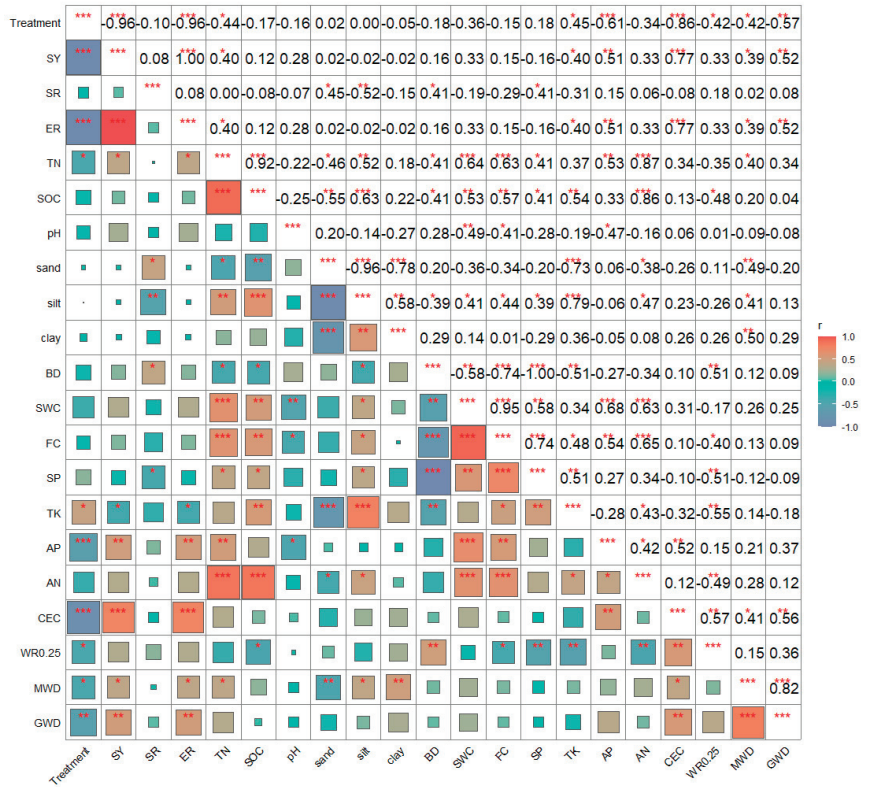


Figure 3. Correlation matrix for vegetation treatments and related soil characteristics. The color of each square is proportional to the value of Pearson’s correlation coefficient. Red indicates a positive correlation (dark green, $r = 1$); blue indicates a negative correlation (dark red, $r = -1$). * $p < 0.05$; ** $p < 0.01$; *** $p < 0.001$. Abbreviations: SY, sediment yield; SR, surface runoff; ER, erosion rate; TN, soil total nitrogen; SOC, soil organic carbon; BD, soil bulk density; SWC, soil water content; FC, field capacity; SP, soil porosity; TK, soil total potassium; AP, soil available phosphorus; AN, soil available N; CEC, cation exchange capacity; WR_{0.25}, water-stable aggregates (>0.25 mm); MWD, aggregate mean weight diameter; GWD, aggregate mean geometric diameter.

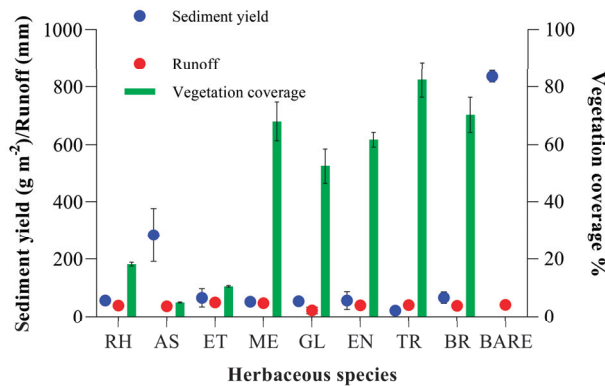


Figure 4. Sediment yield, surface runoff, and vegetation coverage with different species of herbaceous vegetation. Values are mean \pm SE ($n = 3$).

3.4. Responses of Soil Physicochemical Characteristics to Artificial Revegetation

Soil physical characteristics varied with herbaceous species (Figure 5 and Table 1). Soil aggregate fractions varied with species of herbaceous vegetation (Figure 5). Four fractions of soil aggregates were evaluated: macroaggregates (>2.0 mm), small macroaggregates (0.25–2.0 mm), microaggregates (0.053–0.25 mm), and silt plus clay (<0.053 mm). In both 0–5 cm (Figure 5A) and 5–10 cm (Figure 5B) soil layers, the silt plus clay fraction in vegetated plots was larger than that in BARE. To analyze the relations, *t*-tests were used to compare the differences in soil aggregate fractions between BARE and vegetated treatments. In the 0–5 cm layer, the silt plus clay fraction in BARE (1.63% ± 1.86%) was lower than that in vegetated treatments (7.51% ± 3.34%, *p* = 0.020). In the 5–10 cm layer, the silt plus clay fraction in BARE (4.43% ± 3.82%) was also lower than that in vegetated treatments (5.76% ± 2.13%, *p* = 0.471). In the 0–5 cm layer, WR_{0.25} were a larger fraction in BARE (92.11% ± 4.32%) than in vegetated treatments (84.78% ± 4.88%, *p* = 0.049). In the 5–10 cm layer, WR_{0.25} were also a larger fraction in BARE (92.31% ± 2.25%) than in vegetated treatments (84.78% ± 4.88%, *p* = 0.093). Thus, vegetated treatments increased the silt plus clay fraction and decreased the macroaggregate fraction of soil aggregates. However, the differences between BARE and vegetated treatments in the 5–10 cm layer were not significant (*p* > 0.05). In the 0–5 cm soil layer, the MWD (20.68 ± 9.21 mm) and GWD (14.44 ± 13.81 mm) of BARE were greater than those in vegetated treatments (MWD: 8.67 ± 3.97 mm; GWD: 1.82 ± 1.85 mm). By contrast, in the 5–10 cm soil layer, the MWD (3.72 ± 1.59 mm) and GWD (1.34 ± 0.33 mm) of BARE were smaller than those in vegetated treatments (MWD: 7.61 ± 1.66 mm; GWD: 2.30 ± 1.62 mm).

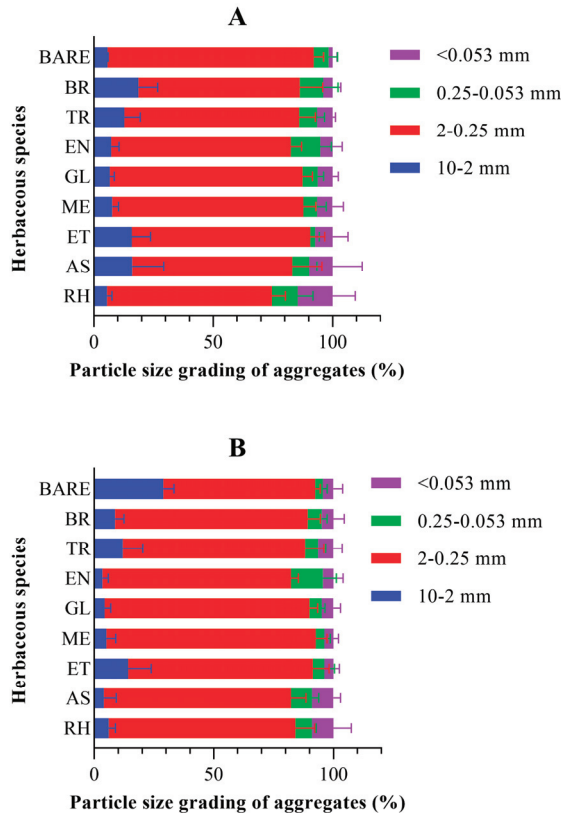


Figure 5. Soil aggregate fractions with different herbaceous species on an erosion gully slope. (A) 0–5 cm soil depth; (B) 5–10 cm soil depth.

Table 1. Soil physical characteristics with different herbaceous species.

Herbaceous Species	Soil Bulk Density (g cm ⁻³)	Soil Water Content (W/V, %)	Field Capacity (V/V, %)	Soil Porosity (%)	Soil Aeration Porosity (%)	WR _{0.25} (%)	MWD (mm)	GWD (mm)	Soil Texture		
									Clay (%)	Silt (%)	Sand (%)
RH	1.34 ± 0.05	33.17 ± 1.40	38.03 ± 1.80	49.32 ± 1.80	11.30 ± 1.33	79.39 ± 1.78	7.38 ± 1.01	0.79 ± 0.16	0.2 ± 0.0	8.0 ± 0.1	91.8 ± 0.1
AS	1.34 ± 0.01	32.16 ± 0.56	37.15 ± 0.36	49.25 ± 0.30	12.10 ± 0.66	82.65 ± 4.41	7.87 ± 2.15	1.27 ± 0.61	0.2 ± 0.0	10.0 ± 0.1	89.8 ± 0.1
ET	1.63 ± 0.01	18.88 ± 4.88	21.40 ± 5.95	38.39 ± 0.41	16.99 ± 5.53	91.03 ± 2.47	5.97 ± 0.08	1.46 ± 0.19	0.2 ± 0.0	2.0 ± 0.0	97.8 ± 0.0
ME	1.41 ± 0.09	36.50 ± 0.59	38.25 ± 0.27	46.78 ± 3.37	8.54 ± 3.09	90.21 ± 1.93	6.75 ± 2.91	2.5 ± 1.97	2.2 ± 0.1	5.8 ± 0.2	92.0 ± 0.2
GL	1.37 ± 0.02	29.93 ± 0.23	33.47 ± 0.30	48.40 ± 0.92	14.94 ± 1.80	88.71 ± 1.76	7.12 ± 1.35	1.7 ± 0.32	2.2 ± 0.2	12.0 ± 0.2	85.8 ± 0.0
EN	1.40 ± 0.03	31.87 ± 0.64	35.87 ± 0.45	47.28 ± 1.14	11.42 ± 1.59	82.38 ± 1.76	7.97 ± 1.08	1.16 ± 0.11	2.2 ± 0.0	14.1 ± 0.2	83.7 ± 0.2
TR	1.30 ± 0.08	33.69 ± 0.90	36.86 ± 0.98	51.08 ± 3.03	14.22 ± 2.06	87.11 ± 0.78	9.75 ± 4.46	3.53 ± 3.81	2.2 ± 0.0	14.0 ± 0.0	83.8 ± 0.0
BR	1.57 ± 0.02	29.38 ± 0.54	31.81 ± 0.46	40.59 ± 0.60	9.28 ± 1.06	87.81 ± 1.72	12.34 ± 2.81	4.09 ± 3.59	6.2 ± 0.0	14.0 ± 0.0	79.8 ± 0.0
BARE	1.49 ± 0.06	36.68 ± 2.43	36.58 ± 1.51	43.88 ± 2.32	7.31 ± 2.16	92.21 ± 2.7	12.2 ± 4.09	7.89 ± 6.75	2.2 ± 0.0	10.0 ± 0.0	87.8 ± 0.0

Note: soil water content and field capacity using volumetric water content (V/V). RH: *Rhizum palmatum* L., AS: *Asparagus officinalis* L., ET: *Elymus dahuricus* Turcz. ME: *Medicago sativa* L., GL: *Glycyrrhiza pallidiflora* Maxim., EN: *Elytrigia repens* (L.) Desv.ex Nevski, TR: *Trifolium repens* L., BR: *Bromus inermis* Leyss. BARE: no vegetation coverage.

Soil chemical properties (Table 2) are expressed as the difference between vegetated treatments and BARE at the 0–10 cm depth in Figure S1. The mean value of the CEC under vegetated treatments ($19.55 \pm 0.67 \text{ cmol kg}^{-1}$) was lower by approximately 15% than that under the BARE condition ($22.94 \pm 1.43 \text{ cmol kg}^{-1}$, Figure S1d). The mean values of total N ($0.92 \pm 0.40 \text{ g kg}^{-1}$, Figure S1e) and AP ($23.94 \pm 5.67 \text{ mg kg}^{-1}$, Figure S1b) were lower under vegetated treatments by approximately 39% than those under the BARE condition (TN: $1.53 \pm 0.35 \text{ g kg}^{-1}$; AP: $36.08 \pm 0.84 \text{ mg kg}^{-1}$). By contrast, the mean value of TK ($7.07 \pm 1.86 \text{ g kg}^{-1}$, Figure S1a) under vegetated treatments increased by more than 59% compared with that under the BARE condition ($4.43 \pm 0.08 \text{ g kg}^{-1}$). The mean value of the AN/TN ratio under vegetated treatments (0.07 ± 0.05 , Figure S1f) was greater by approximately 134% than that under the BARE condition (0.03 ± 0.01). The not-significant related factors ($p > 0.05$) in Figure 3 are AN (Figure S1c) and SOC (Figure S1g), which were lower under vegetated treatments ($42.66 \pm 3.28 \text{ mg kg}^{-1}$ and $10.39 \pm 5.71 \text{ g kg}^{-1}$) than those under the BARE condition ($46.00 \pm 1.24 \text{ mg kg}^{-1}$ and $13.46 \pm 0.97 \text{ g kg}^{-1}$).

Table 2. Soil chemical characteristics with different herbaceous species.

Soil Layer	Species	pH (mol L^{-1})	CEC (cmol kg^{-1})	SOC (g kg^{-1})	TN (g kg^{-1})	AN (mg kg^{-1})	AN/TN	AP (mg kg^{-1})	TK (g kg^{-1})
0–10 cm	RH	5.95 ± 0.24	18.72 ± 1.31	16.10 ± 4.20	1.37 ± 0.30	46.22 ± 3.08	0.04 ± 0.01	31.91 ± 2.93	6.38 ± 2.15
	AS	6.17 ± 0.08	18.87 ± 0.77	8.68 ± 1.31	0.92 ± 0.07	43.29 ± 3.04	0.05 ± 0.00	19.12 ± 8.91	8.44 ± 1.33
	ET	6.17 ± 0.10	19.34 ± 0.90	1.03 ± 0.45	0.23 ± 0.07	37.68 ± 6.05	0.19 ± 0.08	18.13 ± 8.66	3.45 ± 0.44
	ME	5.81 ± 0.18	19.37 ± 1.80	6.74 ± 5.66	0.74 ± 0.53	41.83 ± 7.89	0.11 ± 0.13	31.04 ± 3.48	6.11 ± 1.13
	GL	6.03 ± 0.09	20.50 ± 1.53	6.17 ± 1.61	0.54 ± 0.17	38.81 ± 1.50	0.08 ± 0.03	22.22 ± 5.37	6.34 ± 3.62
	EN	6.03 ± 0.04	19.35 ± 1.05	17.80 ± 7.70	1.31 ± 0.54	47.33 ± 10.79	0.04 ± 0.02	19.82 ± 7.22	8.90 ± 0.68
	TR	5.92 ± 0.13	20.51 ± 1.11	14.28 ± 6.03	1.23 ± 0.44	43.18 ± 0.29	0.04 ± 0.02	28.71 ± 0.40	8.60 ± 0.82
	BR	6.00 ± 0.08	19.78 ± 0.79	12.35 ± 7.19	1.06 ± 0.44	42.95 ± 3.00	0.05 ± 0.02	20.61 ± 7.05	8.33 ± 0.81
	BARE	6.07 ± 0.05	22.94 ± 1.43	13.46 ± 0.97	1.53 ± 0.35	46.00 ± 1.24	0.03 ± 0.01	36.08 ± 0.84	4.43 ± 0.08
	Mean value of vegetated treatments		6.01 ± 0.12	19.55 ± 0.67	10.39 ± 5.71	0.92 ± 0.40	42.66 ± 3.28	0.07 ± 0.05	23.94 ± 5.67

Note: RH: *Rheum palmatum* L., AS: *Asparagus officinalis* L., ET: *Elymus dahuricus* Turcz. ME: *Medicago sativa* L., GL: *Glycyrrhiza pallidiflora* Maxim., EN: *Elytrigia repens* (L.) Desv.ex Nevski, TR: *Trifolium repens* L., BR: *Bromus inermis* Leys. BARE: no vegetation coverage.

3.5. Evaluation of Short-Term Artificial Revegetation

Principal component analysis was conducted to evaluate the short-term effects of artificial revegetation on an erosion gully. The evaluation was based on effects on soil and water conservation, soil quality, and vegetation growth (Table 3). The evaluation of soil and water conservation was based on SY, SR, τ , ω , Re, and Fr (Table S3). The weighting of each parameter was 18.19%, 14.40%, 17.32%, 16.25%, 17.75%, and 16.09%, and the evaluation scores for the eight herbaceous species were ranked AS > RH > ET > ME > GL > BR > EN > TR. In this evaluation, the higher the ranking was, the worse the soil and water conservation effect. The evaluation of soil quality was based on SOC, TN, C/N ratio, sand, silt, clay, pH, BD, FC, SP, TK, AP, AN, CEC, $WR_{0.25}$, MWD, and GWD. The weighting of each parameter was 5.24%, 5.50%, 4.98%, 5.91%, 6.11%, 4.77%, 4.89%, 6.29%, 5.62%, 6.29%, 5.70%, 5.59%, 5.99%, 4.70%, 5.91%, 5.49%, and 4.82%, and the evaluation scores were ranked TR > BR > EN > RH > ME > GL > AS > ET. The evaluation of vegetation growth was based on VC, SDW, SRL, RSR, RLD, RSD, and RV. The weighting of each parameter was 12.67%, 13.50%, 13.79%, 15.06%, 14.39, 15.23%, and 15.37%, and the evaluation scores were ranked BR > EN > TR > AS > ET > ME > RH > GL.

Table 3. Comprehensive evaluation scores for effects of artificial revegetation by different herbaceous species in an erosion gully on soil and water conservation, soil quality, and vegetation growth.

Species	Evaluation Aspects		
	Soil and Water Conservation	Soil Quality	Vegetation Growth
RH	0.08	0.15	−1.26
AS	3.16	−0.61	−0.06
ET	−0.01	−3.42	−0.26
ME	−0.11	−0.02	−0.37
GL	−0.44	−0.13	−1.50
EN	−0.97	0.87	0.86
TR	−0.98	1.79	0.68
BR	−0.73	1.37	1.92

Note: RH: *Rheum palmatum* L., AS: *Asparagus officinalis* L., ET: *Elymus dahuricus* Turcz. ME: *Medicago sativa* L., GL: *Glycyrrhiza pallidiflora* Maxim., EN: *Elytrigia repens* (L.) Desv.ex Nevski, TR: *Trifolium repens* L., BR: *Bromus inermis* Leyss.

The selection of suitable herbaceous species for artificial revegetation is very important in preventing soil degradation in erosion gullies. Based on the objectives, the suitable herbaceous species varied a bit. However, the TR, BR, and EN consistently had the top three rankings by score in all three aspects evaluated. This means that the three herbaceous species (TR, BR, and EN) were suitable for preventing soil degradation in erosion gullies. Based on the characteristics and growing period of the herbaceous vegetation planted (Tables S1 and S2), TR was better than BR and EN. Therefore, TR was the most suitable species for use in artificial revegetation to prevent soil degradation in an erosion gully.

4. Discussion

4.1. The Effects of Artificial Revegetation with Herbaceous Species on Soil Erosion

Reducing soil erosion is critical for controlling gully development [4]. Artificial revegetation can quickly alter soil surface properties and reduce soil losses during surface runoff [23]. In Figure 3, vegetation treatments had a strong relationship with sediment yield (SY) and erosion rate (ER). MWD and GWD were significant factors influencing the SY and ER. Increased aggregate stability will reduce soil erosion by minimizing rainfall-induced aggregate disturbance and increasing soil pores [26,27]. However, the lower MWD and GWD with revegetated treatments (Table 1) did not result in increased sediment output (Figure 3). This meant that vegetation cover played an essential role in lowering sediment yield.

Figure 4 shows how vegetation treatments reduced soil erosion. Soil erosion was directly linked to vegetation features [7]. Previous research has shown that vegetation coverage, and shoot and root traits all have an impact on soil erosion. However, in our investigation, vegetation coverage was not significantly related to sediment output ($p > 0.05$). In prior research, the role of vegetation coverage was to minimize rainfall kinetic energy and prevent soil particles from dispersing [11]. The influence of herbaceous vegetation cover was not investigated because our study focused on runoff scouring tests. However, the roots of herbaceous vegetation play an important role in soil stabilization [28]. AS produced more sediment than other vegetated treatments due to its poor vegetation coverage (Figure 4).

4.2. Changes in Soil Physicochemical Characteristics

Short-term (16 months) artificial revegetation of an erosion gully slope with herbaceous vegetation did not improve soil quality. It significantly decreased soil nutrient concentrations (except TK), $WR_{0.25}$, and aggregate water stability compared with bare soil.

Although sediment yield decreased with revegetated treatments, the $WR_{0.25}$, MWD, and GWD suggested short-term herbaceous species revegetation destroyed soil structure and, instead of conserving nutrients, released them for plant uptake. Abiotic and biotic

processes (e.g., SOM and microorganisms) interact to form soil aggregates as a result of aggregation and fragmentation processes [29]. The decreased aggregate stability can be attributed to vegetation root penetration. By affecting the size of aggregates and the connectivity or size by producing [30] or clogging [31] pores, root penetration primarily affects soil structure. Growing roots can cause soil particles and aggregates to become pressed by growing roots during the initial stages of vegetation growth [32,33]. It is unavoidable that the growth of roots leads to a reduction in the porosity of rhizosphere soil when the penetration resistance of soil is greater than the pressure. Also, thickened and lengthened roots can disperse soil particles or aggregates [34] and crack macroaggregates [35]. Although short-term artificial revegetation did not increase aggregate stability in this study (Figure 3), aggregate stability appeared to tend toward future increases, with increased large macroaggregates (Figure 5).

In previous studies, soil nutrients increased after vegetation restoration [36–38]. However, in our study, SOC and AN were not sensitive to short-term artificial revegetation. The soil nutrient-preserving capability (represented by the CEC) decreased with the vegetated treatments (Figure 3). With the exception of TK, soil nutrients were generally lower under vegetation treatment than in bare soil. One reason to explain the lack of sensitivity could be that because the herbaceous litter input was relatively small, the C input to the soil was also relatively small during the experiment. Secondly, a shallow root system, weak soil consolidation, and the need for plants to absorb nutrients are also factors to consider. The input of soil nutrients was less than the nutrients consumed by vegetation growth in the short term. The third reason was the breakdown of soil aggregate. Newly imported nutrients can benefit from soil aggregates because they provide physical protection and reduce their accessibility by microbes [39–41]. However, with the breakdown of soil aggregate by root penetration, the soil nutrients are mineralized and lost [42]. The decrease in $WR_{0.25}$ (Figure 5) mainly caused by the breakdown of soil aggregates could contribute to the loss of SOC and soil nutrients. The last reason could be the “priming effect”. The input of vegetation litter with a high C:N ratio can lead to priming effects and accelerate the decomposition of native SOC [43]. Compared with farmland soils, the addition of exogenous organic matter (vegetation litter) to gully slope soil with a relatively low SOC content may lead to greater stimulation of microbial activity and consequently drive increases in the decomposition of native SOC [44]. Although the TN under vegetated treatments ($0.09\% \pm 0.04\%$) was lower than that under bare soil ($0.15\% \pm 0.04\%$), the AN was not significantly different between bare soil and vegetated treatments. The results indicated that short-term artificial revegetation increases the AN/TN ratio. Available N consists of “temporary and slow-acting reservoirs” of SON, which are the main sources of easily mineralized N in soil [45]. As herbaceous vegetation has a relatively short life cycle and turnover, the soil microorganisms use readily decomposable litter from herbaceous vegetation to increase their AN/TN ratios. The increased AN/TN ratio can lead to a relatively rapid rate of soil N cycling [46]. The increase in TK indicated that soil K in an erosion gully could be restored under artificial revegetation in a short time, consistent with the results of Liu and Wang [47]. One reason for the rapid recovery could be that K is not a limiting element in the black soil area. Another reason for the increase could be the high contents of K returned in plant litter leading to soil K enrichment.

4.3. The Evaluation of Herbaceous Species

The goal of our study was to find suitable herbaceous species to prevent soil degradation in a black soil erosion gully based on three aspects. To our surprise, the top-ranked three species (BR, EN, and TR, in Section 3.5) were the same in all aspects evaluated. Vegetation coverage is a critical factor affecting soil and water loss [11]. Yan et al. [23] found that increasing vegetation coverage will reduce soil and water loss in the same place. In that regard, the TR was best in controlling gully development. Improving soil quality is another role of artificial revegetation [48]. TR revegetation increased the SOC contents, reduced soil nutrient loss, and functioned best among the herbaceous species, followed

by BR and EN. The vegetation growth status is also very important in controlling gully development [23]. Root characteristics are important vegetation growth indexes that decide the role of herbaceous species in changing soil characteristics (Figure S2). A root density increase leads to the formation of stable macroaggregates because roots and associated fungi form a mesh that entangles fine soil particles. In addition, roots produce exudates that can serve as adhesives and may stimulate the activity of microbes, both of which contribute to soil aggregate stability [49,50]. Based on the above reasons, the BR was best in preventing soil degradation among the herbaceous species, followed by TR and EN. Although BR, EN, and TR were the top-ranked three species in all aspects evaluated, the TR was the best of them based on the germination rate, clarity, and resume growth ratio.

Artificial revegetation is typically accomplished with trees and shrubs in degraded areas [51]. However, comparing the results with herbaceous species with those with trees and shrubs, herbaceous species played a more important role in reducing soil and water loss, soil nutrient loss, and soil carbon loss [13,52]. Especially in some serious eroding environments like erosion gully slopes, trees and shrubs have been difficult to grow, with few nutrients and poor soil structure [53]. Herbaceous species were demonstrated to be a viable alternative in our study.

5. Conclusions

The effects of short-term artificial revegetation with herbaceous species in preventing soil degradation in an erosion gully of a black soil area were evaluated. A field runoff scouring experiment verified that artificial revegetation conserved soil and water, conserving soil by decreasing sediment yields. There were significant differences in soil TN, TK, and AP between vegetated treatments and bare soil. With a decrease in CEC, soil TK and AN/TN increased under short-term vegetated treatments. Although $WR_{0.25}$ decreased under vegetated treatments, the silt plus clay fraction (<0.053 mm) was greater than that with bare soil. On the basis of a comprehensive evaluation of the effects on soil and water conservation, soil quality, and vegetation growth, TR is recommended as the most suitable herbaceous species to prevent soil degradation on an erosion gully slope. Although short-term revegetation did not improve soil quality in gullies, continuous vegetation growth will strengthen the potential to regulate gully formation and soil degradation. Leguminosae herbaceous species such as TR, which have a high vegetation coverage, are excellent alternatives for gully restoration. Artificial revegetation with herbaceous species has been shown to be an effective method for reducing soil erosion in gullies. Given the cost and time involved with herbaceous species, we believe that artificial revegetation with herbaceous species or a combination of trees, shrubs, and herbaceous species is a sustainable strategy to minimize soil degradation in a black soil erosion gully in Northeast China.

Supplementary Materials: The following supporting information can be downloaded at: <https://www.mdpi.com/article/10.3390/land13091486/s1>, Figure S1: Soil nutrient properties expressed as the difference between vegetated treatments and bare soil at the 0–10-cm depth under different herbaceous species. (a) Total potassium (TK), (b) available phosphorus (AP), (c) available nitrogen (AN), (d) cation exchange capacity (CEC), (e) total N (TN), (f) AN/TN ratio, and (g) soil organic carbon (SOC). Values are Mean \pm SE ($n = 3$). RH: *Rheum palmatum* L., AS: *Asparagus officinalis* L., ET: *Elymus dahuricus* Turcz. ME: *Medicago sativa* L., GL: *Glycyrrhiza pallidiflora* Maxim., EN: *Elytrigia repens* (L.) Desv.ex Nevski, TR: *Trifolium repens* L., BR: *Bromus inermis* Leyss.; Figure S2: Correlation matrix for vegetation treatments and related soil and vegetation characteristics. The color of each square is proportional to the value of Pearson's correlation coefficient. red indicates a positive correlation (dark green, $r = 1$); blue indicates a negative correlation (dark red, $r = -1$). * $p < 0.05$; ** $p < 0.01$; *** $p < 0.001$. Abbreviations: VC, vegetation coverage; SDW, shoot dry weight; SRL, specific root length; R/S, root shoot ratio; RLD, root length density; RSAD, root surface area density; RV, root volume; TN, soil total nitrogen; SOC, soil organic carbon; BD, soil bulk density; SWC, soil water content; FC, field capacity; SP, soil porosity; TK, soil total potassium; AP, soil available phosphorus; AN, soil available N; CEC, cation exchange capacity; $WR_{0.25}$, water stable aggregates (>0.25 mm); MWD, aggregate mean weight diameter; GWD, aggregate mean geometric diameter volume; Table S1: Species and characteristics of

herbaceous vegetation planted on an erosion gully slope with 12° gradient; Table S2: Dates of growth stages of herbaceous species used in vegetation restoration of a gully slope (2018–2019); Table S3: Soil erosion and flow hydraulic parameters under different herbaceous species.

Author Contributions: Methodology, J.L. (Jielin Liu) and X.Z.; Validation, X.K.; Investigation, X.W.; Resources, X.Z.; Data curation, Y.Z., J.L. (Jianye Li) and X.W.; Writing—original draft, J.L. (Jianye Li); Writing—review & editing, Y.Z. and J.L. (Jianye Li); Visualization, Q.Z.; Supervision, D.P.; Project administration, D.P.; Funding acquisition, J.L. (Jielin Liu) and X.Z. All authors have read and agreed to the published version of the manuscript.

Funding: This research was funded by the National Key Research & Development Program of China (2021YFD1500800) and the Provincial Key Research and Development Program of Heilongjiang (GA23B004), with further joint support by the Program of Scientific and Technological Innovation Project in the Heilongjiang Academy of Agricultural Science (CX23GG08), the Scientific Research Operation Expenses for Provincial Scientific Research Institutes in Heilongjiang Province (CZKYF2024-1-A004), and the Young Scientist Group Project of Northeast Institute of Geography and Agroecology, Chinese Academy of Sciences (2023QNXX03).

Data Availability Statement: The original contributions presented in the study are included in the article, further inquiries can be directed to the corresponding author.

Conflicts of Interest: The authors declare that they have no known competing financial interests or personal relationships that may have affected the research presented in this article.

References

1. Wen, H.; Ni, S.; Wang, J.; Cai, C. Changes of soil quality induced by different vegetation restoration in the collapsing gully erosion areas of southern China. *Int. Soil Water Conserv. Res.* **2021**, *9*, 195–206. [CrossRef]
2. Chen, Y.; Jiao, J.; Yan, X.; Li, J.; Vanmaercke, M.; Wang, N. Response of gully morphology and density to the spatial and rainy-season monthly variation of rainfall at the regional scale of the Chinese Loess Plateau. *Catena* **2024**, *236*, 107773. [CrossRef]
3. Liu, X.; Li, H.; Zhang, S.; Cruse, R.M.; Zhang, X. Gully Erosion Control Practices in Northeast China: A Review. *Sustainability* **2019**, *11*, 5065. [CrossRef]
4. Valentin, C.; Poesen, J.; Li, Y. Gully erosion: Impacts, factors and control. *Catena* **2005**, *63*, 132–153. [CrossRef]
5. Rickson, R.J. Water induced soil erosion. In *Encyclopedia of Soils in the Environment*, 2nd ed.; Goss, M.J., Oliver, M., Eds.; Academic Press: Oxford, UK, 2023; pp. 193–207.
6. Wei, B.; Li, Z.; Duan, L.; Gu, Z.; Liu, X. Vegetation types and rainfall regimes impact on surface runoff and soil erosion over 10 years in karst hillslopes. *Catena* **2023**, *232*, 107443. [CrossRef]
7. Chen, H.; Zhang, X.; Abla, M.; Lü, D.; Yan, R.; Ren, Q.; Ren, Z.; Yang, Y.; Zhao, W.; Lin, P.; et al. Effects of vegetation and rainfall types on surface runoff and soil erosion on steep slopes on the Loess Plateau, China. *Catena* **2018**, *170*, 141–149. [CrossRef]
8. Kou, M.; Jiao, J. Structure of Erosion-Resistant Plant Community in the Hill-Gully Region of the Loess Plateau. *Res. Soil Water Conserv.* **2018**, *25*, 7.
9. Vásquez-Méndez, R.; Ventura-Ramos, E.; Oleschko, K.; Hernández-Sandoval, L.; Parrot, J.-F.; Nearing, M.A. Soil erosion and runoff in different vegetation patches from semiarid Central Mexico. *Catena* **2010**, *80*, 162–169. [CrossRef]
10. Michaelides, K.; Lister, D.; Wainwright, J.; Parsons, A.J. Vegetation controls on small-scale runoff and erosion dynamics in a degrading dryland environment. *Hydrol. Process.* **2009**, *23*, 1617–1630. [CrossRef]
11. Zuazo, V.H.D.; Pleguezuelo, C.R.R. Soil-erosion and runoff prevention by plant covers: A review. *Agron. Sustain. Dev.* **2008**, *28*, 65–86. [CrossRef]
12. Yu, Y.; Wei, W.; Chen, L.; Feng, T.; Daryanto, S. Quantifying the effects of precipitation, vegetation, and land preparation techniques on runoff and soil erosion in a Loess watershed of China. *Sci. Total. Environ.* **2019**, *652*, 755–764. [CrossRef] [PubMed]
13. Li, J.; Fu, B.; Liu, S.; Dargush, P.; Gao, G.; Liu, J.; Wei, F. Vegetation restoration changes topsoil biophysical regulations of carbon fluxes in an eroding soil landscape. *Land Degrad. Dev.* **2018**, *29*, 4061–4070. [CrossRef]
14. Mohammad, A.G.; Adam, M.A. The impact of vegetative cover type on runoff and soil erosion under different land uses. *Catena* **2010**, *81*, 97–103. [CrossRef]
15. Bochet, E.; Poesen, J.; Rubio, J.L. Runoff and soil loss under individual plants of a semi-arid Mediterranean shrubland: Influence of plant morphology and rainfall intensity. *Earth Surf. Process. Landforms* **2006**, *31*, 536–549. [CrossRef]
16. Gysels, G.; Poesen, J.; Bochet, E.; Li, Y. Impact of plant roots on the resistance of soils to erosion by water: A review. *Prog. Phys. Geogr.* **2005**, *29*, 189–217. [CrossRef]
17. Li, Y.; Zhu, X.M.; Tian, J.Y. Effectiveness of plant roots to increase the anti-scourability of soil on the Loess Plateau. *Chin. Sci. Bull.* **1991**, *36*, 2077–2082.
18. Lin, J.; Huang, Y.; Wang, M.-K.; Jiang, F.; Zhang, X.; Ge, H. Assessing the sources of sediment transported in gully systems using a fingerprinting approach: An example from South-east China. *Catena* **2015**, *129*, 9–17. [CrossRef]

19. Guo, S.; Han, X.; Li, H.; Wang, T.; Tong, X.; Ren, G.; Feng, Y.; Yang, G. Evaluation of soil quality along two revegetation chronosequences on the Loess Hilly Region of China. *Sci. Total. Environ.* **2018**, *633*, 808–815. [CrossRef]
20. Wu, C.; Deng, L.; Huang, C.; Chen, Y.; Peng, C. Effects of vegetation restoration on soil nutrients, plant diversity, and its spatiotemporal heterogeneity in a desert–oasis ecotone. *Land Degrad. Dev.* **2020**, *32*, 670–683. [CrossRef]
21. Raiesi, F.; Kabiri, V. Identification of soil quality indicators for assessing the effect of different tillage practices through a soil quality index in a semi-arid environment. *Ecol. Indic.* **2016**, *71*, 198–207. [CrossRef]
22. Wang, S.; Zhang, Z.; McVicar, T.R.; Zhang, J.; Zhu, J.; Guo, J. An event-based approach to understanding the hydrological impacts of different land uses in semi-arid catchments. *J. Hydrol.* **2012**, *416–417*, 50–59. [CrossRef]
23. Yan, Y.; Zhang, X.; Liu, J.; Li, J.; Ding, C.; Qi, Z.; Shen, Q.; Guo, M. The effectiveness of selected vegetation communities in regulating runoff and soil loss from regraded gully banks in the Mollisol region of Northeast China. *Land Degrad. Dev.* **2021**, *32*, 2116–2129. [CrossRef]
24. Marcos, M.S.; Bertiller, M.B.; Cisneros, H.S.; Olivera, N.L. Nitrification and ammonia-oxidizing bacteria shift in response to soil moisture and plant litter quality in arid soils from the Patagonian Monte. *Pedobiologia* **2016**, *59*, 1–10. [CrossRef]
25. Holliday, V.T. Methods of Soil Analysis, Part 1, Physical and Mineralogical Methods. In *American Society of Agronomy, Agronomy Monographs*; Klute, A., Ed.; Wiley Online Library: Madison, WI, USA, 1986; 1188p.
26. Shi, P.; Arter, C.; Liu, X.; Keller, M.; Schulin, R. Soil aggregate stability and size-selective sediment transport with surface runoff as affected by organic residue amendment. *Sci. Total. Environ.* **2017**, *607–608*, 95–102. [CrossRef]
27. Obalum, S.; Uteau-Puschmann, D.; Peth, S. Reduced tillage and compost effects on soil aggregate stability of a silt-loam Luvisol using different aggregate stability tests. *Soil Tillage Res.* **2019**, *189*, 217–228. [CrossRef]
28. Liu, B.; Xie, G.; Zhang, X.; Zhao, Y.; Yin, X.; Cheng, C. Vegetation root system, soil erosion and ecohydrology system: A review. In Proceedings of the 2015 International Forum on Energy, Environment Science and Materials, Shenzhen, China, 25–26 September 2015; Choi, S.B., Ed.; Atlantis Press: Paris, France, 2015; pp. 271–279.
29. Bronick, C.J.; Lal, R. Soil structure and management: A review. *Geoderma* **2005**, *124*, 3–22. [CrossRef]
30. Lucas, M.; Schlüter, S.; Vogel, H.-J.; Vetterlein, D. Roots compact the surrounding soil depending on the structures they encounter. *Soil. Rep.* **2019**, *9*, 16236. [CrossRef]
31. Sullivan, P.; Billings, S.; Hirmas, D.; Li, L.; Zhang, X.; Ziegler, S.; Murenbeeld, K.; Ajami, H.; Guthrie, A.; Singha, K.; et al. Embracing the dynamic nature of soil structure: A paradigm illuminating the role of life in critical zones of the Anthropocene. *Earth-Sci. Rev.* **2022**, *225*, 103873. [CrossRef]
32. Colombi, T.; Torres, L.C.; Walter, A.; Keller, T. Feedbacks between soil penetration resistance, root architecture and water uptake limit water accessibility and crop growth—A vicious circle. *Sci. Total Environ.* **2018**, *626*, 1026–1035. [CrossRef]
33. Chen, W.; Chen, Y.; Siddique, K.H.; Li, S. Root penetration ability and plant growth in agroecosystems. *Plant Physiol. Biochem.* **2022**, *183*, 160–168. [CrossRef]
34. Hallett, P.D.; Marin, M.; Bending, G.D.; George, T.S.; Collins, C.D.; Otten, W. Building soil sustainability from root–soil interface traits. *Trends Plant Sci.* **2022**, *27*, 688–698. [CrossRef] [PubMed]
35. Lu, J.; Zhang, Q.; Werner, A.D.; Li, Y.; Jiang, S.; Tan, Z. Root-induced changes of soil hydraulic properties—A review. *J. Hydrol.* **2020**, *589*, 125203. [CrossRef]
36. Liu, J.; Wang, J.; Morreale, S.J.; Schneider, R.L.; Li, Z.; Wu, G.-L. Contributions of plant litter to soil microbial activity improvement and soil nutrient enhancement along with herb and shrub colonization expansions in an arid sandy land. *Catena* **2023**, *227*, 107098. [CrossRef]
37. Liu, R.; Wang, D. C:N:P stoichiometric characteristics and seasonal dynamics of leaf-root-litter-soil in plantations on the loess plateau. *Ecol. Indic.* **2021**, *127*, 107772. [CrossRef]
38. Zhang, Y.; Xu, X.; Li, Z.; Liu, M.; Xu, C.; Zhang, R.; Luo, W. Effects of vegetation restoration on soil quality in degraded karst landscapes of southwest China. *Sci. Total. Environ.* **2019**, *650*, 2657–2665. [CrossRef]
39. Deng, L.; Kim, D.; Peng, C.; Shanguan, Z. Controls of soil and aggregate-associated organic carbon variations following natural vegetation restoration on the Loess Plateau in China. *Land Degrad. Dev.* **2018**, *29*, 3974–3984. [CrossRef]
40. Six, J.; Bossuyt, H.; Degryze, S.; Denef, K. A history of research on the link between (micro)aggregates, soil biota, and soil organic matter dynamics. *Soil Tillage Res.* **2004**, *79*, 7–31. [CrossRef]
41. Six, J.; Guggenberger, G.; Paustian, K.; Haumaier, L.; Elliott, E.T.; Zech, W. Sources and composition of soil organic matter fractions between and within soil aggregates. *Eur. J. Soil Sci.* **2001**, *52*, 607–618. [CrossRef]
42. Zheng, J.; Zhao, J.; Shi, Z.; Wang, L. Soil aggregates are key factors that regulate erosion-related carbon loss in citrus orchards of southern China: Bare land vs. grass-covered land. *Agric. Ecosyst. Environ.* **2021**, *309*, 107254. [CrossRef]
43. Cheng, H.; Zhou, X.; Dong, R.; Wang, X.; Liu, G.; Li, Q. Priming of soil organic carbon mineralization and its temperature sensitivity in response to vegetation restoration in a karst area of Southwest China. *Sci. Total. Environ.* **2022**, *851 Pt 2*, 158400. [CrossRef]
44. Blagodatskaya, E.; Kuzyakov, Y. Mechanisms of real and apparent priming effects and their dependence on soil microbial biomass and community structure: Critical review. *Biol. Fertil. Soils* **2008**, *45*, 115–131. [CrossRef]
45. Lü, H.; He, H.; Zhao, J.; Zhang, W.; Xie, H.; Hu, G.; Liu, X.; Wu, Y.; Zhang, X. Dynamics of fertilizer-derived organic nitrogen fractions in an arable soil during a growing season. *Plant Soil* **2013**, *373*, 595–607. [CrossRef]

46. Wang, C.; Yang, Q.; Zhang, C.; Zhou, B.; Li, X.; Zhang, X.; Chen, J.; Liu, K. Soil Organic Nitrogen Components and N–Cycling Enzyme Activities Following Vegetation Restoration of Cropland in Danxia Degraded Region. *Forests* **2022**, *13*, 1917. [CrossRef]
47. Liu, R.; Wang, D. Soil C, N, P and K stoichiometry affected by vegetation restoration patterns in the alpine region of the Loess Plateau, Northwest China. *PLoS ONE* **2020**, *15*, e0241859. [CrossRef] [PubMed]
48. Dong, L.; Li, J.; Zhang, Y.; Bing, M.; Liu, Y.; Wu, J.; Hai, X.; Li, A.; Wang, K.; Wu, P.; et al. Effects of vegetation restoration types on soil nutrients and soil erodibility regulated by slope positions on the Loess Plateau. *J. Environ. Manag.* **2022**, *302 Pt A*, 113985. [CrossRef]
49. Bast, A.; Wilcke, W.; Graf, F.; Lüscher, P.; Gärtner, H. The use of mycorrhiza for eco-engineering measures in steep alpine environments: Effects on soil aggregate formation and fine-root development. *Earth Surf. Process. Landf.* **2014**, *39*, 1753–1763. [CrossRef]
50. Rillig, M.C.; Aguilar-Trigueros, C.A.; Bergmann, J.; Verbruggen, E.; Veresoglou, S.D.; Lehmann, A. Plant root and mycorrhizal fungal traits for understanding soil aggregation. *New Phytol.* **2015**, *205*, 1385–1388. [CrossRef]
51. Lázaro-González, A.; Andivia, E.; Hampe, A.; Hasegawa, S.; Marzano, R.; Santos, A.M.; Castro, J.; Leverkus, A.B. Revegetation through seeding or planting: A worldwide systematic map. *J. Environ. Manag.* **2023**, *337*, 117713. [CrossRef]
52. Feng, Q.; Zhao, W.; Wang, J.; Zhang, X.; Zhao, M.; Zhong, L.; Liu, Y.; Fang, X. Effects of Different Land-Use Types on Soil Erosion Under Natural Rainfall in the Loess Plateau, China. *Pedosphere* **2016**, *26*, 243–256. [CrossRef]
53. Xiao, T.; Li, P.; Fei, W.; Wang, J. Effects of vegetation roots on the structure and hydraulic properties of soils: A perspective review. *Sci. Total. Environ.* **2023**, *906*, 167524. [CrossRef]

Disclaimer/Publisher’s Note: The statements, opinions and data contained in all publications are solely those of the individual author(s) and contributor(s) and not of MDPI and/or the editor(s). MDPI and/or the editor(s) disclaim responsibility for any injury to people or property resulting from any ideas, methods, instructions or products referred to in the content.

Article

Co-Management Effects on Forest Restoration in Protected Areas of Bangladesh: A Remote Sensing and GIS-Based Analysis

Md Rezaul Karim ^{1,*}, Md Abdul Halim ^{1,†}, Imrul Kayes ¹, Wenxi Liao ¹, Sharif A. Mukul ^{2,3,4,*}, H. M. Tuihedur Rahman ⁵ and Sean C. Thomas ¹

¹ Institute of Forestry and Conservation, John H. Daniels Faculty of Architecture, Landscape, and Design, University of Toronto, 33 Willcocks Street, Toronto, ON M5S 3B3, Canada; abdul.halim@mail.utoronto.ca (M.A.H.); imrul.kayes@mail.utoronto.ca (I.K.); wenxi.liao@mail.utoronto.ca (W.L.); sc.thomas@utoronto.ca (S.C.T.)

² Department of Environment and Development Studies, United International University, Dhaka 1212, Bangladesh

³ Tropical Forests and People Research Centre, University of the Sunshine Coast, Maroochydore DC, QLD 4556, Australia

⁴ Department of Earth and Environment, Florida International University, Miami, FL 33199, USA

⁵ Department of Agricultural and Resource Economics, University of Saskatchewan, 51 Campus Dr, Saskatoon, SK S7N 5A8, Canada; ucd269@mail.usask.ca

* Correspondence: rezaul.karim@mail.utoronto.ca (M.R.K.); smukul@usc.edu.au (S.A.M.)

† These authors contributed equally to this work.

Abstract: Co-management is a promising forest governance strategy that integrates local communities' traditional rights and forest dependencies while aiming to improve forest cover and ecosystem health. Bangladesh, facing high deforestation rates and limited per capita forest area, has implemented co-management initiatives since 2003 to restore forest cover and support the livelihoods of forest-dependent communities. While the socio-economic impacts of co-management are well studied, its effects on forest cover remain underexplored. This study addresses that gap by using three common spectral vegetation indices (NDVI, EVI, and MSAVI), calculated from Landsat 7 data, to analyze forest cover changes in five major protected areas under co-management. The results indicated that dense forest cover (41–71%) was initially prevalent in these areas, but a significant decline occurred between 2004 and 2015, with slope values ranging from -3.7 to -0.96 . In contrast, the non-co-managed control site exhibited a much smaller decline (slope: -0.48 to -0.62) across all indices. Notable increases in agricultural land and forest–agriculture mosaics were also observed in the protected areas under co-management. Global Forest Watch data further confirmed substantial forest cover loss, particularly in CWS (158.77 ha) and SNP (0.49 ha). These findings highlight the need to reassess co-management strategies to address ongoing forest degradation.

Keywords: co-management; protected area; vegetation cover; vegetation indices; tropical forest; Bangladesh

Citation: Karim, M.R.; Halim, M.A.; Kayes, I.; Liao, W.; Mukul, S.A.; Rahman, H.M.T.; Thomas, S.C. Co-Management Effects on Forest Restoration in Protected Areas of Bangladesh: A Remote Sensing and GIS-Based Analysis. *Land* **2024**, *13*, 1709. <https://doi.org/10.3390/land13101709>

Academic Editors: Le Yu, Jianye Li, Weida Gao, Wei Hu, Qiang Chen and Xingyi Zhang

Received: 13 August 2024

Revised: 4 October 2024

Accepted: 16 October 2024

Published: 18 October 2024



Copyright: © 2024 by the authors. Licensee MDPI, Basel, Switzerland. This article is an open access article distributed under the terms and conditions of the Creative Commons Attribution (CC BY) license (<https://creativecommons.org/licenses/by/4.0/>).

1. Introduction

Forest ecosystems require innovative and sustainable management approaches to maintain their social, economic, and environmental functions [1]. The growing dependency on forest resources necessitates shared responsibilities among stakeholders, including forest resource users and decision-makers, for sustainable forest management [2]. In recent years, influential actors such as governments and international donors have promoted forest management models that involve resource users and other stakeholders in forest conservation efforts [3].

Co-management, which distributes roles, responsibilities, authority, and entitlements among government and non-government actors, aims to conserve and restore forest ecosystems while supporting the livelihoods of forest-dependent communities [4]. By

fostering partnerships between forest-dependent communities and government actors, co-management integrates the social, political, cultural, economic, and environmental factors contributing to forest destruction and resource inequality [5]. It also facilitates knowledge exchange between local communities and government actors for informed decision-making and awareness of forest conservation challenges and opportunities [6]. While several studies [7–9] have examined the socio-economic and environmental components of co-management, fewer [10,11] have addressed its effects on forest cover, particularly in developing countries.

The efficacy of co-management in conserving forest cover and biodiversity varies globally. In countries like Ethiopia [12], Malawi [13], Honduras [14], and Nepal [14,15], co-management has proven effective, while in the Miombo woodlands of Malawi [16] and in Haui Lu Luang, Thailand [17], it has shown limited success. Studies highlight that co-management works best when local communities are engaged from the planning to implementation stages (e.g., co-management in Nepal) [6]. Since project planning and implementation contexts vary across countries, it is important to evaluate co-management outcomes at a national level to identify best forest management practices that can be replicated globally.

Bangladesh launched its first community forestry project, Betagi-Pomora, in 1979 to address severe deforestation pressure [18]. Despite a nationwide logging ban from 1970 to 1980, the Betagi-Pomora project demonstrated the potential for community involvement in forest restoration and improving local livelihoods [19]. However, legal constraints, including the Bangladesh Forest Act 1927 and the Wildlife Preservation Act 1974, limited the broader adoption of co-management [20]. To address this gap, the Bangladesh Forest Department (BFD) initiated the Nishorgo Support Project (NSP) from 2004 to 2008, funded by the US Agency for International Development (USAID), involving five protected areas: Lawachara National Park (LNP), Satchari National Park (SNP), Rema-Kalenga Wildlife Sanctuary (RKWS), Chunati Wildlife Sanctuary (CWS), and Teknaf Wildlife Sanctuary (TWS) [20]. The NSP aimed to involve local stakeholders in managing and conserving forests and implementing socio-economic programs to reduce forest dependency [21]. The NSP was later expanded to 12 more protected areas under the Integrated Protected Area Co-management (IPAC) project (2007–2013) [22] with a focus on stakeholder engagement and capacity building [23]. This was further extended to 21 protected areas under the Climate-Resilient Ecosystems and Livelihoods (CREL) project (2013–2018) [24]. Later, co-management was expanded to a total of 38 protected areas under the Sustainable Forests and Livelihoods (SUFAL) (2018–2023) and Bangladesh Ecosystems Activity (2021–2026) projects [25]. Thus, we are not considering the CREL and SUFAL timeframe (2016–2024) in the present study because our main goals involve the initial five protected areas.

Despite these efforts, understanding the national success of co-management is challenging due to varying management goals and the implementation context of the projects across different socio-ecological zones. Previous studies have predominantly assessed the socio-economic impacts of co-management [8,26], with limited focus on forest restoration outcomes. To bridge this knowledge gap, this study uses ‘forest cover change’ as a proxy of forest restoration for evaluating the effectiveness of co-management [27] in the five protected areas where the NSP started in 2004 using remote sensing and GIS techniques.

Assessing the impact of co-management on vegetation cover change through remote sensing and GIS techniques requires methodological rigor. Many previous studies mostly relied on Landsat 5–8 [12,14,28] and Sentinel [29] data to generate land-use maps or spectral vegetation indices. However, the discontinuation of Landsat 5 in 2013 and the Landsat 7 scan-line corrector (SLC) failure in 2003 complicated the creation of continuous time series prior to Landsat 8’s launch in 2013. Studies that combine data from Landsat 5, 7, and 8 without cross-calibration [12,29] may introduce biases in vegetation cover estimates [30]. The use of land-use maps derived from individual bands can be misleading in heterogeneous vegetation canopies without proper ground-truthing [31]. Spectral vegetation indices, such as the widely used NDVI [12,17], are generally more reliable than land-use

maps for assessing vegetation cover change [32] but are sensitive to atmospheric conditions and background soil moisture conditions [31]. Combining multiple vegetation indices can effectively mitigate this issue and improve accuracy [31,32]. Some studies have used MODIS (~1 km resolution) images for vegetation cover change detection [17], but its coarse spatial resolution limits the detection of small-scale changes. Therefore, employing a more robust method is essential for accurately evaluating the impact of co-management on forest cover.

Previous studies [8,33] on co-management in Bangladesh suffer from the methodological shortcomings discussed above, potentially leading to unreliable outcomes. For example, Islam et al. [8] observed an overall improvement in forest cover in CWS under co-management, while Islam et al. (2016) [34] reported rapid forest cover loss in the same forest. Similarly, no significant forest cover change was observed in LNP and TWS by Islam et al. [8], whereas Ahmed et al. [35], observed negative trends in LNP, SNP, and RKWS. However, no comprehensive study has explored the spatial and temporal forest cover change across all five protected areas (LNP, SNP, RKWS, CWS, and TWS) during the NSP-IPAC project period (2004–2013) or compared these changes to non-co-managed protected areas.

A comprehensive evaluation of the impact of co-management on forest cover is essential to determine the effectiveness of this approach in Bangladesh. This study addresses this need by assessing forest cover changes in five protected areas (SNP, LNP, RKWS, CWS, and TWS) under co-management compared to a non-co-managed control site, Rajkandi Reserve Forest (RRF). Using Landsat 7 imagery (2003–2015) and multiple spectral vegetation indices (NDVI, EVI, and MSAVI), this study aims to assess whether co-management schemes have positively influenced forest cover. The findings may help guide decision-makers in refining site-specific co-management practices.

2. Materials and Methods

2.1. Description of the Five Study Protected Areas

Teknaf Wildlife Sanctuary (TWS), with an area of 11,615 ha (Figure 1), includes 115 small villages with varying degrees of forest dependency [36]. TWS is dominated by evergreen trees with a total of 535 species, of which 178 are herbs, 110 are shrubs, 150 are trees, 87 are climbers, and 10 are epiphytes [36]. The Asian elephant (*Elephas maximus*) is an important species of conservation at TWS. The sanctuary area has a moist subtropical climate (temperature: 15–32 °C) with frequent and heavy rainfall (130–940 mm) during the monsoon season (May to October) [37]. In 2006, a total of eight co-management committees covering 48 villages around the TWS were formed.

Rema Kalenga Wildlife Sanctuary (RKWS) has an area of 1095 ha (Figure 1). The sanctuary includes 45 villages with 24,000 inhabitants with a diverse range of dependency on forest resources [38]. The forest hosts a rich biodiversity, comprising 634 plant species, 167 bird species, 7 amphibian species, 18 reptile species, and 37 mammal species. Endangered primates such as *Hoolock hoolock* and *Trachypithecus phayrei* are found in the sanctuary [39]. The region exhibits a moist tropical climate, with an average annual rainfall of 4162 mm and temperatures ranging from 9.6 °C to 34.8 °C [39]. Management of the RKWS sanctuary is overseen by a co-management council and committee focused on conserving forest resources and landscape integrity while promoting alternative income sources to reduce local dependence on forest resources [21].

Satchari National Park (SNP) has an area of 243 ha (Figure 1). There are 73 villages in and around SNP with various degrees of involvement of local communities with the park [26]. Vegetation of the SNP is evergreen, with 200 ha of “natural” forest and the rest with secondary vegetation and planted forest. The national park is critical for protecting globally threatened mammals like the Western hoolock gibbon (*Hylobates hoolock*), capped langur (*Trachypithecus pileatus*), and Phayre’s leaf monkey (*Trachypithecus phayrei*) [26]. The average annual rainfall in this area is 4162 mm, and temperatures usually range from 12 °C to 32 °C [40]. Co-management at SNP comprises a co-management council, co-management

committee, people's forum, village conservation forums, community patrol groups, and forest conservation clubs/youth clubs [26].

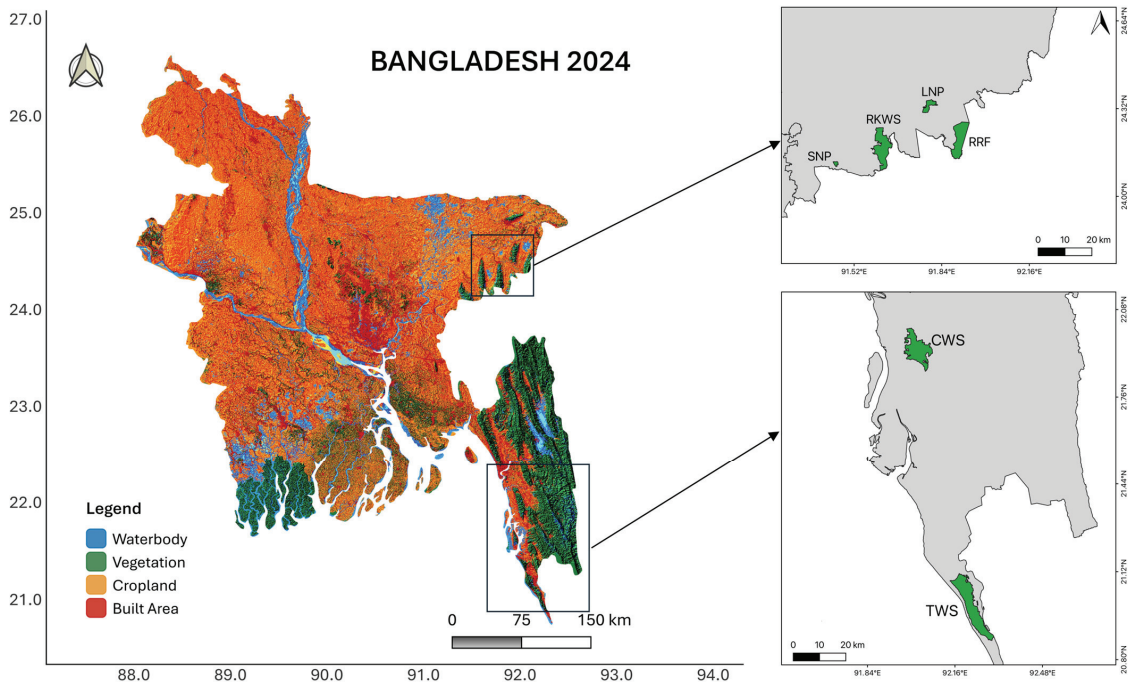


Figure 1. Map of the study areas. Here, TWS = Teknaf Wildlife Sanctuary, RKWS = Rema-Kalenga Wildlife Sanctuary, SNP = Satchari National Park, LNP = Lawachara National Park, CWS = Chunati Wildlife Sanctuary, and RRF = Rajkandi Reserve Forest. The left figure shows the relative position of the study areas within the Bangladesh context. The land-use map is generated from true color band composite (B4, B3, B2) of Sentinel-2A images of October/November 2024.

Lawachara National Park (LNP) was declared a protected forest in 1996 with an area of 1250 ha (Figure 1). There are 26 villages, mostly with ethnic community settlements located within the LNP, and the villagers have varying degrees of forest dependence [41]. LNP is a faunal biodiversity hotspot with 26 mammals (including five primates), 246 birds, 4 amphibians, and 6 reptile species [42]. The average air temperature varies between 26.8 °C (February) and 36.1 °C (June). The annual average rainfall of this area is ~4000 mm, with maximum rainfall from June to September [43]. In 2005, the LNP formed a co-management committee involving members from the local grassroots to administrative level to create alternative income opportunities to reduce the forest dependency of local people.

Chunati Wildlife Sanctuary (CWS) has a hilly to mountainous physiography and an area of 7764 ha (Figure 1) [44]. The climate of CWS is typically subtropical, with an average annual rainfall of 2493 mm, and the average temperature varies from 25.7 °C in January to 32.5 °C in May [22]. There are 60 villages in and around the CWS with various degrees of dependency on forest resource collection and betel leaf (*Piper betel*) cultivation [8]. The forest comprises 890 ha bush, 84 ha garjan (*Dipterocarpus* spp.), 13 ha small crown high forest, 11 ha open, 1458 ha plantation, 2761 scattered forest area, and 9 ha water bodies. CWS is one of the most important protected areas of Bangladesh as it is an important habitat of globally threatened Asian elephants (*Elephas maximus*). Co-management activities were implemented under two co-management committees to reduce over-exploitation and increase forest cover [8].

Rajkandi Reserve Forest (RRF) in north-eastern Bangladesh ($24^{\circ}15'0''$ N, $91^{\circ}55'0''$ E) spans 5295.55 ha with medium to steep slopes and water streams (Figure 1). As this forest has not been under co-management but falls within the same eco-region, we considered RRF as a control site. The brown, sandy clay loam to clay loam soils of RRF support a diverse forest ecosystem that includes a total of 549 angiosperm species across 123 families [45]. RRF experiences warm, humid weather, with temperatures averaging 27°C in February and reaching up to 36°C in June. High humidity prevails, ranging from 74% in March to 89% in July. Annual rainfall averages 4000 mm, peaking during the southwest monsoon from June to September [45].

2.2. Satellite Image Collection and Processing

Given that the projects with core co-management objectives were implemented between 2004 and 2013, other projects, such as SUFAL (2016–2024), which had different objectives, were excluded from this analysis. For the purposes of this study, 2003 was selected as the baseline year, with 2015 designated as the endpoint for assessing the co-management effects on forest cover restoration.

2.2.1. Base Map Collection

The base maps for the six protected areas (LNP, SNP, RKWS, TWS, CWS, and RRF) were collected from the Nishorgo Support Project reports. These maps include boundary, mouza, and Upazila maps [46]. Shapefiles of these protected areas were collected from the World Database of Protected Areas [47].

2.2.2. Acquisition of Long-Term Satellite Image

Since our temporal window of interest spans from 2003 to 2015, we initially considered using Landsat 5, 7, and 8 for data acquisition. However, their respective operational periods—Landsat 5 (1984–2013) and Landsat 8 (2013–present)—did not fully align with the study timeframe. Consequently, Landsat 7 was selected as the optimal choice to ensure continuous data availability throughout the period of interest.

The Landsat 7 ETM+ satellite data from 2003 to 2015 for the six protected areas were downloaded from the United States Geological Survey (USGS) official website (<https://earthexplorer.usgs.gov>; accessed on 5 March 2022). All the downloaded images had a spatial resolution of $30\text{ m} \times 30\text{ m}$ and a cloud cover of less than 20%. A total of 1105 images were downloaded for the six study areas (406 for TWS, 207 for SNP, 164 for RKWS, 99 for LNP, 112 for CWS, and 117 for RRF) from 2003–2015. For each study site in each year, we considered images from winter (November–February), summer (March–June), and rainy (July–October) seasons to accommodate seasonal changes that can induce strong differences in vegetated scenes [48]. Landsat 7 data used for this study were standard Level-2 terrain-corrected (L2T) products that are already radiometrically adjusted and atmospherically corrected [49,50]. Through the LEDAPS project, the digital number values were finally converted to surface reflectance values [51].

2.2.3. Filtering the Bad-Quality Pixels

Filtering bad pixels is important for time series analysis, particularly with vegetation indices. If, for example, bad pixels are included in a phenology study, the results might not show the true surface characteristics of seasonal vegetation growth [52]. Cloud-contaminated pixels can lower the indices' values and measurements; for example, the timings of 'green up' or peak maturity will appear later than they occurred [53]. A quality assessment (QA) band is included with each Landsat 7 image to filter affected pixels. QA bits enhance the reliability of Landsat-derived analyses by identifying pixels potentially impacted by surface conditions, cloud contamination, or sensor issues [54]. The pixel values in the Level-2 QA band were converted into 16-bit binary form before use, and a criteria table was developed (Table S1) to filter out the bad-quality pixels.

2.2.4. Scan Line Error (SLC) Correction

Landsat 7 enhanced thematic mapper (ETM+) sensor had a failure of the scan line corrector (SLC) on 31 May 2003, resulting in images with wedge-shaped gaps on both sides of each scene. Scaramuzza et al. [55] developed a technique that can fill gaps in one scene with data from the nearest (same season) Landsat 7 scene. On an array of good-quality pixels, a linear transform is applied to the ‘filling’ image to adjust it based on the standard deviation and mean values of each band of each scene. We implemented this algorithm using the ENVI 5.3. The ENVI plugin ‘landsat_gapfill.sav’ [56] performs this correction by utilizing a secondary image from the same season (with minimal cloud cover) as a reference. A linear transformation is applied to the reference image to adjust its mean and standard deviation for each band, ensuring compatibility with the SLC-off image. This process effectively fills the missing data, restoring the image for further analysis [57] (Figure 2).

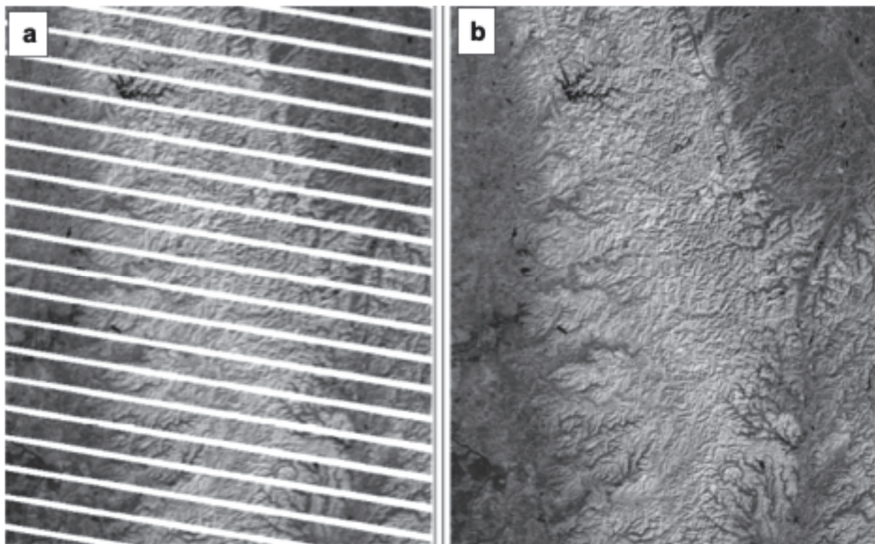


Figure 2. (a) Landsat 7 image (path 136 row 35) with SLC failure (9 November 2008) (b) SLC-corrected images through the nearest Landsat images (25 November 2008) using [56] algorithm.

2.3. Calculation of Spectral Vegetation Indices

Before finalizing the approach for determining forest cover change, we evaluated both pixel-based classification (PBC) and object-based classification (OBC) methods. While OBC can offer advantages in certain contexts, its performance is highly dependent on the segmentation scale and the availability of high-resolution imagery. Given that our study site contains numerous small and highly fragmented areas, we opted for PBC, as it allowed us to classify each pixel individually, minimizing the risk of over- or under-segmentation errors [58].

In PBC approach, several spectral vegetation indices have been proposed for the enhancement and extraction of vegetation information from satellite images. In this study, we used the most common indices such as vegetation index (NDVI), enhanced vegetation index (EVI), soil-adjusted vegetation index (SAVI), and modified soil-adjusted vegetation index (MSAVI) [59]. Using the surface reflectance values, NDVI was calculated as Equation (1):

$$\text{NDVI} = \frac{\text{NIR} - \text{R}}{\text{NIR} + \text{R}} \quad (1)$$

where NIR and R represent surface reflectance in near-infrared and red bands.

EVI was calculated as Equation (2):

$$EVI = G \frac{NIR - R}{NIR + C_1R - C_2B + L} \quad (2)$$

where, NIR, R, and B represent the surface reflectance in the near-infrared, red, and blue bands, respectively. G is the gain factor, while C1 and C2 are aerosol scattering correction coefficients for the red band, using the blue band. L is the soil adjustment factor [60]. In this study, G = 2.5, C1 = 6.0, C2 = 7.5, and L = 1 were applied [59].

SAVI is employed to correct NDVI for soil brightness effects in areas with low vegetation cover. SAVI, derived from Landsat surface reflectance, is calculated as the ratio between R and NIR values, incorporating a soil brightness correction factor (L), set to 0.5 to account for most land cover types [61]:

$$SAVI = \frac{NIR - R}{NIR + R + L} \times (1 + L) \quad (3)$$

The MSAVI minimizes the effect of bare soil on the SAVI. It is calculated as Equation (4), a ratio between the R and NIR values with an inductive L function applied to maximize the reduction of soil effects on the vegetation signal [59]:

$$MSAVI = 2 \times \rho_{NIR} + 1 - \frac{\sqrt{(2\rho_{NIR} + 1)^2 - 8(\rho_{NIR} - \rho_{RED})}}{2} \quad (4)$$

Here, ρ represents the atmospherically corrected surface reflectance in a particular band, while L is the canopy background adjustment factor, accounting for nonlinear radiant transfer of NIR and R through the canopy. At higher vegetation (NDVI > 0.6), this L factor value was considered 0 and in medium to lower vegetation cover (NDVI < 0.6) it was 0.5 [62].

For each year and study area, we had at least one image per season, resulting in at least three vegetation index rasters annually. Prior to trend analysis, we calculated multi-season composite images using the median value of each pixel, rather than the mean, to minimize the influence of outliers and extreme seasonal or atmospheric variations. This approach ensured a more robust representation of long-term trends.

Using the annual composite spectral vegetation rasters, we analyzed the net change in vegetation indices relative to the base year of 2003. First, we subtracted the vegetation index rasters from 2004 to 2015 from the 2003 base raster, generating new rasters with pixel values indicating either an increase (positive) or decrease (negative) in vegetation indices compared to 2003. Second, we calculated the net change (%) annually using Equation (5), which considered the area:

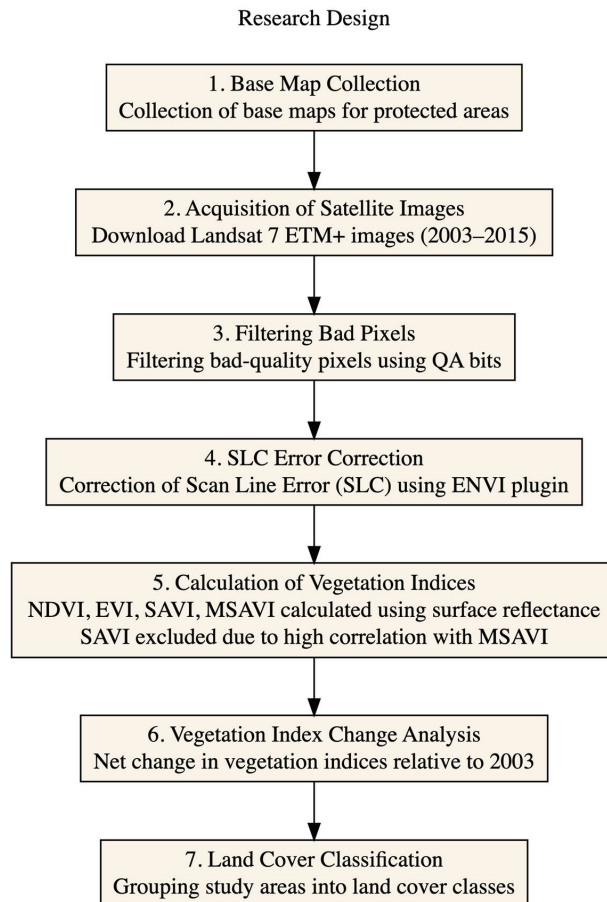
$$\text{Net change (\%)} = \frac{\text{positive change pixel number} - \text{Negative change pixel number}}{\text{Total pixel number}} \times 100 \quad (5)$$

2.4. Land Cover Classification

Although we initially considered NDVI, MSAVI, SAVI, and EVI for analyzing forest cover change, SAVI was excluded due to its high correlation with MSAVI ($r = 0.9$, $p = 0.01$). Using spectral vegetation indices derived from Landsat 7 ETM+ satellite images, we classified each protected area into one of five land-use and land-cover (LULC) types: (a) barren, waterbodies, and built-up areas; (b) agriculture; (c) a mix of agriculture and forest; (d) dense forest; and (e) highly dense forest. Threshold values for NDVI, MSAVI, and EVI were employed to determine these land use classes. Standard vegetation index thresholds (Table 1) were adapted from the USGS website and refined for our study areas by testing several points against Google Maps imagery from the same year (Figure 3).

Table 1. Adjusted threshold of spectral index values used in this study for LULCC.

Land Use Land Cover Classes	Threshold Value		
	NDVI	EVI	MSAVI
Barren, with waterbodies, and built-up	0–0.19	0–0.14	0–0.19
Agriculture	0.2–0.4	0.15–0.29	0.2–0.3
A mix of agriculture and forest	0.41–0.6	0.3–0.34	0.31–0.41
Dense forest	0.61–0.8	0.35–0.54	0.42–0.65
Highly dense forest	>0.8	>0.55	>0.65

**Figure 3.** Schematic flowchart illustrating the sequence of satellite image processing steps used in this study.

2.5. Statistical Analysis

Satellite image bulk downloading, pre-processing, spectral indices calculations, and statistical analyses were conducted in the R statistical software (version 4.0.3) [63]. To test the significance and the magnitude (increasing or decreasing) of trends in LULC classes in the protected areas of Bangladesh since the initiation of the co-management approach, the Mann–Kendall (M–K) trend test and the Theil–Sen slope estimator were

utilized in this study, respectively. The Mann–Kendall test was conducted using the “Kendall” R-package [64]; slope analysis was done using “Robslopes” R-package [65].

3. Results

The LULC classification based on NDVI, MSAVI, and EVI values indicated that in all six protected areas, the largest proportion of land was covered by dense forests (~41–71%) followed by forest–agriculture mosaic (~19–47%), agriculture (~4–8%), highly dense forests (~0.5–2.2%), and barren-building-waterbody (~0.3–0.4%). The overall pattern in land cover was consistent for the three vegetation indices, but the proportion of land cover classes varied among the protected areas (Table 2 and Figure 4).

Table 2. Summary of Mann–Kendall (M–K) tests and Theil–Sen slopes for land use and land cover (LULC) change trends based on NDVI, MSAVI, and EVI values over the period of 2003 to 2015 for five pilot protected areas in Bangladesh for co-management project.

PAs	LULC Classes	NDVI			MSAVI			EVI		
		Tau	<i>p</i>	Slope	Tau	<i>p</i>	Slope	Tau	<i>p</i>	Slope
Overall	Barren-building-waterbody	−0.38	<0.01	$−2.1 \times 10^{-17}$	−0.25	<0.01	9.8×10^{-16}	−0.29	<0.01	1.05×10^{-16}
	Agriculture	−0.17	0.04	0.01	−0.22	<0.01	0.04	−0.15	0.07	0.09
	Forest–agriculture mosaic	0.13	0.12	2.59	0.37	<0.01	1.00	−0.13	0.10	1.13
	Dense forest	−0.15	0.07	−3.7	−0.28	<0.01	−1.74	0.29	<0.01	−0.96
	Highly dense forest	−0.15	0.08	1.3×10^{-17}	−0.28	<0.01	$−6.9 \times 10^{-2}$	−0.12	0.16	−0.003
CWS	Barren-building-waterbody	−0.02	0.95	0.00	0.38	0.07	0.01	0.05	0.85	0.0009
	Agriculture	0.46	0.03	0.25	0.76	<0.01	0.91	0.48	0.02	0.63
	Forest–agriculture mosaic	0.28	0.20	2.43	0.53	0.01	1.34	0.64	<0.01	2.94
	Dense forest	−0.25	0.24	−2.15	−0.59	<0.01	−1.74	−0.12	0.58	−0.96
	Highly dense forest	−0.66	<0.01	−0.04	−0.82	<0.01	−0.023	−0.28	0.20	−0.009
TWS	Barren-building-waterbody	0.87	<0.01	1.73	0.77	<0.01	0.455	0.30	0.16	0.05
	Agriculture	0.69	<0.01	1.87	0.35	0.09	0.57	0.74	<0.01	1.39
	Forest–agriculture mosaic	−0.25	0.24	−3.75	0.05	0.85	0.202	0.17	0.42	0.43
	Dense forest	0.07	0.76	0.25	−0.33	0.12	−1.28	−0.43	0.04	−1.11
	Highly dense forest	0.24	0.28	0.002	−0.30	0.19	−0.0007	−0.35	0.09	−0.016

Table 2. Cont.

PAs	LULC Classes	NDVI			MSAVI			EVI		
		Tau	<i>p</i>	Slope	Tau	<i>p</i>	Slope	Tau	<i>p</i>	Slope
LNP	Barren-building-waterbody	1.0	1.0	0.00	−0.14	0.56	0.00	0.19	0.50	0.00
	Agriculture	−0.23	0.31	−0.0006	−0.46	0.03	−0.61	−0.15	0.50	−0.023
	Forest-agriculture mosaic	−0.05	0.854	−0.017	−0.56	<0.01	−4.62	−0.05	0.85	−0.22
	Dense forest	−0.10	0.669	−0.387	0.667	<0.01	6.55	0.05	0.85	0.08
	Highly dense forest	0.38	0.09	0.158	0.49	0.03	0.03	0.20	0.38	0.02
SNP	Barren-building-waterbody	−0.32	0.22	0.00	0.09	0.738	0.00	−0.07	0.84	0.00
	Agriculture	0.55	0.01	0.021	−0.19	0.389	−0.12	0.185	0.43	0.00
	Forest-agriculture mosaic	0.53	0.01	2.53	0.64	<0.01	3.62	0.41	0.05	1.70
	Dense forest	−0.61	<0.01	−2.08	−0.69	<0.01	−3.64	−0.48	0.02	−1.78
	Highly dense forest	−0.05	0.86	0.00	−0.05	0.86	0.00	−0.37	0.10	−0.023
RKWS	Barren-building-waterbody	−0.02	1.0	0.00	−0.14	0.54	−0.003	−0.25	0.27	−0.0002
	Agriculture	−0.23	0.29	−0.01	0.33	0.12	0.47	−0.20	0.36	−0.23
	Forest-agriculture mosaic	0.61	<0.01	5.42	0.53	0.01	3.92	0.43	0.04	1.14
	Dense forest	−0.53	0.01	−4.58	−0.48	0.02	−4.27	−0.33	0.12	−0.62
	Highly dense forest	0.07	0.79	0.00	−0.13	0.61	0.00	0.20	0.38	0.006
RRF	Barren-building-waterbody	0.008	0.92	0.024	0.05	0.51	0.02	0.01	0.87	0.02
	Agriculture	0.14	0.08	1.35	0.11	0.16	1.02	0.15	0.05	0.99
	Forest-agriculture mosaic	0.23	<0.01	2.44	0.14	0.07	2.22	0.29	<0.001	2.09
	Dense forest	−0.32	<0.001	−2.88	−0.20	0.01	−2.63	−0.21	<0.01	−2.36
	Highly dense forest	−0.05	0.55	−0.47	−0.11	0.20	−0.46	−0.13	0.09	−0.52

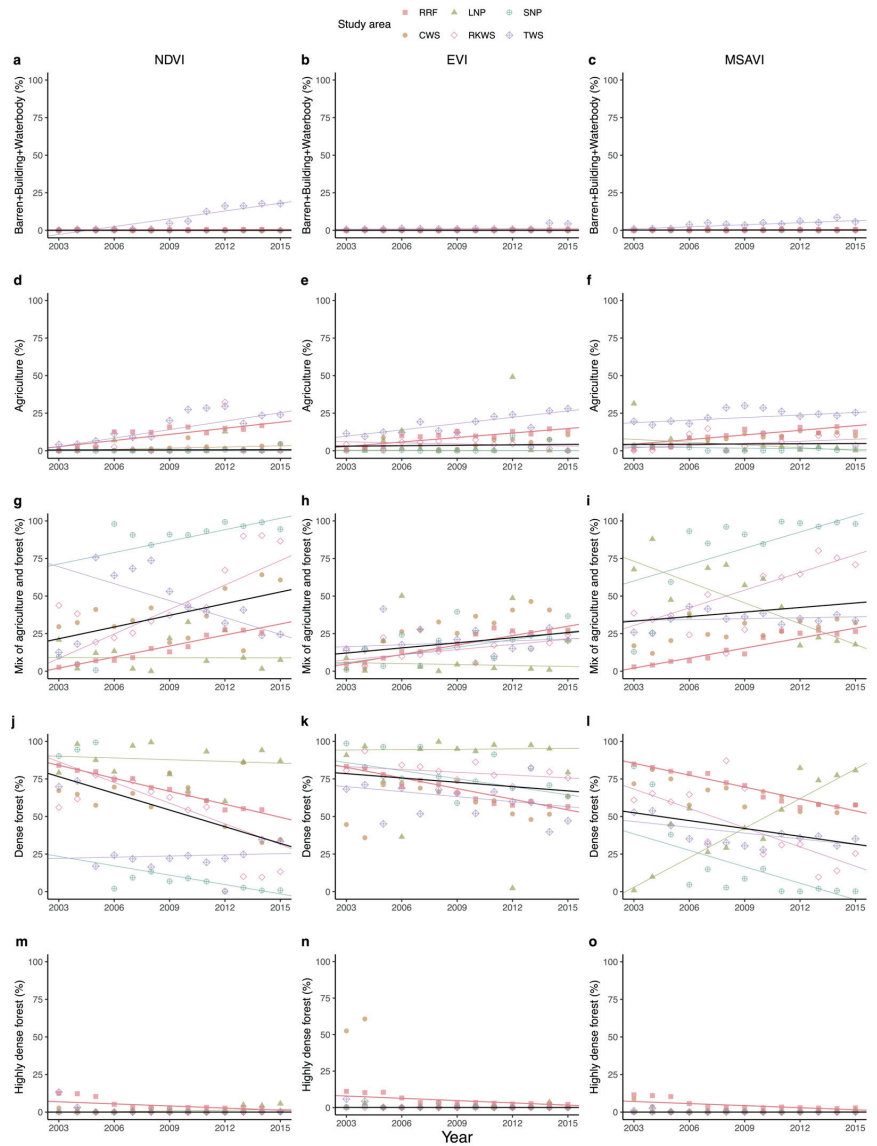


Figure 4. Theil–Sen LULC change trends in five co-managed protected areas in Bangladesh over time (2003–2015) based on NDVI, MSAVI, and EVI. Black solid lines indicate overall trends, while colored lines indicate corresponding protected areas, including CWS (Chunati Wildlife Sanctuary), LNP (Lawachara National Park), RKWS (Rema-Kalenga Wildlife Sanctuary), SNP (Satchari National Park), TWS (Teknaf Wildlife Sanctuary), and one non-co-managed area Rajkandi Reserve Forest (RRF) as control site.

3.1. Overall Trend of Land Cover Change in the Six Study Areas over the Co-Management Period

The Mann–Kendall (M–K) test was used to assess significance, and the Theil–Sen test was applied for slope estimation. Our overall results indicated that the proportion of dense forest decreased significantly (MSAVI and EVI: $p < 0.01$; NDVI: $p = 0.07$) over the co-management period in the five protected areas, with higher slopes (−3.7 to −0.96) compared to other land cover classes. RRF showed similarly large decreases in

dense forest areas in non-co-managed areas, with NDVI, EVI, and MSAVI ranging between -2.88 to -2.36 ($p < 0.01$) for slopes. Conversely, both agriculture and forest-agriculture mosaic land cover classes increased significantly, with agriculture having lower slope values (0.01 – 0.09 , $p < 0.05$) than those of the forest-agriculture mosaic (1 – 2.53 ; MSAVI: $p < 0.01$) in co-management sites. On the other hand, highly dense forest and barren-building-waterbody land cover classes remained unchanged with fluctuating (positive/negative) but extremely low slope values. For the highly dense forest cover class, the slope values ranged from -6.9×10^{-2} to 1.3×10^{-17} , and for the barren-building-waterbody classes, slope values ranged from 9.8×10^{-16} to -2.1×10^{-17} (see Table 1 and Figure 4). In the control site RRF, the barren-building-waterbody class showed minimal change with non-significant slope values (NDVI: 0.024, MSAVI: 0.05, EVI: 0.02). Agriculture exhibited a positive trend with significant slope values (NDVI: 1.35, MSAVI: 1.02, EVI: 0.99). The forest-agriculture mosaic displayed significant growth with highly significant slope values (NDVI: 2.44, MSAVI: 2.22, EVI: 2.09). Dense forests experienced a significant decline ($p < 0.001$) in slope values (NDVI: -2.88 , MSAVI: -2.63 , EVI: -2.36). Highly dense forest showed non-significant trends (NDVI: -0.47 , MSAVI: -0.11 , EVI: -0.13) with p -values ranging from 0.55 to 0.20, indicating stability in this land cover class within the RRF.

3.2. Protected Area-Specific Trends in Land Cover Change during the Co-Management Period

Our analysis showed a highly variable land cover change among the protected areas during the co-management period. The proportion of dense forest declined with time in the SNP, TWS, RKWS, and CWS while increasing in LNP. On the other hand, the proportion of agriculture and forest-agriculture mosaic increased in the SNP, TWS, RKWS, and CWS while declining in LNP. The patterns of the highly dense forest and barren-building-waterbody classes were similar across the protected areas during the study period.

Although the dense forest cover was dominant, the proportion of dense forest in SNP declined significantly [NDVI slope: -2.08 ($p < 0.01$); MSAVI: -3.64 ($p < 0.01$); EVI: -1.78 ($p = 0.02$)] from $\sim 90\%$ to 0.5 – 1% (Figure 4d,i,n). The largest decline slope in dense forest cover was observed in RKWS [NDVI slope: -4.58 ($p < 0.01$); MSAVI slope: -4.27 ($p < 0.05$)]. Similarly, in CWS [EVI slope: -1.11 ($p < 0.05$)] and TWS [EVI slope: -1.11 ($p < 0.05$)], the proportion of dense forest cover declined significantly. The proportion of dense forests in CWS, as indicated by NDVI, decreased from $\sim 70\%$ in 2003 to $\sim 34.5\%$ in 2015. The MSAVI and EVI also showed similar decreasing trends of dense forest cover with slightly different magnitudes in TWS throughout the period. Unlike other protected areas, in LNP, there was a significant increase [MSAVI slope: 6.55 ($p < 0.01$)] in the dense forest from $\sim 1\%$ (in 2003) to $\sim 80\%$ (in 2015); however, non-significant trends were found in NDVI and EVI (see Table 2).

Similarly, the forest-agriculture mosaic in SNP increased significantly (Table 2) from 10 – 17% in 2003 to 94.5 – 98% in 2015 (see Figure 4c,h,m). A similar pattern was also observed for the forest-agriculture mosaic in RKWS [NDVI slope: 5.42 ($p < 0.01$); MSAVI slope: 3.92 ($p = 0.01$); EVI slope: 1.14 ($p = 0.04$)] throughout the co-management period (Figure 4c,h,m), with a decreasing trend in the first few years and then increasing to reach ~ 80 – 90% cover. The forest-agriculture mosaic in CWS also showed a significant increasing trend [NDVI slope: 2.43 ($p = 0.20$); MSAVI slope: 1.34 ($p = 0.01$); EVI slope: 2.94 ($p < 0.01$)]. In LNP, however, this pattern was the opposite and showed a significant decreasing trend [NDVI slope: -0.017 ($p = 0.85$); MSAVI slope: -4.62 ($p \leq 0.01$); EVI slope: -0.22 ($p = 0.85$)] throughout the study period.

The agriculture land cover in SNP increased slightly from 0% (2003) to 4.5 – 7.5% (2015) with a slope ranging from -0.12 to 0.02 and was only significant (Table 1) for NDVI-based classification (slope = 0.021 ; $p = 0.01$) (Figure 4b,g,i). Although the overall trend was not significant in RKWS, NDVI-based classification showed that agriculture land cover was below 1% in 2003, increased to $\sim 3\%$ during 2005–2006, decreased to $\sim 1\%$, and remained the same afterward. MSAVI and EVI-based classification also showed a similar pattern for RKWS. In TWS, the agriculture land cover trend showed a significant positive slope with values ranging from 0.57 – 1.87 . Agriculture land cover increased significantly

[NDVI slope: 0.25 ($p = 0.03$); MSAVI slope: 0.91 ($p < 0.01$); EVI slope: 0.63 ($p = 0.02$)] in CWS during the co-management. In 2003, the proportion of agricultural land use accounted for ~4%, ~19%, and 11.5%, while in 2015, they reached ~24%, ~25%, and ~28% based on NDVI, MSAVI, and EVI classifications, respectively. Unlike other protected areas, in LNP, there was a significant decreasing trend in agricultural land cover throughout the study period [NDVI slope: -0.0006 ($p = 0.31$); MSAVI slope: -0.61 ($p = 0.03$); EVI slope: -0.023 ($p = 0.50$)].

There were no significant trends in highly dense forest land cover in SNP in 2003–2015 except a slight temporary gain in 2007–2009 (~2% based on MSAVI) (Figure 4e,j,o) with trend slope values ranging from 0.00–0.023 (Table 1). In CWS, highly dense forest cover decreased significantly with very low slope values [NDVI slope: -0.04 ($p \leq 0.01$); MSAVI slope: -0.02 ($p \leq 0.01$); EVI slope: -0.009 ($p = 0.20$)]. The proportion of highly dense forest cover in RKWS was below ~1% at the beginning of co-management and remained the same throughout the study period with no significant trend. Likewise, based on both NDVI and EVI, the proportion of highly dense forests in TWS declined from 6–13% (2003) to below ~1% (2015), although the trend was not significant. EVI-based classification showed a marginally significant ($p = 0.09$) decline with a low slope value (-0.016). Unlike other protected areas, a significant increasing trend was observed for highly dense forest cover in LNP from 2003 (0%) to 2015 (~5.5%) based on MSAVI (slope = 0.03, $p = 0.03$), while the NDVI-based trend (slope = 0.158, $p = 0.09$) was marginally significant.

Moreover, no trend was observed for the proportion of the barren-building-waterbody class over time in SNP, CWS, LNP, and RKWS, which was below ~1% at the inception of the co-management approach in 2004 and remained the same throughout the study period based on all spectral indices (Table 2; Figure 4a,f,k). In contrast, in TWS, this land cover class increased significantly [NDVI slope: 1.73 ($p < 0.01$); MSAVI slope: 0.45 ($p < 0.01$)] throughout the study period. The proportion of the barren-building-waterbody class increased from ~1% to ~17.5% (NDVI), ~1% to ~5.5% (MSAVI), and ~1% to ~4.5% (EVI).

In RRF as our control site, our analysis of land cover dynamics revealed distinctive patterns across various classes. The barren-building-waterbody class exhibited minimal changes with non-significant trends (NDVI slope: 0.024, $p = 0.92$; MSAVI slope: 0.02, $p = 0.51$; EVI slope: 0.02, $p = 0.87$) (Table 2, Figure 4a,f,k). Agriculture showed a significant positive trend (NDVI slope: 1.35, $p = 0.08$; MSAVI slope: 1.02, $p = 0.16$; EVI slope: 0.99, $p = 0.05$), indicating an increase over the study period (Table 2, Figure 4b,g,l). The forest-agriculture mosaic experienced substantial growth with highly significant trends across all spectral indices (NDVI slope: 2.44, $p < 0.01$; MSAVI slope: 2.22, $p = 0.07$; EVI slope: 2.09, $p < 0.001$) (Table 2, Figure 4c,h,m). Dense forests exhibited a significant decline (NDVI slope: -2.88 , $p < 0.001$; MSAVI: -2.63 , $p = 0.01$; EVI: -2.36 , $p < 0.01$), indicating a noteworthy reduction in coverage (Table 2, Figure 4d,i,n). Highly dense forest, however, demonstrated non-significant trends (NDVI slope: -0.47 , $p = 0.55$; MSAVI slope: -0.46 , $p = 0.20$; EVI slope: -0.52 , $p = 0.09$) in this land cover class within the RRF (Table 2, Figure 4e,j,o).

3.3. Pixel-to-Pixel Changes of Spectral Indices over Time

The pixel-to-pixel change expressed as the percentage of area change of NDVI, MSAVI, and EVI values to the 2003 pixel values provided detailed dynamics of land cover change in the study areas over the co-management period. Starting from 2004, all study areas showed a similar pattern until 2006, and they diverged during 2011–2012, where CWS and TWS had a net negative change and LNP, SNP, and RKWS had a net positive change in NDVI, MSAVI, and EVI values (Figure 5). After that, the pattern was reversed for all protected areas and turned into a negative change except for TWS. From 2013 onwards, the negative change continued for CWS and SNP, TWS oscillated between positive and negative changes, and LNP and RKWS started to show positive change for the rest of the study period. On the other hand, our non-co-managed protected area RRF exhibited a continuous negative trend from 2003 to 2015.

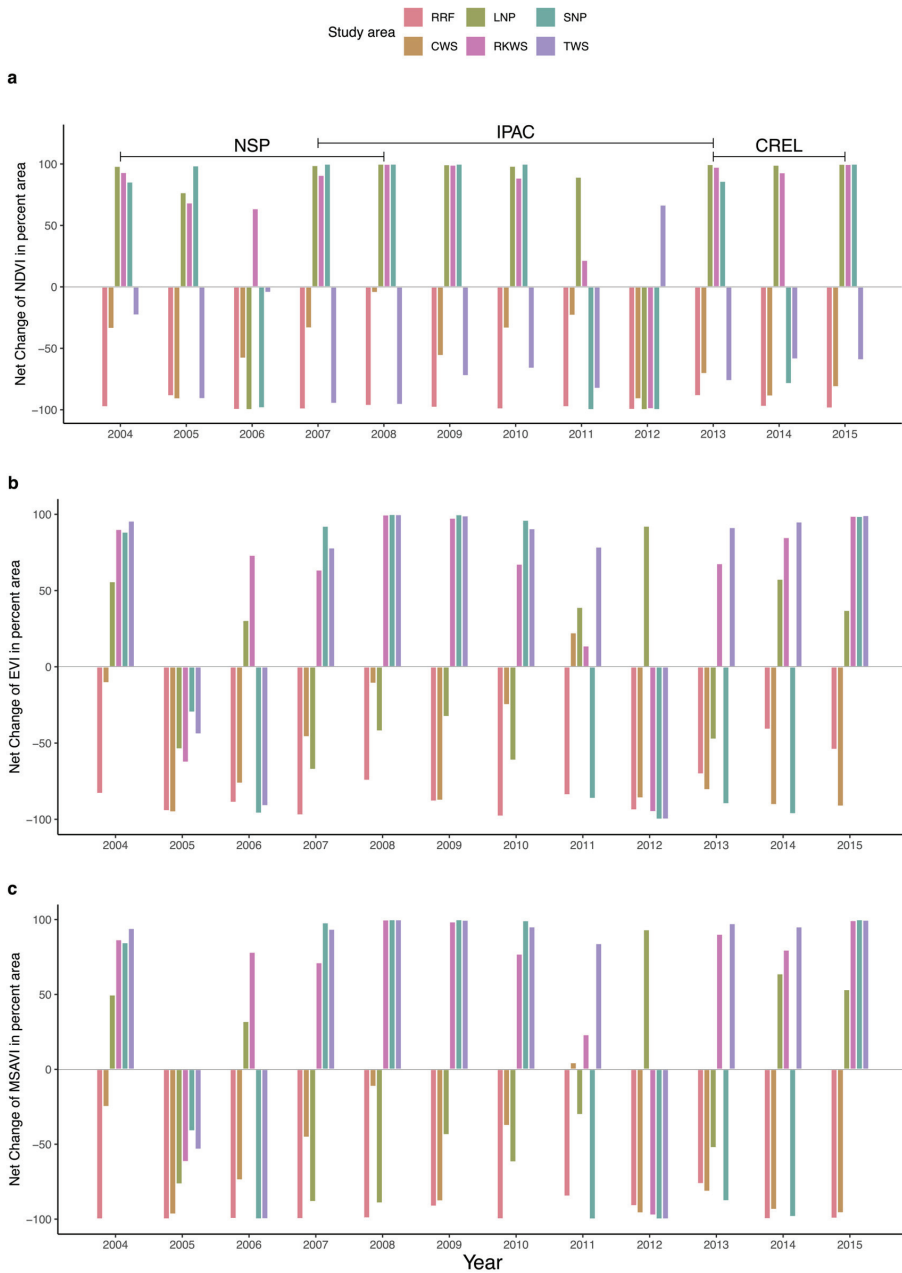


Figure 5. Net change (%) of vegetation indices (NDVI, EVI, and MSAVI) compared to the base year (2003) (Calculated from Equation (5) in the Methods). The NSP co-management project timeline was from 2004 to 2008, the IPAC timeline was from 2007 to 2013, and the CREL projects were from 2013 to 2015.

3.4. Forest Cover Change from Global Forest Watch Data

To support our current analysis, historical forest cover loss (ha/year) for the six protected areas included in this study was retrieved from the Global Forest Watch database to assess the general deforestation trend (2003–2015) in the area (Figure 6). Over 10 years,

the highest total forest cover loss occurred in CWS (158.77 ha), while the lowest was in SNP (0.49 ha). In LNP, the total forest cover loss was estimated to be 15.45 ha throughout 2005–2015 with a peak loss of 5.8 ± 0.44 ha (mean \pm SD) in 2009. In CWS, the peak forest cover loss occurred in 2006 (36.2 ± 1.3 ha), 2009 (24.2 ± 1.3 ha), and 2012 (36 ± 1.7 ha). In RKWS, total forest cover loss over the period was 128.42 ha with a peak loss of 68.6 ± 5.36 ha in 2007. In TWS, a total of 154.42 ha and the highest loss (16.4 ± 1.3 ha) occurred in 2011 (Figure 6). In the control site RRF, the total forest cover loss over the study period amounted to 77.8 ha. The most substantial annual loss occurred in 2006, reaching 48.2 ± 2.17 ha. Notably, 2008 and 2009 witnessed significant losses of 34.6 ± 0.8 ha and 37.2 ± 4.38 ha, respectively (Figure 6).

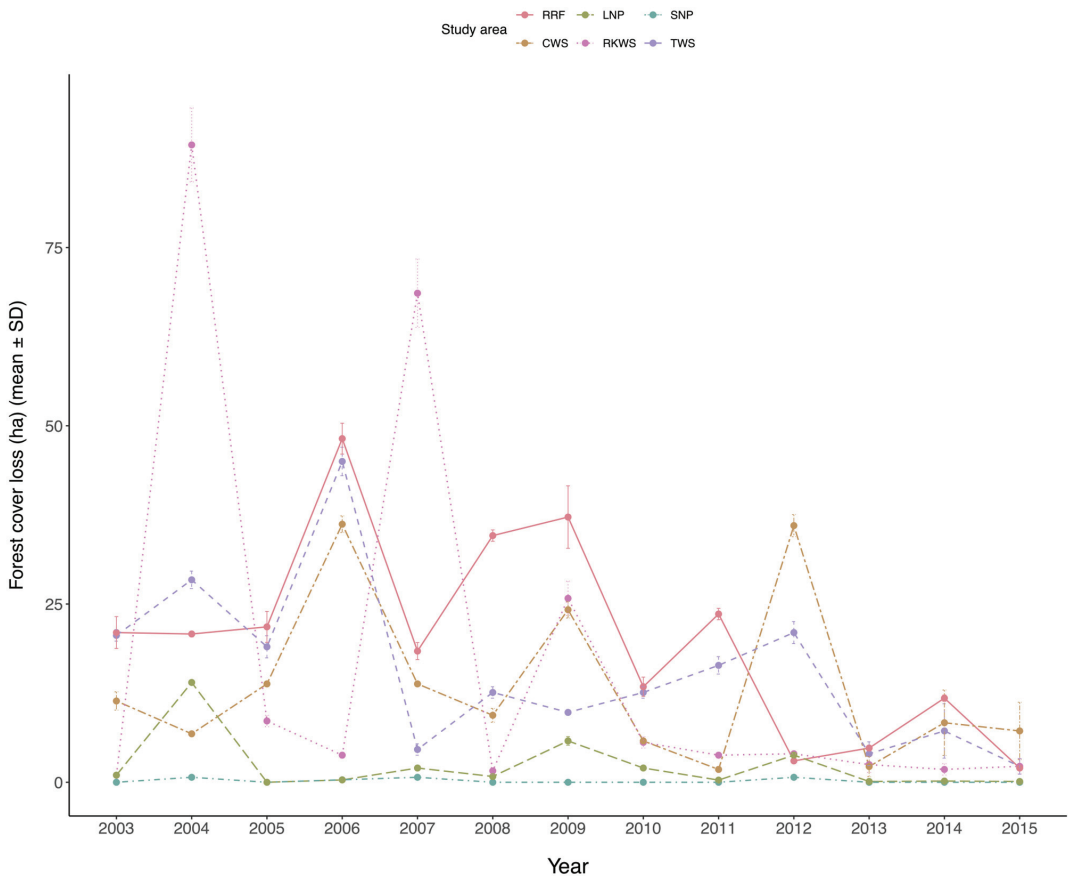


Figure 6. Forest cover loss (ha) from the Global Forest Watch data in six protected areas from 2005 to 2015. Here, RRF = Rajkandi Reserve Forest, CWS = Chunati Wildlife Sanctuary, LNP = Lawachara National Park, RKWS = Rema-Kalenga Wildlife Sanctuary, SNP = Satchari National Park, and TWS = Teknaf Wildlife Sanctuary.

4. Discussion

4.1. Co-Management Reduces Forest Cover in Major Protected Areas of Bangladesh

A decline in dense forest cover was found in SNP, TWS, RKWS, and CWS during the co-management period (2004–2015), with the CWS also showing a significant decrease in highly dense forests (Figure 4). This is consistent with findings from prior studies that reported deforestation during certain co-management periods in the TWS [36], RKWS [66,67], SNP [68], and CWS [33,44,69,70]. One of the major drivers for the reduced forest cover

was the expansion of agricultural land, with the overall increase in agriculture and forest-agriculture mixed land cover being observed for most protected areas (Figure 4; Table 2). High economic return was likely the major motivation for the conversion of forests to agricultural land. With agricultural land, local communities can generate more annual income by growing cash crops with short-term returns, such as betel leaf [33,36]. Due to a similar economic incentive, Islam et al. (2020) [71] found that the co-management approach reduced forest biodiversity because fast-growing, exotic, and valuable timber species were preferred over slow-growing native tree species in tree plantation programs in protected areas.

Urban expansion, forest dependency, and ineffective policy enforcement also play important roles in the decreased forest cover in the protected areas. Land expansion due to increased population may result in land encroachment for human settlement and infrastructure development [36], which require tree removal and land clearance. In addition, local communities and ethnic communities have a high dependency on forests and forest resources [36], which may directly contribute to forest cover loss through activities such as illegal logging and cattle grazing [33]. The high forest dependency of local households may be due to the lack of alternative non-forest income sources, suggesting the necessity of reducing the forest dependency of local people to enhance forest conservation. Studies on RKWS [38] and SNP [26] revealed that the co-management approach shifted strong forest dependency toward alternative income generation activities, which may potentially reduce the loss of forest cover. Ineffective co-management policy enforcement may also contribute to the failure of forest conservation in the protected areas. The different demands and mistrust among different stakeholders and the limited engagement of local communities in decision-making and enforcement processes [36,44] likely resulted in the local communities' fear of losing the forest land and the resources and unwillingness to protect the forests [66]. In addition, since long-term land tenure is not available and the benefits of protecting forests are unclear [22], the incentive for forest protection was weak for local people. Other land cover types, such as barren land, buildings, and waterbodies, were found to gradually increase during the co-management period, being consistent with the increased barren land from 2005–2015 in the study conducted by Islam et al., (2018) [44].

4.2. Co-Management Increases Forest Cover in LNP

In general, the co-management approach has been effective in increasing highly dense and dense forests in LNP during 2004–2015 (see Figure 4; Table 2). The results contradict the findings from Islam et al. (2019) [8] that indicated a decreased forest cover in LNP from 2011–2017 due to illegal logging but are consistent with recent studies [69] that revealed the fluctuating but increasing trend of dense forest cover during the co-management period. The increased dense and highly dense forests were mainly due to the conversion of agricultural and forest-agricultural mixed land into forests, indicated by the significant declines of agricultural and forest-agricultural mosaic land areas (Figure 4; Table 2). Such land cover changes likely resulted from the creation of alternative income-generation activities and reduced forest dependency of local communities in LNP [72,73]. The co-management approach provided alternative income-generating activities, such as training and educational programs, and diverse employment opportunities, such as jobs associated with ecotourism, that generated higher and stable income and/or returns but lower risks relative to intense forest wood extraction and illegal logging, so deforestation activities in the protected areas decreased [72]. The increased forest cover was also likely attributed to the experimental plantation in the LNP by the Bangladesh Forest Research Institute (BFRI) in 2015 [8]. In addition, economic incentives (e.g., paid jobs associated with forest conservation) were provided for forest protection and the close participation and engagement of local households in forest conservation, and decision-making processes were encouraged in the co-management approach in the LNP; thus, forest cover and biodiversity both improved under the co-management practice [69,74]. However, some studies have shown a decreased biodiversity in the LNP during the co-management period due to the establishment of fast-growing valuable timber species (e.g., *Acacia auriculiformis*)

as a monocultural tree plantation [71]. Overall, the involvement of local communities in the co-management has been found to be the key factor in improving the livelihood of the communities from financial, social, physical, natural, and human aspects and enhancing sustainable forest restoration [73,75]. In addition, the moderate to high scores that the forest conservation outcomes received in the survey of local people indicate high satisfaction with the co-management practices [76]. This indicates the importance of inclusion and/or enforcement of indigenous and mixed-species plantations in reforestation practice in future co-management plans.

4.3. Co-Management Impact on Total Vegetation Cover in the Five Pilot Protected Areas

Co-management had varying effects on total vegetation cover across the five pilot protected areas. Specifically, vegetation cover increased in LNP, SNP, and RKWS, while declines were observed in CWS and TWS relative to the pre-co-management baseline in 2003 (Figure 4). The sharp reduction in vegetation cover in CWS aligns with Global Forest Watch data, which highlights significant vegetation loss, particularly in 2006, 2009, and 2012 (Figures 4 and 5). Similarly, LNP experienced notable vegetation declines in 2006 and 2012, which corresponds to the Global Forest Watch observations. These reductions may be attributed to illegal tree removal activities, particularly in 2011 [8].

Overall, the findings in our study are consistent with the previous studies that highlight the differential impacts of co-management on vegetation cover, which can vary depending on specific protected areas and management strategies. For instance, the observed loss of vegetation in CWS is consistent with studies by Islam et al. (2018) [44] and Rahman and Islam (2021) [70], who reported significant declines in vegetation cover during co-management periods, likely driven by agricultural expansion and illegal logging. These findings underscore the challenges of implementing effective co-management in areas experiencing high socioeconomic pressures, where forest conservation often competes with local livelihood needs.

Conversely, the positive impacts of co-management observed in LNP, SNP, and RKWS are consistent with recent studies [69,73], suggesting that co-management can mitigate deforestation by providing alternative income-generation activities for local communities. Community-based conservation initiatives, such as ecotourism employment and other livelihood programs, have likely contributed to reduced dependence on forest resources, thereby alleviating deforestation pressures [26,72]. The net positive values of NDVI, EVI, and MSAVI in LNP, SNP, and RKWS can be attributed to increased total vegetation cover in the forests and crops in agricultural land. Nevertheless, while these gains are promising, prioritizing the enhancement of forest cover remains critical to preserving dense forests and maintaining biodiversity [69,74].

Several studies have emphasized the integral role of forest cover restoration and biodiversity conservation in sustaining forest ecosystem services. For example, Masum et al. (2023) [69] and Ferdous (2015) [74] advocate for reforestation and conservation policies that prioritize mixed-species planting, which enhances forest health and biodiversity. These strategies are critical for ensuring the long-term ecological stability of protected areas under co-management frameworks.

4.4. Forest and Total Vegetation Cover in Forests Without Co-Management Practices

While recent studies have extensively examined the effects of co-management on land use and vegetation cover dynamics in protected areas [36,66,68,69], the Rajkandi Reserve Forest (RRF), which operates without a co-management framework and served as the control site in this study, has received comparatively little attention. Our findings indicate that RRF experienced a decline in dense forest cover alongside an increase in agricultural lands and forest–agriculture mosaic areas between 2003 and 2015 (Table 2; Figure 4). Additionally, the overall forest cover in RRF showed a decreasing trend during this period (Figures 5 and 6).

These observations are consistent with projections of declining forest cover in RRF, with the mean forest cover estimated to decrease from 13,782 ha in 1988–2018 to 11,986 ha by 2100 [35]. This trend suggests that, in the absence of co-management practices, the conversion of forested areas into agricultural lands may accelerate, as local communities prioritize agricultural expansion driven by economic necessity over forest conservation efforts.

Our results also align with findings from Haque et al. (2018) [45], who reported a rich angiosperm flora in RRF but noted significant pressures from land use changes. While the number of angiosperm species in RRF was higher than in CWS, it remained lower than in RKWS and LNP, underscoring the need for targeted conservation interventions in this region. The identification of 25 threatened species in RRF highlights the critical need to protect both forest cover and biodiversity [45].

Since the effectiveness of the co-management practice strongly varies across protected areas, the development of policies tailored specifically to RRF is essential. Our study suggests the importance of incorporating reforestation efforts and engaging local communities in forest management strategies to mitigate further deforestation and promote biodiversity conservation.

5. Conclusions

Our study conducted a rigorous assessment of the impact of co-management on forest cover in five pilot protected areas where co-management initiatives began in Bangladesh. Using spectral vegetation indices derived from remote sensing data, we identified significant decreases in dense forest coverage alongside increases in agricultural lands and forest-agriculture mosaics. These findings highlight the urgent need for enhanced co-management strategies that more effectively address the underlying drivers of deforestation.

Methodologically, our research fills a critical gap by providing a comprehensive analysis of overall forest cover changes resulting from co-management practices. The use of rigorous remote sensing techniques allowed for precise quantification of spatial and temporal variations in vegetation cover, thereby strengthening the reliability of our conclusions. This robust approach offers valuable insights into the effectiveness of co-management strategies and their impact on forest conservation.

The implications of our study are significant for policy formulation in Bangladesh and globally. Targeted conservation efforts are imperative, especially in areas experiencing substantial forest loss such as CWS and SNP. Our findings underscore the importance of developing adaptive forest governance frameworks that prioritize community engagement and enhance ecosystem resilience. By incorporating scientific evidence into policymaking, stakeholders can devise more effective strategies for deforestation mitigation and biodiversity conservation.

Globally, this research contributes to the discourse on sustainable forest management by demonstrating both the potential benefits and limitations of co-management approaches. It emphasizes the necessity for policies that are context-specific, addressing local socioeconomic pressures while fostering community participation. The methodologies and insights presented in this study can inform policymakers, conservationists, and community leaders worldwide, aiding in the development of more effective forest conservation strategies across diverse ecological, political, and cultural landscapes.

Supplementary Materials: The following supporting information can be downloaded at: <https://www.mdpi.com/article/10.3390/land13101709/s1>. Table S1. Quality assessment conditions for each pixel based on QA Pixel quality band.

Author Contributions: Conceptualization: M.R.K., M.A.H., I.K., S.A.M. and S.C.T.; methodology: M.R.K. and M.A.H.; software: M.R.K. and M.A.H.; validation: M.R.K. and M.A.H.; formal analysis: M.R.K., M.A.H. and I.K.; investigation, M.R.K.; resources, M.R.K.; data curation, M.R.K. and M.A.H.; writing—original draft, M.R.K. and M.A.H.; writing—review and editing, M.A.H., I.K., W.L., S.A.M., H.M.T.R. and S.C.T.; writing—result, I.K. and M.R.K.; writing—discussion, W.L., M.R.K. and S.A.M.; supervision, M.A.H. and S.C.T. All authors have read and agreed to the published version of the manuscript.

Funding: This research received no external funding.

Data Availability Statement: The raw data supporting the conclusions of this article will be made available by the authors on request.

Acknowledgments: The authors would like to thank anonymous reviewers for providing valuable comments and suggestions.

Conflicts of Interest: The authors declare no conflicts of interest.

References

1. Krsnik, G.; Reynolds, K.M.; Murphy, P.; Paplanus, S.; Garcia-Gonzalo, J.; González Olabarria, J.R. Forest Use Suitability: Towards Decision-Making-Oriented Sustainable Management of Forest Ecosystem Services. *Geogr. Sustain.* **2023**, *4*, 414–427. [CrossRef]
2. Poudyal, B.H.; Maraseni, T.; Cockfield, G. Scientific Forest Management Practice in Nepal: Critical Reflections from Stakeholders' Perspectives. *Forests* **2020**, *11*, 27. [CrossRef]
3. Charmakar, S.; Kimengsi, J.N.; Giessen, L. Power in Forest Management Institutions: A Systematic Review. *Trees For. People* **2024**, *15*, 100465. [CrossRef]
4. De Pourcq, K.; Thomas, E.; Arts, B.; Vranckx, A.; Léon-Sicard, T.; Van Damme, P. Conflict in Protected Areas: Who Says Co-Management Does Not Work? *PLoS ONE* **2016**, *10*, e0144943. [CrossRef]
5. Begum, F.; Lobry de Bruyn, L.; Kristiansen, P.; Islam, M.A. Institutionalising Co-Management Activities for Conservation of Forest Resources: Evidence from the Sundarban Mangrove Forest Management of Bangladesh. *J. Environ. Manag.* **2021**, *298*, 113504. [CrossRef] [PubMed]
6. Kimengsi, J.N.; Bhusal, P.; Aryal, A.; Fernandez, M.V.; Owusu, R.; Chaudhary, A.; Nielsen, W. What (De)Motivates Forest Users' Participation in Co-Management? Evidence from Nepal. *Forests* **2019**, *10*, 512. [CrossRef]
7. Ghorbani, M.; Azadi, H. A Social-Relational Approach for Analyzing Trust and Collaboration Networks as Preconditions for Rangeland Co-management. *Rangel. Ecol. Manag.* **2021**, *75*, 170–184. [CrossRef]
8. Islam, K.N.; Rahman, M.M.; Jashimuddin, M.; Hossain, M.M.; Islam, K.; Faroque, M.A. Analyzing Multi-Temporal Satellite Imagery and Stakeholders' Perceptions to Have an Insight into How Forest Co-Management Is Changing the Protected Area Landscapes in Bangladesh. *For. Policy Econ.* **2019**, *101*, 70–80. [CrossRef]
9. Quimby, B.; Levine, A. Participation, Power, and Equity: Examining Three Key Social Dimensions of Fisheries Co-management. *Sustainability* **2018**, *10*, 3324. [CrossRef]
10. Bardsley, D.K.; Bardsley, A.M.; Moskwa, E.; Weber, D.; Robinson, G.M. Challenges to the Co-Management of Biodiversity in a Reflexive Modernity. *Geogr. Res.* **2021**, *59*, 362–377. [CrossRef]
11. Plummer, R.; Baird, J. Adaptive Co-Management for Climate Change Adaptation: Considerations for the Barents Region. *Sustainability* **2013**, *5*, 629–642. [CrossRef]
12. Negassa, M.D.; Mallie, D.T.; Gemed, D.O. Forest Cover Change Detection Using Geographic Information Systems and Remote Sensing Techniques: A Spatio-Temporal Study on Komto Protected Forest Priority Area, East Wollega Zone, Ethiopia. *Environ. Syst. Res.* **2020**, *9*, 1. [CrossRef]
13. Chinangwa, L.L.; Pullin, A.S.; Hockley, N. Impact of Forest Co-Management Programs on Forest Conditions in Malawi. *J. Sustain. For.* **2017**, *36*, 338–357. [CrossRef]
14. Nagendra, H.; Tucker, C.; Carlson, L.; Southworth, J.; Karmacharya, M.; Karna, B. Monitoring Parks through Remote Sensing: Studies in Nepal and Honduras. *Environ. Manag.* **2004**, *34*, 748–760. [CrossRef]
15. Niraula, R.R.; Gilani, H.; Pokharel, B.K.; Qamer, F.M. Measuring Impacts of Community Forestry Program through Repeat Photography and Satellite Remote Sensing in the Dolakha District of Nepal. *J. Environ. Manag.* **2013**, *126*, 20–29. [CrossRef]
16. Gondwe, M.F.; Cho, M.A.; Chirwa, P.W.; Geldenhuys, C.J. Land Use Land Cover Change and the Comparative Impact of Co-Management and Government-Management on the Forest Cover in Malawi (1999–2018). *J. Land Use Sci.* **2019**, *14*, 281–305. [CrossRef]
17. Kaiser, E.T.; Roberts, K.; Pawkham, J.; Thongdi, B.; Morikawa, R.; Satre, D. Healthy Forest, Healthy People: Remote Sensing and Monitoring Support Implementation of Community Forestry in Thailand. In Proceedings of the 2012 IEEE Global Humanitarian Technology Conference, Seattle, WA, USA, 21–24 October 2012; pp. 111–116.
18. Rasheed, K.B.S. Participatory Forestry as a Strategy for Reforestation in Bangladesh. *GeoJournal* **1995**, *37*, 39–44. [CrossRef]
19. Sarker, S.K.; Deb, J.C.; Halim, M.A. A Diagnosis of Existing Logging Bans in Bangladesh. *Int. For. Rev.* **2011**, *13*, 461–475. [CrossRef]
20. Chowdhury, M.S.H.; Koike, M. An Overview on the Protected Area System for Forest Conservation in Bangladesh. *J. For. Res.* **2010**, *21*, 111–118. [CrossRef]
21. Chowdhury, M.S.H.; Gudmundsson, C.; Izumiyama, S.; Koike, M.; Nazia, N.; Rana, M.P.; Mukul, S.A.; Muhammed, N.; Redowan, M. Community Attitudes toward Forest Conservation Programs through Collaborative Protected Area Management in Bangladesh. *Environ. Dev. Sustain.* **2014**, *16*, 1235–1252. [CrossRef]
22. Rahman, M.M.; Mahmud, M.A.A.; Ahmed, F.U. Restoration of Degraded Forest Ecosystem through Non-Forestry Livelihood Supports: Experience from the Chunati Wildlife Sanctuary in Bangladesh. *For. Sci. Technol.* **2017**, *13*, 109–115. [CrossRef]

23. Rashid, A.Z.M.M.; Craig, D.; Mukul, S.A.; Khan, N.A. A Journey towards Shared Governance: Status and Prospects for Collaborative Management in the Protected Areas of Bangladesh. *J. For. Res.* **2013**, *24*, 599–605. [CrossRef]
24. Rahman, M.S.; Miah, S.; Giessen, L. A New Model of Development Coalition Building: USAID Achieving Legitimate Access and Dominant Information in Bangladesh's Forest Policy. *World Dev.* **2018**, *105*, 248–261. [CrossRef]
25. Islam, M.W.; Ahmed, S.; Mahin, R.T. Motivation in Community-Based Tourism: Linking Locals to Internationals in Promoting Community Development and Conservation of Natural Resources. In *Strategic Tourism Planning for Communities: Restructuring and Rebranding (Building the Future of Tourism)*; Sharma, A., Arora, S., Eds.; Emerald Publishing Limited: Leeds, UK, 2024; pp. 221–245. ISBN 978-1-83549-016-7.
26. Mukul, S.A.; Rashid, A.Z.M.M.; Quazi, S.A.; Uddin, M.B.; Fox, J. Local Peoples' Responses to Co-Management Regime in Protected Areas: A Case Study from Satchari National Park, Bangladesh. *For. Trees Livelihoods* **2012**, *21*, 16–29. [CrossRef]
27. Oldekop, J.A.; Holmes, G.; Harris, W.E.; Evans, K.L. A Global Assessment of the Social and Conservation Outcomes of Protected Areas. *Conserv. Biol.* **2016**, *30*, 133–141. [CrossRef]
28. Bilyaminu, H.; Radhakrishnan, P.; Vidyasagar, K.; Srinivasan, K. Monitoring Land Use and Land Cover Change of Forest Ecosystems of Shendurney Wildlife Sanctuary, Western Ghats, India. *Asian J. Environ. Ecol.* **2021**, *15*, 20–27. [CrossRef]
29. Meli Fokeng, R.; Gadinga Forje, W.; Meli Meli, V.; Nyuyki Bodzemo, B. Multi-Temporal Forest Cover Change Detection in the Metchie-Ngomou Protection Forest Reserve, West Region of Cameroon. *Egypt. J. Remote Sens. Space Sci.* **2020**, *23*, 113–124. [CrossRef]
30. Vogelmann, J.E.; DeFelice, T.P. Characterization of Intra-Annual Reflectance Properties of Land Cover Classes in Southeastern South Dakota Using Landsat TM and ETM+ Data. *Can. J. Remote Sens.* **2003**, *29*, 219–229. [CrossRef]
31. Xue, J.; Su, B. Significant Remote Sensing Vegetation Indices: A Review of Developments and Applications. *J. Sens.* **2017**, *2017*, 1353691. [CrossRef]
32. da Silva, V.S.; Salami, G.; da Silva, M.I.O.; Silva, E.A.; Monteiro Junior, J.J.; Alba, E. Methodological Evaluation of Vegetation Indexes in Land Use and Land Cover (LULC) Classification. *Geol. Ecol. Landsc.* **2020**, *4*, 159–169. [CrossRef]
33. Zafar, T.B.; Ding, W.; Din, S.U.; Khan, G.M.; Hao, C.; He, L. Forest Cover and Land Use Map of the Chunati Wildlife Sanctuary Based on Participatory Mapping and Satellite Images: Insight into Chunati Beat. *Land Use Policy* **2021**, *103*, 105193. [CrossRef]
34. Islam, K.; Jashimuddin, M.; Nath, B.; Nath, T.K. Quantitative Assessment of Land Cover Change Using Landsat Time Series Data: Case of Chunati Wildlife Sanctuary (CWS), Bangladesh. *Int. J. Environ. Geoinformatics* **2016**, *3*, 45–55. [CrossRef]
35. Ahmed, N.; Mahbub, R.B.; Hossain, M.M.; Sujauddin, M. Modelling Spatio-Temporal Changes of Tropical Forest Cover in the North-Eastern Region of Bangladesh. *J. Trop. For. Sci.* **2020**, *32*, 42–51.
36. Ullah, S.M.A.; Tani, M.; Tsuchiya, J.; Rahman, M.A.; Moriyama, M. Impact of Protected Areas and Co-Management on Forest Cover: A Case Study from Teknaf Wildlife Sanctuary, Bangladesh. *Land Use Policy* **2022**, *113*, 105932. [CrossRef]
37. Hossen, A.; Røskaft, E. A Case Study on Conflict Intensity between Humans and Elephants at Teknaf Wildlife Sanctuary, Cox's Bazar, Bangladesh. *Front. Conserv. Sci.* **2023**, *4*, 1067045. [CrossRef]
38. Chowdhury, M.S.H.; Koike, M.; Rana, P.; Muhammed, N. Community Development through Collaborative Management of Protected Areas: Evidence from Bangladesh with a Case of Rema-Kalenga Wildlife Sanctuary. *Int. J. Sustain. Dev. World Ecol.* **2013**, *20*, 63–74. [CrossRef]
39. Chowdhury, M.S.H.; Koike, M. Therapeutic Use of Plants by Local Communities in and around Rema-Kalenga Wildlife Sanctuary: Implications for Protected Area Management in Bangladesh. *Agrofor. Syst.* **2010**, *80*, 241–257. [CrossRef]
40. Karim, M.R.; Sultana, F.; Saimun, M.S.R.; Mukul, S.A.; Arfin-Khan, M.A.S. Plant Diversity and Local Rainfall Regime Mediate Soil Ecosystem Functions in Tropical Forests of North-East Bangladesh. *Environ. Adv.* **2020**, *2*, 100022. [CrossRef]
41. Mukul, S.A. Biodiversity Conservation and Ecosystem Functions of Traditional Agroforestry Systems: Case Study from Three Tribal Communities in and Around Lawachara National Park. In *Forest Conservation in Protected Areas of Bangladesh: Policy and Community Development Perspectives*; Chowdhury, M.S.H., Ed.; Springer International Publishing: Cham, Germany, 2014; pp. 171–179. ISBN 978-3-319-08147-2.
42. Sohel, M.S.I.; Mukul, S.A.; Burkhard, B. Landscape's Capacities to Supply Ecosystem Services in Bangladesh: A Mapping Assessment for Lawachara National Park. *Ecosyst. Serv.* **2015**, *12*, 128–135. [CrossRef]
43. Halim, M.A.; Shahid, A.; Chowdhury, M.S.H.; Nahar, M.N.; Sohel, M.S.I.; Nuruddin, M.J.; Koike, M. Evaluation of Land-Use Pattern Change in West Bhanugach Reserved Forest, Bangladesh, Using Remote Sensing and GIS Techniques. *J. For. Res.* **2008**, *19*, 193–198. [CrossRef]
44. Islam, K.; Rahman, M.F.; Jashimuddin, M. Modeling Land Use Change Using Cellular Automata and Artificial Neural Network: The Case of Chunati Wildlife Sanctuary, Bangladesh. *Ecol. Indic.* **2018**, *88*, 439–453. [CrossRef]
45. Haque, A.K.M.K.; Khan, S.A.; Uddin, S.N.; Shetu, S.S. An Annotated Checklist of the Angiospermic Flora of Rajkandi Reserve Forest of Moulvibazar, Bangladesh. *Bangladesh J. Plant Taxon.* **2018**, *25*, 187. [CrossRef]
46. NSP. *Base Maps, NSP (2003–2008)*; USAID: Dhaka, Bangladesh, 2017.
47. UNEP-WCMC Protected Area Profile for Bangladesh from the World Database on Protected Areas. Available online: <https://www.protectedplanet.net/country/BGD> (accessed on 12 August 2024).
48. Peng, D.; Zhang, B.; Liu, L.; Fang, H.; Chen, D.; Hu, Y.; Liu, L. Characteristics and Drivers of Global NDVI-Based FPAR from 1982 to 2006. *Glob. Biogeochem. Cycles* **2012**, *26*, GB3015. [CrossRef]
49. Claverie, M.; Vermote, E.F.; Franch, B.; Masek, J.G. Evaluation of the Landsat-5 TM and Landsat-7 ETM+ Surface Reflectance Products. *Remote Sens. Environ.* **2015**, *169*, 390–403. [CrossRef]

50. Julia, A.B.; Brian, L.M.; Jeffrey, S.C.M.; Dennis, L.H.; Simon, J.H.; John, R.S.; Haque, M.O. *Landsat-7 ETM+ Radiometric Calibration Status*; SPIE: San Diego, CA, 19 September 2016; Volume 9972, p. 99720C.
51. Masek, J.G.; Vermote, E.F.; Saleous, N.E.; Wolfe, R.; Hall, F.G.; Huemmrich, K.F.; Gao, F.; Kutler, J.; Lim, T.K. A Landsat Surface Reflectance Dataset for North America, 1990–2000. *IEEE Geosci. Remote Sens. Lett.* **2006**, *3*, 68–72. [CrossRef]
52. Ling, X.; Cao, R. A New Spatiotemporal Data Fusion Method to Reconstruct High-Quality Landsat Ndvi Time-Series Data. In Proceedings of the 2021 IEEE International Geoscience and Remote Sensing Symposium IGARSS, Brussels, Belgium, 11–16 July 2021; IEEE: Brussels, Belgium, 2021; pp. 2564–2567.
53. Tahsin, S.; Medeiros, S.C.; Hooshyar, M.; Singh, A. Optical Cloud Pixel Recovery via Machine Learning. *Remote Sens.* **2017**, *9*, 527. [CrossRef]
54. Roy, D.P.; Borak, J.S.; Devadiga, S.; Wolfe, R.E.; Zheng, M.; Descloitres, J. The MODIS Land Product Quality Assessment Approach. *Remote Sens. Environ.* **2002**, *83*, 62–76. [CrossRef]
55. Scaramuzza, P.; Micijevic, E.; Chander, G. *SLC Gap-Filled Products Phase One Methodology*; Landsat Technical Notes; United States Geological Survey (USGS): Reston, VA, USA, 2004; pp. 1–5.
56. Zeng, C.; Shen, H.; Zhang, L. Recovering Missing Pixels for Landsat ETM+ SLC-off Imagery Using Multi-Temporal Regression Analysis and a Regularization Method. *Remote Sens. Environ.* **2013**, *131*, 182–194. [CrossRef]
57. Hossain, M.S.; Bujang, J.S.; Zakaria, M.H.; Hashim, M. Assessment of Landsat 7 Scan Line Corrector-off Data Gap-Filling Methods for Seagrass Distribution Mapping. *Int. J. Remote Sens.* **2015**, *36*, 1188–1215. [CrossRef]
58. Liu, D.; Xia, F. Assessing Object-Based Classification: Advantages and Limitations. *Remote Sens. Lett.* **2010**, *1*, 187–194. [CrossRef]
59. Rokni, K.; Musa, T.A. Normalized Difference Vegetation Change Index: A Technique for Detecting Vegetation Changes Using Landsat Imagery. *CATENA* **2019**, *178*, 59–63. [CrossRef]
60. Jiang, Z.; Huete, A.R.; Didan, K.; Miura, T. Development of a Two-Band Enhanced Vegetation Index without a Blue Band. *Remote Sens. Environ.* **2008**, *112*, 3833–3845. [CrossRef]
61. Huete, A.R. A Soil-Adjusted Vegetation Index (SAVI). *Remote Sens. Environ.* **1988**, *25*, 295–309. [CrossRef]
62. Qi, J.; Chehbouni, A.; Huete, A.R.; Kerr, Y.H.; Sorooshian, S. A Modified Soil Adjusted Vegetation Index. *Remote Sens. Environ.* **1994**, *48*, 119–126. [CrossRef]
63. R Core Team. *R: A Language and Environment for Statistical Computing*; R Core Team: Vienna, Austria, 2024.
64. Helsel, D.R.; Frans, L.M. Regional Kendall Test for Trend. *Environ. Sci. Technol.* **2006**, *40*, 4066–4073. [CrossRef]
65. Dillencourt, M.B.; Mount, D.M.; Netanyahu, N.S. A Randomized Algorithm for Slope Selection. *Int. J. Comput. Geom. Appl.* **1992**, *2*, 1–27. [CrossRef]
66. Rahman, M.H.; Miah, M.D. Are Protected Forests of Bangladesh Prepared for the Implementation of REDD+? A Forest Governance Analysis from Rema-Kalenga Wildlife Sanctuary. *Environments* **2017**, *4*, 43. [CrossRef]
67. Hossain, M.I.; Numata, S. Effects of Land-Related Policies on Deforestation in a Protected Area: The Case Study of Rema-Kalenga Wildlife Sanctuary, Bangladesh. *Conservation* **2021**, *1*, 168–181. [CrossRef]
68. Masum, K.M.; Mehedi, H.M. Assessment of Land Cover Changes from Protected Forest Areas of Satchari National Park in Bangladesh and Implications for Conservation. *J. For. Environ. Sci.* **2020**, *36*, 199–206. [CrossRef]
69. Masum, K.M.; Islam, M.S.; Fahim, M.S.I.; Parvej, M.; Majeed, M.; Hasan, M.M.; Mansor, A. Temporal Comparison of Land-Use Changes and Biodiversity in Differential IUCN Protected-Area Categories of Bangladesh in the Context of Co-Management. *Geol. Ecol. Landsc.* **2023**, 1–16. [CrossRef]
70. Rahman, M.F.; Islam, K. Effectiveness of Protected Areas in Reducing Deforestation and Forest Fragmentation in Bangladesh. *J. Environ. Manag.* **2021**, *280*, 111711. [CrossRef]
71. Islam, K.N.; Rahman, M.M.; Jashimuddin, M.; Islam, K.; Zhang, Y. Impact of Co-Management on Tree Diversity and Carbon Sequestration in Protected Areas: Experiences from Bangladesh. *Trees For. People* **2020**, *2*, 100033. [CrossRef]
72. Islam, M.A.; Jimmy, A.N.; Alam, M.S.; Khan, N.A. The Use of Multi-Temporal Landsat Normalized Difference Vegetation Index (NDVI) Data for Assessing Forest Cover Change of Lawachara National Park. *Environ. Dev. Sustain.* **2021**, *23*, 17702–17722. [CrossRef]
73. Ray, P.C.; Hasan, M.F.; Hossain, M.S.; Hanif, M.A. Forest Co-Management for Improvement of Livelihood and Forest Cover: Experience from Sal Forest of Bangladesh. *Trees For. People* **2023**, *14*, 100450. [CrossRef]
74. Ferdous, F. Co-Management Approach and Its Impacts on Social, Economic and Ecological Developments: Lessons from Lawachara National Park, Bangladesh. *Int. J. Res. Land-Use Sustain.* **2015**, *2*, 91–98. [CrossRef]
75. Jashimuddin, M.; Hasan, M.H.; Baul, T.K.; Chakma, N.; Hossen, S.; Dutta, S.; Ahmed, F.U.; Nath, T.K. Principles of People-Centric Forest Restoration Projects in South-Eastern Bangladesh: Implications for Sustainability. *Restor. Ecol.* **2024**, *32*, e14087. [CrossRef]
76. Islam, K.N.; Jashimuddin, M.; Hasan, K.J.; Khan, M.I.; Kamruzzaman, M.; Nath, T.K. Stakeholders' Perception on Conservation Outcomes of Forest Protected Area Co-Management in Bangladesh. *J. Sustain. For.* **2022**, *41*, 240–256. [CrossRef]

Disclaimer/Publisher's Note: The statements, opinions and data contained in all publications are solely those of the individual author(s) and contributor(s) and not of MDPI and/or the editor(s). MDPI and/or the editor(s) disclaim responsibility for any injury to people or property resulting from any ideas, methods, instructions or products referred to in the content.

Article

Identification of Agricultural Areas to Restore Through Nature-Based Solutions (NbS)

Beatrice Petti¹ and Marco Ottaviano^{1,2,*}

¹ Department of Biosciences and Territory, University of Molise, Cda Fonte Lappone Snc, 86090 Pesche, Italy; b.petti2@studenti.unimol.it

² National Biodiversity Future Center (NBFC), Piazza Marina 61, 90133 Palermo, Italy

* Correspondence: ottaviano@unimol.it

Abstract: This study aims to present a methodological approach based on the objectives of the Nature Restoration Law and the concept of Forest Landscape Restoration to identify areas that are best suited for the implementation of Nature-based Solutions for the improvement of landscape and habitat status in the city of Campobasso (1028.64 km²). Using open data (ISPRA ecosystem services and regional land use capability), an expert based approach (questionnaire), and a multicriteria analysis (Analytical Hierarchy Process), the Total Ecosystem Services Value index was determined as a weighted additive sum of the criteria considered. The index was then classified into eight clusters, and the land use “Cropland” was extracted. Cluster 1 croplands (740.09 Ha) were identified as the areas to be allocated to Nature-based Solutions since they were those characterized by fewer ecosystem services provisioning, while Cluster 8 croplands (482.88 Ha) were identified as valuable areas to be preserved. It was then possible to compare the “Forest” areas currently present in the study area with those of a possible future scenario, represented by the areas occupied today by forest with the addition of Cluster 1 croplands. A landscape analysis was conducted; it showed greater dispersion and fragmentation of forest patches in the future scenario, but also greater connectivity and thus greater ecological functionality of the patches.

Keywords: forest; multicriteria analysis; Urban Atlas; Nature-based Solutions; croplands; ecosystem services; landscape analysis

Citation: Petti, B.; Ottaviano, M. Identification of Agricultural Areas to Restore Through Nature-Based Solutions (NbS). *Land* **2024**, *13*, 1954. <https://doi.org/10.3390/land13111954>

Academic Editors: Jianye Li, Weida Gao, Wei Hu, Qiang Chen and Xingyi Zhang

Received: 30 September 2024

Revised: 14 November 2024

Accepted: 16 November 2024

Published: 19 November 2024



Copyright: © 2024 by the authors. Licensee MDPI, Basel, Switzerland. This article is an open access article distributed under the terms and conditions of the Creative Commons Attribution (CC BY) license (<https://creativecommons.org/licenses/by/4.0/>).

1. Introduction

Urbanization is proceeding at an extremely fast pace; for the first time since 2008, more than half of the world’s population lives in cities [1], and it is estimated that this will affect 66% of 9.8 billion people by 2050, mainly due to the social and economic process that has progressively resulted in the abandonment of rural, hilly, and mountainous areas [2] and the consequent process of urbanization. As a result, built-up land is expanding, while surrounding natural environments and green areas within urban areas are threatened [3]. In fact, urban sprawl has a substantial ecological footprint and is a driver of land use change [4]. Although cities occupy only 2% of the earth’s surface, people are already using 75% of all natural resources [1]. This implies the configuration of available urban green spaces as central elements in increasing the quality of urban settings and local resilience, resulting in positive impacts on people’s health and well-being [5].

It is important to develop a network of green infrastructure, not just ancillary green, so that it can cope with the high complexity and dynamism of urban areas [6]. Another fundamental aspect to consider at the planning level is the structure and choice of areas to be allocated to green spaces, as well as their type. In general, different types of green spaces should be planned with an emphasis on biodiversity and the use of native species [5]. It is necessary for green infrastructures to be well planned as they can contribute differently to the provision of ecosystem services (ES), depending on the vegetation types and different

types of green spaces and corridors (e.g., urban trees and rows), patches (e.g., isolated trees), and matrices (e.g., urban and peri-urban forests) [7]. Urban and Peri-urban forests (UPFs) provide multiple ES; in particular, they mitigate the microclimate and reduce pollution through pollutant sequestration, promote carbon storage, and are crucial for erosion control [8]. In addition, they are important as habitats for rare animal and plant species, as well as for biodiversity and pollination [3]. In some contexts, their role is also relevant in providing citizens with provisioning services such as nuts, berries, mushrooms, herbs, and hunting [9]. In addition, there are numerous physical benefits associated with green spaces; they improve mental health and well-being [10], reduce stress caused by modern lifestyles [11], and may have lasting psychological benefits [12]; benefits related to longevity have also been found [13]. Promoting UPFs by securing the ES they produce is incredibly important for human well-being and future generations; however, UPFs are threatened by accelerated urbanization, deforestation, and climate change, which also affect their ability to provide ES [14]. In addition, according to recent estimates [15], between 60 and 70% of European Union (EU) soils are unhealthy, being subject to erosion, compaction, organic matter reduction, pollution, biodiversity loss, salinization, and sealing. When soil is healthy, it can provide provisioning, regulating, supporting, and cultural services, e.g., EU croplands and grasslands produce ES amounting to 76 billion euros per year, of which only one-third is directly related to agricultural production [15].

According to the Report on Land Consumption, Spatial Dynamics and Ecosystem Services by the SNPA (National Service for Environmental Protection) [16], land consumption affects an average of 19 hectares per day in Italy, with a cemented surface area of about 21,500 km². This phenomenon is mainly due to urban expansion, which makes the soil impermeable, thus resulting in a greater susceptibility to flooding and increased heat waves, to the loss of biodiversity, green areas, and ES, and decreased resilience [17,18], with a damage of 8 billion euros per year [16]. Urban sprawl, together with road networks and constructions, also leads to the loss and fragmentation of agricultural lands, which can impact agricultural process inputs [19]. Peri-urban agriculture represents a substantial contribution to ES, acting as a groundwater table recharge zone and stormwater runoff sink and enhancing the aesthetic appeal while providing food security [20]. Focusing on Nature-based Solutions, increasing green infrastructures could lead to the improvement of ecosystem health by reconnecting fragmented natural and semi-natural environments and restoring damaged habitats to provide more goods and services [21].

The Nature-based Solutions (NbS) term first appeared in the early 2000s, primarily in the context of solving agricultural issues, such as the use of habitats to mitigate farm effluent [22], later giving great emphasis to NbS to major contemporary societal challenges, such as climate change [23]. It is an umbrella concept that encompasses a range of ecosystem-related terms and approaches that address societal challenges [24]. This concept represents a set of environmentally friendly alternatives that support the provision and maintenance of ES, and it integrates into other concepts, such as those of green and blue infrastructure, urban forestry, ecological engineering, etc. The strength of NbS lies in providing co-benefits and generating advantageous solutions (e.g., multifunctionality) [25]. According to the European Commission, an action can be addressed as NbS if it uses nature or natural processes if it enhances or provides social, economic, and environmental benefits, and if it has a net benefit on biodiversity [26], such as vertical forests in urban settings [27]. The accumulated knowledge on NbS demonstrates that they are locally attuned solutions to the social context and generate multiple benefits [28]; their use could address climate change and biodiversity loss while supporting various sustainable development goals [29]. In this regard, governmental and nongovernmental organizations are providing funds globally to implement NbS [30], with the main focus on reforestation and afforestation programs [31] such as the EU's "Three billion trees" [32] and the "Great Green Wall" [33]. Sustainable and successful NbS must deliver benefits for biodiversity and people [34]; trade-offs and synergies play a key role in NbS design [24].

Due to pressure from rapid urbanization and increased vulnerability to risks associated with climate change in cities around the world, NbS are increasingly being promoted and integrated, especially into urban planning [30,35,36]; however, their importance is also increasing in agricultural and forestry landscapes, with a multitude of benefits, as biodiversity conservation [37]. In fact, climate change is affecting European ecosystems and human well-being, and it is estimated that there will soon be even greater threats related to ecosystems and the socioeconomic system [38]. NbS are increasingly seen as central elements in various areas due to their efficiency in coping with climate change-related extreme events through mitigation and adaptation actions, preserving human health and psychosocial well-being, improving air quality, and increasing landscape connectivity [25]. A limitation, however, is land availability, which is a barrier to implementing NbS within cities [35]. Another limitation is associated with the fact that policy instruments for the implementation of NbS are mostly related to the municipal sphere and not at the landscape or higher levels of planning, which would instead allow the multifunctionality of NbS to be enhanced [39]. To make NbS efficient, they require integrated, cross-sectoral planning and governance strategies for their integration and deployment [40], as well as the involvement of numerous stakeholders, whose contribution is essential for NbS' long-term success [41,42]. Despite their widespread deployment in cities, there are still numerous challenges related to NbS, including the lack of information about their benefits, uncertainties about the inadequacy of existing planning systems, as well as how to plan, design, implement, and manage them adequately [43]. In fact, it is more challenging to manage NbS relying on restoration efforts than the conservation and management of native vegetation. It is fundamentally important to consider the presence of barriers to implementing NbS in degraded areas [44].

Brian Alan et al. [45] review shows that most of the studies on NBSs focus on specific aspects, including

- barriers/enablers of NBS;
- public participation/engagement/education;
- monitoring/evaluation of NbS project outcomes;
- policy and governance issues;
- social issues;
- private sector involvement.

Few studies evaluate ecological data or ES for the identification of such areas; preference is given to specific factors based on the function that NbS will have, such as land use [46], intrinsic characteristics of soils [47], landscape elements [48] or, at most, ES are evaluated but not the methodologies for identifying areas for NbS [49].

The aim of this study was to present a proper methodology approach to identify degraded agricultural areas for restoration through NbS interventions to improve the landscape and habitat status. The areas were identified from the level of ES provision and obtained through an expert-based approach.

2. Materials and Methods

2.1. Study Area

The study area is represented by the Urban Atlas [50] of the Province of Campobasso (Figure 1), which includes 38 municipalities in the Molise Region, Italy, which is also part of the study area of the PNRR-NBFC (National Biodiversity Future Center) project [51]. This choice was motivated by the desire to analyze the landscape system and the green infrastructure from a broader perspective than the mere administrative boundaries of the single city (Campobasso), which acts as a hub, in line with the political and planning guidelines of recent years.

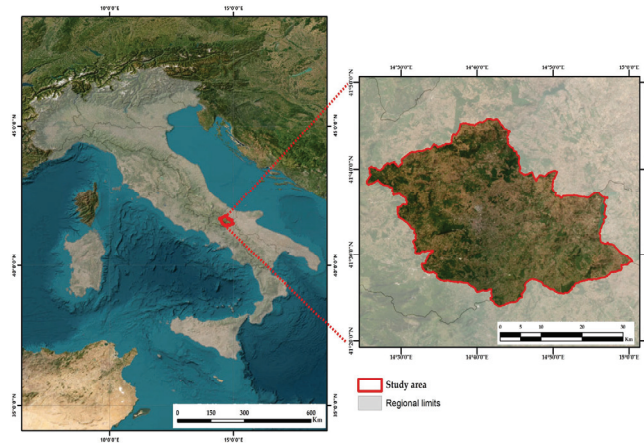


Figure 1. Study area.

The study area is 1028.64 km², the minimum altitude is 148 m above sea level (Municipality of Macchia Valfortore), while the maximum altitude is 1086 m above sea level (Municipality of Cercemaggiore). From a landscape point of view, according to the ISPRA (Higher Institute for Environmental Protection and Research) Map of Types and Physiographic Units of Landscape of Italy [52], the study area is classified as Terrigenous Hills Units consisting of terrigenous lithologies, with contrasted morphology, and Terrigenous Mountains Units in which the mountainous reliefs are characterized by terrigenous lithologies consisting of marls, clays, and sands. The high erodibility of these lithologies, along with the tendency for the drainage network to deepen, contributes to the modest elevation of the reliefs, which are prone to landslides and water erosion.

The 2018 ISPRA National Land Cover Map [53] with a 10 m spatial resolution was used to characterize the land use and cover. The map was obtained through the integration of data from the Copernicus Program's Land Monitoring Service with ISPRA's Land Use data. The choice of data referring to 2018 was dictated by the fact that the most recent ES data used for the computations are available for 2018 only. The study area has a strong agricultural vocation, mainly represented by arable land; in fact, these areas characterize around 63% of the territory, followed by forests that occupy 25%, non-agricultural meadows that occupy just over 6%, and artificial surfaces that occupy just under 5% of the territory, respectively.

According to the last ISPRA Report on Soil Consumption [54], around 20% of the province of Campobasso will be affected by soil consumption in 2022, for a total area of 12,337 hectares. In 2018, the reference year in this study, it is 12,822 hectares [55].

2.2. Methodology

The methodology (Figure 2) is based on the use of a series of available map layers related to ES delivery to develop a model that is extendable to a national scale and replicable in other case studies for the identification of areas characterized by low ES provision or situations of ecological degradation where environmental restoration interventions are needed. Interest fell on agricultural areas, particularly "Croplands", which occupy 50.83% of the entire area, to identify "valuable" areas characterized by high ES provision and adequate land capability and those "degraded" to restore through NbS interventions. Through a Landscape Ecology analysis, a comparison was also made in terms of ecological connectivity and functionality, making a comparison between the current ecological network arrangement present in the study area and a hypothetical scenario in which the areas identified by the above model are subject to NbS interventions.

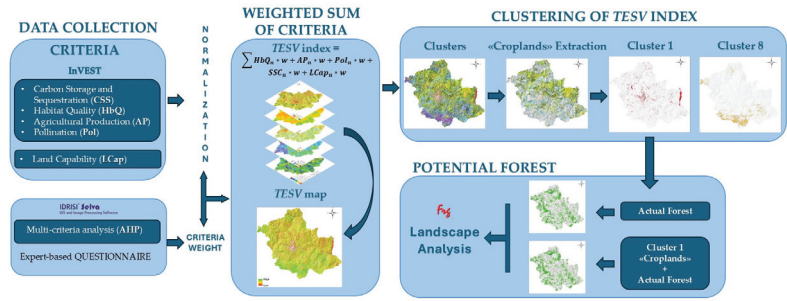


Figure 2. Study workflow.

2.3. Assessment of Ecosystem Services Provided in the Study Area

The ES maps used were created with the InVEST (Integrated Valuation of Ecosystem Services and Tradeoffs, provided by the Natural Capital Project) (ver. 3.3.0) [56] suite of models, which provide biophysical and economic analysis of the ESs delivered by the area. The software consists of several independent packages to evaluate 17 ESs belonging to all four ES categories of the Millennium Ecosystem Assessment (MEA) [18]. The model associates each land use class with a value of ES delivery. What ensures the quality and accuracy of the outputs is the ability to take advantage of accurate inputs on land use and land biophysical characteristics, which are then used by the model to calculate ES delivery in biophysical and, therefore, economic terms [57,58]. InVEST models suite uses cartography derived from the integration of High-Resolution Layers [59], Corine Land Cover, and the 2012 [60] national land use map [58].

According to Munafò [58], four of the 17 ESs selected are the most suitable for the agricultural field—carbon storage and sequestration, habitat quality, agricultural production, and pollution (Figure 3).

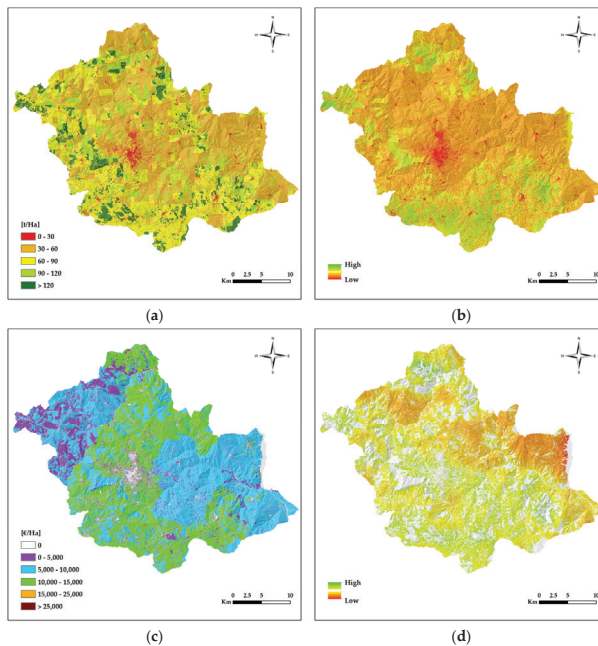


Figure 3. InVEST maps. (a) CSS; (b) HbQ; (c) AP; (d) Pol.

2.3.1. Carbon Storage and Sequestration (CSS)

CCS is a regulating service; to varying degrees, all terrestrial ecosystems contribute to providing this ES. In general, it can be said that the more natural the ecosystem, the greater its capacity to store and sequester carbon. Natural and semi-natural environments have the highest potential for sequestration and storage [57]. The estimation of this service in biophysical terms is achieved by spatializing the tons of carbon stored for each land use type [58].

2.3.2. Habitat Quality (HbQ)

HbQ is a supporting service; in fact, it is used as a proxy for assessing the state of land biodiversity [61]. Due to multiple pressures, such as land use change, sealing, urbanization, etc., habitats are subject to degradation and alteration, ecosystem fragmentation, and reduced ecological resilience. The InVEST model outputs a dimensionless index of quality ranging from 0 to 1; this index expresses values that are not absolute values of quality but rather relative to the environmental conditions of the study area; the value associated with each unit is derived from the relationship between each unit and neighboring units [58].

2.3.3. Agricultural Production (AP)

AP is part of the provisioning services, an important service related to the many areas used for productive purposes in agriculture. This service is influenced by climatic-stational factors, such as latitude, climate, exposure, slope, altitude, etc., and the type of use, whether intensive or extensive. Soil consumption, in the context of agricultural production, leads to loss of service in the present and the future since the soil is a nonrenewable resource [61]. For the assessment of this ES, the average agricultural values were used, divided, and spatialized for each rural region [58]. The study area is characterized by four of the seven rural regions of Molise (specifically 1, 2, 4, and 6) [62].

2.3.4. Pollination (Pol)

Pol is a very important regulating service; it is provided by pollinating animal organisms, such as bees and bumblebees, and by agents, such as wind and water. This service is guaranteed depending on the availability of nesting habitat and floral resources, climate, and the foraging distance of pollinators, that is, the distance that must be traveled to reach nectar and pollen sources. The InVEST model outputs a dimensionless Pol index ranging from 0 to 1, depending on the suitability of a given portion of land to host pollinators [63]. For further details on the InVEST model and the mapping used, see ISPRA [58].

2.4. Land Capability (LCap)

LCap, also referred to as “natural use”, is an indispensable element in land use planning and development policies; it is based on many soil parameters, such as clinometry, erosion, rockiness, flooding frequency, soil depth, soil composition (clay, sand, silt) and hydromorphy. Indeed, land use that deviates greatly from its natural use causes severe impacts on the environment, including soil erosion and reduced fertility [64]. The land capability classification was developed by the U.S. Department of Soil Conservation Service; it is useful for assessing the distribution of constraints, including slope, erosion risk, climatic conditions, and soil depth, that create restrictions in agriculture. Eight classes have been defined; the first four, with different propensities, are found to be appropriate for agricultural activity, while the latter have more restrictions (Figure 4). For further information, see Klingebiel A. & Montgomery [65].

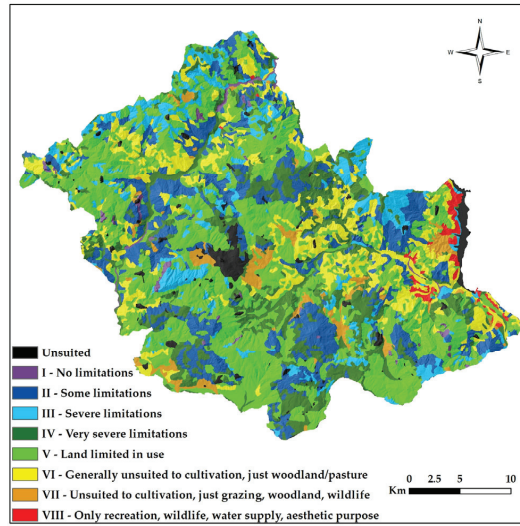


Figure 4. Land capability in the study area.

2.5. Normalization of Criteria

Since the information used was very heterogeneous in terms of data types and units of measurement, it was necessary to harmonize it through normalization to make it comparable and usable by the model.

For the CSS, HbQ, Pol, and AP services, normalization was performed on the minimum and maximum values, i.e., by setting the minimum value of the service in the study area to 0 and the maximum to 1 and scaling the intermediate values linearly again.

As for the normalization of LCap, however, 0 corresponds to built-up areas, which have no propensity for agricultural use, while one corresponds to areas with little or no restrictions and, therefore, with a better propensity for agricultural use.

2.6. Multi-Criteria Analysis for the Assessment of Ecosystem Services and Identification of Valuable and Degraded Areas

The approach used to identify areas for NbS is based on multi-criteria analysis (MCA). MCA represents an umbrella concept that encompasses more than a hundred methods that evaluate an object by considering different dimensions of interest and the interactions between multiple, often conflicting objectives and different decision criteria and metrics. The performance of an option against the various objectives and criteria, which can be assigned different weights, in this case from 0 to 1, are identified by scores. Higher scores are associated with higher performances [66].

The Analytic Hierarchy Process (AHP) method, developed by Thomas L. Saaty between 1971 and 1975 and later improved and integrated within spatially explicit models and tools (e.g., GIS), was chosen. This method organizes information by having different criteria interacting in different ways so that they are able to reflect their relative importance to the objective at hand [67]. The criteria used for the analysis model were the four ESs and the LCap.

To give weight to each of the five criteria, an expert-based approach was followed by administering a questionnaire to 19 experts in academia from the following disciplinary fields: Forestry, Environmental Sciences, Biological Sciences, Economics, and Natural Sciences. This questionnaire was structured to compare all criteria with each other in pairs, in a pairwise comparison, assigning a relative weight based on five options.

- Equally important (1);
- Moderately more important (3);

- Strongly more important (5);
- Clearly more important (7);
- Extremely more important (9).

Sixteen of the 19 experts answered the questionnaire; each questionnaire was subsequently analyzed using the Weight Tool of the IDRISI Selva software (Free ver. 17.0) to determine the relative weight assigned by each expert to each criterion considered.

The software output provides the relative weight of the criteria associated with each questionnaire and the Consistency Ratio (CR). The CR is a measure of the consistency of the judgment matrix, and it shows the probability that the values in the pair comparison matrix are randomly generated [68]. Thomas L. Saaty defines CR as

$$CR = \frac{CI}{Mean\ Random\ CI}$$

The CR is defined as the ratio of the Consistency Index (CI) to the average of the CIs obtained from a large sample of randomly generated matrices.

In turn, CI is defined as

$$CI = \frac{\lambda_{max} - n}{n - 1}$$

where λ_{max} is the largest principal eigenvalue of a positive pairwise comparison matrix. The index, in each case, is only based on pairwise comparisons that have already been made previously.

According to Saaty, the CR is acceptable if its value is less than 10% (between 0 and 0.10); however, a value of up to 20% (<0.20) is also considered tolerable [69]. Of the 16 CR values, six were out of the acceptable/tolerable range because they had a value higher than 0.20; therefore, they were not examined, as they were inconsistent according to the methodology adopted. The average value of all the CRs considered (Table 1) was 0.103, which is considered acceptable.

Table 1. Relative weights of considered criteria.

	HbQ	Pol	LCap	CSS	AP	CR
Q1	0.1687	0.1687	0.4195	0.0743	0.1687	0.03
Q3	0.5557	0.1193	0.0572	0.2337	0.034	0.10
Q4	0.2896	0.1367	0.2552	0.2724	0.0461	0.08
Q5	0.3349	0.1195	0.2945	0.1243	0.1268	0.2
Q7	0.3686	0.2339	0.1335	0.0546	0.2093	0.07
Q8	0.327	0.3643	0.1004	0.1376	0.0707	0.08
Q9	0.5131	0.259	0.0514	0.1481	0.0285	0.08
Q12	0.3257	0.3799	0.1101	0.1451	0.0393	0.08
Q13	0.4533	0.1148	0.1353	0.0821	0.2145	0.16
Q16	0.3188	0.2832	0.0699	0.2969	0.0311	0.15

The relative values of the individual criteria defined by the questionnaires are shown in Table 1.

The final weights to be given to the five criteria are shown in Table 2 and are equal to the average of the relative weights given in Table 1. This sum must always be equal to 1.

Table 2. Weights assigned to layers using expert based approach and respective standard deviation.

Criteria	Weight	Standard Dev.
HbQ	0.36554	0.11
Pol	0.21793	0.10
LCap	0.1627	0.12
CSS	0.15691	0.08
AP	0.0969	0.08

For completeness, the standard deviation was also calculated for each criterion considered.

2.6.1. Weighted Sum of the Considered Criteria

Once all criteria were normalized, the weighted sum was performed using the weights obtained previously. The final index, the Total Ecosystem Services Value (TESV) [70], was then equal to

$$TESV = \sum HbQ_n * w + AP_n * w + Pol_n * w + SSC_n * w + LCap_n * w$$

where subscript *n* denotes the normalized (0 to 1) scale value of the individual ES while *w* denotes its relative weight obtained by the expert-based approach. The TESV values range from a minimum of 0 to a maximum of 1.

2.6.2. Clustering of TESV Index: K-Means for Grids

To clearly identify valuable and degraded areas, the TESV index was clustered using the K-means clustering algorithm “Hill-Climbing” in the SAGA GIS environment.

According to the eight land capability classes, eight clusters were generated, with a distribution of increasing values from cluster 1 to cluster 8; cluster 1, i.e., the one characterized by lower ES provision and lower agricultural land use predisposition, was considered, from which the areas of “Cropland” were extracted to identify the areas to be targeted for NbS interventions.

2.7. Analysis of Changes in Terms of Landscape Fragmentation and Ecological Connectivity

2.7.1. Current Forest and Future Scenarios

Once the arable land to be targeted for NbS interventions was identified, starting from the current forest area map (current scenario), a hypothetical future scenario (potential scenario) was created, in which the current forest area is added to the newly created areas related to the “Cropland” areas of Cluster 1. To assess the possible changes in terms of ecological connectivity and functionality in the two scenarios, maps of both the current and potential forests were produced. This analysis was conducted using Landscape Ecology techniques, the discipline that studies and implements the relationship between spatial patterns and ecological processes at multiple scales and organizational levels [71].

2.7.2. Landscape Metrics

The ecological connectivity and functionality analysis of the two scenarios was conducted using a set of class and landscape metrics referring to the land use class “Forest” by means of the Fragstats 4.2 software [72].

The selected metrics are shown in Table 3.

Table 3. Selected class and landscape metrics.

Class Metrics	Landscape Metrics
Patch Density (PD)	Average Area (AREA_MN)
Landscape Similarity Index (LSI)	Mean Radius of Gyration (GYRATE_MN)
Total Core Area (TCA)	Number of Disjunct Core Area (NDCA)
Euclidean Nearest Neighbor Distance (ENN_MN)	Disjunct Core Area Density (DCAD)
Euclidean Nearest Neighbor Distance (Area-Weighted Mean) (ENN_AM)	Aggregation Index (AI)
Percentage of like adjacencies (PLADJ)	
Normalized Landscape shape index (NLSI)	

3. Results

3.1. Processing of the Final Cartography (TESV Index)

The analysis of data (Table 4) showed that the spatial distribution of the TESH index in the study area ranges from 0.046 to 0.823, with an average value of around 0.451 and a coefficient of a variation of 19.06%. Almost 45% of the area is classified as intermediate clusters 4 and 5; the highest values are concentrated in the south, particularly the southwest and northwest, while the lowest values are in the east. The spatial distribution of the TESH index is shown in Figure 5a.

Table 4. Range of values for each identified cluster (A), and area both in hectares and percentage by cluster (B).

Cluster	A		B		
	Minimum Value	Maximum Value	Cluster	Area (Ha)	Area %
1	0.046	0.268	1	3470.3	3.37
2	0.268	0.348	2	8139.9	7.91
3	0.348	0.403	3	12,930.2	12.57
4	0.403	0.446	4	18,292.2	17.78
5	0.446	0.484	5	25,334.4	24.63
6	0.484	0.529	6	20,966.9	20.38
7	0.529	0.597	7	9011.6	8.76
8	0.597	0.823	8	4718.2	4.59

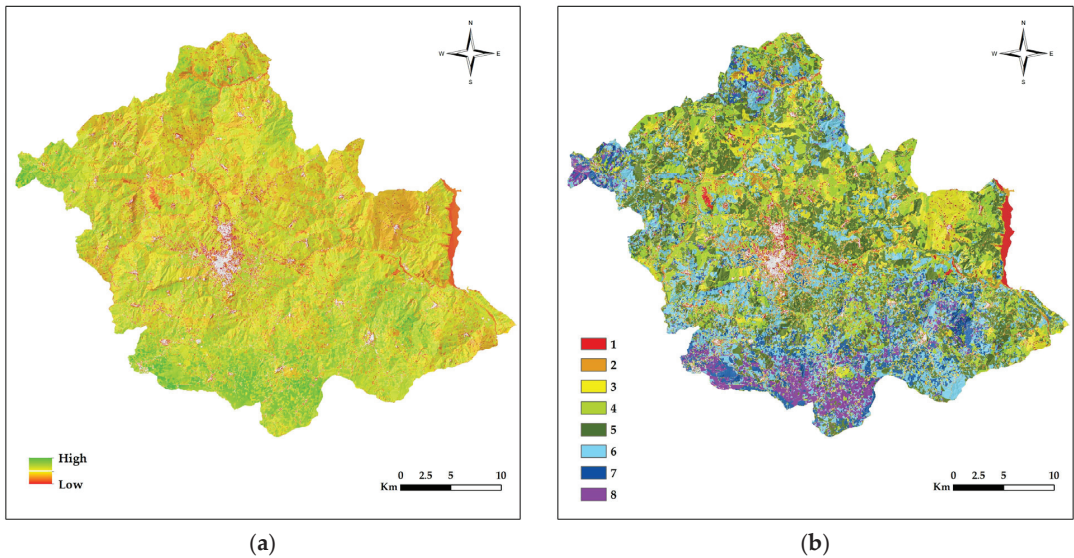


Figure 5. (a) Spatialized TESH index; (b) Clusters identified with K-means for grids from SAGA GIS.

After the spatialization of the TESH index, it was clustered into eight clusters according to the index values. Figure 5b shows the spatial distribution of the TESH index ranked in the eight clusters mentioned above.

Following the identification of the eight clusters, it was possible to extract only the cluster area of “Cropland” (Table 5) in order to analyze the distribution of the clusters within this land use class. As for the total area, the highest values are mostly concentrated in the southern part of the study area, while the lowest ones are in the eastern part (Figure 6).

Table 5. Percentage of individual clusters compared to the area of the class “Croplands”.

Cluster	Area (Ha)	Area %
1	740.09	1.42
2	3450.09	6.60
3	5991.32	11.46
4	10,637.76	20.35
5	16,843.73	32.22
6	12,116.36	23.18
7	2012.49	3.85
8	482.88	0.92

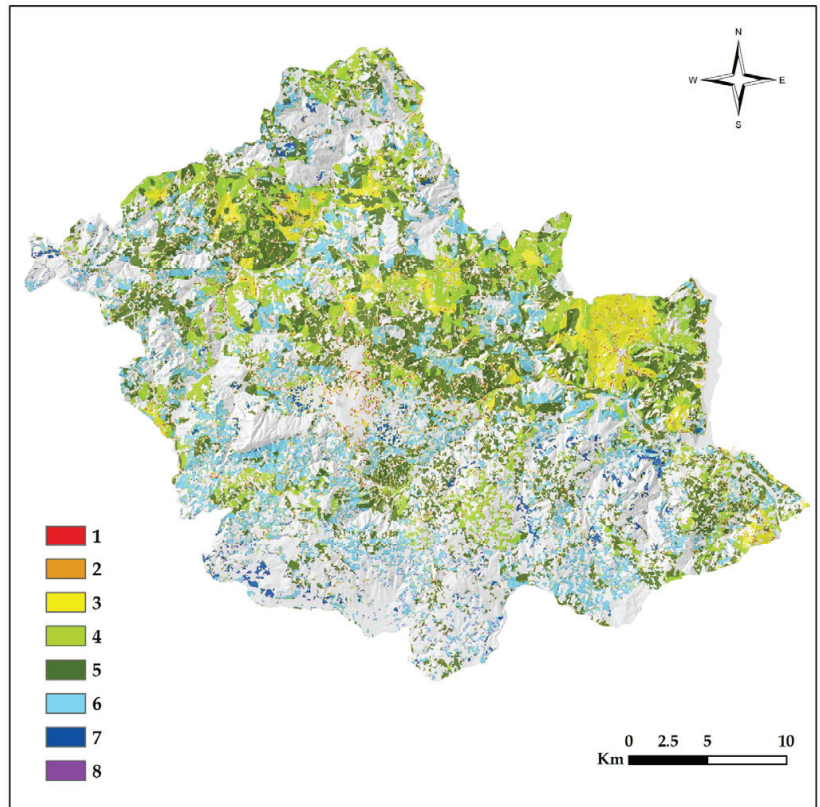


Figure 6. Distribution of clusters according to “Croplands”.

More than 70% of “Croplands” are represented by intermediate clusters (4, 5, and 6), with a range from 0.403 to 0.529.

3.2. Cartographies of Valuable Areas and Degraded Areas

Cluster 8 is identified as the one representing the most valuable areas based on the highest TESV values, with a range between 0.597 and 0.823 (Figure 7b). These areas cover a total of 4718.2 hectares, accounting for just 4.59% of the study area, and are predominantly located in the southwest. Only 9.5% of total valuable areas (448.23 Ha) fall within Natura2000 sites. In addition, just 10.23% of cluster 8 areas (482.88 Ha) are classified under the “Croplands” land use class.

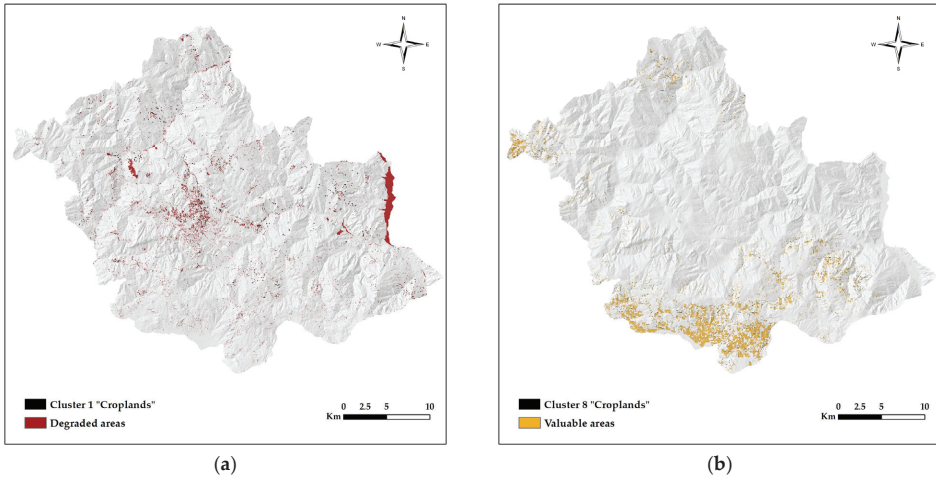


Figure 7. (a) Cluster 1 detailing those falling under Croplands; (b) Cluster 8 detailing those falling under Croplands.

On the other hand, the areas to be designated for NbS have the most degraded agricultural land use, particularly those in Cluster 1 of the “Croplands” class (Figure 7a), which represent 1.42% of this land use class (740.09 hectares). This portion represents 0.72% of the entire study area, and 22.62% (750.21 hectares) of “Croplands” in cluster 1 fall within the Natura2000 protected areas.

3.3. Future Scenarios: Potential Forest

By transforming the “Croplands” land use of Cluster 1 into forests and adding them to the “Forest” class, it was possible to obtain the map of potential forests, which would occur if these agricultural areas were subject to NbS interventions (Figure 8). The current “Forest” covers an area of 25,976.06 hectares, while the potential forest would have an area of 26,718.36 hectares, with an increase of 2.86% over the present situation (+742.30 hectares).

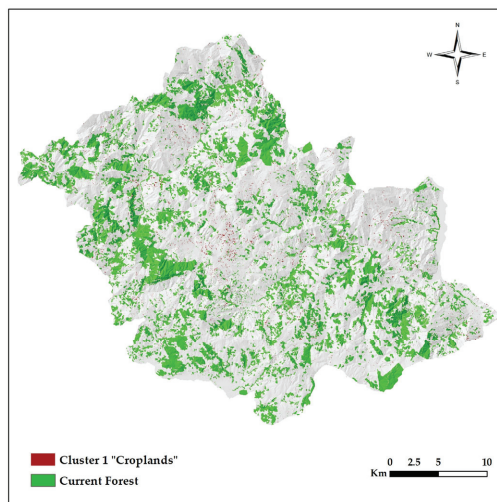


Figure 8. Potential Forest. In red are the newly added areas (cluster 1 Croplands).

In the current scenario, 18.20% of the “Forest” (4727.38 hectares) are Natura2000 areas; in the potential scenario, however, these increase to 49.38 hectares.

3.4. Analysis of Metrics

To investigate how connectivity and ecological functionality vary between the two scenarios, current forest, and potential forest, class, and landscape metrics were calculated using Fragstats software (ver. 4.2.1).

Table 6 shows the results obtained as outputs for the class metrics.

Table 6. Class metrics comparison between current and potential forest.

Metrics	Current Forest	Potential Forest
PD	4.8177	7.6036
LSI	96.6678	109.9036
TCA	26,269.55	27,011.85
ENN_MN	50.9801	44.3603
ENN_AM	28.2223	26.0803
PLADJ	94.0350	93.3110
NLSI	0.0591	0.0663

Analyzing the difference between current forest and potential forest (Table 6), it is evident that PD increases, in line with the addition of new patches from agricultural land. The same trend can be seen with the LSI, as the increase in forest class patches automatically makes them less rare. The increase in TCA is interesting, and it denotes an increase in patch contiguity and a reduction in fragmentation and edge effect; ENN_MN decreases, which means that the distance between patches decreases as their number increases, even in areas initially lacking “Forest” land use class, which was confirmed by ENN_AM. The reduction in the PLADJ shows a reduction in patch density not due to a reduction in number but to a greater dispersion of patches, resulting in greater fragmentation of the forest due to the addition of new patches. In addition, the increase in NLSI is indicative of greater class complexity and irregularity.

Table 7 shows the results obtained as outputs for the landscape metrics.

Table 7. Landscape metrics comparison between current and potential forest.

Metrics	Current Forest	Potential Forest
AREA_MN	2.7146	1.7686
GYRATE_MN	28.9786	22.7855
NDCA	9677	15,273
DCAD	4.8177	7.6036
AI	94.0930	93.3679

The “landscape” metrics considered (Table 7) are in line with the considerations made above for the “class” metrics. The AREA_MN increases due to the addition of new smaller forest patches. Also, the decrease in GYRATE_MN represents a reduction in the dispersion of patches around their center of mass, hence greater connectivity. The increase in NDCA denotes the increase in core areas, i.e., the increase in portions of habitat that are far from the edge and not affected by the edge effect, supported by the increase in DCAD. The reduction in AI, moreover, tends to emphasize a lower aggregation of particles, mainly due to the increase of forest patches even in areas that were initially devoid and, consequently, a greater dispersion of patches.

4. Discussion

4.1. Analysis Model

While developing the analysis model, it soon became clear that there was limited literature on the subject, not for what concerns mapping ESs, which are widely covered

and studied, but more for identifying areas characterized by poor ES delivery to be improved and for the extraction of degraded areas. Fahrudin et al. [73] stand out among the studies; its aim was to identify priority areas for afforestation and reforestation using an approach that integrates MCA and machine learning techniques based on indicators of ES, fire susceptibility, and environmental pressure. It is a multi-indicator approach, as this study, but uses different ES—carbon sequestration for climate change mitigation, biodiversity, and clean water. The present study differs both in the choice of parameters and areas, which in this case was achieved through the historical analysis of areas that have experienced deforestation due to various factors; however, the Fahrudin et al. survey was conducted on areas that were, in any case, characterized by disturbance, while the present study investigates low ES provision and inappropriate land use, according to the Land Capability map.

Another study examined was that of Coelho et al. [68], who developed a similar methodology, using AHP to develop an EVI (Environmental Vulnerability Index) based on four criteria—land use adequacy (like LCap), a burned area, erosion susceptibility, and quantitative water balance. The weights of the criteria derive from an expert-based approach. The final index was then spatialized, and five areas of equal size were divided within the study area. However, in addition to environmental factors, our study also considers economic factors, which were ignored by Coelho et al.

Among the few examples of models found, it was then decided to base this study on the one conducted by the working group of the University of Molise, in collaboration with ISPRA, on the Metropolitan City of Rome (MCR) [74], whose aim was the identification of agricultural areas of greater and lesser value. The MCR model used 4 ESs (CSS, QHb, Imp, and AP), then normalized and summed them together. In this study, as well as adding the information related to LCap, which influences the capacity of ESs to be delivered, it was decided to include an expert-based approach to get the weight of individual criteria to finally define the TESV index.

However, there are still some aspects that could be improved. The choice to submit the questionnaire only to experts was dictated by the need to have competent people in the investigation, but in a subsequent phase, stakeholders could also be involved, such as policymakers, local communities, as well as environmental NGOs, to obtain a broader opinion, not in particular in the definition of this index, but first for the choice of priority areas for intervention and what other needs the NbS to be created should satisfy, thus giving indications on the type and characteristics of the NbS to be created.

Another possible aspect to consider is related to the nature of ownership, public or private, of the identified areas. This information is fundamental for defining the management and restoration policies of the territory. In Italy, this information is accessible thanks to the national land cadastre, which is totally computerized and georeferenced, allowing it to be interrogated in order to know the ownership of each parcel. The system also allows a WMS (Web Map Service) to be used with all GIS software. Starting from the cartography of degraded agricultural areas to improve through NbS would make it possible to overlap the two layers and identify the parcels of interest and, thus, also the ownership in an exact manner. Nevertheless, areas around infrastructures are mostly publicly owned but managed by different entities depending on the infrastructure typology, so it would be possible to access public funding for NbS interventions in these areas. It would be useful to check the feasibility of projects aimed at improving the delivery of ES by minimizing the implications for private properties or by providing for public/private agreements aimed at improving the return for both [75].

The proposed model could be easily replicable for most of the Italian Regions; the availability of national data regarding the 4 ESs considered would allow for a large-scale analysis. In addition to this, it has been verified that 14 of the Italian regions have publicly accessible land capability maps available online, while the remaining seven may also have such maps, though they are not directly accessible online. For example, the Molise land

capability map was not directly accessible, but it was provided by the Molise Regional Geological Services.

4.2. Distribution of Clusters

Looking at the distribution of the TESV index throughout the study area, it is possible to state that the most prevalent values are the average ones. In fact, the most represented clusters are Clusters 4, 5, and 6 (values between 0.403 and 0.529), with an average TESV of 0.451. In fact, the valuable areas (Cluster 8), together with those of lesser value (Cluster 1), occupy less than 8% of the entire territory; if only agricultural areas are analyzed, out of the total of about 52,274 hectares, the percentage of the territory occupied by Clusters 1 and 8 is 2.34%. Parallel to the need to act on the rehabilitation of low TESV areas, the low presence of high value agricultural areas triggers considerations as to whether NbS should be used to increase them.

To analyze the location of degraded areas, a 60 m buffer was made around the urban land use of the ISPRA land use map (code 11000), in accordance with SNPA [16], to identify areas subject to influence by anthropogenic disturbances and to assess the percentage of degraded areas that fall within this buffer. Of the 3470.3 total hectares in Cluster 1, 70.61% fall within the buffer, while of the 740.09 hectares of arable land in the same Cluster, 86.18% (2990.7 Ha) fall within the buffer (Figure 9).

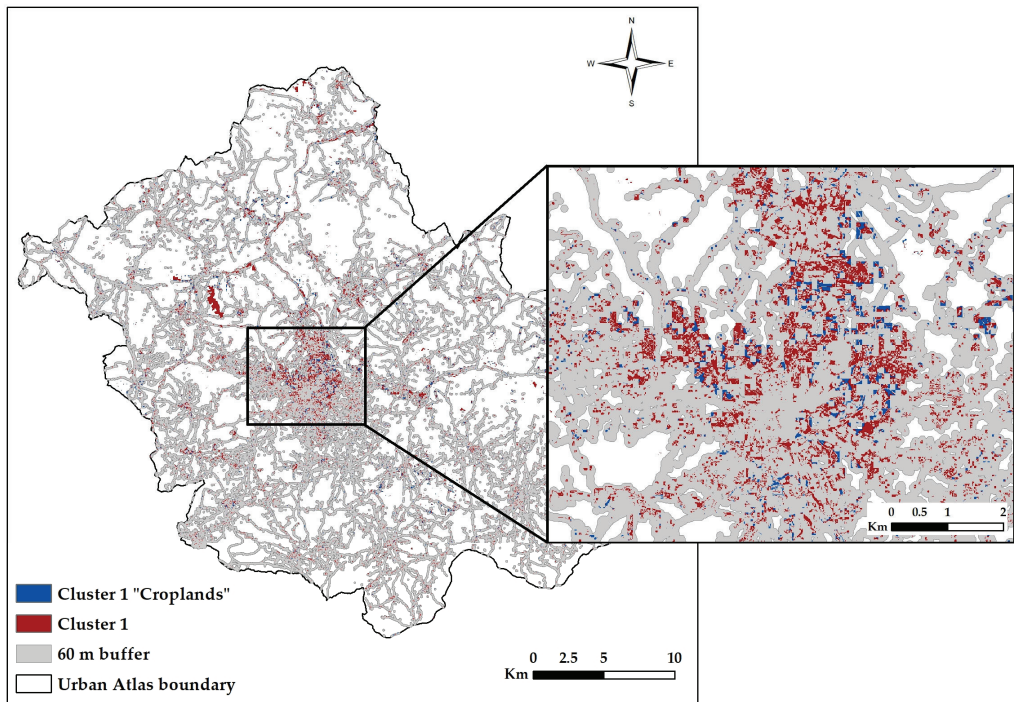


Figure 9. Degraded areas and 60 m urban buffer.

The output is in line with the values of the HbQ service, which is also the ES given the highest relative weight by most experts. As stated by Sallustio et al. [61], the quality and degradation of habitats are highly dependent on the distribution and intensity of anthropogenic impacts, and consequently also on the proximity of the disturbance, as well as on the suitability of a given portion of land to host species and habitats. The impact on HbQ increases as the distance from the disturbance decreases. The fact that the areas of greatest degradation fall largely within the buffer is a significant finding. Targeted

interventions could, in fact, encourage an increase in the quality of contiguous agricultural areas (e.g., through agroforestry facilities, which would increase the supply of ESs within the areas under consideration). In addition, they also prevent further land consumption due to unprofitable agricultural areas, which could be abandoned or built upon, further implementing land consumption and the deterioration of the structural and functional characteristics of the landscape matrix as a whole.

4.3. Connectivity

Linear soil sealing (e.g., roads and highways) plays a real barrier effect on migratory routes and animal movements in general, thus resulting in a serious threat to biodiversity [76].

The Landscape Ecology analysis was useful in highlighting an increase in the dispersion of the forest land use class, due, however, not to the fragmentation of existing patches, as they have not been reduced or converted to other land uses, but to the increase in the number of small forest patches (“Croplands”, Cluster 1) within areas initially devoid of this land use. A further problem is that, unfortunately, in some agricultural landscapes, these small forest patches are decreasing, including in Molise [77]. Another relevant aspect is the increase in core areas as well as increased patch complexity and irregularity, highlighted, respectively, by the TCA and NLSI class metrics together with the DCAD landscape metric. Despite forest fragmentation and disaggregation increase, the ENN_MN and ENN_AM class metrics emphasize greater connectivity. In fact, the increase in the number of smaller patches decreases their spacing, which renders better connectivity at the landscape level, which is highlighted by the GYRATE_MN landscape metric. The newly added patches can be configured as true steppingstones, fostering the connectivity and movement of species, and represent the starting point for the creation of continuous linear elements and green corridors, mainly close to the road network, also in line with the National Urban Green Strategy [2], whose purpose is to implement the Ecological Network at the national level, fostering connectivity between different areas (human, agricultural and natural).

4.4. Which NbS?

The choice of NbS to use to improve the delivery of ES is mainly dictated by the characteristics and location of degraded areas. For the rehabilitation and improvement of areas close to roads, one might consider investing mainly in green corridors or peri-urban forests. Much depends, however, on the type of ES to be enhanced, the available budget for its implementation and maintenance [78,79], or other policy-planning requirements.

It is crucial to plant trees, either isolated or in groups, as they are considered the best natural element to increase the spectrum of ES provisions [25], and they have the potential to reach high-standard restoration goals [80]; tree planting, in fact, would play a positive role in increasing connectivity and ecological restoration. Also not to be underestimated is the aesthetic perception of the landscape and how it might improve because of tree planting. A survey conducted by Di Cristofaro et al. [81] emphasized the aesthetic preference towards landscapes rich in out-of-forest trees in anthropized contexts, confirming the theory that the most common landscape preference is for increased exposure to nature, even more so in highly built-up areas.

Ultimately, the present experiment has highlighted the validity of the TESV index for identifying degraded areas and areas of value as a tool to support wide area spatial planning, as a connecting element between guidelines and policies, and the detailed planning level at a municipal scale, in line with Munafò et al. [74]. Since most works focus on the city and site scales [82], it could be an important approach to assess areas for NbS implementation at different scales.

The choice of the most suitable NbS for each case can be made with specific tools, such as those provided by the NBFC Project—Nature-based Solutions and Ecological Restoration (Spoke 4) [51]. The objectives of this project also included the implementation of a catalog and tool to support the design of NbS for the restoration and maximization of ecosystem services based on scientific evidence obtained in the field and laboratory through innovative

approaches. Planned actions include the cataloging of NbS case studies in degraded areas and the assessment of their impact, identification and testing of the most suitable tree and herbaceous species for NbS implementation.

5. Conclusions

The MCA applied for the identification of agricultural areas for NbS interventions seemed suitable for achieving our outlined objective; this method can be improved, but it is already possible to extend it to most of the national regions. The provision of ES in urban and peri-urban areas is an increasingly topical and relevant issue, considering that built-up land is expanding, urban permeable unforested lands are decreasing [83], and this brings with it a number of future challenges; land consumption is increasingly impactful and, in order to improve the lives of citizens, as well as the quality of productive agricultural land, it is important to incentivize such provisions. NbS could ultimately be the central aspect of achieving this goal in a variety of ways. The first way could be Agroforestry restoration [84], encouraged and financed by the European Union policy from the Common Agricultural Policy (CAP) [85], which provides numerous provisioning, regulating, cultural, and supporting ecosystem services and environmental benefits while promoting eointensification based on more efficient use of the resources [86].

Moreover, this methodology could be excellent support at various levels of planning, first and foremost at the municipal level, where there is often a shortage of funds to conduct ground surveys, direct management policies, and implement the structure of ecological networks at the national level. In addition, reducing fragmentation and fostering greater connectivity between urban, agricultural, and natural areas could improve the delivery of a multitude of ES, including cultural ones.

Author Contributions: Conceptualization, B.P., and M.O.; methodology, M.O.; software, M.O., and B.P.; validation, M.O.; formal analysis, B.P.; investigation, M.O., and B.P.; resources, M.O.; data curation, M.O.; writing—original draft preparation, M.O.; writing—reviewing and editing, B.P.; supervision, M.O. All authors have read and agreed to the published version of the manuscript.

Funding: This research was funded by National Biodiversity Future Center (NBFC); project funded under the National Recovery and Resilience Plan (NRRP), Mission 4 Component 2 Investment 1.4—Call for tender No. 3138 of 16 December 2021, rectified by Decree n.3175 of 18 December 2021 of the Italian Ministry of University and Research funded by the European Union—NextGenerationEU; Award Number Project code CN_00000033, Concession Decree No. 1034 of 17 June 2022 adopted by the Italian Ministry of University and Research, CUP H73C22000300001, Project title “National Biodiversity Future Center—NBFC”.

Data Availability Statement: The data that support the findings of this study are available from the corresponding author upon reasonable request and approval from the study site representative coauthors. The data are not publicly available because they are part of ongoing research.

Acknowledgments: The authors would like to thank Lorenzo Sallustio for the methodological support and supervision of some phases of this study.

Conflicts of Interest: The authors declare no conflict of interest.

References

1. Salbitano, F.; Borelli, S.; Conigliaro, M.; Chen, Y. *Guidelines on Urban and Peri-Urban Forestry*; Food and Agriculture Organization of the United Nations (FAO): Rome, Italy, 2016; ISBN 9789251094426.
2. Atelli, M.; Blasi, C.; Boldini, G.; Cignini, B.; Cosenza, G.; Emiliani, V.; Marchetti, M.; Maria Maggiore, A.; Pericoli, T.; Ricciardi, A.; et al. *Strategia Nazionale Del Verde Urbano (Comitato Del Verde Pubblico)*; Ministero dell’Ambiente e della Sicurezza Energetica: Rome, Italy, 2018.
3. Baumeister, C.F.; Gerstenberg, T.; Plieninger, T.; Schraml, U. Exploring Cultural Ecosystem Service Hotspots: Linking Multiple Urban Forest Features with Public Participation Mapping Data. *Urban For. Urban Green.* **2020**, *48*, 126561. [CrossRef]
4. Churkina, G. Modeling the Carbon Cycle of Urban Systems. *Ecol Modell* **2008**, *216*, 107–113. [CrossRef]
5. World Health Organization—Regional Office for Europe. *Urban Green Spaces: A Brief for Action*; WHO: Geneva, Switzerland, 2017.

6. Fusaro, L.; Salvatori, E.; Mereu, S.; Marando, F.; Scassellati, E.; Abbate, G.; Manes, F. Urban and Peri-Urban Forests in the Metropolitan Area of Rome: Ecophysiological Response of *Quercus ilex* L. in Two Green Infrastructures in an Ecosystem Services Perspective. *Urban For. Urban Green*. **2015**, *14*, 1147–1156. [CrossRef]
7. Gill, S.E.; Handley, J.F.; Ennos, A.R.; Pauleit, S. Adapting Cities for Climate Change: The Role of the Green Infrastructure. *Built Environ.* **2007**, *33*, 115–133. [CrossRef]
8. Pulighe, G.; Fava, F.; Lupia, F. Insights and Opportunities from Mapping Ecosystem Services of Urban Green Spaces and Potentials in Planning. *Ecosyst. Serv.* **2016**, *22*, 1–10. [CrossRef]
9. Poe, M.R.; LeCompte, J.; McLain, R.; Hurley, P. Urban Foraging and the Relational Ecologies of Belonging. *Soc. Cult. Geogr.* **2014**, *15*, 901–919. [CrossRef]
10. Lee, A.C.K.; Maheswaran, R. The Health Benefits of Urban Green Spaces: A Review of the Evidence. *J. Public Health* **2011**, *33*, 212–222. [CrossRef]
11. Campagnaro, T.; Vecchiato, D.; Arnberger, A.; Celegato, R.; Da Re, R.; Rizzetto, R.; Semenzato, P.; Sitzia, T.; Tempesta, T.; Cattaneo, D. General, Stress Relief and Perceived Safety Preferences for Green Spaces in the Historic City of Padua (Italy). *Urban For. Urban Green*. **2020**, *52*, 126695. [CrossRef]
12. Sacker, A.; Cable, N. Do Adolescent Leisure-Time Physical Activities Foster Health and Well-Being in Adulthood? Evidence from Two British Birth Cohorts. *Eur. J. Public Health* **2006**, *16*, 331–335. [CrossRef]
13. Takano, T.; Nakamura, K.; Watanabe, M. Urban Residential Environments and Senior Citizens' Longevity in Megacity Areas: The Importance of Walkable Green Spaces. *J. Epidemiol. Community Health* **2002**, *56*, 913–918. [CrossRef]
14. Cueva, J.; Yakouchenkova, I.A.; Fröhlich, K.; Dermann, A.F.; Dermann, F.; Köhler, M.; Grossmann, J.; Meier, W.; Bauhus, J.; Schröder, D.; et al. Synergies and Trade-Offs in Ecosystem Services from Urban and Peri-urban Forests and Their Implication to Sustainable City Design and Planning. *Sustain. Cities Soc.* **2022**, *82*, 103903. [CrossRef]
15. Munafò, M. (Ed.) *Consumo Di Suolo, Dinamiche Territoriali e Servizi Ecosistemici. Edizione 2021*; Report SNPA 22/21; SNPA: Rome, Italy, 2021; ISBN 978-88-448-1059-7.
16. Munafò, M. (Ed.) *Consumo Di Suolo, Dinamiche Territoriali e Servizi Ecosistemici. Edizione 2022*; Report SNPA 32/22; SNPA: Rome, Italy, 2022; ISBN 978-88-448-1124-2.
17. Marull, J.; Pino, J.; Tello, E.; Cordobilla, M.J. Social Metabolism, Landscape Change and Land-Use Planning in the Barcelona Metropolitan Region. *Land Use Policy* **2010**, *27*, 497–510. [CrossRef]
18. Millennium Ecosystem Assessment (MEA). *Ecosystems and Human Well-Being: A Report of the Millennium Ecosystem Assessment*; Island Press: Washington, DC, USA, 2005.
19. Youssef, A.; Sewilam, H.; Khadr, Z. Impact of Urban Sprawl on Agriculture Lands in Greater Cairo. *J. Urban Plan. Dev.* **2020**, *146*, 05020027. [CrossRef]
20. Parece, T.E.; Campbell, J.B. Geospatial Evaluation for Urban Agriculture Land Inventory. *Int. J. Appl. Geospat. Res.* **2017**, *8*, 43–63. [CrossRef]
21. European Union. *Building a Green Infrastructure for Europe*; Publ. Office of the European Union: Luxembourg, 2013; ISBN 978-92-793-3428-3.
22. Potschin, M.; Haines-Young, R.H. *Nature-Based Solutions ESMEALDA-Enhancing Ecosystem Services Mapping for Policy and Decision Making View Project*; European Commission: Luxembourg, 2015.
23. Eisenberg, B. *Nature Based Solutions-Technical Handbook INTERESS-I: Integrierte Strategien Zur Stärkung Urbaner Blau-Grüner Infrastrukturen View Project Space Syntax and Open Space Planning View Project*; UnaLab: Eindhoven, The Netherlands, 2019. [CrossRef]
24. Price, R. *Nature-Based Solutions (NbS)-What Are They and What Are the Barriers and Enablers to Their Use?* Institute of Development Studies: Brighton, UK, 2021.
25. Di Pirro, E.; Sallustio, L.; Castellari, J.A.C.; Sgrigna, G.; Marchetti, M.; Lasserre, B. Facing Multiple Environmental Challenges through Maximizing the Co-Benefits of Nature-Based Solutions at a National Scale in Italy. *Forests* **2022**, *13*, 548. [CrossRef]
26. Science for Environment Policy. *FUTURE BRIEF: The Solution is in Nature-Issue 24*; Brief Produced for the European Commission DG Environment; Science Communication Unit, UWE Bristol: Bristol, UK, 2021.
27. Sowińska-Świerkosz, B.; García, J. What Are Nature-Based Solutions (NBS)? Setting Core Ideas for Concept Clarification. *Nat.-Based Solut.* **2022**, *2*, 100009. [CrossRef]
28. Nesshöver, C.; Assmuth, T.; Irvine, K.N.; Rusch, G.M.; Waylen, K.A.; Delbaere, B.; Haase, D.; Jones-Walters, L.; Keune, H.; Kovacs, E.; et al. The Science, Policy and Practice of Nature-Based Solutions: An Interdisciplinary Perspective. *Sci. Total Environ.* **2017**, *579*, 1215–1227. [CrossRef]
29. Seddon, N.; Chausson, A.; Berry, P.; Girardin, C.A.J.; Smith, A.; Turner, B. Understanding the Value and Limits of Nature-Based Solutions to Climate Change and Other Global Challenges. *Philos. Trans. R. Soc. B Biol. Sci.* **2020**, *375*, 20190120. [CrossRef]
30. Frantzeskaki, N.; McPhearson, T.; Collier, M.J.; Kendal, D.; Bulkeley, H.; Dumitru, A.; Walsh, C.; Noble, K.; van Wyk, E.; Ordóñez, C.; et al. Nature-Based Solutions for Urban Climate Change Adaptation: Linking Science, Policy, and Practice Communities for Evidence-Based Decision-Making. *Bioscience* **2019**, *69*, 455–466. [CrossRef]
31. Chausson, A.; Turner, B.; Seddon, D.; Chabaneix, N.; Girardin, C.A.J.; Kapos, V.; Key, I.; Roe, D.; Smith, A.; Woroniecki, S.; et al. Mapping the Effectiveness of Nature-based Solutions for Climate Change Adaptation. *Glob. Chang. Biol.* **2020**, *26*, 6134–6155. [CrossRef]

32. European Commission. 3 Billion Trees Pledge. Available online: https://knowledge4policy.ec.europa.eu/publication/commission-staff-working-document-swd2021651-3-billion-tree-planting-pledge-2030_en (accessed on 15 June 2024).
33. Goffner, D.; Sinare, H.; Gordon, L.J. The Great Green Wall for the Sahara and the Sahel Initiative as an Opportunity to Enhance Resilience in Sahelian Landscapes and Livelihoods. *Reg. Environ. Chang.* **2019**, *19*, 1417–1428. [CrossRef]
34. Seddon, N.; Smith, A.; Smith, P.; Key, I.; Chausson, A.; Girardin, C.; House, J.; Srivastava, S.; Turner, B. Getting the Message Right on Nature-based Solutions to Climate Change. *Glob. Chang. Biol.* **2021**, *27*, 1518–1546. [CrossRef] [PubMed]
35. Kapos, V.; Wicander, S.; Salvaterra, T.; Dawkins, K.; Hicks, C. *The Role of the Natural Environment in Adaptation, Background Paper for the Global Commission on Adaptation*; Global Commission on Adaptation: Rotterdam, The Netherlands; Washington, DC, USA, 2019.
36. Zhu, D.; Zhang, Y.; Kendal, D.; Fraser, L.; Flies, E.J. Nature-Based Solutions in Australia: A Systematic Quantitative Literature Review of Terms, Application and Policy Relevance. *Nat.-Based Solut.* **2023**, *4*, 100092. [CrossRef]
37. Molloy, A.; Collier, M.; Buckley, Y.M. *Identification and Assessment of Best Practice in Nature-Based Solutions for Climate Action and Ecosystem Restoration in Ireland*; Working Paper No. 26; Climate Change Advisory Council: Dublin, Ireland, 2024.
38. Di Pirro, E.; Mendes, R.; Fidélis, T.; Sallustio, L.; Roebeling, P.; Marchetti, M.; Lasserre, B. The Embeddedness of Nature-Based Solutions in the Recovery and Resilience Plans as Multifunctional Approaches to Foster the Climate Transition: The Cases of Italy and Portugal. *Land* **2022**, *11*, 1254. [CrossRef]
39. Mendonça, R.; Roebeling, P.; Fidélis, T.; Saraiva, M. Policy Instruments to Encourage the Adoption of Nature-Based Solutions in Urban Landscapes. *Resources* **2021**, *10*, 81. [CrossRef]
40. Dorst, H.; van der Jagt, A.; Raven, R.; Runhaar, H. Urban Greening through Nature-Based Solutions—Key Characteristics of an Emerging Concept. *Sustain. Cities Soc.* **2019**, *49*, 101620. [CrossRef]
41. Chazdon, R.L. Beyond Deforestation: Restoring Forests and Ecosystem Services on Degraded Lands. *Science* **2008**, *320*, 1458–1460. [CrossRef]
42. Urgenson, L.S.; Ryan, C.M.; Halpern, C.B.; Bakker, J.D.; Belote, R.T.; Franklin, J.F.; Haugo, R.D.; Nelson, C.R.; Waltz, A.E.M. Visions of Restoration in Fire-Adapted Forest Landscapes: Lessons from the Collaborative Forest Landscape Restoration Program. *Environ. Manag.* **2017**, *59*, 338–353. [CrossRef]
43. Voskamp, I.M.; de Luca, C.; Polo-Ballinas, M.B.; Hulsman, H.; Brolsma, R. Nature-Based Solutions Tools for Planning Urban Climate Adaptation: State of the Art. *Sustainability* **2021**, *13*, 6381. [CrossRef]
44. Standish, R.J.; Hobbs, R.J.; Mayfield, M.M.; Bestelmeyer, B.T.; Suding, K.N.; Battaglia, L.L.; Eviner, V.; Hawkes, C.V.; Temperton, V.M.; Cramer, V.A.; et al. Resilience in Ecology: Abstraction, Distraction, or Where the Action Is? *Biol. Conserv.* **2014**, *177*, 43–51. [CrossRef]
45. Johnson, B.A.; Kumar, P.; Okano, N.; Dasgupta, R.; Shivakoti, B.R. Nature-Based Solutions for Climate Change Adaptation: A Systematic Review of Systematic Reviews. *Nat.-Based Solut.* **2022**, *2*, 100042. [CrossRef]
46. Battisti, L.; Giacco, G.; Moraca, M.; Pettenati, G.; Dansero, E.; Larcher, F. Spatializing Urban Forests as Nature-Based Solutions: A Methodological Proposal. *Cities* **2024**, *144*, 104629. [CrossRef]
47. Yimer, E.A.; De Trift, L.; Dondeyne, S.; Speijer, L.; Huysmans, M.; Cools, J.; Nossent, J.; van Griensven, A. Framework for Mapping Large-Scale Nature-Based Solutions for Drought Mitigation: Regional Application in Flanders. *Water Res.* **2024**, *261*, 122003. [CrossRef] [PubMed]
48. Guerrero, P.; Haase, D.; Albert, C. Locating Spatial Opportunities for Nature-Based Solutions: A River Landscape Application. *Water* **2018**, *10*, 1869. [CrossRef]
49. Balzan, M.V.; Zulian, G.; Maes, J.; Borg, M. Assessing Urban Ecosystem Services to Prioritise Nature-Based Solutions in a High-Density Urban Area. *Nat.-Based Solut.* **2021**, *1*, 100007. [CrossRef]
50. European Commission. Mapping Guide Urban Atlas. 2023. Available online: <https://insitu.copernicus.eu/library/reports/summary-report-of-the-methodological-improvement-of-urban-atlas-layer-1-2-00-jan-2024> (accessed on 23 September 2024).
51. NBFC (National Biodiversity Future Center) Project. Funded under the National Recovery and Resilience Plan (NRRP), Mission 4 Component 2 Investment 1.4. 2021. Available online: <https://www.nbfc.it/progetto> (accessed on 29 October 2024).
52. Amadei, M.; Bagnaia, R.; Di Bucci, D.; Laureti, L.; Luger, F.R.; Nisio, S.; Salvucci, R. Carta Della Natura Alla Scala 1:250.000: Carta Dei Tipi e Delle Unità Fisiografiche Di Paesaggio d'Italia, 2003rd ed. 2000. Available online: <https://www.isprambiente.gov.it/it/servizi/sistema-carta-della-natura/cartografia/carta-della-natura-a-scala-nazionale/la-carta-dei-tipi-e-delle-unita-fisiografiche-di-paesaggio-d2019italia> (accessed on 1 June 2024).
53. ISPRA. *Carta Di Copertura Del Suolo 2018 Basata Su Dati Copernicus e Su Dati ISPRA*; ISPRA: Rome, Italy, 2018.
54. Munafo, M. (Ed.) *Consumo Di Suolo, Dinamiche Territoriali e Servizi Ecosistemici. Edizione 2023*; Report SNPA 37/23; SNPA: Rome, Italy, 2023; ISBN 978-88-448-1178-5.
55. Munafo, M. (Ed.) *Consumo Di Suolo, Dinamiche Territoriali e Servizi Ecosistemici. Edizione 2018*; Report SNPA 08/19; SNPA: Rome, Italy, 2019; ISBN 978-88-448-0964-5.
56. Stanford University; University of Minnesota; Chinese Academy of Sciences; The Nature Conservancy; World Wildlife Fund; Stockholm Resilience Centre; Royal Swedish Academy of Sciences. Natural Capital Project, InVEST 0.0. 2024. Available online: <https://naturalcapitalproject.stanford.edu/software/invest> (accessed on 15 July 2024).
57. Sallustio, L.; Quatrini, V.; Geneletti, D.; Corona, P.; Marchetti, M. Assessing Land Take by Urban Development and Its Impact on Carbon Storage: Findings from Two Case Studies in Italy. *Environ. Impact Assess Rev.* **2015**, *54*, 80–90. [CrossRef]

58. Munafò, M. (Ed.) *Consumo Di Suolo, Dinamiche Territoriali e Servizi Ecosistemici. Edizione 2016*; Report SNPA 248/16; SNPA: Rome, Italy, 2016; ISBN 978-88-448-0776-4.
59. European Environment Agency. *High Resolution Layers*; European Environment Agency: Copenhagen, Denmark, 2023.
60. EEA. *CORINE Land Cover 2012 (Vector/Raster 100 m), Europe, 6-Yearly*; EEA: Copenhagen, Denmark, 2012.
61. Sallustio, L.; De Toni, A.; Strollo, A.; Di Febbraro, M.; Gissi, E.; Casella, L.; Geneletti, D.; Munafò, M.; Vizzarri, M.; Marchetti, M. Assessing Habitat Quality in Relation to the Spatial Distribution of Protected Areas in Italy. *J. Environ. Manag.* **2017**, *201*, 129–137. [CrossRef]
62. Agenzia Entrate Valori Agricoli Medi. Available online: <https://www.agenziaentrate.gov.it/portale/web/guest/schede/fabbricatierreni/omi/banche-dati/valori-agricoli-medi/valori-agricoli-medi-molise> (accessed on 12 June 2024).
63. Bellucci, V.; Bianco, P.M.; Strollo, A.; Marchetti, M.; Marino, D.; Marucci, A.; Munafò, M.; Palmieri, M.; Sallustio, L.; Soraci, M. Distribuzione Potenziale Degli Impollinatori Nelle Aree Agricole Secondo Il Modello InVest. *L'apicoltore Ital.* **2016**, *7*, 9–12.
64. Araújo Costa, R.C.; Pereira, G.T.; Tarlé Pissarra, T.C.; Silva Siqueira, D.; Sanches Fernandes, L.F.; Vasconcelos, V.; Fernandes, L.A.; Pacheco, F.A.L. Land Capability of Multiple-Landform Watersheds with Environmental Land Use Conflicts. *Land Use Policy* **2019**, *81*, 689–704. [CrossRef]
65. Klingebiel, A.A.; Montgomery, P.H. *Land-Capability Classification*; Soil Conservation Service, US Department of Agriculture: Washington, DC, USA, 1961; Volume 210.
66. Dean, M. A Practical Guide to Multi-Criteria Analysis MORE (Multi-Modal Optimisation of Road-Space in Europe) Project View Project Achieving Transitions to Zero Carbon Emissions and Sustainable Urban Mobility View Project. 2022. Available online: <https://www.researchgate.net/publication/358131153> (accessed on 2 June 2024). [CrossRef]
67. Saaty, R.W. The Analytic Hierarchy Process—What It Is and How It Is Used. *Math. Model.* **1987**, *9*, 161–176. [CrossRef]
68. Coelho, C.D.; da Silva, D.D.; Amorim, R.S.S.; Vasconcelos, B.N.F.; Possato, E.L.; Filho, E.I.F.; Brandão, P.C.; Ferreira Neto, J.A.; Silva, L.V. Development and Application of an Environmental Vulnerability Index (EVI) for Identifying Priority Restoration Areas in the São Francisco River Basin, Brazil. *Land* **2024**, *13*, 1475. [CrossRef]
69. Wedley, W.C. Consistency Prediction for Incomplete AHP Matrices. *Math. Comput. Model.* **1993**, *17*, 151–161. [CrossRef]
70. Vizzarri, M.; Sallustio, L.; Travaglini, D.; Bottalico, F.; Chirici, G.; Garfi, V.; Laforteza, R.; Veca, D.S.L.M.; Lombardi, F.; Maetke, F.; et al. The MIMOSE Approach to Support Sustainable Forest Management Planning at Regional Scale in Mediterranean Contexts. *Sustainability* **2017**, *9*, 316. [CrossRef]
71. Wu, J. Landscape Ecology. In *Ecological Systems*; Springer: New York, NY, USA, 2013; pp. 179–200.
72. McGarigal, K.; Marks, B.J. *FRAGSTATS: Spatial Pattern Analysis Program for Quantifying Landscape Structure*; US Department of Agriculture, Forest Service, Pacific Northwest Research Station: Portland, OR, USA, 1995.
73. Fahrudin; Sakti, A.D.; Komara, H.Y.; Sumarga, E.; Choiruddin, A.; Hendrawan, V.S.A.; Hati, T.; Anna, Z.; Wikantika, K. Optimizing Afforestation and Reforestation Strategies to Enhance Ecosystem Services in Critically Degraded Regions. *Trees For. People* **2024**, *18*, 100700. [CrossRef]
74. Munafò, M.; Strollo, A.; Tonti, D.; Marchetti, M. Consumo Di Suolo e Dinamiche Territoriali Ed Ecologiche. In *Roma Città-Territorio—Abitare Un Contesto Metropolitano*; Quodlibet: Macerata, Italy, 2024; ISBN 978-88-229-2251-9.
75. ETIFOR Oltrepò Pavese: Governance e Finanziamenti. Available online: <https://www.etifor.com/it/portfolio/oltrepo-pavese/> (accessed on 19 October 2024).
76. De Toni, A.; Casella, L.; Marchetti, M. *ISPRA_2016_QualitàHabitatDeToni*; ISPRA: Rome, Italy, 2016.
77. Ottaviano, M.; Marchetti, M. Census and Dynamics of Trees Outside Forests in Central Italy: Changes, Net Balance and Implications on the Landscape. *Land* **2023**, *12*, 1013. [CrossRef]
78. Raymond, C.M.; Frantzeskaki, N.; Kabisch, N.; Berry, P.; Breil, M.; Nita, M.R.; Geneletti, D.; Calfapietra, C. A Framework for Assessing and Implementing the Co-Benefits of Nature-Based Solutions in Urban Areas. *Environ. Sci. Policy* **2017**, *77*, 15–24. [CrossRef]
79. Connop, S.; Vandergert, P.; Eisenberg, B.; Collier, M.J.; Nash, C.; Clough, J.; Newport, D. Renaturing Cities Using a Regionally-Focused Biodiversity-Led Multifunctional Benefits Approach to Urban Green Infrastructure. *Environ. Sci. Policy* **2016**, *62*, 99–111. [CrossRef]
80. Standish, R.J.; Parkhurst, T. Interventions for Resilient Nature-based Solutions: An Ecological Perspective. *J. Ecol.* **2024**, *112*, 2502–2509. [CrossRef]
81. Di Cristofaro, M.; Sallustio, L.; Sitzia, T.; Marchetti, M.; Lasserre, B. Landscape Preference for Trees Outside Forests along an Urban–Rural–Natural Gradient. *Forests* **2020**, *11*, 728. [CrossRef]
82. Ernstson, H.; Barthel, S.; Andersson, E.; Borgström, S.T. Scale-Crossing Brokers and Network Governance of Urban Ecosystem Services: The Case of Stockholm. *Ecol. Soc.* **2010**, *15*, 28. [CrossRef]
83. Di Cristofaro, M.; Di Pirro, E.; Ottaviano, M.; Marchetti, M.; Lasserre, B.; Sallustio, L. Greener or Greyer? Exploring the Trends of Sealed and Permeable Spaces Availability in Italian Built-Up Areas during the Last Three Decades. *Forests* **2022**, *13*, 1983. [CrossRef]
84. Quintero-Angel, M.; Cerón-Hernández, V.A.; Ospina-Salazar, D.I. Applications and Perspectives for Land Restoration through Nature-Based Solutions. *Curr. Opin. Environ. Sci. Health* **2023**, *36*, 100518. [CrossRef]

85. European Commission. *The Common Agricultural Policy*; European Commission: Luxembourg, 2023.
86. Pantera, A.; Mosquera-Losada, M.R.; Herzog, F.; den Herder, M. Agroforestry and the Environment. *Agrofor. Syst.* **2021**, *95*, 767–774. [CrossRef]

Disclaimer/Publisher’s Note: The statements, opinions and data contained in all publications are solely those of the individual author(s) and contributor(s) and not of MDPI and/or the editor(s). MDPI and/or the editor(s) disclaim responsibility for any injury to people or property resulting from any ideas, methods, instructions or products referred to in the content.

Article

Impacts of Different Vegetation Types on Soil Aggregate Stability in the Key Ecological Rehabilitation Area of the Tarim River Basin, Northwest China

Qin Zhang ^{1,2,3}, Chunfang Yue ^{1,2,*}, Pujia Yu ^{4,5}, Hailiang Xu ^{3,6,*}, Kun Liu ^{1,2,3}, Jie Wu ^{1,2,3} and Fangyu Sheng ^{1,2,3}

- ¹ College of Hydraulic and Civil Engineering, Xinjiang Agricultural University, Urumqi 830052, China; zqin28@outlook.com (Q.Z.)
 - ² Xinjiang Key Laboratory of Hydraulic Engineering Security and Water Disasters Prevention, Xinjiang Agricultural University, Urumqi 830052, China
 - ³ State Key Laboratory of Desert and Oasis Ecology, Xinjiang Institute of Ecology and Geography, Chinese Academy of Sciences, Urumqi 830011, China
 - ⁴ Chongqing Jinpo Mountain Karst Ecosystem National Observation and Research Station, School of Geographical Sciences, Southwest University, Chongqing 400715, China
 - ⁵ Chongqing Engineering Research Center for Remote Sensing Big Data Application, School of Geographical Sciences, Southwest University, Chongqing 400715, China
 - ⁶ Chinese Academy of Sciences, Beijing 100049, China
- * Correspondence: yuecf12@xjau.edu.cn (C.Y.); xuhl2024@163.com (H.X.)

Abstract: Disentangling the responses of total soil organic carbon (SOC), organic carbon fractions and soil aggregate stability to various vegetation types is essential for better understanding the carbon cycling process in terrestrial ecosystems, maintaining soil quality and mitigating global warming. To study the effects of vegetation types on soil aggregates in a specific area, the desert riverbanks of arid regions were studied. We set up experiments using three typical vegetation types in the arid zone of the Tarim River Basin (TRB), including Forestland, Shrubland, and Grassland. The total SOC content in the bulk soil and different soil aggregates was determined by oxidation with $K_2Cr_2O_7$ and H_2SO_4 , and three carbon fractions (F1, very labile; F2, inert; F3, oxidizable resistant) were classified according to the degree of oxidation using the modified Walkley-Black method. The total SOC and three carbon fractions in the soil were significantly greater in the Forestland than in the other vegetation types, and the effect was more pronounced in macro-aggregate (MA) than in the other aggregates. In the bulk soil and soil aggregates, the percentages of F1, F2 and F3 in the total SOC with mean values of 0.36%, 0.28% and 0.36%, respectively, at soil depths of 0–20 cm, indicated that stabilizing carbon is the major carbon fraction of the SOC. The stability of the SOC in the aggregates across each vegetation type was greater in the lower layer (10–20 cm) than in the topsoil layer (0–10 cm). The SOC stability and MA content were positively related to the SOC in the soil aggregates and its F2 and F3 fractions ($p < 0.05$). In summary, the Forestland significantly increased the SOC content and enhanced SOC stability. Conservation measures for poplar forests in vulnerable arid zones can sustainably accumulate SOC sequestration.

Citation: Zhang, Q.; Yue, C.; Yu, P.; Xu, H.; Liu, K.; Wu, J.; Sheng, F. Impacts of Different Vegetation Types on Soil Aggregate Stability in the Key Ecological Rehabilitation Area of the Tarim River Basin, Northwest China. *Land* **2024**, *13*, 2157. <https://doi.org/10.3390/land13122157>

Academic Editors: Jianye Li, Weida Gao, Wei Hu, Qiang Chen and Xingyi Zhang

Received: 5 November 2024
Revised: 8 December 2024
Accepted: 10 December 2024
Published: 11 December 2024

Keywords: vegetation type; aggregate composition; oxidizable carbon fraction; SOC stability



Copyright: © 2024 by the authors. Licensee MDPI, Basel, Switzerland. This article is an open access article distributed under the terms and conditions of the Creative Commons Attribution (CC BY) license (<https://creativecommons.org/licenses/by/4.0/>).

1. Introduction

Soil is the reservoir of the greatest amount of carbon in terrestrial ecosystems, with a carbon storage capacity approximately 3–4 times that of vegetation carbon pools, and 2–3 times that of atmospheric carbon pools [1,2]. Therefore, even minor fluctuations in SOC storage can have significant implications for atmospheric CO₂ concentrations, thereby influencing climate change [3,4]. Additionally, soil organic carbon (SOC) is one of the core characteristics of soil, playing a crucial role in plant growth and soil fertility, and directly affects soil quality [5]. The composition of soil aggregates and the stability of organic

carbon in the aggregates determine the soil structure and are considered effective targets of soil quality [6]. Vegetation type is a primary factor influencing the composition of soil aggregates and their ability to sequester carbon, as it alters the input of organic residues and modifies soil management practices [7]. Vegetation rehabilitation and afforestation can significantly increase the number of carbon sinks within terrestrial ecosystems and serve as crucial pathways for achieving carbon neutrality and mitigating global climate change [8,9]. Consequently, a comprehensive understanding of the soil aggregate composition and aggregate stability across various vegetation types is critical for sustaining SOC storage and enhancing the ecological functions of soil ecosystems [2].

Soil aggregates are the basic units of soil structure and are significant indicators of soil quality and health [10]. Macro-aggregate (MA) ($>250\ \mu\text{m}$) exhibits greater porosity, providing sufficient moisture and oxygen to facilitate the microbial decomposition of organic carbon. In contrast, as the pore size decreases in micro-aggregate (MI) ($53\ \mu\text{m}$ – $250\ \mu\text{m}$) and silt–clay aggregates (SC) ($<53\ \mu\text{m}$), the reduction in moisture and oxygen contents hinders the microbial degradation of the organic carbon encapsulated within the aggregates [11]. Vegetation type changes can lead to significant alterations in the composition of soil aggregates through the formation or disruption of aggregates, thereby affecting the SOC content of various soil aggregates [12]. Vegetation rehabilitation increases the input of organic carbon by increasing vegetation biomass, which in turn contributes to the formation of soil aggregates and improves aggregate stability [13]. Research has revealed that with increasing duration of vegetation rehabilitation, soil aggregate stability improves, and both the mean weight diameter and geometric mean diameter tend to increase [14]. Additionally, the SOC content within soil aggregates of various particle sizes also increases over time [15]. Vegetation rehabilitation enhances the accumulation of SOC in MA while also increasing the content of inert components in MI, thereby improving the stability of SOC [16]. Increased MA helps maintain soil aggregate stability during the rehabilitation of vegetation protection [17]. The increase in aggregate stability can increase the physical protection of SOC within the aggregates [18]. Moreover, recent studies have employed stable carbon isotope technology to examine the stability and turnover of organic carbon within soil aggregates during vegetation rehabilitation. This research further aids in understanding the direction and intensity of carbon flow [19]. As forest succession progresses, the movement of organic carbon toward MI intensifies, which increases the stability of SOC [20].

The stability of SOC is a crucial element that controls soil carbon emissions and storage [21], and plays a significant role in maintaining the carbon balance and addressing global climate change [22]. In recent years, the study of SOC stabilization mechanisms during vegetation rehabilitation processes has become a focus and a challenge of research [23]. Stable SOC has a longer average residence time in the soil [24]. As vegetation rehabilitation progresses, the accumulation and decomposition of root biomass and litter increase the SOC content [25]. SOC is a continuous complex composed of a range of molecular structures, from simple to complex [26]. Carbohydrates and proteins that enter the soil initially decompose under the selective action of microorganisms and enzymes, resulting in the accumulation of more complex and resistant chemical structures [27]. It is widely known that the percentage of variable and stable SOC fractions in the total SOC content could be used to determine the stability of the SOC [28,29]. To elucidate the stability of SOC during the vegetation rehabilitation process, physical, chemical, and biological measures are employed to isolate organic carbon components with varying properties and stabilities [30,31]. On this basis, researchers both domestically and internationally have employed acid or alkaline extraction methods to quantify the recalcitrance of organic carbon [32,33]. Research has shown that afforestation significantly increases the levels of SOC, active organic carbon, recalcitrant organic carbon, and microbial biomass carbon. Additionally, both the soil carbon stock index and the carbon management index gradually increased [34,35]. The transition from agricultural land to forest increases the content of SOC components, particularly the levels of recalcitrant organic carbon [16,36]. In summary, vegetation rehabilitation effectively improved the stability of the SOC while also increasing

the stability of the SOC pool. At this stage, the response of the labile and stabilizing carbon components in relation to soil aggregates to vegetation types in arid zones has not been well explained. This lack of knowledge is not conducive to an in depth understanding of the mechanisms of SOC sequestration and SOC stabilization in fragile dryland vegetation.

Over the past two decades, the Chinese government and the Basin Authority have implemented a series of vegetation restoration measures in the Tarim River Basin (TRB) [37]. However, the effects of vegetation type on the carbon dynamics of different soil aggregates remain unclear. In this study, we hypothesized that rehabilitation measures in poplar forests could increase the concentration and stability of soil organic carbon in soil aggregates to promote long-term SOC sequestration. The main objectives of this study were (1) to determine the composition of the soil aggregates of three different size classes, (2) to compare the changes in the contents of total SOC and different carbon fractions with different levels of oxidizability associated with aggregates in various vegetation types, and (3) to evaluate the stability of SOC in the soil aggregates of various vegetation types and the correlation of their related indicators. This research can elucidate the mechanisms of SOC sequestration with different vegetation types, providing valuable insights for future ecological rehabilitation and carbon sink management in arid regions.

2. Materials and Methods

2.1. Study Area

This study area is a natural poplar forest and desert shrub forest in the TRB Key Ecological Protection Area, Xinjiang ($39^{\circ}35' \sim 40^{\circ}25' \text{ N}$, $79^{\circ}45' \sim 80^{\circ}55' \text{ E}$) (Figure 1). It is a key area for ensuring the ecological security of southern and northwestern Xinjiang. The study area has a typical warm temperate arid desert climate, with a multiyear average temperature of 10.4° C , a high potential evaporation rate of 1899.8 mm and an annual precipitation of 50.5 mm. The soils in this area are saline–alkali soils according to the Chinese soil classification system. The vegetation types are mainly forest dominated by *euphratica*, shrubs and semishrubs dominated by *tamarix ramosissima* and *lycium ruthenicum* Murr. The ecological degradation of natural vegetation, mainly poplar forests, can be attributed to a combination of natural elements such as climate change and anthropogenic factors such as increased agricultural land use [38].

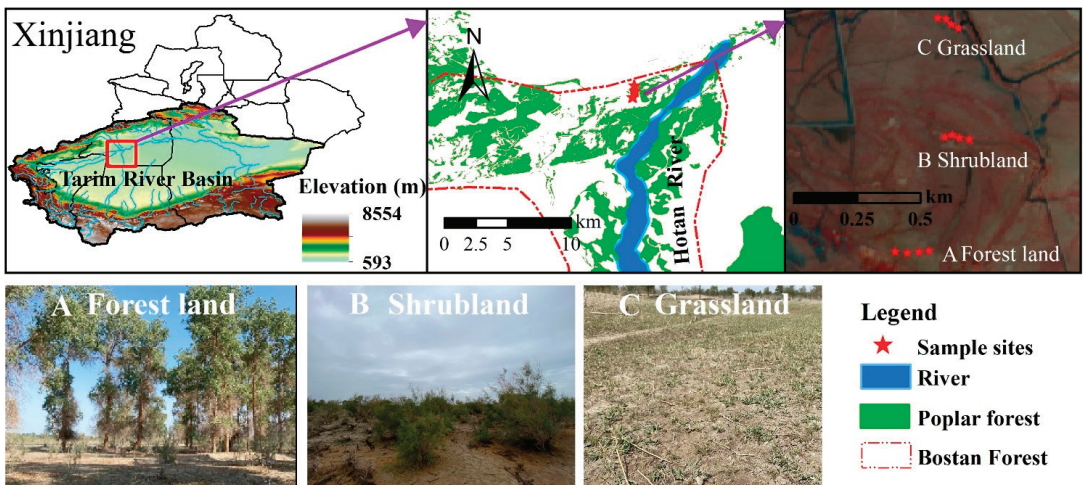


Figure 1. Map of the study area and the sampling sites.

The trend of ecological degradation in the source area has become increasingly evident, which can be attributed to the high level of ecological impact on the oasis economy, agriculture, and animal husbandry within the TRB. In June 2016, Xinjiang comprehensively

carried out an integrated program for safeguarding poplar forests in the study area, and the TRB Management Bureau took advantage of the favorable timing of the incoming water during the flood season to provide emergency water replenishment to the key rehabilitation areas of poplar forests. Therefore, at this stage, the region shows a tendency for desert land to be converted to vegetation-type land [39].

2.2. Experimental Design and Soil Sampling

After a comprehensive inventory of vegetation types was conducted, soil samples were acquired from the forest, shrubland, and grassland areas in August 2022. Four replicate standard collection points were randomly established within the area of each monoculture vegetation type. The distance between any soil collection sample point for each vegetation type was greater than 40 m. The separation among sampling points beyond the spatial dependence of most soil properties (>13.5 m) should be adequately ensured [40–42]. A total of 12 standard soil sample collection areas (three vegetation types \times four samples) were set up for the study. After the removal of the soil surface litter and biomass, samples were obtained from soil depths ranging from 0 to 10 cm and from 10 to 20 cm depth at each sample plot by using a soil auger. At each sample collection site for each vegetation type, four soil samples were again randomly collected within every soil horizon, and the soil was mixed to homogeneity at the same soil depth. The obtained soil samples were placed in the laboratory and dried naturally in a room temperature environment. After the removal of visible plant debris, all the soil samples collected were equally separated into two parts. One part was sieved through a 2 mm sieve, milled and processed, and then further passed through a 0.25 mm sieve and used to survey and evaluate the SOC content and SOC fraction in the bulk soil; the other part was used to measure the aggregate fraction.

The wet sieve method was used to make accurate measurements of the percentage of the particle size composition of the soil aggregates [36]. The soil samples were first placed in a container filled with distilled water, slowly wetted for 5 min and then submerged in distilled water for another 5 min. The soil samples were then transferred to the sieve set of the soil aggregates analyzer. The amplitude of the soil aggregate analyzer was set at 3 cm, and the oscillation frequency was 32 r min⁻¹ for 10 min. Pretreated bulk soil samples of 60 g were separated by passing them through sieves of 0.25 and 0.053 mm. Three soil aggregate samples with diameters greater than 0.25 mm (MA), 0.25–0.053 mm (MI) and less than 0.053 mm (SC) were obtained. The sieved samples were dried at 50 °C for more than 36 h until a steady weight was reached, after which they were weighed to obtain the contents of all the aggregates. The percentages of aggregates of various particle sizes were calculated. Finally, the dried soil aggregate samples were ground to a powdery consistency, passed through a 0.25 mm sieve and stored in sample packets for SOC measurement.

The total SOC content was measured by oxidation with K₂Cr₂O₇ and H₂SO₄ [43]. Depending on the degree of oxidation of the SOC, this study was based on previous studies in which the SOC fractions were detected [33]. The modified Walkley and Black method is as follows; 10 mL of 0.5 M K₂Cr₂O₇ was mixed with 2.5 and 10 mL of 18 M H₂SO₄ to obtain two ratios of 0.25:1 and 1:1 acid-aqueous solutions. The proportions of the solutions were equivalent to 3 M and 9 M H₂SO₄, respectively. The three carbon fractions were tested under conditions of increased oxidizing intensity [29,33]. F1: very labile carbon (organic carbon oxidizable under 3 M H₂SO₄), F2: inert carbon (organic carbon oxidizable among 3 M H₂SO₄ and 9 M H₂SO₄), and F3: oxidizable resistant carbon (difference between total SOC and organic carbon oxidizable under 9 M H₂SO₄). F3 represents organic carbon that cannot be oxidized with 9 M H₂SO₄.

2.3. Calculation of SOC Stability

SOC stability involves the accumulation of SOC in the soil, its retention time, and its response to environmental influences. The change in the ratio of F1 fractions to stabilized

carbon fractions in total SOC provides an effective measure for the analysis of SOC stability under ecological rehabilitation measures in different vegetation types [44,45]. Therefore, the proportions of the three SOC fractions were calculated with the following formula:

$$\text{Proportion of oxidizable SOC fraction} = \frac{\text{Content of SOC fractions}}{\text{Total SOC content}} \quad (1)$$

where the SOC fractions are F1 (very labile carbon), F2 (inert carbon), and F3 (oxidizable resistant carbon), respectively (g kg^{-1}). The total SOC content is the organic carbon content of the bulk soil and aggregates of different grain sizes (g kg^{-1}).

The ratio of the F1 content to the difference in the total SOC content and the labile carbon content is defined as the stability of the SOC [28,46]. Building on previous research, we used methodologies for calculating SOC stability indicators. The calculation formula is as follows:

$$\text{Stability of SOC} = 1 - \frac{\text{F1 content}}{\text{total SOC content} - \text{F1 content}} \quad (2)$$

where the stability of the SOC represents the soil stability indicator (SSI). F1 (very labile carbon) is the very labile carbon content (g kg^{-1}).

2.4. Statistical Analyses

The raw data were processed and summarized with Microsoft Excel 2019 software. SPSS 24.0 was used for statistical analysis of all the data. The effects of various indicators involved in soil organic carbon stability were compared across the three vegetation types using one-way ANOVA and two-way ANOVA. Origin 8.0 software was used for graphing and correlation analysis.

3. Results

3.1. Composition Characteristics of the Soil Aggregates

Vegetation type significantly affects the formation of soil aggregates (Figure 2). However, there was no significant effect of soil depth on aggregate composition in the 0–10 and 10–20 cm soil depth ranges, with similar trends in aggregate composition in the surface and underlying soils. The MA content under Forest (14.72%) was significantly higher than that under Shrubland (3.95%) and Grassland (3.28%), and the MI content under Shrubland (56.10%) was significantly higher than that under Forest (32.51%) and Grassland (29.81%) at soil depths of 0–20 cm. While the SC content under Grassland was significantly greater than that under Forest and Shrubland at the soil depths of 0–10 cm, the SC content and MA content under Forest and Grassland were significantly greater than that under Shrubland at soil depths of 10–20 cm.

The proportions of the various soil aggregates at the 0–20 cm depth differed significantly among the vegetation types. The total amount of SC content in the Forest was the highest, followed by that in the MI content, and that in the MA content was the lowest. The total amount of MI content in the Shrubland was the highest, followed by that in the SC content, and that in the MA content was the lowest. The total amount of SC content in the Grassland was the highest, followed by that in the MI content, and that in the MA content was the lowest. The average contents of MA, MI, and SC at the 0–20 cm depth under the three vegetation types were 7.31%, 39.47% and 53.21%, respectively.

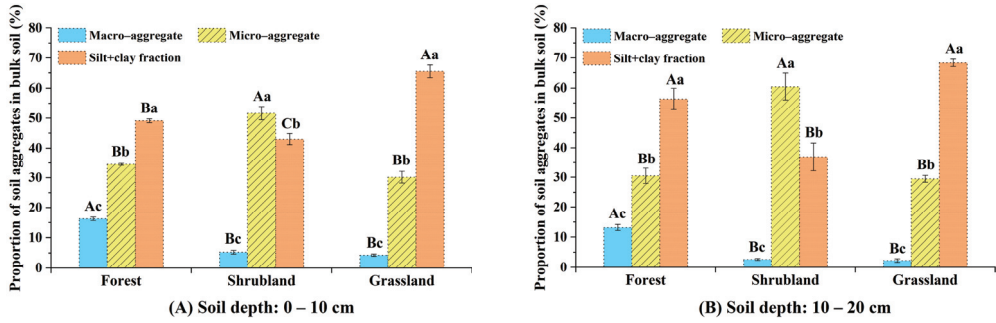


Figure 2. Percentages of the various soil aggregates in the bulk soil of the three vegetation types. (Different capital letters show significant differences between different vegetation types. Different lowercase letters show significant differences between different soil aggregate classes. The whiskers represent the standard deviation among the four repetitions for each vegetation type ($p < 0.05$)).

3.2. SOC Content in the Bulk Soil and Soil Aggregates

Vegetation type, soil depth and soil aggregate size had important effects on the total SOC content (Table 1). For all the vegetation types, the SOC content in the surface soil (0–10 cm) aggregates was significantly higher than that in the lower soil aggregates (10–20 cm) (Table 2). Compared with the SOC content at the 10–20 cm depth, the average SOC contents in the bulk soil, MA, MI and SC under the three vegetation types were 3.66, 10.15, 2.83 and 2.56 g kg⁻¹ higher in 0–10 cm. Forests, shrublands, and grasslands all had the highest total SOC content in MA. Among the three vegetation types at the 0–20 cm depth, the average total SOC content was greater and statistically higher in MA (145.16%), MI (183.72%), and SC (203.97%).

Table 1. The vegetation type, soil aggregate size and fraction of SOC were analyzed by two-way ANOVA.

Target Group	SOC		F1		F2		F3		Stability of SOC		
	Df	F	p	F	p	F	p	F	p	F	p
0–10 cm											
Vegetation types (VT)	2	12.34	<0.001	13.23	<0.001	17.65	<0.001	3.47	0.046	2.40	0.110
Aggregates (AG)	3	11.33	<0.001	11.93	<0.001	11.15	<0.001	5.36	0.011	2.67	0.087
VT × AG	6	2.34	0.081	3.21	0.028	2.06	0.115	1.03	0.409	2.45	0.070
10–20 cm											
Vegetation types (VT)	2	10.66	<0.001	6.53	0.005	15.93	<0.001	7.64	0.002	1.77	0.189
Aggregates (AG)	3	6.89	0.004	6.04	0.007	6.68	0.004	6.04	0.007	0.08	0.928
VT × AG	6	3.25	0.027	2.78	0.047	3.10	0.032	3.24	0.027	0.91	0.471

Table 2. Content of SOC under the various vegetation types (unit: g kg⁻¹) (the meanings of the uppercase and lowercase letters are the same as those in the notes to Figure 2). The values are the means ± standard errors.

Vegetation Types	Bulk Soil	MA	MI	SC
Soil depth 0–10 cm				
Forest	16.88 (±1.35) Ab	39.92 (±10.55) Aa	14.94 (±4.65) Ab	10.62 (±2.75) Ab
Shrubland	4.52 (±2.83) Bab	12.04 (±3.97) Ba	2.80 (±1.09) Bb	5.67 (±0.39) Bab
Grassland	4.06 (±1.75) Bb	12.24 (±2.95) Ba	3.77 (±0.90) Bb	3.66 (±0.22) Bb
Soil depth 10–20 cm				
Forest	8.87 (±2.12) Ab	23.44 (±7.44) Aa	7.52 (±2.35) Ab	6.19 (±0.91) Ab
Shrubland	2.64 (±0.41) Bab	4.79 (±1.07) Ba	2.09 (±0.56) Bb	3.37 (±0.38) Bab
Grassland	2.98 (±0.25) Bb	5.51 (±0.83) Ba	3.40 (±0.75) Bb	2.71 (±0.10) Bb

The organic carbon contents of the soil MA, MI and SC varied in the ranges of 4.79–39.92, 2.09–14.94, and 2.71–10.62 g kg⁻¹, respectively, across the three vegetation types in the study area. Underneath the forest, the average SOC content (16.05 g kg⁻¹) in the bulk soil and different soil aggregates was significantly higher than that in the Shrubland and Grassland at depths of 0–20 cm. There were no significant differences in the organic carbon contents of the shrubs and grasses, with mean values of 4.05 g kg⁻¹ and 4.79 g kg⁻¹, respectively.

3.3. Content of the SOC Fractions with Various Degrees of Oxidizability

The contents of the SOC fractions (F1–F3) in the soil aggregates of the various vegetation types varied significantly at the 0–10 cm and 10–20 cm depths (Tables 1 and 3). Among the soil aggregates of all vegetation types, the organic carbon content of each F fraction was the highest for aggregates with particle sizes greater than 0.25 mm (MA), which was significantly higher than those with particle sizes of 0.25–0.053 mm (MI) and 0.053 mm (SC), with the exception of shrubland MI and SC in F1. Moreover, in the Forest types, the organic carbon content of the 0.25–0.053 mm (MI) particles in the aggregates of the F2 fraction was higher than that of the MI particles in the F1 and F3 fractions. For the oxidizable resistant carbon fraction (F3), the organic carbon content in the soil aggregates with a particle size greater than that in the 0.25 mm (MA) was significantly higher than 0.25–0.053 mm (MI) and 0.053 mm (SC) under the forest type. Under the shrubland and grassland types, the organic carbon content of the soil aggregates > 0.25 mm (MA) was higher than that of the 0.053 mm (SC) and 0.25–0.053 mm (MI). In the bulk soil, MA, MI and SC, the contents of the different carbon fractions at the 0–10 cm depths were 2.98, 7.43, 2.75, and 2.12 g kg⁻¹ for F1; 2.95, 7.61, 2.53, and 2.20 g kg⁻¹ for F2; and 2.56, 6.35, 1.88, and 2.33 g kg⁻¹ for F3, respectively. In contrast, at the 10–20 cm depths, the contents of the F1 to F3 carbon fractions decreased significantly, specifically by 1.68, 4.09, 1.33, and 1.44 g kg⁻¹ for F1; 1.42, 3.71, 1.44, and 1.03 g kg⁻¹ for F2; and 1.73, 3.45, 1.56, and 1.62 g kg⁻¹ for F3, respectively.

There were significant differences in the content of SOC in the soil and its fractions across the various vegetation types (Tables 1 and 3). The average contents of F1, F2 and F3 in the bulk soil, MA, MI, and SC in the Forest land were greater than those in the Shrubland and Grassland. The highest F1, F2 and F3 contents among the three vegetation types were found in the Forest. The differences in the F1 contents in the soil among the Shrubland types were not significant. Irrespective of soil aggregates, contents of F1, F2, and F3 in the Forest were significantly greater than those in the other two vegetation types (Table 3).

Table 3. Oxidative degradability of SOC fractions among aggregate size classes and vegetation types (unit: g kg⁻¹) (the meanings of the uppercase and lowercase letters are the same as those in the notes to Figure 2).

Soil Aggregates		Forest	Shrubland	Grassland
Soil depth: 0–10 cm				
F1	Bulk soil	5.75 (±1.67) Ab	1.58 (±0.28) Ba	1.60 (±0.13) Bb
	MA	14.18 (±3.50) Aa	3.26 (±1.07) Ba	4.86 (±0.64) Ba
	MI	5.63 (±1.94) Ab	1.19 (±0.30) Ba	1.42 (±0.31) Bb
	SC	3.05 (±1.10) Ab	1.83 (±0.25) Aa	1.48 (±0.20) Ab
F2	Bulk soil	6.78 (±1.76) Ab	0.88 (±0.41) Bb	1.18 (±0.53) Bb
	MA	14.99 (±2.98) Aa	3.52 (±1.88) Ba	4.33 (±1.75) Ba
	MI	5.79 (±2.11) Ab	0.65 (±0.53) Bb	1.16 (±0.58) Bb
	SC	4.77 (±1.25) Ab	0.84 (±0.12) Bb	0.98 (±0.45) Bb
F3	Bulk soil	4.34 (±0.84) Ab	2.06 (±0.26) Bb	1.28 (±0.38) Bb
	MA	10.75 (±5.16) Aa	5.26 (±1.15) ABa	3.04 (±1.07) Ba
	MI	3.52 (±0.70) Ab	0.95 (±0.29) Bc	1.18 (±0.32) Bb
	SC	2.79 (±0.46) Ab	2.99 (±0.59) Aab	1.21 (±0.48) Ab

Table 3. Cont.

	Soil Aggregates	Forest	Shrubland	Grassland
Soil depth: 10–20 cm				
F1	Bulk soil	2.91 (± 0.89) Aab	0.89 (± 0.13) Bab	1.25 (± 0.26) ABa
	MA	8.39 (± 3.07) Aa	1.88 (± 0.50) Ba	1.99 (± 0.39) Ba
	MI	1.89 (± 0.66) Ab	0.81 (± 0.17) Ab	1.30 (± 0.23) Aa
	SC	2.17 (± 0.66) Ab	0.94 (± 0.21) Aab	1.20 (± 0.29) Aa
F2	Bulk soil	3.29 (± 0.70) Ab	0.46 (± 0.24) Ba	0.50 (± 0.21) Ba
	MA	8.45 (± 2.51) Aa	1.01 (± 0.53) Ba	1.67 (± 0.82) Ba
	MI	3.43 (± 0.90) Ab	0.32 (± 0.18) Ba	0.58 (± 0.35) Ba
	SC	2.01 (± 0.24) Ab	0.66 (± 0.33) Ba	0.42 (± 0.15) Ba
F3	Bulk soil	2.67 (± 0.56) Ab	1.29 (± 0.16) Bab	1.23 (± 0.08) Ba
	MA	6.60 (± 1.91) Aa	1.90 (± 0.27) Ba	1.85 (± 0.64) Ba
	MI	2.20 (± 0.85) Ab	0.97 (± 0.31) Ab	1.52 (± 0.33) Aa
	SC	2.00 (± 0.17) Ab	1.77 (± 0.20) Aab	1.08 (± 0.12) Ba

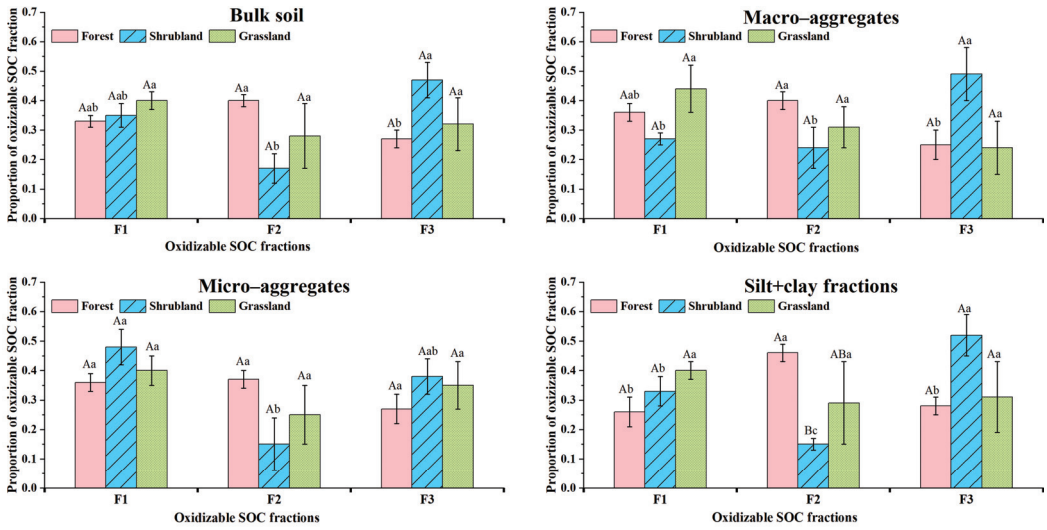
3.4. Stability of SOC Under Various Vegetation Types

The percentage of SOC in the total SOC content varied with vegetation type (Figure 3), as did that in the bulk soils and various soil aggregates. F1, F2 and F3 in the total SOC showed mean values of 0.36%, 0.28% and 0.36%, respectively, at soil depths of 0–20 cm. In bulk soil, the F1 percentage under the Grassland was greater than that across the Forest and Shrubland, the F2 percentage in the Forest was greater than that across the Shrubland and Grassland, and the F3 percentage across the Shrubland was greater than that across the Forest and Grassland. In MA, the percentages of F1 and F2 in the Forestland and Grassland areas were greater than those in the Shrubland area, whereas the F3 percentages in the Shrubland were greater than those in the Forest and Grassland. No difference was found for F1, F2, and F3 in the MA between the Forest and Grassland. Different from MA, the percentages of F1 in MI under the Shrubland were significantly greater than those across the Forest and Grassland. The percentages of F2 in the SC in the Forest were greater than those across the Shrubland and Grassland, and the percentages of F1 and F3 were lower than those in the other two vegetation types.

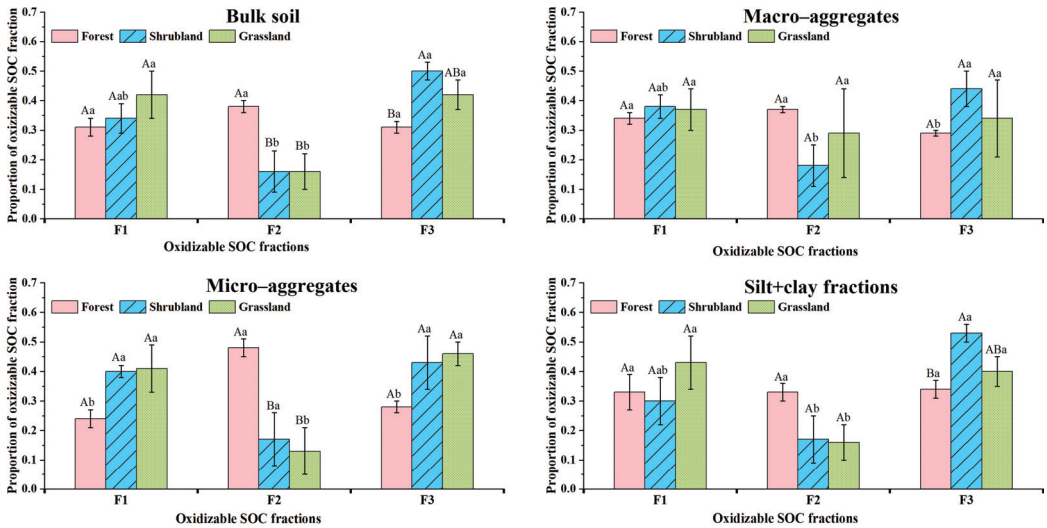
The percentages of the SOC fractions in the total SOC content were similar at the 10–20 cm soil depth compared to 0–10 cm across the different vegetation types. In MI, the percentages of F1 in the Shrubland were greater than those in the Forest and Grassland. The percentages of F2 in MA under Forest were greater than those across the Shrubland and Grassland.

The mean values of the stability of SOC in the bulk soil, MA, MI and SC were 0.44, 0.44, 0.38 and 0.46 for all the vegetation types in the 0–20 cm soil layer range, respectively (Figure 4). The results of one-way ANOVA indicated that the effects of vegetation type on SOC stability were numerically different but not significant. In bulk soil (soil depth: 0–10 cm: $F = 1.275$, $p = 0.325$; soil depth: 10–20 cm; $F = 0.681$, $p = 0.53$), MA (soil depth: 0–10 cm: $F = 3.173$, $p = 0.091$; soil depth: 10–20 cm; $F = 0.273$, $p = 0.767$), MI (soil depth: 0–10 cm: $F = 1.728$, $p = 0.232$; soil depth: 10–20 cm; $F = 4.664$, $p = 0.041$), and SC (soil depth: 0–10 cm: $F = 2.592$, $p = 0.129$; soil depth: 10–20 cm; $F = 0.411$, $p = 0.675$).

The highest SOC stabilization values were found in the Forestland with soil depths of 0–10 cm in the bulk soils, MI and SC. The highest SOC stabilization values were found in the Forest land in the 10–20 cm soil layers of the bulk, MA and MI soils. The highest values for SOC of stability under Shrubland were found only in the 0–10 cm MA and 10–20 cm SC layers. However, Grasslands had lower values for SOC stability in 0–20 cm soil layer, and the differences were not significant (Figure 4).



(A) Soil depth: 0–10 cm



(B) Soil depth: 10–20 cm

Figure 3. Proportion of the F1–F3 fractions in the bulk soil and aggregates. (Different capital letters indicate significant differences between different vegetation types. Different lowercase letters indicate significant differences between SOC fractions ($p < 0.05$)).

3.5. Correlation Analysis Between the SOC Stability and SOC Fractions of Different Aggregates and SOC Content

The SOC stability indices (SSIs) and MA content were positively correlated with the SOC content in the soil aggregates, but negatively correlated with the SC content (Figure 5). The organic carbon content of the aggregates had a more pronounced positive correlation with the F2 and F3 fractions. The MI content was negatively correlated with the SC content, MA-associated carbon content and content of the SOC fractions with MA, but positively correlated with the F3 fractions in terms of the MI-associated carbon content. The SC content was negatively correlated with the SOC content in the soil aggregates and its

fractions (Figure 5). There was a positive correlation between the SOC content associated with the various aggregates and the SOC fractionation content (Figure 5).

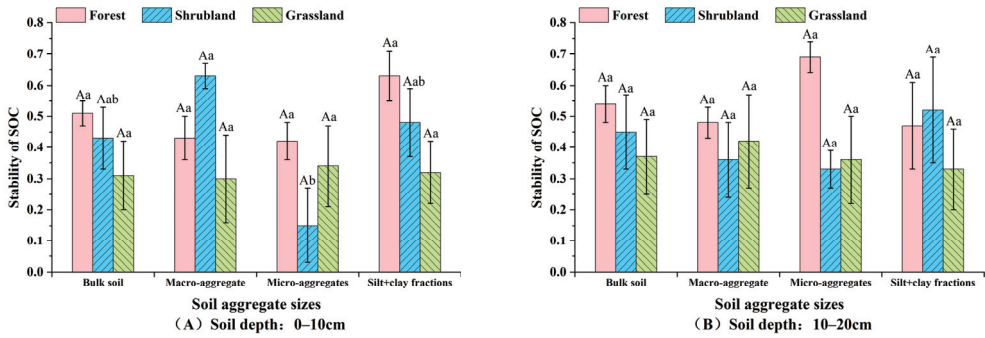


Figure 4. Stability of SOC in soil under various vegetation types and aggregate sizes. (The meanings of the uppercase and lowercase letters are the same as those in the notes to Figure 2).

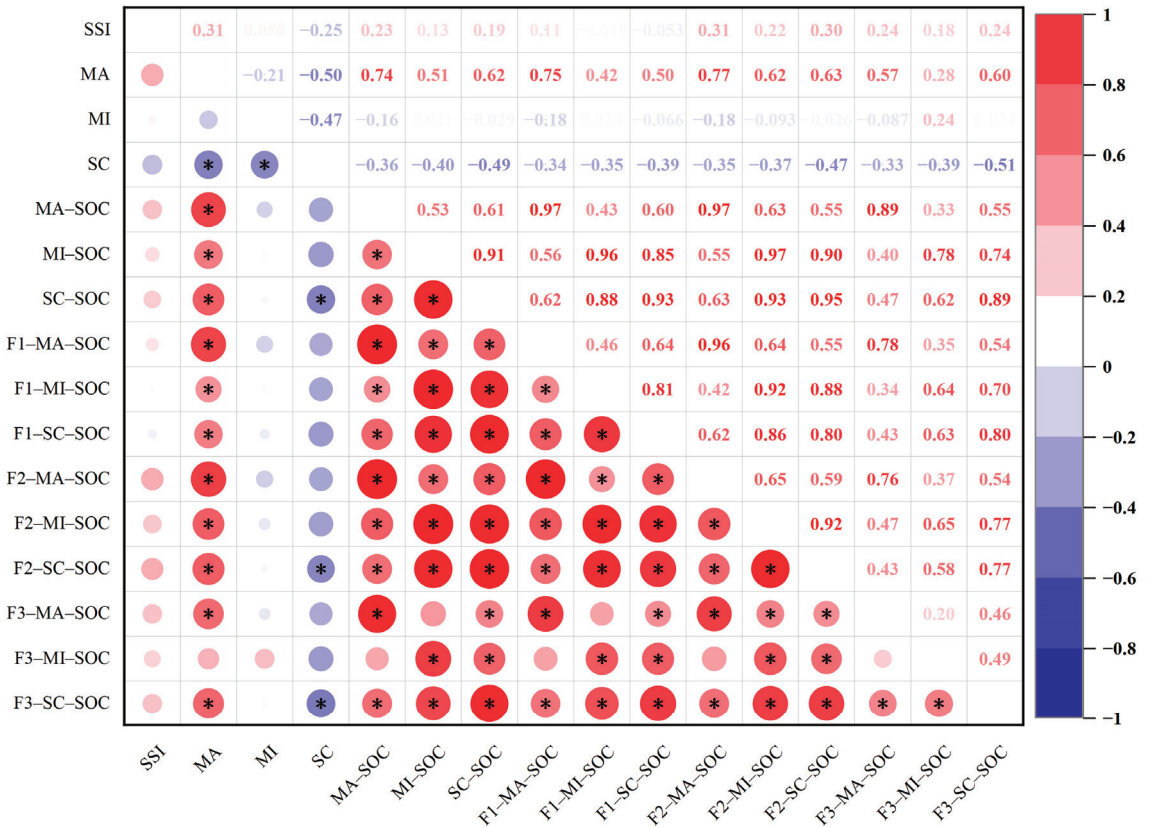


Figure 5. Correlation of the SOC stability index impact indicators. (* represents significant correlations at $p < 0.05$).

4. Discussion

4.1. Dynamic Characterization of the Composition of Soil Aggregates and Its SOC Content

Soil aggregation is an important pathway for soil carbon sequestration [47]. The higher the content of MA, the better the structure and erosion resistance of the soil. Vegetation type has a significant effect on the composition of soil aggregates (Figure 2). In the present study, it was found that the composition of soil aggregates in the surface layer (0–10 cm) and the lower layer (10–20 cm) were characterized similarly. Grassland had the highest levels of SC, shrublands had the highest levels of MI, and forestlands had significantly higher levels of MA than shrublands and grasslands. The study showed that grassland soils were the least structured and had the lowest erosion resistance, and that shrublands had a significant role in promoting MI formation, whereas forestlands had the best stability of soil aggregates, soil structure, and soil erosion resistance. This finding supported the results of [12]. Differences in organic matter inputs and outputs, soil physical properties and microbial activity across vegetation types affect the composition of SOC across grain size aggregates [48,49].

Previous studies have shown that the SOC content increases with the size of the soil aggregates and that new organic matter derived from plant litter or roots is predominantly stored within MA [50]. In this study, the SOC content in forestland areas was significantly greater than that in shrublands and grasslands, indicating substantial potential for SOC sequestration at the research site. An increase in SOC content can lead to the production of more resistant binding agents, such as humic acid compounds, polysaccharides, and root exudates, thereby enhancing the formation of soil aggregates [51,52]. The positive correlation between the MA content and the SOC content in the soil was confirmed (Figure 5), suggesting that the increase in MA content can be attributed to the increase in the SOC content. Furthermore, soil MA serves as the primary reservoir for SOC, and the results of this study support this conclusion. Therefore, the implementation of poplar forest conservation projects can promote positive vegetation succession. This, to some extent, can facilitate the sequestration of organic carbon in soil MI and increase the organic carbon content in soil MA, ultimately improving soil quality (Table 2) (Figure 6).

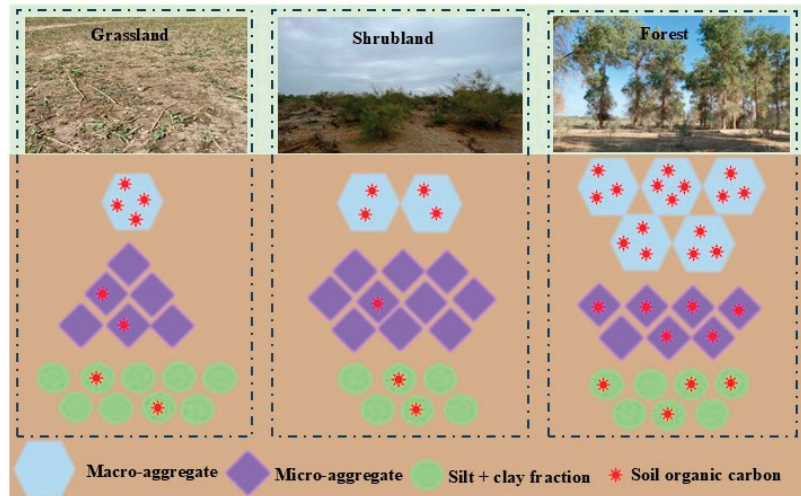


Figure 6. SOC fraction content in soil across the various vegetation types.

Previous studies have demonstrated that the SOC content in soil aggregates decreases with increasing soil depth [6,53]. In this study, the SOC content in soil aggregates from the top soil layer (0–10 cm) showed a more significant variation compared to that in aggregates from the lower layer (10–20 cm) (Table 1). This difference is attributed to the accumulation

of fresh organic matter in the topsoil, such as plant biomass, litter, and root exudates. Owing to the protective effects of vegetation growth on soil, forested areas can significantly reduce soil erosion caused by rainfall and wind [5,53]. This is a key reason why the SOC content in forested soils is significantly higher in the topsoil than in the lower layer.

Additionally, previous studies have reported that vegetation type significantly affects the content of SOC in deep soils, particularly at depths greater than 20 cm [54,55]. In this study, we focused only on investigating the influences of vegetation type on the stability of soil aggregates and associated carbon in surface soils (0–20 cm). Therefore, the impact of vegetation type on the stability of soil aggregate-associated carbon in deep soils (greater than 20 cm) represents a valuable direction for future research.

4.2. Characteristics of Oxidizable SOC Fractions in Soil Aggregates and SOC Stability

Separating stable carbon into more components with varying stability can elucidate the differences in stable carbon fractions among the three vegetation types. This approach aids in gaining a deeper understanding of how vegetation type changes affect SOC fractions and their stability [32]. Changes in the sources of SOC (such as plant litter, microbial products, and root exudates) resulting from different vegetation types directly affect the contents of carbon fractions with varying stabilities in the soil [56,57]. The contents of different SOC fractions exhibit varying trends of change with increasing aggregate size. This study demonstrated significant differences in the SOC fractions in the soil across the various vegetation types (Table 3 and Figure 7). The results of this study are similar to those of previous studies, showing that the SOC content in forest soils is significantly greater than that in other vegetation types, both in bulk soil and across the F1 to F3 carbon fractions (Table 3) [49]. These results further confirm that forest conservation and rehabilitation measures are beneficial for carbon sequestration.

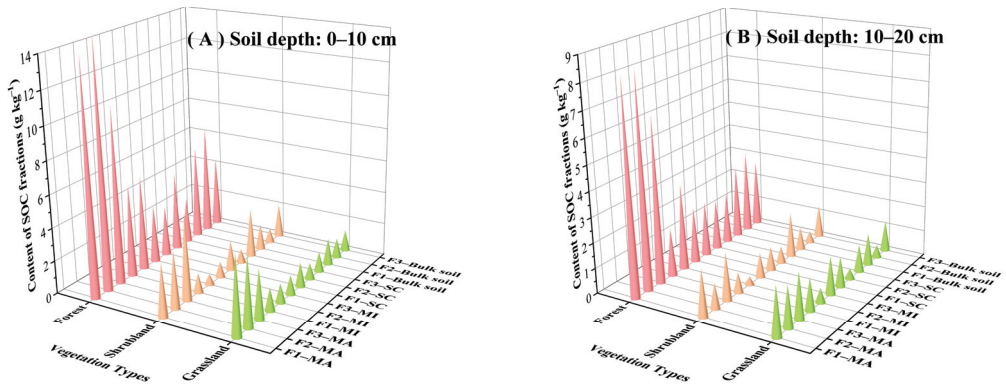


Figure 7. Contents of the SOC fractions in the bulk soil and soil aggregates.

The F1 fraction is extremely oxidizable and sensitive to changes in vegetation type. Monitoring the changes in this carbon fraction is scientifically important for revealing the adaptation mechanism of ecosystems to environmental perturbations. Changes in the percentage of F1 fraction and stabilized carbon fraction in the total SOC are important indicators for assessing changes in SOC stability [4]. In the results of this study, under all vegetation type patterns, in the bulk soil and soil aggregates, the percentages of F1, F2, and F3 in the total SOC, with mean values of 0.36%, 0.28% and 0.36%, respectively, at soil depths of 0–20 cm, showed that stable carbon was the predominant carbon fraction in this study area (Figure 3). The stability of organic carbon in the aggregates under each vegetation type was increased in the lower layer (10–20 cm) compared with the top soil layer (0–10 cm). The SOC Stability and MA content were positively correlated with the SOC in the soil aggregates and their F2 and F3 fractions.

Soil stability and erosion resistance are significantly correlated with the content of MA (>250 μm) in the soil [18]. Therefore, the composition of soil aggregates of different sizes directly influences the stability of soil aggregates. The positive correlations between the soil aggregate stability indices and the SOC content and the MA content (Figure 5), showed that the highest soil aggregate stability indices values under the Forestland were mainly attributed to the formation of MA [50,58] and the organic matter inputs from forest litter [12,51]. Previous studies have also confirmed the positive response of soil aggregate stability to afforestation, showing an increase in aggregate stability at a soil depth of 0–20 cm following afforestation [12,59]. Furthermore, soil aggregate stability is influenced by various factors, including vegetation composition type, ecological management measures, soil characteristics and climatic conditions.

In future vegetation rehabilitation efforts, SOC in the TRB is expected to continue accumulating. This study examines the variations and mechanisms of SOC stability under various vegetation types. The increased stability of soil aggregates during vegetation rehabilitation may contribute to the enhanced stability of SOC [13,47,60]. Owing to the intricacies of elements influencing organic carbon stability, research in this area varies across regions. For example, some studies have focused on aggregate protection mechanisms [36], whereas others have emphasized microbial-driven mechanisms [61]. There is a lack of comprehensive exploration of the main driving mechanisms of SOC stability. An increasing number of researchers are inclined to believe that the mechanisms governing SOC stability result from a complex interplay of multiple processes [15]. Therefore, future research should consider the combined effects of multiple mechanisms to obtain a thorough understanding of the factors influencing SOC stability and identify the dominant mechanisms involved.

5. Conclusions

Taking the key ecological rehabilitation area of the TRB in the arid zone as the research object, the effects of vegetation type changes on the stability of total SOC, SOC fractions with different degrees of oxidation and bulk soils as well as the SOC stability of different soil aggregates were quantitatively analyzed. The results of the study showed that the total SOC and three carbon fractions were significantly greater in forestland than in the other two vegetation types, and the effect was more pronounced in MA than in the other aggregates, revealing that MA made a greater contribution to the increase in total SOC in the soil. In the bulk soil and soil aggregates, F1 to F3 were found in total SOC with mean values of 0.36, 0.28 and 0.36 (at soil depths of 0–20 cm), which showed that stable carbon was the major carbon fraction. The stability of organic carbon in aggregates with each vegetation type was increased in the lower layer compared with the top soil layer. The SOC Stability and MA content were positively correlated with the SOC in the soil aggregates and their F2 and F3 fractions. The implementation of special actions for the ecological protection of poplar forests in ecologically important rehabilitation areas may be the best measure to increase SOC sequestration under different vegetation types. The results clarified the dynamics of SOC in soil aggregates under the three vegetation types, which is of great significance for regional soil carbon sequestration and provides valuable insights into the improvement of SOC storage in the TRB key ecological rehabilitation areas in Northwest China.

Author Contributions: Conceptualization, Q.Z., C.Y. and P.Y.; Methodology, Q.Z., C.Y. and P.Y.; Investigation, Q.Z., P.Y., K.L., J.W. and F.S.; Writing original draft, Q.Z.; Writing—reviewing and editing, C.Y., P.Y. and H.X.; Supervision, P.Y.; Funding acquisition, H.X. All authors have read and agreed to the published version of the manuscript.

Funding: This research was supported by The Graduate Innovation Project of Xinjiang Uygur Autonomous Region (grant number: XJ2023G129).

Data Availability Statement: The original contributions presented in this study are included in the article. Further inquiries can be directed to the corresponding authors.

Conflicts of Interest: The authors declare no conflicts of interest.

References

- Falkowski, P.; Scholes, R.J.; Boyle, E.; Canadell, J.; Canfield, D.; Elser, J.; Gruber, N.; Hibbard, K.; Höglberg, P.; Linder, S.; et al. The Global Carbon Cycle: A Test of Our Knowledge of Earth as a System. *Science* **2000**, *290*, 291–296. [CrossRef] [PubMed]
- Lehmann, J.; Kleber, M. The Contentious Nature of Soil Organic Matter. *Nature* **2015**, *528*, 60–68. [CrossRef] [PubMed]
- Bradford, M.A.; Wieder, W.R.; Bonan, G.B.; Fierer, N.; Raymond, P.A.; Crowther, T.W. Managing Uncertainty in Soil Carbon Feedbacks to Climate Change. *Nat. Clim. Chang.* **2016**, *6*, 751–758. [CrossRef]
- Liu, X.; Chen, D.; Yang, T.; Huang, F.; Fu, S.; Li, L. Changes in Soil Labile and Recalcitrant Carbon Pools after Land-Use Change in a Semi-Arid Agro-Pastoral Ecotone in Central Asia. *Ecol. Indic.* **2020**, *110*, 105925. [CrossRef]
- Briedis, C.; Baldock, J.; De Moraes Sá, J.C.; Dos Santos, J.B.; McGowan, J.; Milori, D.M.B.P. Organic Carbon Pools and Organic Matter Chemical Composition in Response to Different Land Uses in Southern Brazil. *Eur. J. Soil Sci.* **2021**, *72*, 1083–1100. [CrossRef]
- Liu, D.; Ju, W.; Jin, X.; Li, M.; Shen, G.; Duan, C.; Guo, L.; Liu, Y.; Zhao, W.; Fang, L. Associated Soil Aggregate Nutrients and Controlling Factors on Aggregate Stability in Semiarid Grassland under Different Grazing Prohibition Timeframes. *Sci. Total Environ.* **2021**, *777*, 146104. [CrossRef]
- Basak, N.; Mandal, B.; Datta, A.; Kundu, M.C.; Rai, A.K.; Basak, P.; Mitran, T. Stock and Stability of Organic Carbon in Soils under Major Agro-Ecological Zones and Cropping Systems of Sub-Tropical India. *Agric. Ecosyst. Environ.* **2021**, *312*, 107317. [CrossRef]
- Fang, J. Ecological perspectives of carbon neutrality. *Chin. J. Plant Ecol.* **2021**, *45*, 1173–1176. [CrossRef]
- Józefowska, A.; Pietrzykowski, M.; Woś, B.; Cajthaml, T.; Frouz, J. The Effects of Tree Species and Substrate on Carbon Sequestration and Chemical and Biological Properties in Reforested Post-Mining Soils. *Geoderma* **2017**, *292*, 9–16. [CrossRef]
- Zhang, S.; Ren, T.; Zhou, X.; Fang, Y.; Liao, S.; Cong, R.; Lu, J. Effects of Rapeseed/Wheat-Rice Rotation and Fertilization on Soil Nutrients and Distribution of Aggregate Carbon and Nitrogen. *Acta Pedol. Sin.* **2022**, *59*, 194–205.
- Witzgall, K.; Vidal, A.; Schubert, D.I.; Höschen, C.; Schweizer, S.A.; Buegger, F.; Pouteau, V.; Chenu, C.; Mueller, C.W. Particulate Organic Matter as a Functional Soil Component for Persistent Soil Organic Carbon. *Nat. Commun.* **2021**, *12*, 4115. [CrossRef] [PubMed]
- Bai, Y.; Zhou, Y.; He, H. Effects of Rehabilitation through Afforestation on Soil Aggregate Stability and Aggregate-Associated Carbon after Forest Fires in Subtropical China. *Geoderma* **2020**, *376*, 114548. [CrossRef]
- Deng, L.; Wang, K.; Tang, Z.; Shangguan, Z. Soil Organic Carbon Dynamics Following Natural Vegetation Restoration: Evidence from Stable Carbon Isotopes ($\delta^{13}C$). *Agric. Ecosyst. Environ.* **2016**, *221*, 235–244. [CrossRef]
- Zhang, Q.; Liu, J.; Yang, L.; Wei, W. Effect of vegetation restoration on stability and erosion resistance of soil aggregates in semi-arid loess region. *Acta Ecol. Sin.* **2022**, *42*, 9057–9068.
- Pan, Y.; He, Z.; Liu, Y.; Dong, L.; Lv, W.; Shangguan, Z.; Deng, L. Dynamics of soil aggregate-associated organic carbon during secondary forest succession in the Loess Plateau, China. *Acta Ecol. Sin.* **2021**, *41*, 5195–5203.
- Wang, A.; Zha, T.; Zhang, Z. Variations in Soil Organic Carbon Storage and Stability with Vegetation Restoration Stages on the Loess Plateau of China. *CATENA* **2023**, *228*, 107142. [CrossRef]
- Wang, B.; Xu, G.; Ma, T.; Chen, L.; Cheng, Y.; Li, P.; Li, Z.; Zhang, Y. Effects of Vegetation Restoration on Soil Aggregates, Organic Carbon, and Nitrogen in the Loess Plateau of China. *Catena* **2023**, *231*, 107340. [CrossRef]
- Deng, L.; Kim, D.; Peng, C.; Shangguan, Z. Controls of Soil and Aggregate-associated Organic Carbon Variations Following Natural Vegetation Restoration on the Loess Plateau in China. *Land Degrad. Dev.* **2018**, *29*, 3974–3984. [CrossRef]
- Gunina, A.; Kuzyakov, Y. Pathways of Litter C by Formation of Aggregates and SOM Density Fractions: Implications from ^{13}C Natural Abundance. *Soil Biol. Biochem.* **2014**, *71*, 95–104. [CrossRef]
- Shi, J.; Deng, L.; Gunina, A.; Alharbi, S.; Wang, K.; Li, J.; Liu, Y.; Shangguan, Z.; Kuzyakov, Y. Carbon Stabilization Pathways in Soil Aggregates during Long-Term Forest Succession: Implications from $\delta^{13}C$ Signatures. *Soil Biol. Biochem.* **2023**, *180*, 108988. [CrossRef]
- Tao, F.; Lehmann, J.; Wang, Y.-P.; Jiang, L.; Ahrens, B.; Viatkin, K.; Manzoni, S.; Houlton, B.Z.; Huang, Y.; Huang, X.; et al. Reply to “Beyond Microbial Carbon Use Efficiency”. *Natl. Sci. Rev.* **2024**, *11*, nwae058. [CrossRef]
- Jha, P.; Lakaria, B.L.; Biswas, A.K.; Saha, R.; Mahapatra, P.; Agrawal, B.K.; Sahi, D.K.; Wanjari, R.H.; Lal, R.; Singh, M.; et al. Effects of Carbon Input on Soil Carbon Stability and Nitrogen Dynamics. *Agric. Ecosyst. Environ.* **2014**, *189*, 36–42. [CrossRef]
- Schmidt, M.W.I.; Torn, M.S.; Abiven, S.; Dittmar, T.; Guggenberger, G.; Janssens, I.A.; Kleber, M.; Kögel-Knabner, I.; Lehmann, J.; Manning, D.A.C.; et al. Persistence of Soil Organic Matter as an Ecosystem Property. *Nature* **2011**, *478*, 49–56. [CrossRef] [PubMed]
- Wang, Q.-K.; Wang, S.-L.; Zhong, M.-C. Ecosystem Carbon Storage and Soil Organic Carbon Stability in Pure and Mixed Stands of *Cunninghamia lanceolata* and *Michelia macclurei*. *Plant Soil* **2013**, *370*, 295–304. [CrossRef]
- Feng, X.; Fu, B.; Piao, S.; Wang, S.; Ciais, P.; Zeng, Z.; Lü, Y.; Zeng, Y.; Li, Y.; Jiang, X.; et al. Revegetation in China’s Loess Plateau Is Approaching Sustainable Water Resource Limits. *Nat. Clim. Chang.* **2016**, *6*, 1019–1022. [CrossRef]
- Feng, X.; Simpson, M.J. The Distribution and Degradation of Biomarkers in Alberta Grassland Soil Profiles. *Org. Geochem.* **2007**, *38*, 1558–1570. [CrossRef]
- Huang, X.; Liu, X.; Liu, J.; Chen, H. Iron-Bound Organic Carbon and Their Determinants in Peatlands of China. *Geoderma* **2021**, *391*, 114974. [CrossRef]

28. Liu, H.; Zhang, J.; Ai, Z.; Wu, Y.; Xu, H.; Li, Q.; Xue, S.; Liu, G. 16-Year Fertilization Changes the Dynamics of Soil Oxidizable Organic Carbon Fractions and the Stability of Soil Organic Carbon in Soybean-Corn Agroecosystem. *Agric. Ecosyst. Environ.* **2018**, *265*, 320–330. [CrossRef]
29. Hazra, K.K.; Nath, C.P.; Singh, U.; Praharaj, C.S.; Kumar, N.; Singh, S.S.; Singh, N.P. Diversification of Maize-Wheat Cropping System with Legumes and Integrated Nutrient Management Increases Soil Aggregation and Carbon Sequestration. *Geoderma* **2019**, *353*, 308–319. [CrossRef]
30. Yuan, X.; Qin, W.; Xu, H.; Zhang, Z.; Zhou, H.; Zhu, B. Sensitivity of Soil Carbon Dynamics to Nitrogen and Phosphorus Enrichment in an Alpine Meadow. *Soil Biol. Biochem.* **2020**, *150*, 107984. [CrossRef]
31. Cheng, M.; An, S. Responses of Soil Nitrogen, Phosphorous and Organic Matter to Vegetation Succession on the Loess Plateau of China. *J. Arid Land* **2015**, *7*, 216–223. [CrossRef]
32. Plante, A.F.; Conant, R.T.; Paul, E.A.; Paustian, K.; Six, J. Acid Hydrolysis of Easily Dispersed and Microaggregate-derived Silt- and Clay-sized Fractions to Isolate Resistant Soil Organic Matter. *Eur. J. Soil Sci.* **2006**, *57*, 456–467. [CrossRef]
33. Chan, K.Y.; Bowman, A.; Oates, A. Oxidizable organic carbon fractions and soil quality changes in an oxic paleustalf under different pasture leys. *Soil Sci.* **2001**, *166*, 61–67. [CrossRef]
34. Shi, J.; Song, M.; Yang, L.; Zhao, F.; Wu, J.; Li, J.; Yu, Z.; Li, A.; Shanguan, Z.; Deng, L. Recalcitrant Organic Carbon Plays a Key Role in Soil Carbon Sequestration along a Long-Term Vegetation Succession on the Loess Plateau. *Catena* **2023**, *233*, 107528. [CrossRef]
35. Yu, P.; Li, Y.; Liu, S.; Liu, J.; Ding, Z.; Ma, M.; Tang, X. Afforestation Influences Soil Organic Carbon and Its Fractions Associated with Aggregates in a Karst Region of Southwest China. *Sci. Total Environ.* **2022**, *814*, 152710. [CrossRef]
36. Yu, P.; Liu, J.; Tang, H.; Ci, E.; Tang, X.; Liu, S.; Ding, Z.; Ma, M. The Increased Soil Aggregate Stability and Aggregate-Associated Carbon by Farmland Use Change in a Karst Region of Southwest China. *Catena* **2023**, *231*, 107284. [CrossRef]
37. Qian, K.; Ma, X.; Yan, W.; Li, J.; Xu, S.; Liu, Y.; Luo, C.; Yu, W.; Yu, X.; Wang, Y.; et al. Trade-Offs and Synergies among Ecosystem Services in Inland River Basins under the Influence of Ecological Water Transfer Project: A Case Study on the Tarim River Basin. *Sci. Total Environ.* **2024**, *908*, 168248. [CrossRef]
38. Zhang, Q.; Sun, C.; Chen, Y.; Chen, W.; Xiang, Y.; Li, J.; Liu, Y. Recent Oasis Dynamics and Ecological Security in the Tarim River Basin, Central Asia. *Sustainability* **2022**, *14*, 3372. [CrossRef]
39. Zhang, J.; Li, J.; Bao, A.; Bai, J.; Liu, Y.; Huang, Y. Effectiveness assessment of ecological restoration of *Populus euphratica* forest in the Tarim River Basin during 2013–2020. *Arid Land Geogr.* **2022**, *45*, 1824–1835.
40. Zhong, Z.; Han, X.; Xu, Y.; Zhang, W.; Fu, S.; Liu, W.; Ren, C.; Yang, G.; Ren, G. Effects of Land Use Change on Organic Carbon Dynamics Associated with Soil Aggregate Fractions on the Loess Plateau, China. *Land Degrad. Dev.* **2019**, *30*, 1070–1082. [CrossRef]
41. Marriott, C.A.; Hudson, G.; Hamilton, D.; Neilson, R.; Boag, B.; Handley, L.L.; Wishart, J.; Scrimgeour, C.M.; Robinson, D. Spatial Variability of Soil Total C and N and Their Stable Isotopes in an Upland Scottish Grassland. *Plant Soil* **1997**, *196*, 151–162. [CrossRef]
42. Yu, P.; Liu, J.; Tang, H.; Sun, X.; Liu, S.; Tang, X.; Ding, Z.; Ma, M.; Ci, E. Establishing a Soil Quality Index to Evaluate Soil Quality after Afforestation in a Karst Region of Southwest China. *Catena* **2023**, *230*, 107237. [CrossRef]
43. Yu, P.; Liu, S.; Zhang, L.; Li, Q.; Zhou, D. Selecting the Minimum Data Set and Quantitative Soil Quality Indexing of Alkaline Soils under Different Land Uses in Northeastern China. *Sci. Total Environ.* **2018**, *616–617*, 564–571. [CrossRef]
44. Modak, K.; Ghosh, A.; Bhattacharyya, R.; Biswas, D.R.; Das, T.K.; Das, S.; Singh, G. Response of Oxidative Stability of Aggregate-Associated Soil Organic Carbon and Deep Soil Carbon Sequestration to Zero-Tillage in Subtropical India. *Soil Tillage Res.* **2019**, *195*, 104370. [CrossRef]
45. Yu, P.; Han, K.; Li, Q.; Zhou, D. Soil Organic Carbon Fractions Are Affected by Different Land Uses in an Agro-Pastoral Transitional Zone in Northeastern China. *Ecol. Indic.* **2017**, *73*, 331–337. [CrossRef]
46. Diederich, K.M.; Ruark, M.D.; Krishnan, K.; Arriaga, F.J.; Silva, E.M. Increasing Labile Soil Carbon and Nitrogen Fractions Require a Change in System, Rather Than Practice. *Soil Sci. Soc. Am. J.* **2019**, *83*, 1733–1745. [CrossRef]
47. Panettieri, M.; Rumpel, C.; Dignac, M.-F.; Chabbi, A. Does Grassland Introduction into Cropping Cycles Affect Carbon Dynamics through Changes of Allocation of Soil Organic Matter within Aggregate Fractions? *Sci. Total Environ.* **2017**, *576*, 251–263. [CrossRef]
48. Ran, Y.; Ma, M.; Liu, Y.; Zhou, Y.; Sun, X.; Wu, S.; Huang, P. Hydrological Stress Regimes Regulate Effects of Binding Agents on Soil Aggregate Stability in the Riparian Zones. *Catena* **2021**, *196*, 104815. [CrossRef]
49. Nandan, R.; Singh, V.; Singh, S.S.; Kumar, V.; Hazra, K.K.; Nath, C.P.; Poonia, S.; Malik, R.K.; Bhattacharyya, R.; McDonald, A. Impact of Conservation Tillage in Rice-Based Cropping Systems on Soil Aggregation, Carbon Pools and Nutrients. *Geoderma* **2019**, *340*, 104–114. [CrossRef]
50. Huang, R.; Lan, M.; Liu, J.; Gao, M. Soil Aggregate and Organic Carbon Distribution at Dry Land Soil and Paddy Soil: The Role of Different Straws Returning. *Environ. Sci. Pollut. Res.* **2017**, *24*, 27942–27952. [CrossRef]
51. Zhong, Z.; Wu, S.; Lu, X.; Ren, Z.; Wu, Q.; Xu, M.; Ren, C.; Yang, G.; Han, X. Organic Carbon, Nitrogen Accumulation, and Soil Aggregate Dynamics as Affected by Vegetation Restoration Patterns in the Loess Plateau of China. *Catena* **2021**, *196*, 104867. [CrossRef]

52. An, J.; Wu, Y.; Wu, X.; Wang, L.; Xiao, P. Soil Aggregate Loss Affected by Raindrop Impact and Runoff under Surface Hydrologic Conditions within Contour Ridge Systems. *Soil Tillage Res.* **2021**, *209*, 104937. [CrossRef]
53. Yu, P.; Liu, S.; Han, K.; Guan, S.; Zhou, D. Conversion of Cropland to Forage Land and Grassland Increases Soil Labile Carbon and Enzyme Activities in Northeastern China. *Agric. Ecosyst. Environ.* **2017**, *245*, 83–91. [CrossRef]
54. Kochiieru, M.; Feiziene, D.; Feiza, V.; Volungevicius, J.; Velykis, A.; Slepeliene, A.; Deveikyte, I.; Seibutis, V. Freezing-Thawing Impact on Aggregate Stability as Affected by Land Management, Soil Genesis and Soil Chemical and Physical Quality. *Soil Tillage Res.* **2020**, *203*, 104705. [CrossRef]
55. Yang, S.; Dong, Y.; Song, X.; Wu, H.; Zhao, X.; Yang, J.; Chen, S.; Smith, J.; Zhang, G.-L. Vertical Distribution and Influencing Factors of Deep Soil Organic Carbon in a Typical Subtropical Agricultural Watershed. *Agric. Ecosyst. Environ.* **2022**, *339*, 108141. [CrossRef]
56. Somasundaram, J.; Chaudhary, R.S.; Awanish Kumar, D.; Biswas, A.K.; Sinha, N.K.; Mohanty, M.; Hati, K.M.; Jha, P.; Sankar, M.; Patra, A.K.; et al. Effect of Contrasting Tillage and Cropping Systems on Soil Aggregation, Carbon Pools and Aggregate-associated Carbon in Rainfed Vertisols. *Eur. J. Soil Sci.* **2018**, *69*, 879–891. [CrossRef]
57. Bordonal, R.D.O.; Lal, R.; Ronquim, C.C.; De Figueiredo, E.B.; Carvalho, J.L.N.; Maldonado, W.; Milori, D.M.B.P.; La Scala, N. Changes in Quantity and Quality of Soil Carbon Due to the Land-Use Conversion to Sugarcane (*Saccharum officinarum*) Plantation in Southern Brazil. *Agric. Ecosyst. Environ.* **2017**, *240*, 54–65. [CrossRef]
58. Okolo, C.C.; Gebresamuel, G.; Zenebe, A.; Haile, M.; Eze, P.N. Accumulation of Organic Carbon in Various Soil Aggregate Sizes under Different Land Use Systems in a Semi-Arid Environment. *Agric. Ecosyst. Environ.* **2020**, *297*, 106924. [CrossRef]
59. Demenois, J.; Rey, F.; Ibanez, T.; Stokes, A.; Carriconde, F. Linkages between Root Traits, Soil Fungi and Aggregate Stability in Tropical Plant Communities along a Successional Vegetation Gradient. *Plant Soil* **2018**, *424*, 319–334. [CrossRef]
60. Luan, H.; Gao, W.; Tang, J.; Li, R.; Li, M.; Zhang, H.; Chen, X.; Masiliunas, D.; Huang, S. Aggregate-Associated Changes in Nutrient Properties, Microbial Community and Functions in a Greenhouse Vegetable Field Based on an Eight-Year Fertilization Experiment of China. *J. Integr. Agric.* **2020**, *19*, 2530–2548. [CrossRef]
61. Liu, Y.; Zhu, G.; Hai, X.; Li, J.; Shangguan, Z.; Peng, C.; Deng, L. Long-Term Forest Succession Improves Plant Diversity and Soil Quality but Not Significantly Increase Soil Microbial Diversity: Evidence from the Loess Plateau. *Ecol. Eng.* **2020**, *142*, 105631. [CrossRef]

Disclaimer/Publisher’s Note: The statements, opinions and data contained in all publications are solely those of the individual author(s) and contributor(s) and not of MDPI and/or the editor(s). MDPI and/or the editor(s) disclaim responsibility for any injury to people or property resulting from any ideas, methods, instructions or products referred to in the content.

Impact of Climate Change on Snowmelt Erosion Risk

Jana Podhrázská^{1,2,*}, Jan Szturc², Josef Kučera¹ and Filip Chuchma³

¹ Department of Landscape Planning, Research Institute for Soil and Water Conservation, 602 00 Brno, Czech Republic; kucera.josef.jr@vumop.cz

² Department of Applied and Landscape Ecology, Faculty of AgriSciences, Mendel University in Brno, 613 00 Brno, Czech Republic; jan.szturc@mendelu.cz

³ Czech Hydrometeorological Institute, 143 06 Prague, Czech Republic; filip.chuchma@chmi.cz

* Correspondence: podhraszka.jana@vumop.cz; Tel.: +420-737-879-678

Abstract: Climate change affects all sectors of human activity. Agricultural management is influenced by changes in temperature and precipitation distribution both during the growing season and in the non-growing period. The contribution of snowmelt erosion to the total annual loss of arable soil has not yet been sufficiently emphasized. Based on the USLE principle, an equation for soil loss caused by snowmelt was derived, and the erosion potential of snow was determined for the conditions in the Czech Republic. In the foothill area of Větkovice, an analysis of changes in selected climatic characteristics in the years 1961–2020 was elaborated. It was shown that the area is warming and the number of days with temperatures below 0 °C is decreasing. The total annual precipitation decreased by 18 mm. Furthermore, the erosion potential was compared in two referential periods for both the entire Czech Republic and the Větkovice area, and a case study of soil loss due to snowmelt erosion was prepared. Despite a slight reduction in the erosion potential in the model area, the erosion shear from snowmelt reaches values higher than the permissible limit.

Keywords: erosion potential; climatic characteristics; foothill area; soil loss; non-vegetation period; snow water equivalent

Academic Editors: Jianye Li,
Weida Gao, Wei Hu, Qiang Chen and
Xingyi Zhang

Received: 18 October 2024

Revised: 9 December 2024

Accepted: 23 December 2024

Published: 30 December 2024

Citation: Podhrázská, J.; Szturc, J.;
Kučera, J.; Chuchma, F. Impact of
Climate Change on Snowmelt
Erosion Risk. *Land* 2025, 14, 55.
[https://
doi.org/10.3390/land14010055](https://doi.org/10.3390/land14010055)

Copyright: © 2024 by the authors.
Licensee MDPI, Basel, Switzerland.
This article is an open access article
distributed under the terms and
conditions of the Creative Commons
Attribution (CC BY) license
([https://creativecommons.org/
licenses/by/4.0/](https://creativecommons.org/licenses/by/4.0/)).

1. Introduction

Snow is one of the most variable elements of the hydrological cycle [1]; therefore, snowmelt combined with rain and soil freezing can lead to severe erosion, even in less vulnerable areas [2]. According to [3], soil erosion is one of the main global environmental problems limiting the sustainable development of the ecological environment. As stated [4], soil loss caused by snowmelt runoff constitutes a significant part of the total annual soil erosion in mid to high latitudes, as confirmed by [5–7]. In these vulnerable areas, snowmelt erosion can cause serious damage to soil quality and health, water quality, crop yields, and overall ecological balance [8,9]. With the increasing melting of glaciers and decreasing snow cover, the impact of snowmelt on hydrological processes and soil erosion is becoming more serious [10]. Annual snowfall only accounts for 5% of the total global precipitation, as stated by [11]. Due to the spatial heterogeneity of snow distribution and the complexity of snowmelt processes, snowmelt runoff in mid to high latitudes likely causes even more severe soil erosion than water erosion [12–15], as evidenced by erosion studies [16–18]. This is further confirmed by [19], who demonstrated that water flows much faster on a frozen slope than on a thawed slope. Erosion caused by snowmelt has its own distinct characteristics [20], such as snowmelt runoff being sensitive to changes in radiation and air

temperature, the soil surface being affected by freezing and thawing, the frozen-soil layer reducing infiltration, and low vegetation cover during the snowmelt period.

The primary characteristic of snowmelt erosion is the freezing of soil during the winter, leading to the exclusion of water from the soil, which forms ice crystals around soil aggregates. These crystals break up soil aggregates, resulting in fine particles that are released and transported during snowmelt [10]. The thawed topsoil becomes muddy and susceptible to erosional damage. Another effect of soil freezing is increased soil erodibility in the spring months, when the potential for water infiltration into lower layers is significantly reduced [9]. In this period, relatively strong erosion occurs in the surface layer, even though the amount of melting snow is small. The erosion process during snowmelt is accelerated by the arrival of warm air masses accompanied by rainfall [21,22]. According to [23], the temporal variability of snow cover and the spatial heterogeneity of soil freezing, together with rain-on-snow events, cause complex and dynamic runoff. Ref. [24] found that the rate of snowmelt and infiltration of rain into frozen soil depends largely on the initial water content, frost depth, and soil temperature.

Snow cover is also an important indicator of the climatic character of winter. The analysis of spatial and temporal variability of snow cover in a watershed helps to assess changes in flood regimes [25], predicting snowmelt runoff in the spring period [26]; it is also an important indicator for assessing air temperature in climate studies [27].

Snowmelt, soil freezing, and related erosion events exhibit significant spatial variability [28]. According to [29], spring snowmelt, as well as repeated snowmelt during winter, contributes to annual water runoff and soil particle removal from the entire watershed. Soil particles released by melting snow water are deposited at the foot of slopes when their velocity decreases. Fine soil particles, however, are transported to watercourses, where they constitute most of the sediment. This unchanneled runoff from melting snow causes soil loss if not protected by vegetation and can lead to seasonal flooding [30–32]. Soil erosion increases with slope steepness and length and depends on spring weather conditions as well as those during winter and autumn [33]. The microrelief of cultivated land also significantly affects soil erosion. The most intense soil erosion is observed on fields plowed along the slope and is significantly less intense on fields cultivated along the contour lines, as ridges and furrows reduce and impede the flow of water from melting snow. It was also found by [18] that the protective effect of vegetation in the spring is small, and the risk of erosion is particularly high in areas where autumn plowing leaves the soil unprotected. According to [34], there has been a significant increase in temperature characteristics in the Czech Republic between 1961 and 2019. Due to rising temperatures, an increase in the ratio of rainfall to snowfall, especially at the beginning and end of the cold season, and thus less snow accumulation during the winter season, is expected [35].

In practice, two approaches are used to calculate snowmelt runoff. The first is the energy balance method and the second is the temperature index method. A more accurate alternative to represent snowpack processes is the energy balance method. The energy balance approach is data-intensive because melting is derived from the balance of incoming and outgoing energy components. In contrast, temperature-index models, also called degree-day models, use only air temperature to estimate melt rates [36]. The use of temperature indices (degree days) is based on an assumed relationship between ablation and air temperature, which is usually expressed as positive temperature sums [37].

Snow accumulation and melt are further influenced by various factors, primarily elevation, wind, exposure, slope, and vegetation cover. According to [38], vegetation is the most significant influencing factor. Other factors such as elevation, orientation, and exposure to the prevailing wind direction act in combination and it is not possible to clearly determine a dominant factor. The melting rate is usually significantly lower

than the intensity of rainfall, which is commonly recorded in $\text{mm}\cdot\text{day}^{-1}$. However, the soil is frozen and saturated with water in the surface layer during winter, reducing the infiltration rate. As a result, a significant portion of the meltwater runs off, and thus the runoff coefficient from snowmelt on frozen soil is usually higher than that of rainwater. Normal values of snowmelt runoff range from 1.0 to $15\text{ mm}\cdot\text{day}^{-1}$. Although erosion caused by meltwater does not reach the same intensity as erosion caused by rainfall runoff, it acts over a larger area with little vegetation protection, making soil erosion one of the primary consequences [21,22].

Erosion models provide a powerful tool for investigating snowmelt erosion. Conceptual models, which are based on empirical relationships between variables, and physical models, which are grounded in the physics of snowmelt, are commonly employed in such studies [39]. Some of the physical models used include SWAT (Soil and Water Assessment Tool), WEPP (Water Erosion Prediction Project), EUROSEM (European Soil Erosion Models), and LISEM (Limburg Soil Erosion Model). The Czech hydrometeorological institute (CHMI) uses the SNOW17 model to simulate the accumulation and melting of snow cover. The model combines the two main approaches to snow cover modeling. A simple energy balance is used in the case of liquid precipitation. In other cases, a degree-day approach is used.

Empirical models are mostly based on the derivation of a universal soil loss equation (USLE) (e.g., RUSLE—Revised Universal Soil Loss Equation, MUSLE—Modified Universal Soil Loss Equation, SHI—The Russian State Hydrological Institute model), as stated by [10].

Based on the USLE principle, ref. [21] derived an equation for soil loss caused by snowmelt for the conditions of the Czech Republic. This equation has been further used in other studies [40] by determining the R factor value in the post-harvest period and the snowmelt erosion, calculating the total annual soil loss for a selected area using the approach according to [21]. The application of USLE and its modification according to [21] was also dealt with by [41], who presented a method for assessing the erosive potential of snow cover based on data available from the Czech Hydrometeorological Institute (CHMI). The study by [42] presents an evaluation of the erosive potential of snow for the territory of the Czech Republic in the cold periods of 1980/1981 to 2009/2010.

This study focuses on the application of a method developed by [21,42] for determining changes in snow erosion potential in the conditions of the Czech Republic during two referential periods and the interpretation of this method for specific conditions of a foothill area.

2. Materials and Methods

The intensity of erosion caused by snowmelt, according to [21], is based on the universal soil loss equation [43], where the rainfall erosivity factor R is replaced by the snowmelt rate factor m ($\text{mm}\cdot\text{day}^{-1}$) in a maximum 20-day period, in which the most intense thawing takes place and the factor of amount of water derived from snow during the 20-day period is h (cm). The combination of both factor m and h could be assigned as erosive potential of snow cover. The amount of water produced by snowmelt (h) and the snowmelt rate (m) can be derived from long-term measurements at meteorological stations using databases of snow water equivalent (SWE) and snow cover depth (SCE) [41,44].

2.1. Determination of the Potential of Snowmelt Erosion

The combination of SWE and SCE factors can be collectively referred to as the erosion potential of water accumulated in the snow cover (E_p). The determination of E_p values using data from available climatic stations can be used for the areal distribution of the risk

of soil erosion caused by snowmelt. This approach was used to assess the erosion potential for the conditions of the Czech Republic.

To evaluate the impact of climate change on factors causing snowmelt erosion, two periods were selected for the analysis: 1981–2010 and 1991–2020.

The erosion potential was calculated for a dataset of 235 Czech Hydrometeorological Institute (CHMI) climatological and precipitation stations, selected based on data availability. The daily values of SWE and SCE were used for the so-called cold period of the year, specifically from October to the following May. In total, data from 1980/1981 to 2019/2020 were processed. Starting from the day with the highest snow water equivalent, the number of days until the total snow depth reached zero was counted. If this did not happen, a maximum of 20 melting days was considered for the erosion potential calculation. From the annual values, average erosion potential values (E_p) were calculated for two periods of 1981–2010 and 1991–2020).

2.2. Regionalization of the Potential of Snowmelt Erosion in the Czech Republic

A point layer was processed in ArcGIS Pro 3.3.1 from the set of snowmelt erosion potential values for the periods 1981–2010 and 1991–2020. The snowmelt erosion potential values for individual stations were interpolated across the Czech Republic using regression kriging, dependent on several parameters such as altitude, slope, and aspect, including corrections to the estimated value to maintain the value corresponding to the station's location. The interpolation was performed using tools contained in the ProClimDB software (Climahom, Prague, Czech Republic, www.climahom.eu). The resulting raster model with a spatial resolution of 500 m × 500 m was subsequently processed in the ArcGIS software environment, and the raster was smoothed using the low-pass filter method.

The categorization of values was carried out by classifying the erosion potential raster into 5 categories. The boundaries of each category were set at the 20th, 40th, 60th, and 80th percentiles of the raster erosion potential values for the given periods. This categorization using the percentiles was carried out to determine relatively equally extensive areas within the Czech Republic. Subsequently, the area of land falling into each category and period was calculated.

2.3. Study Area Větkovice

The study area of Větkovice—located in the foothills of the Nížký Jeseník mountains in the northeastern part of the Czech Republic—(Figure 1) was selected for interpreting the risk of erosion from snowmelt using erosion potential values.

The average altitude of this area is 480–500 m above sea level. The area is characterized by a climate with a very short, moderately cool, and humid summer, a long transition period with a moderately cool spring and mild autumn, and a long, mild to moderately humid winter with a long duration of snow cover. The average annual air temperature in the locality is 7.6 °C, and in winter it is −1.7 °C, with the coldest month being January.

As part of the analysis of climatic characteristics, average values for individual months, the year, and seasons were calculated for the locality, focusing on the evaluation primarily in winter and the cold half-year (October to March). To assess the possible change in the occurrence of snowmelt erosion, trends in the time series of climatic characteristics related to erosion in winter period were also processed. The trends were determined from long-term climate data for the period 1961–2020.

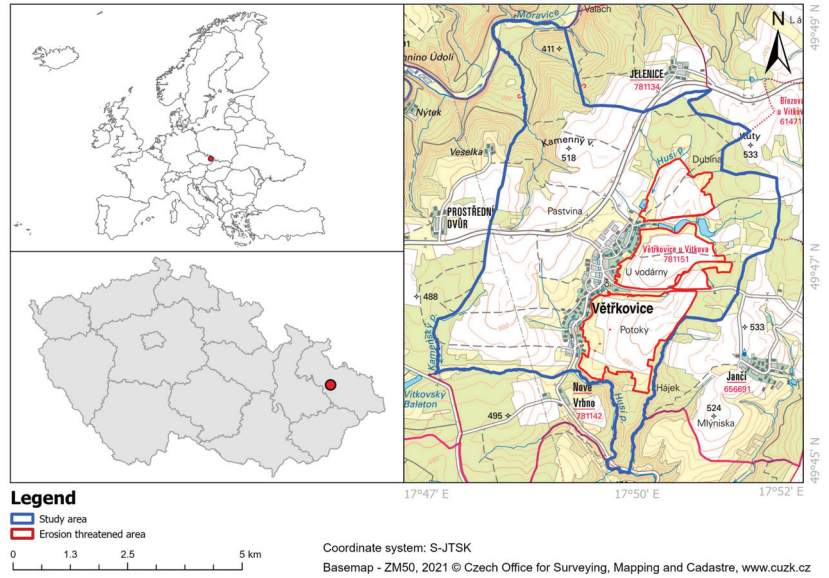


Figure 1. Location of the study area and the analyzed land blocks (EHP).

To compare the impact of changing climatic characteristics on the risk of erosion from snowmelt, long-term average soil loss was analyzed on selected land blocks in the Větrkovice locality, depending on the snow erosion potential (E_p) for the two referential periods of 1981/2010 and 1991/2020 according to the modified equation by [21].

$$E_S = E_p \cdot k \cdot LS \cdot C \cdot P \cdot K \text{ [t} \cdot \text{ha}^{-1} \cdot \text{year}^{-1}\text{]} \quad (1)$$

E_S —Intensity of erosion [$\text{t} \cdot \text{ha}^{-1} \cdot \text{year}^{-1}$];

E_p —The erosion potential [–];

k —The runoff coefficient.

LS —The topographic factors [–];

C —The cropping management factor in the period of dangerous snowmelt [–];

P —The supporting practices factor [–];

K —The soil erodibility factor [$\text{t} \cdot \text{ha}^{-1}$].

The calculation of erosion intensity using the equation required the determination of specific factor values.

2.4. Factors LS , P , and K

These factors are determined using standard procedures according to the calculation method for water erosion.

2.5. The Runoff Coefficient (k)

The value of the runoff coefficient during the snowmelt period varies between 0.7 and 1.5 depending on the soil freezing. In the case where data on soil freezing are not available, it is possible to use the mean value of the runoff water coefficient $k = 1$.

2.6. The Vegetation Cover Efficiency Factor in the Period of Dangerous Snowmelt (C)

This factor was determined based on the equation [45,46].

$$C_{NO} = 0.8656 \cdot C_{VO} + 0.128 \quad (2)$$

C_{NO} —C factor for non-vegetation season;

C_{VO} —C factor for vegetation season.

3. Results

3.1. Overview of Climatological Characteristics of the Větrkovice Area Regard to Snowmelt Erosion and Its Trend

From the daily values of a set of climatic characteristics from the Vítkov meteorological station near Opava, data on the average, minimum, and maximum air temperature, total precipitation, new snow cover (i.e., daily increase in snow cover), number of days with a minimum temperature below 0 °C, and number of days with total high of snow cover above 1 cm were processed. The results are documented in Tables 1 and 2.

Table 1. Average annual, monthly, and seasonal values of climatological characteristics for the period 1961–2020.

Trends—Period 1961–2020	Year	Winter	Spring	Summer	Autumn	X.-III.	IV.-IX.
mean temperature °C	7.60	−1.70	7.40	16.70	7.90	1.30	13.80
maximum temperature °C	12.00	1.20	12.30	22.30	12.00	4.70	19.20
minimum temperature °C	3.30	−4.70	2.60	11.20	4.20	−1.90	8.50
number of days with minimum temperature below 0 °C	119.00	72.60	27.50	0.00	18.60	110.70	8.70
number of days with total snow depth above 1 cm	70.80	53.30	11.90	0.00	5.70	68.90	1.90
depth of new snow (cm)	119.20	80.90	22.60	0.00	15.00	113.50	6.40
precipitation total (mm)	679.70	105.30	170.20	254.10	149.70	233.80	445.10

Table 2. Trend values of individual characteristics for months, years, and seasons for the period 1961–2020 at Větrkovice (orange is statistically significant trend, $p = 0.05$).

Trends—Period 1961–2020	Year	Winter	Spring	Summer	Autumn	X.-III.	IV.-IX.
mean temperature °C	0.380	0.390	0.350	0.500	0.230	0.360	0.400
maximum temperature °C	0.400	0.350	0.410	0.580	0.230	0.360	0.460
minimum temperature °C	0.370	0.430	0.250	0.470	0.300	0.400	0.350
number of days with minimum temperature below 0 °C	−5.100	−2.010	−1.250	0.00	−1.310	−4.590	−0.610
number of days with total snow depth above 1 cm	−6.405	−3.370	−1.699	−0.016	−0.784	−5.606	−0.134
depth of new snow (cm)	−14.005	−6.896	−2.097	−0.016	−3.341	−13.609	−1.013
precipitation total (mm)	−18.017	−5.606	−10.130	−5.678	4.186	−12.030	−7.936

As part of the trend analysis, linear trends for temperature characteristics were tested using the *t*-test, and for precipitation characteristics, the Mann–Kendall non-parametric trend test was performed. The results are presented in Figures 2–4. (The graph shows the trend value, i.e., the change in the value of the characteristic over 10 years for months, years, and seasons. Orange columns indicate whether the trend is statistically significant; gray indicates insignificance).

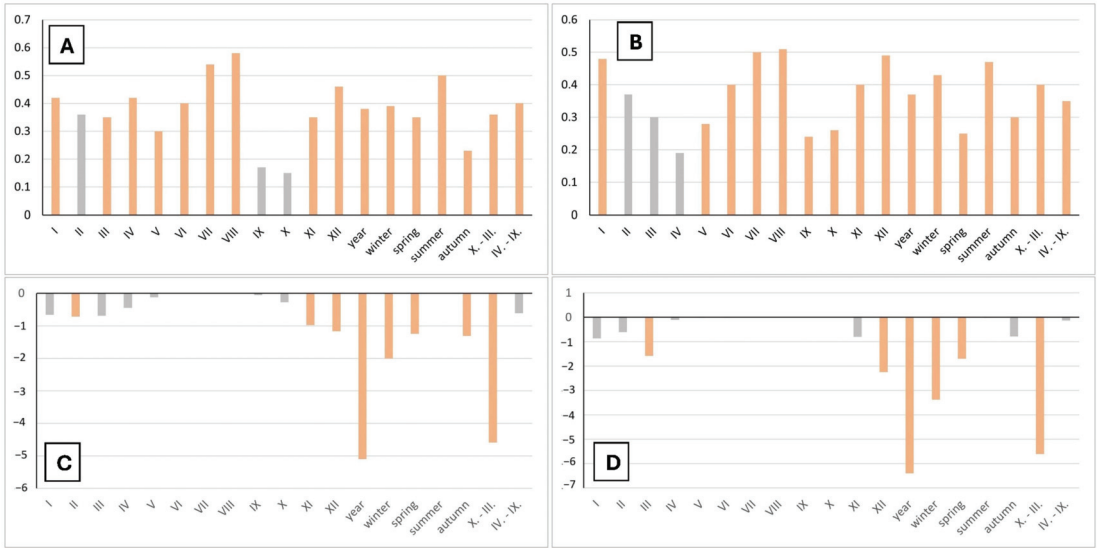


Figure 2. Values of the linear trend in mean temperature (A), minimum temperature (B), number of days with minimum temperature below 0 °C (C), and number of days with total snow cover above 1 cm (D) in °C/10 years for months, years, and seasons for the period 1961–2020 at Větrkovice (orange indicates statistically significant trend, $p = 0.05$).

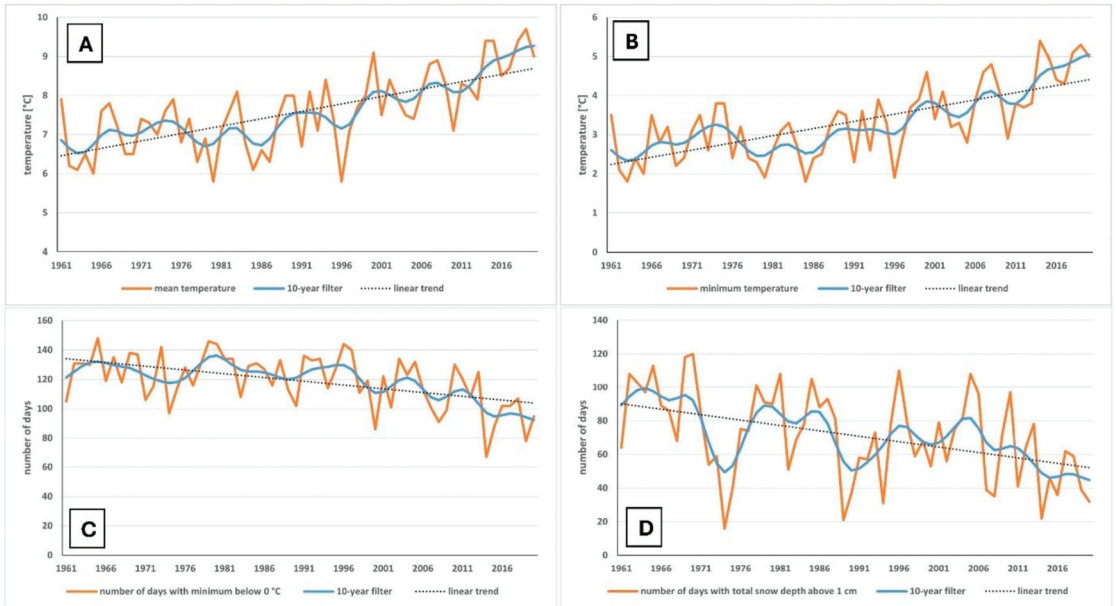


Figure 3. Values and course of mean temperature (A), minimum temperature (B), number of days with minimum temperature below 0 °C (C), and number of days with total snow cover above 1 cm (D) in °C/10 years for the period 1961–2020 at Větrkovice.

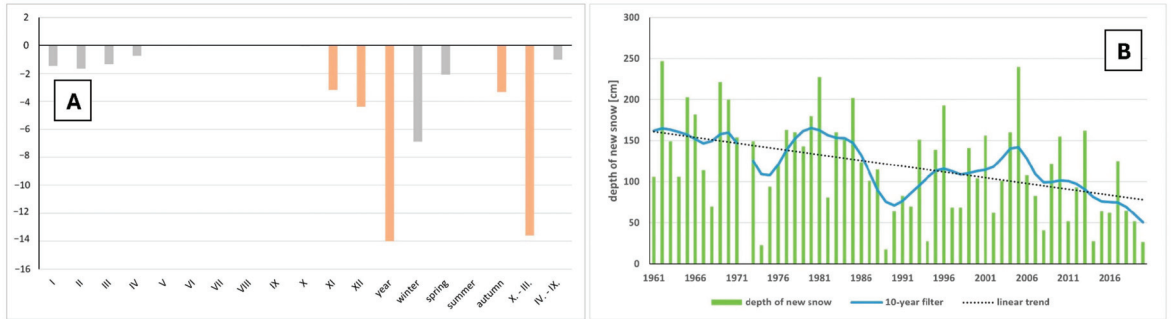


Figure 4. Linear trend (A) and course of values (B) of the amount of new snow cover (in cm/10 years) for months, years, and seasons from 1961 to 2020 at Větrkovice (orange indicates statistically significant trend, $p = 0.05$).

The analysis of annual and seasonal averages, minimums, and maximums temperatures clearly shows a significant increase in values towards the present. This is confirmed by the identified trends, where a statistically significant increasing trend in temperature characteristics is evident for most months, as well as for annual and seasonal values. In the winter period, a temperature increase trend of $0.4\text{ }^{\circ}\text{C}$ per 10 years was found, while in spring, the average and maximum temperatures show an increase of $0.4\text{ }^{\circ}\text{C}$ per 10 years, and the minimum temperature has a slightly lower increase of approximately $0.3\text{ }^{\circ}\text{C}$ per 10 years. Consistent with this, there is also a trend in a decreasing number of days with a minimum temperature below $0\text{ }^{\circ}\text{C}$. The annual number of these days, which averages 119 per year, is decreasing at a rate of about 5 days per 10 years. This means that there is a gradual and significant increase in the occurrence of days with snowmelt or precipitation in the form of rain during the winter period. Regarding precipitation, the average annual precipitation in the period 1961–2020 is 679.7 mm, and in the cold half-year, it is 233.8 mm. A statistically significant decreasing trend in precipitation is evident both in annual values and in values for the spring season, and it is also present in the amounts in the cold half-year. The trend in decreasing annual precipitation is 18 mm per 10 years, in the spring season it is approximately 10 mm per 10 years, and in the cold half-year, a decrease of 12 mm per 10 years is recorded (see Table 2). Similarly, there is a change in the recorded sums of total new snow depth, which averages 119.2 cm in the locality. A significant decreasing trend of 14 cm per 10 years was proven for annual values, and in the autumn season, the total sum of new snow decreases by a trend of 3.3 cm per 10 years. An interesting indicator for the future estimation of snowmelt erosion development can also be the characteristic of the number of days with a total high of snow cover above 1 cm. On average, there are about 71 such days in the locality per year. According to the trend analysis, a statistically significant decreasing trend of 6.4 days per 10 years was recorded in annual values; for the winter season this was 3.4 days/10 years and in the spring season 1.7 days/10 years.

Warming is also evident from observed measurements across Europe, and the frequency of weather extremes is increasing [47]. The average annual air temperature increased by $0.3\text{ }^{\circ}\text{C}$ per decade between 1961 and 2018, and in the last 28 years (1991–2018), it has risen by $0.9\text{ }^{\circ}\text{C}$ compared to the 1961–1990 average, such as in the Czech Republic [48]. The trends in increasing temperatures within the three reference periods are also confirmed by [34].

The trends in climatic characteristics in the Větrkovice area correspond with the scenarios processed by [48] for the Czech Republic, where we can expect an increase in air temperature of at least $2\text{ }^{\circ}\text{C}$ by the end of this century compared to the reference period 1981–2010. The highest increase in maximum air temperatures will occur in winter and

the lowest in spring. Furthermore, it is expected that by the end of the century, the annual average precipitation in the Czech Republic will increase by 7–16%. There will be an increase in winter precipitation, which may rise by up to 35% by the end of the 21st century, while summer precipitation will decrease. Based on analyses of climatic characteristics and their scenarios in the territory of Ukraine, ref. [49] indicates that episodes of snowmelt will likely decrease, but solid precipitation will be replaced by liquid precipitation. This phenomenon will require further study of the impact of liquid precipitation in the winter period on soil erosion.

3.2. The Differences in Erosion Potential Values for the Given Periods

Table 3 shows a gradual trend in decreasing areas with high erosion potential (>85.1) and, conversely, an increase the area of regions where lower E_p values (6.1–26) were analyzed. This may indicate a decrease in the risk of erosion events in higher-altitude areas, where the amount of fallen snow is decreasing. However, areas with lower erosion potential in the winter period may be affected over a larger area. Since these are mostly areas with intensive farming on arable land than in the foothill areas, more significant erosion events associated with snowmelt may occur here.

Table 3. Area representation of individual categories of erosion potential values for two periods within years 1981–2020 as a percentage of the area of Czech Republic.

Erosion Potential	1981–2010	1991–2020
0–6	17.5	18.8
6.1–26	20.0	22.9
26.1–49	19.4	20.8
49.1–85	19.8	19.9
>85.1	23.2	17.6

By interpolating the erosion potential values across the area of the Czech Republic, erosion potential maps were generated for the analyzed periods of 1981–2010 and 1991–2020 (Figures 5 and 6).

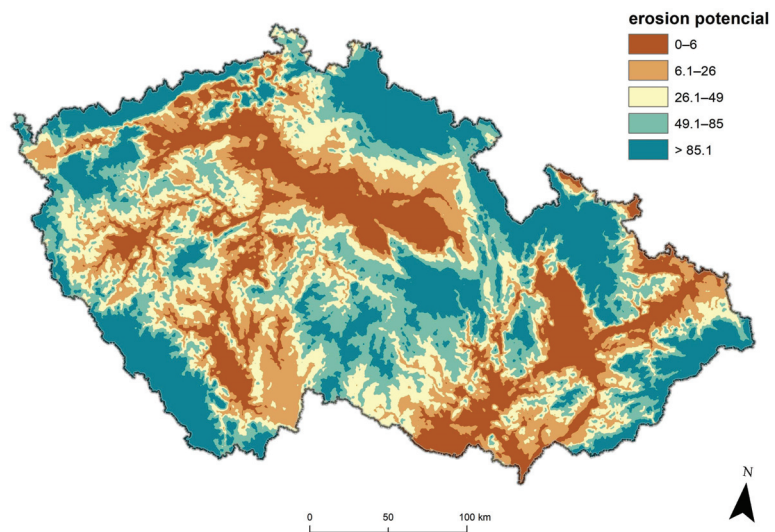


Figure 5. The erosion potential map for the referential period 1981–2010.

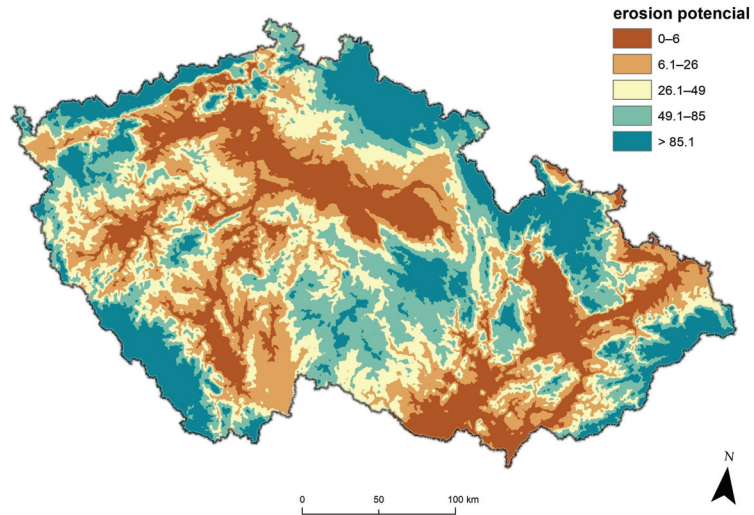


Figure 6. The erosion potential map for the referential period 1991–2020.

These maps were used to determine erosion potential values for two referential periods in the Větrkovice locality. Using a modified equation [21], the amount of erosion runoff on erosion-assessed areas was calculated and their difference compared. Methods for quantifying erosion processes from snowmelt are still rarely published. Most publications present complex models for quantifying erosion from snowmelt [50] or its intensity [51].

An erosion potential map for the referential period of 1981–2010 published by [42] presented results of erosion potential analysis from only 50 climatic stations. The newly processed maps in Figures 5 and 6 represent a more detailed distribution of erosion potential and newly define the boundaries of individual categories. They allow the comparison of changes in erosion potential during the two referential periods.

3.3. Analysis of Erosion Risk in the Větrkovice Area Using Erosion Potential Maps

The erosion potential (E_p) for the studied area was determined from the erosion potential maps. The E_p value was used in two variants: erosion potential from the referential period of 1981–2010 (E_p past = 54.40) and erosion potential from the referential period of 1991–2020 (E_p pres = 50.45).

For the factor of runoff water, a value of $k = 1$ was determined. The LS factor was determined based on the digital elevation model (DEM) using the USLE2D program algorithm (McCool). The K factor was determined according to the soil characteristics of the area (main soil type). Its value is 0.41 (soils highly susceptible to erosion). The C_{NO} factor was recalculated based on the determined C_{VO} for the area of interest ($C_{VO} = 0.024$). For the non-vegetation period, $C_{NO} = 0.305$. The limit value for soil loss was set according to [52] (decree on the protection of agricultural land against erosion) at $9 \text{ t}\cdot\text{ha}^{-1}\cdot\text{y}^{-1}$.

GIS tools were used on a digital elevation model (DEM) to calculate the degree of erosion risk. Four land blocks (EHP 1–4) were evaluated (see Figure 1). The results of the analysis are shown in Table 4.

Table 4. Intensity of snowmelt erosion for two values of erosion potential. (Exceeded erosion limit in red).

EHP	Area [ha]	The Percentage Share of the E_s Value Interval [$t \cdot ha^{-1} \cdot y^{-1}$]						E_s (°)	E_{sp} (Permissible)
		<4	4.01–8	8.01–12	12.01–16	16.01–20	>20		
E_P pres 50.40 (1991–2020)									
1	138.70	34.80	16.00	13.30	10.90	7.90	17.10	11.45	9.00
2	81.93	42.80	15.80	9.70	8.30	8.30	15.00	9.78	9.00
3	58.43	48.20	11.30	6.80	6.10	5.30	22.20	10.31	9.00
4	16.65	41.20	20.30	13.20	9.30	7.10	9.00	8.06	9.00
								⊙ 9.90	9.00
E_P past 54.40 (1981–2010)									
1	168.70	33.50	15.40	12.60	10.40	8.70	19.50	12.36	9.00
2	81.93	41.10	15.60	10.00	7.10	8.30	17.90	10.56	9.00
3	58.43	46.80	11.20	7.40	5.30	5.20	24.10	11.13	9.00
4	16.65	38.90	20.50	12.60	9.50	7.20	11.20	8.70	9.00
								⊙ 10.69	9.00

The results of the analysis indicate a slight decrease in the intensity of erosion caused by snowmelt due to changing climatic conditions. However, the observed values still exceed the limits set by legislation [52]. Considering the erosion potential derived from the map processed for the referential period 1991–2020, the average soil loss due to erosion is $9.9 t \cdot ha^{-1} \cdot y^{-1}$. When considering the past E_P values determined from the data of 1981–2010, the average soil loss is $10.69 t \cdot ha^{-1} \cdot y^{-1}$. Overall, there is an average reduction in erosion intensity in the winter period by $0.79 t \cdot ha^{-1} \cdot y^{-1}$. Nevertheless, attention must be paid to erosion from snowmelt, as demonstrated by [4], who found that soil losses were higher during snowmelt periods than during rainfall periods in the northeastern China watershed due to higher surface runoff in early spring. Reduced soil infiltrability during snowmelt periods also significantly contributed to this higher surface runoff. Work by [17] studied the causes of erosion in potato fields and found large soil losses ($10\text{--}15 t \cdot ha^{-1} \cdot y^{-1}$) caused by snowmelt. In agricultural areas of European Russia, [53] determined the intensity of soil erosion over periods of snowmelt and storm runoff, as well as the total annual soil loss. The average soil erosion in the studied area is $4.04 t \cdot ha^{-1} \cdot y^{-1}$, considering the soil protection coefficients of agricultural vegetation. In the annual soil loss due to erosion, rainfall runoff erosion predominates at $3.78 t \cdot ha^{-1} \cdot y^{-1}$, while snowmelt erosion is significantly lower at only $0.26 t \cdot ha^{-1} \cdot y^{-1}$. In the Czech Republic, [46] calculated the average long-term soil loss due to water from melting snow for selected localities. The calculated soil loss in the non-vegetation period was up to $36 t \cdot ha^{-1} \cdot y^{-1}$.

4. Conclusions

The analysis of the development of climatic characteristics of the studied area in the years 1961–2020, with an emphasis on the winter period, showed the following significant results:

- i. There is an increase in average, maximum, and minimum air temperatures, and accordingly, a decrease in the number of days with temperatures below $0^\circ C$. The warming of the area is also associated with a decrease in the total depth of new snow cover by 3.3 cm per 10 years and a decrease in the number of days with snow cover height above 1 cm by 6.4 days per 10 years.
- ii. The total decrease in precipitation amounts is 12 mm per 10 years in the cold half of the year, and for annual totals, it is 18 mm per 10 years.

- iii. From the CHMI database, the erosion potential of snow was calculated at 235 climatic stations. The erosion potential values for individual stations were interpolated across the area of the Czech Republic using the method of regression kriging into an erosion potential map for two referential periods. The results show a change in the spatial distribution of erosion potential values. High E_p values, occurring in foothill and mountainous areas that are mostly grass-covered, are decreasing in area. The spatial share of lower E_p values, located mainly in lower altitudes and predominantly arable, is increasing. In these areas, more significant erosion events associated with snowmelt on arable land may occur.
- iv. The comparison of erosion potential calculated for two referential periods (1981–2010 and 1991–2020) in the Větrkovice case area showed a slight decrease in erosion potential value in the referential period of 1991–2020, which corresponds with the analyses of changes in climatic characteristics in the studied area. However, the soil loss due to snowmelt erosion, calculated for selected localities, still exceeds the values set by current legislation by $0.9 \text{ t}\cdot\text{ha}^{-1}\cdot\text{y}^{-1}$.

In view of the above findings from the analyses, it follows that in the future, the locality is expected to experience further increases in temperatures, both in annual values and in the winter season, along with a decrease in the number of days supporting the formation of continuous snow cover and the total precipitation in the form of snow. However, considering that despite the decrease in the number of days with snow cover, snow still occurs sufficiently in the locality during the winter period, this, combined with the trend in rising winter temperatures and thus a higher probability of rainfall, may indicate more frequent episodes of rapid snowmelt in the future, leading to intensified soil erosion processes.

This fact can be alarming because soil losses due to erosion from both snowmelt and winter liquid precipitation must be considered in the context of year-round erosion events. The total soil loss due to erosion, including that in the non-vegetation period, has not yet been summarized within the Czech Republic, despite potentially exceeding the set limits. Temperature fluctuations can promote more intense snowmelt, leading to more frequent soil particle transport in the winter period and increased sediment presence in watercourses. For these reasons, despite the decreasing amount of snow cover in the winter period, it is necessary to continue addressing the issue of erosion processes in the non-vegetation period. Currently, there are various models for determining erosion from snowmelt; however, the application of snowmelt erosion models in practical research is minimal, which hinders the updating and development of snowmelt erosion models and leads to low model adaptability in the current climate change and multi-extreme event-prone environment.

Author Contributions: Conceptualization: J.P. and J.K.; methodology: J.P. and F.C.; software: F.C. and J.K.; validation: J.S., F.C. and J.K.; formal analysis: F.C.; investigation: J.K. and J.S.; resources: F.C.; data curation: J.K.; writing—original draft preparation: J.P. and J.S.; writing—review and editing: J.P.; visualization, J.K.; supervision: J.P.; project administration: J.P. and J.K.; funding acquisition: J.P. All authors have read and agreed to the published version of the manuscript.

Funding: This research was funded by Technology Agency of the Czech Republic, grant number TH 04030363 and by Institutional support of Ministry of Agriculture of the Czech Republic—number RO0223. The APC was funded by a publisher.

Data Availability Statement: The raw data supporting the conclusions of this article will be made available by the authors on request.

Acknowledgments: The authors would like to acknowledge all the reviewers and editors. We also thank the CHM Institute for providing valuable data.

Conflicts of Interest: The funders had no role in the design of the study; in the collection, analyses, or interpretation of data; in the writing of the manuscript; or in the decision to publish the results.

References

1. Doesken, N.J.; Robinson, D.A. The Challenge of Snow Measurements. In *Historical Climate Variability and Impacts in North America*; Springer: Heidelberg, Germany, 2009.
2. Øygarden, L. Rill and gully development during an extreme winter runoff event in Norway. *Catena* **2003**, *50*, 217–242. [CrossRef]
3. Quinton, J.N.; Fiener, P. Soil erosion on arable land: An unresolved global environmental threat. *Prog. Phys. Geogr. Earth Environ.* **2024**, *48*, 136–161. [CrossRef]
4. Wu, Y.; Ouyang, W.; Hao, Z.; Yang, B.; Wang, L. Snowmelt water drives higher soil erosion than rainfall water in a mid-high latitude upland watershed. *J. Hydrol.* **2018**, *556*, 438–448. [CrossRef]
5. Lana-Renault, N.; Alvera, B.; García-Ruiz, J.M. Runoff and Sediment Transport during the Snowmelt Period in a Mediterranean High-Mountain Catchment. *Arct. Antarct. Alp. Res.* **2018**, *43*, 213–222.
6. Gusarov, A.V. The impact of contemporary changes in climate and land use/cover on tendencies in water flow, suspended sediment yield and erosion intensity in the northeastern part of the Don River basin, SW European Russia. *Environ. Res.* **2019**, *175*, 468–488. [CrossRef]
7. Zhang, L.; Ren, F.P.; Li, H.; Cheng, D.B.; Sun, B.Y. The Influence Mechanism of Freeze-Thaw on Soil Erosion: A Review. *Water* **2021**, *13*, 1010. [CrossRef]
8. Lu, Y.F.; Liu, C.; Ge, Y.; Hu, Y.L.; Wen, Q.; Fu, Z.L.; Wang, S.B.; Liu, Y. Spatiotemporal Characteristics of Freeze-Thawing Erosion in the Source Regions of the Chin-Sha, Ya-Lung and Lantsang Rivers on the Basis of GIS. *Remote Sens.* **2021**, *13*, 309. [CrossRef]
9. Liu, B.; Fan, H.; Jiang, Y.; Ma, R. Linking pore structure characteristics to soil strength and their relationships with detachment rate of disturbed Mollisol by concentrated flow under freeze–thaw effects. *J. Hydrol.* **2023**, *617*, 129052. [CrossRef]
10. Wu, Z.; Fang, H. Snowmelt erosion: A review. *Earth-Sci. Rev.* **2024**, *250*, 104704. [CrossRef]
11. Li, S.; Liu, M.; Adam, J.C.; Pi, H.; Su, F.; Li, D.; Liu, Z.; Yao, Z. Contribution of snow-melt water to the streamflow over the Three-River Headwater region, China. *Remote Sens.* **2021**, *13*, 1585. [CrossRef]
12. Hu, W.; Fan, H.; Li, H.; Zhai, X.Y.; Zhang, X.Y. Snowmelt erosion characteristics of controlled gully in black soil region. *J. Soil Water Conserv.* **2018**, *32*, 84–90.
13. Aygün, O.; Kinnard, C.; Campeau, S. Responses of soil erosion to warming and wetting in a cold Canadian agricultural catchment. *Catena* **2021**, *201*, 105184. [CrossRef]
14. Tang, J.; Liu, G.; Xie, Y.; Dun, X.; Wang, D.; Zhang, S. Ephemeral gullies caused by snowmelt: A ten-year study in northeastern China. *Soil Tillage Res.* **2021**, *212*, 105048. [CrossRef]
15. Wang, L.; Zheng, F.; Liu, G.; Zhang, X.; Wilson, G.; Shi, H.; Liu, X. Seasonal changes of soil erosion and its spatial distribution on a long gentle hillslope in the Chinese Mollisol region. *Int. Soil Water Conserv. Res.* **2021**, *9*, 394–404. [CrossRef]
16. Demidov, V.; Ostroumov, V.; Nikitishena, I.; Lichko, V. Seasonal freezing and soil erosion during snowmelt. *Eurasian Soil Sci.* **1995**, *28*, 78–87.
17. Edwards, L.; Richter, G.; Bernsdorf, B.; Schmidt, R.-G.; Burney, J. Measurement of rill erosion by snowmelt on potato fields under rotation in Prince Edward Island (Canada). *Can. J. Soil Sci.* **1998**, *78*, 449–458. [CrossRef]
18. Lundekvam, H.; Romstad, E.; Oygarden, L. Agricultural policies in Norway and effects on soil erosion. *Environ. Sci. Policy* **2003**, *6*, 57–67. [CrossRef]
19. Ban, Y.; Lei, T.; Liu, Z.; Chen, C. Comparison of rill flow velocity over frozen and thawed slopes with electrolyte tracer method. *J. Hydrol.* **2016**, *534*, 630–637. [CrossRef]
20. Zhai, J.B.; Zhang, Z.; Melnikov, A.; Zhang, M.Y.; Yang, L.Z.; Jin, D.D. Experimental Study on the Effect of Freeze-Thaw Cycles on the Mineral Particle Fragmentation and Aggregation with Different Soil Types. *Minerals* **2021**, *11*, 913. [CrossRef]
21. Zachar, D. *Soil Erosion*; Elsevier Scientific Publishing Company: Amsterdam, The Netherlands, 1982; ISBN 0-444-99725-3.
22. Bai, Q.; Zhou, L.; Fan, H.; Huang, D.; Yang, D.; Liu, H. Effects of frozen layer on composite erosion of snowmelt and rainfall in a typical black soil of northeast China. *Water* **2023**, *16*, 2131. [CrossRef]
23. Sui, J.; Koehler, G. Rain-on-snow induced flood events in Southern Germany. *J. Hydrol.* **2001**, *252*, 205–220. [CrossRef]
24. Watanabe, K.; Kito, T.; Dun, S.; Wu, J.Q.; Greer, R.C.; Flury, M. Water infiltration into a frozen soil with simultaneous melting of the frozen layer. *Vadose Zone J.* **2013**, *12*, vzt2011.0188. [CrossRef]
25. Hall, D.K.; Riggs, G.A.; DiGirolamo, N.E. Comparison of the NASA Standard MODerate-Resolution Imaging Spectroradiometer and Visible Infrared Imaging Radiometer Suite Snow-Cover Products for Creation of a Climate Data Record: A Case Study in the Great Basin of the Western United States. *Remote Sens.* **2024**, *16*, 3029. [CrossRef]
26. Nester, T.; Kimbauer, R.; Parajka, J.; Blöschl, G. Evaluating the snow component of a flood forecasting model. *Hydrol. Res.* **2012**, *43*, 762–779. [CrossRef]

27. Pepin, N.; Bradley, R.S.; Diaz, H.F.; Baraer, M.; Caceres, E.B.; Forsythe, N.; Fowler, H.; Greenwood, G.; Hashmi, M.Z.; Liu, X.D.; et al. Elevation-dependent warming in mountain regions of the world. *Nat. Clim. Change* **2015**, *5*, 424–430.
28. Ollesch, G.; Sukhanovskii, Y.; Kistner, I.; Rode, M.; Meissner, R. Characterization and modelling of the spatial heterogeneity of snowmelt erosion. *Earth Surf. Process. Landf.* **2005**, *30*, 197–211. [CrossRef]
29. Rekolainen, S. Effect of snow and soil frost melting on the concentrations of suspended solids and phosphorus in two rural watersheds in Western Finland. *Aquat. Sci.* **1989**, *51*, 211–223. [CrossRef]
30. Henn, B.; Musselman, K.N.; Lestak, L.; Ralph, F.M.; Molotch, N.P. Extreme runoff generation from atmospheric river driven snowmelt during the 2017 Oroville Dam spillways incident. *Geophys. Res. Lett.* **2020**, *47*, e2020GL088189. [CrossRef]
31. Zhu, G.; Xiao, C.; Chen, B.; Zhao, Y. Spring snowmelt flood estimate in the upper Heihe River under climate change. *Clim. Change Res.* **2020**, *16*, 667–678.
32. Huang, D.; Su, L.; Zhou, L. Gully is the dominant sediment source of snowmelt erosion in the black soil region—A case study. *Soil Tillage Res.* **2022**, *215*, 105232. [CrossRef]
33. Presnijkakova, G. *Soil Erosion Caused by the Unregulated Runoff from Melting Snow and Its Control*; Symposium of Bari 1–8 October 1962—Commission of Land Erosion: Gentbrugge, Belgium, 1962; 450p, Publication no 59.
34. Zahradníček, P.; Brázdil, R.; Štěpánek, P.; Trnka, M. Reflection of global warming in trends of temperature characteristics in the Czech Republic, 1961–2019. *Int. J. Climatol.* **2020**, *41*, 1211–1229. [CrossRef]
35. Potopová, V.; Boroneat, C.; Možný, M.; Soukup, J. Driving role of snowcover on soil moisture and drought developing during the growing season in the Czech Republic. *Int. J. Climatol.* **2016**, *36*, 3741–3758. [CrossRef]
36. Ismail, M.F.; Bogacki, W.; Disse, M.; Schäfer, M.; Kirschbauer, L. Estimating degree-day factors of snow based on energy flux components. *Cryosphere* **2023**, *17*, 211–231. [CrossRef]
37. Hock, R. Temperature index melt modelling in mountain areas. *J. Hydrol.* **2003**, *282*, 104–115. [CrossRef]
38. Jeníček, M.; Beitlerová, H.; Hasa, M.; Kučerová, D.; Pevná, H.; Podzimek, S. Modelling Snow Accumulation and Snowmelt Runoff—Present Approaches and Results AUC. *Geographica* **2012**, *47*, 15–24.
39. Zhou, G.; Cui, M.; Wan, J.; Zhang, S. A review on snowmelt models: Progress and models prospect. *Sustainability* **2021**, *13*, 11485. [CrossRef]
40. Brychta, J. Calculation of average annual soil loss in nongrowing period for South-Moravian region using GIS. Mendel University in Brno. In *Mendelnet*. 2019, pp. 293–298, ISBN 978-80-7509-688-3. Available online: <https://1url.cz/M1g5l> (accessed on 10 October 2024).
41. Středová, H.; Středa, T.; Rožnovský, J. Snow as a Cause of Soil Erosion—Methodological Approach of Determination. In Proceedings of the Snow an Ecological Phenomenon, Smolenice, Slovakia, 19–21 September 2017; ISBN 978-80-89703-47-0.
42. Středová, H.; Toman, F. Erosion potential of snow cover in the Czech Republic. *Acta Univ. Agric. Silvic. Mendel. Brun.* **2012**, *60*, 117–124. [CrossRef]
43. Wischmeier, W.H.; Smith, D.D. Predicting the Rainfall Erosion Losses—A Guide to Conservation Planning. In *Agricultural Handbook No. 537*; US Department of Agriculture: Washington, DC, USA, 1978.
44. Janeček, M.; Dostál, T.; Kozlovský-Dufkova, J.; Dumbrovský, M.; Hůla, J.; Kadlec, V.; Konečná, J.; Kovář, P.; Krása, J.; Kubátová, E.; et al. *Ochrana Zemědělské Půdy Před Erozí, Metodika*; Česká Zemědělská Univerzita: Prague, Czech Republic, 2012; ISBN 978-80-87415-42-9. (In Czech)
45. Pokladníková, H.; Toman, F.; Středa, T. Negative impacts of snowmelting on the soil. *Acta Univ. Agric. Silvic. Mendel. Brun.* **2008**, *56*, 143–148. [CrossRef]
46. Podhrázská, J.; Kučera, J.; Karásek, P.; Křížek, P.; Sobotková, V.; Dumbrovský, M. *Postupy Hodnocení Intenzity Eroze v Mimovegetačním Období a Návrhy Opatření na Zemědělské Půdě*; Výzkumný Ústav Meliorací a Ochrany Půdy: Brno, Czech Republic, 2022; ISBN 978-80-88323-76-1. (In Czech)
47. Pradhan, P.; Seydewitz, T.; Zhou, B.; Lüdeke, M.K.B.; Kropp, K.P. Climate Extremes are Becoming More Frequent, Co-occurring, and Persistent in Europe. *Anthr. Sci.* **2022**, *1*, 264–277. [CrossRef]
48. Czech Hydrometeorological Institute. Update of the 2015 Comprehensive Study of Impacts, Vulnerability and Sources of Climate Change Risks in the Czech Republic. 2019 (In Czech). Available online: <https://1url.cz/juuDy> (accessed on 10 October 2024).
49. Svetlitchnyi, O.A. Long-term forecast of changes in soil erosion losses during springsnowmelt caused by climate within the plain part of Ukraine. *J. Geol. Geograph. Geoeol.* **2020**, *29*, 591–605. [CrossRef]
50. Starkloff, T.; Stolte, J.; Hessel, R.; Ritsema, C.; Jetten, V. Integrated, spatial distributed modelling of surface runoff and soil erosion during winter and spring. *Catena* **2018**, *166*, 147–157. [CrossRef]
51. Zhang, J.; Liu, S.; Yang, S. The classification and assessment of freeze-thaw erosion in Tibet. *J. Geogr. Sci.* **2007**, *17*, 165–174. [CrossRef]

52. Decree, No. 240/2021 Coll. Decree on the Protection of Agricultural Land Against Erosion (In Czech). Available online: <https://1url.cz/z1g5P> (accessed on 10 October 2024).
53. Maltsev, K.; Yermolaev, O. Assessment of soil loss by water erosion in small river basins in Russia. *Catena* **2020**, *195*, 04726. [CrossRef]

Disclaimer/Publisher's Note: The statements, opinions and data contained in all publications are solely those of the individual author(s) and contributor(s) and not of MDPI and/or the editor(s). MDPI and/or the editor(s) disclaim responsibility for any injury to people or property resulting from any ideas, methods, instructions or products referred to in the content.

Article

Land Cover Transformations in Mining-Influenced Areas Using PlanetScope Imagery, Spectral Indices, and Machine Learning: A Case Study in the Hinterlands de Pernambuco, Brazil

Admilson da Penha Pacheco ¹, João Alexandre Silva do Nascimento ¹, Antonio Miguel Ruiz-Armenteros ^{2,3,4,*}, Ubiratan Joaquim da Silva Junior ⁵, Juarez Antonio da Silva Junior ⁵, Leidjane Maria Maciel de Oliveira ⁵, Sylvana Melo dos Santos ⁵, Fernando Dacal Reis Filho ¹ and Carlos Alberto Pessoa Mello Galdino ¹

- ¹ Department of Cartographic and Surveying Engineering, Center for Technology and Geosciences, Federal University of Pernambuco, Av. Prof. Moraes Rego, 1235, Cidade Universitária, Recife 50670-901, Brazil; admilson.pacheco@ufpe.br (A.d.P.P.); joao.asnascimento@ufpe.br (J.A.S.d.N.); fernando.dacal@ufpe.br (F.D.R.F.); carlos.galdino@ufpe.br (C.A.P.M.G.)
 - ² Department of Cartographic, Geodetic and Photogrammetry Engineering, University of Jaén, Campus Las Lagunillas s/n, 23071 Jaén, Spain
 - ³ Microgeodesia Jaén Research Group (PAIDI RNM-282), University of Jaén, Campus Las Lagunillas s/n, 23071 Jaén, Spain
 - ⁴ Center for Advanced Studies on Earth Sciences, Energy and Environment (CEACTEMA), University of Jaén, Campus Las Lagunillas, s/n, 23071 Jaén, Spain
 - ⁵ PostGraduate Program in Civil Engineering (PPGEC), Department of Civil and Environmental Engineering, Federal University of Pernambuco, Recife 50050-000, Brazil; ubiratan.joaquim@ufpe.br (U.J.d.S.J.); juarez.silvajunior@ufpe.br (J.A.d.S.J.); leidjane.oliveira@ufpe.br (L.M.M.d.O.); sylvana.santos@ufpe.br (S.M.d.S.)
- * Correspondence: amruiz@ujaen.es

Academic Editors: Todd Robinson, Jianye Li, Xingyi Zhang, Weida Gao, Wei Hu and Qiang Chen

Received: 30 November 2024

Revised: 25 January 2025

Accepted: 3 February 2025

Published: 6 February 2025

Citation: Pacheco, A.d.P.; Nascimento, J.A.S.d.; Ruiz-Armenteros, A.M.; da Silva Junior, U.J.; Junior, J.A.d.S.; de Oliveira, L.M.M.; Melo dos Santos, S.; Filho, F.D.R.; Pessoa Mello Galdino, C.A. Land Cover Transformations in Mining-Influenced Areas Using PlanetScope Imagery, Spectral Indices, and Machine Learning: A Case Study in the Hinterlands de Pernambuco, Brazil. *Land* **2025**, *14*, 325.

<https://doi.org/10.3390/land14020325>

Copyright: © 2025 by the authors. Licensee MDPI, Basel, Switzerland. This article is an open access article distributed under the terms and conditions of the Creative Commons Attribution (CC BY) license (<https://creativecommons.org/licenses/by/4.0/>).

Abstract: The uncontrolled expansion of mining activities has caused severe environmental impacts in semi-arid regions, endangering fragile ecosystems and water resources. This study aimed to propose a decision-making model to identify land use and land cover changes in the semi-arid region of Pernambuco, Brazil, caused by mining through a spatiotemporal analysis using high-resolution images from the PlanetScope satellite constellation. The methodology consisted of monitoring and evaluating environmental impacts using the k-Nearest Neighbors (kNN) algorithm, spectral indices (Normalized Difference Vegetation Index (NDVI) and Normalized Difference Water Index (NDWI)), and hydrological data, covering the period from 2018 to 2023. As a result, a 3.28% reduction in vegetated areas and a 6.62% increase in urban areas were identified over five years, suggesting landscape transformation, possibly influenced by the expansion of mining and development activities. The application of kNN yielded an Overall Accuracy (OA) greater than 99% and a Kappa index of 0.98, demonstrating the effectiveness of the adopted methodology. However, challenges were encountered in distinguishing between constructions and bare soil, with the Jeffries–Matusita distance (JMD) analysis indicating a value below 0.34, while the similarity between water and vegetation highlights the need for more comprehensive training data. The results indicated that between 2018 and 2023, there was a marked degradation of vegetation and a significant increase in built-up areas, especially near water bodies. This trend reflects the intense human intervention in the region and reinforces the need for public policies aimed at mitigating these impacts, as well as promoting environmental recovery in the affected areas. This approach proves the potential of remote sensing and machine learning techniques to effectively monitor environmental changes, reinforcing strategies for sustainable management in mining areas.

Keywords: mining; land use and land cover; remote sensing; PlanetScope; spectral indices; kNN

1. Introduction

Land use has been one of the main drivers of landscape transformations over the years, with human activities such as agriculture, urbanization, and mining exerting significant pressure on natural ecosystems. In this context, remote sensing technologies have emerged as crucial tools for mapping and monitoring these changes, providing essential data for the sustainable management of natural resources.

Areas under the influence of mining are regions densely occupied by enterprises or exploited lands, often marked by intense conflicts between economic interests and environmental protection [1]. According to Buczyńska et al. [2], the impacts of mineral extraction from surface or underground mining methods include continuous deformations, large-scale land leveling, groundwater depletion, soil and groundwater contamination, and dust pollution. All these effects can negatively influence the preservation of vegetation within and around the mining area. In this context, robust analysis of social and environmental data at local and regional scales is essential for regulators and mining companies to identify, monitor, mitigate, and sustainably manage the environmental and socioeconomic impacts of mining [3].

Mining has been one of the main landscape transformation agents over the years. Estimates suggest that mining and quarrying activities have altered approximately 0.3 to 0.8 million square kilometers of land worldwide, and this trend continues to grow [4,5]. However, existing research highlights gaps related to understanding the specific impacts of mining in semi-arid areas, where the effects of soil degradation, water contamination, and deforestation are exacerbated by adverse climatic conditions [6,7]. In the case of gold mining near protected areas in South America, significant deforestation has occurred, driven by the rise in gold prices during the global economic crisis of 2008 [8–10].

In Northeastern Brazil, mining activities have been identified as a catalyst for environmental degradation, affecting soil quality, water resources, biodiversity, and human health [11,12]. Changes associated with Artisanal and Small-Scale Gold Mining in the landscape (roads and airstrips) typically include deforestation to access gold deposits and settlements [13]. Unregulated mineral processing also leads to soil and water body pollution by heavy metals, especially increased mercury levels [14–16].

The National Mining Agency (ANM) highlights the importance of the region for mineral production in Brazil, with Pernambuco being a small center for gold exploration [11]. Brazilian legislation, including the National Environmental Policy (Law No. 6.938/81), the Mining Code (Decree-Law No. 227/1967), and Federal Decree No. 97.632/1989, which regulates the Degraded Area Recovery Plan (PRAD), emphasizes the need for responsible mining practices to minimize negative impacts on the environment and local communities [17].

Mining activities impact land cover, vegetation, and soil properties, requiring effective monitoring approaches [18]. The growing interest in monitoring illegal mining activities through remote sensing (RS) is a response to the increasing environmental and socioeconomic impacts these activities pose globally [19]. Camalan et al. [20] presented a socio-environmental approach to unregulated mining in various ecosystems, emphasizing the importance of RS techniques in mitigating these environmental impacts.

The environmental impacts of gold mining, such as water pollution and land degradation, are well-detected using RS data and techniques. Therefore, their use provides

substantial benefits for detecting, mapping, and monitoring gold mining activities and their effects, especially those associated with local mining [21].

Images from different satellites with medium and high spatial resolutions have been used to identify various mining activities and their environmental impacts on the Earth's surface. According to Shikhov et al. [7], optical images are analyzed using multiple approaches such as supervised and unsupervised classification, spectral indices, time-series analysis, and several machine learning algorithms, including k-Nearest Neighbors (kNN), artificial neural networks (ANNs), decision trees (DTs), support vector machines (SVMs), random forests (RFs), and classification and regression trees. According to Lua and Weng (2007), the results of soil surface mapping are influenced not only by the adequacy of the images but also by the correct choice of processing and classification methods.

Based on the results of an extensive literature review, Song et al. [22] presented progress in RS monitoring research regarding land use and land cover changes in mining areas. The authors focused on the application and perspectives of RS techniques in the context of biodiversity ecological environment monitoring, highlighting aspects related to landscape structure, vegetation changes, soil environment, surface conditions, and atmospheric environment in mining areas.

RS technologies are widely used to identify natural features or physical objects on the Earth's surface, utilizing various spatial, temporal, spectral, and resolution datasets [23–26], serving as effective sources for identifying the environmental impacts of gold mining, such as water contamination and soil degradation [21]. These technologies offer significant advantages for detecting, mapping, and monitoring gold mining activities and their effects [27–29].

To overcome the limitations of spatiotemporal frequency in land use and land cover surveys, the availability of optical images from PlanetScope Planet Labs' constellation of nanosatellites emerged in 2016. The PlanetScope constellation, consisting of more than 180 CubeSats in sun-synchronized orbits, capable of capturing multispectral images with a resolution ranging from 3.7 to 4.1 m depending on altitude [30], has a daily revisit, making it essential for the immediate detection of land changes as well as monitoring the expansion or maintenance of existing activities. This network has the unique capability of daily capturing free images of the entire planet, achieving an impressive coverage of up to 200,000,000 km² [30].

The Normalized Difference Vegetation Index (NDVI) [31] and the Normalized Difference Water Index (NDWI) [32] can, respectively, provide information on vegetation and water presence in mining areas. Several studies over the past five years have demonstrated the potential of the NDVI and NDWI spectral indices for mapping and monitoring land use and land cover in mining areas. Padró et al. [33] used high-resolution multispectral images acquired with an Unmanned Aerial System (UAV) and Soil Adjusted Vegetation Index (SAVI), Modified Soil Adjusted Vegetation Index (MSAVI), NDVI, and NDWI indices to evaluate vegetation development in a restored limestone quarry. Nascimento et al. [34] developed a systematic image analysis approach based on geographic objects (GEOBIA) to map revegetated areas and quantify land use and land cover changes in open-pit mines in the Carajás/Amazon region/Brazil from high spatial resolution satellite images (GeoEye, WorldView-3, and IKONOS) from 2011 to 2015 and the NDVI and NDWI spectral indices. Stančič et al. [35] used Landsat 8 and Sentinel-2 data to monitor the Soča River area in Slovenia using SAM (Spectral Angle Mapper) and fuzzy SSMA (Spectral Signal Mixture Analysis) classification methods, additionally introducing NDVI, NDWI, and other complementary indices into the classification algorithm. McKenna et al. [36] presented an extensive RS literature review, focusing on the ecological rehabilitation of mining sites.

RS data are used to observe three main aspects related to gold mining: deforestation or changes in land cover, water pollution from mining near rivers, detection of turbidity levels in river channels, and estimating the presence of mercury [37–39]. Fonseca et al. [10] analyzed land use and cover changes in gold ore areas in the Brazilian Amazon rainforest using Landsat images and the RF classifier. Shikhov et al. [7] evaluated the extent of soil degradation caused by gold mining in the Magadan region of China and its changes in the 21st century, based on Landsat/Sentinel-2 satellite data. Zaki et al. [40] used the kNN machine learning algorithm to estimate mineral resources (predicting the gold grade in the Quartz Ridge area) and analyze the impact of its unregulated extraction on land use and land cover.

The integration of RS techniques and machine learning algorithms, such as kNN, combined with spectral sensitivity studies of targets using indices, emerge as essential tools in monitoring land cover in mining areas, enabling spatiotemporal analysis with precision and effectiveness [41,42]. This methodological approach allows for identifying and quantifying changes in vegetation and soil moisture, providing crucial data to assess the environmental impacts resulting from mining activities. Pacheco et al. [43] demonstrated the applicability of this technique in mapping areas affected by forest fires in Portugal, efficiently using kNN to classify Landsat-8, Sentinel-2, and Terra satellite images. Noi and Kappas [44] highlight that, although kNN may be slightly more sensitive to training sample size compared to other algorithms like SVM, it still presents high Overall Accuracy, especially when the sample size is sufficient.

In this context, this study proposes a decision support model for sustainable monitoring of mining activities in semi-arid regions of Brazil, offering an innovative integrated analysis of sensing and machine learning using high-resolution orbital images to spatially analyze environmental variability within and around areas impacted by mining. The approach combines the kNN classifier with spectral indices such as NDVI and NDWI, derived from PlanetScope satellite images, covering the period from 2018 to 2023. This model aims to address existing gaps in the literature by offering an integrated analysis that tackles both the socio-environmental impacts and the efficiency in monitoring landscape transformations in semi-arid scenarios, with an emphasis on the Serita-Cedro region. However, it is noteworthy that the methodology proposed in this study can be implemented to evaluate the spatiotemporal behavior of land cover in other mining regions with arid and/or semi-arid climatic characteristics.

2. Materials and Methods

The methodology adopted to identify changes in the landscape of the semi-arid region of Pernambuco, caused by the presence of mining areas, consisted of the following steps: data acquisition, processing, and results generation (Figure 1).

In the first step, data acquisition was carried out with the selection of scenes, considering factors such as broad coverage, absence of clouds, periods of low rainfall incidence, and availability of data sharing via cloud platforms. Additionally, as the vegetation of the Caatinga biome, present in the study area, is sensitive to rainfall [45], it is necessary to analyze the response of spectral indices concerning vegetation, considering the effects of precipitation. In this regard, precipitation data for the study region during the image acquisition period was obtained from the Pernambuco Water and Climate Agency (APAC).

Next, land use and land cover mapping were developed. Initially, the spectral indices were calculated, followed by class training. At this stage, due to factors such as the sensor's spatial resolution and the diversity of land uses in the area, four classes were chosen: water, vegetation, bare soil, and urban patches (built-up areas). The vegetation class was grouped

into herbaceous and shrub vegetation, while the water class included both watercourses and water bodies.

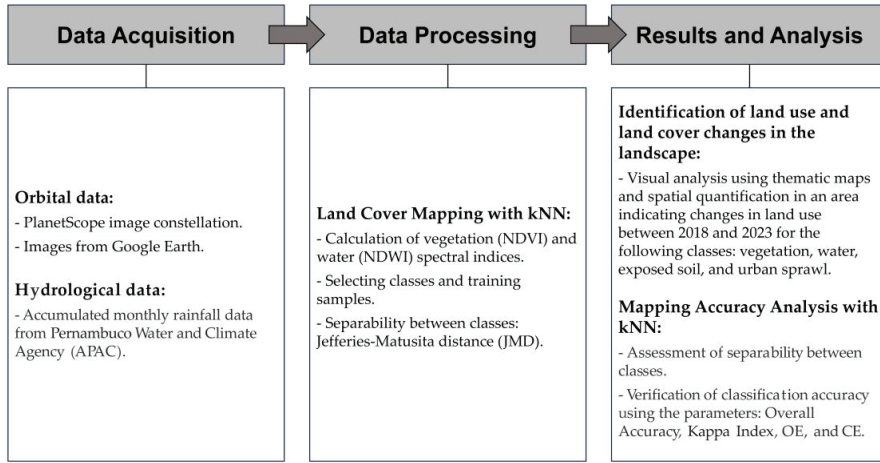


Figure 1. Workflow of the methodology employed in this study. The diagram illustrates the sequential steps, including data acquisition, data processing, and results and analysis, leading to the final results. Key processes such as “Satellite and hydrological data”, “Land cover mapping with kNN”, “Identification of land use and land cover changes”, and “Mapping accuracy analysis with kNN” are highlighted to emphasize the core components of the approach.

As a result, the landscape changes caused by mining infrastructure were identified through thematic maps and quantified using class extraction and separability. The classification accuracy relative to the image was established through evaluation parameters: Overall Accuracy (OA), Kappa index, Omission Errors (OEs), and Commission Errors (CEs).

2.1. Study Area

The investigated region (Figure 2) is a polygon designated for gold mining activities, covering an area of 459.33 km², with a 6 km buffer zone from the Serrita-Cedro Project, which is part of the National Program for the Study of Mining Districts, conducted by the National Department of Mineral Production (DNPM), in the semi-arid region of the Brazilian state of Pernambuco.

This area, in its first phase (1994–1995), focused on the investigation of gold mineralization, encompassing an area of 580 km² [46]. Over the years, the area has been subject to exploration, with increased investment since 2020 by the mining company Trilha Gold Capital (TGC). According to the Brazilian Mining Institute (IBRAM), all studies conducted in the Serrita Project follow the standards of the Australian Joint Ore Reserves Committee (JORC) code, along with environmental regulations and laws from the relevant authorities, ensuring maximum credibility and accuracy in the research activities in the area [47].

However, gold mining is often accompanied by soil and vegetation destruction, landscape fragmentation, and biodiversity loss, as well as the disruption of ecosystem services flows [48]. Additionally, it stands as a significant driver of deforestation, unique in the severity of its impacts, leaving behind a highly altered landscape [36].

The climate of the region is semi-arid and hot, classified as Bshw according to Köppen (<https://www.gloh2o.org/koppen/>, accessed on 1 April 2024), with a distinct rainy season (from February to May) and dry periods (from June to January). The vegetation cover consists of xerophytic Caatinga, characterized by heterogeneous vegetation, whose vegetative

vigor is sensitive to precipitation [45]. The terrain is hilly, with elevations averaging around 480 m above sea level.

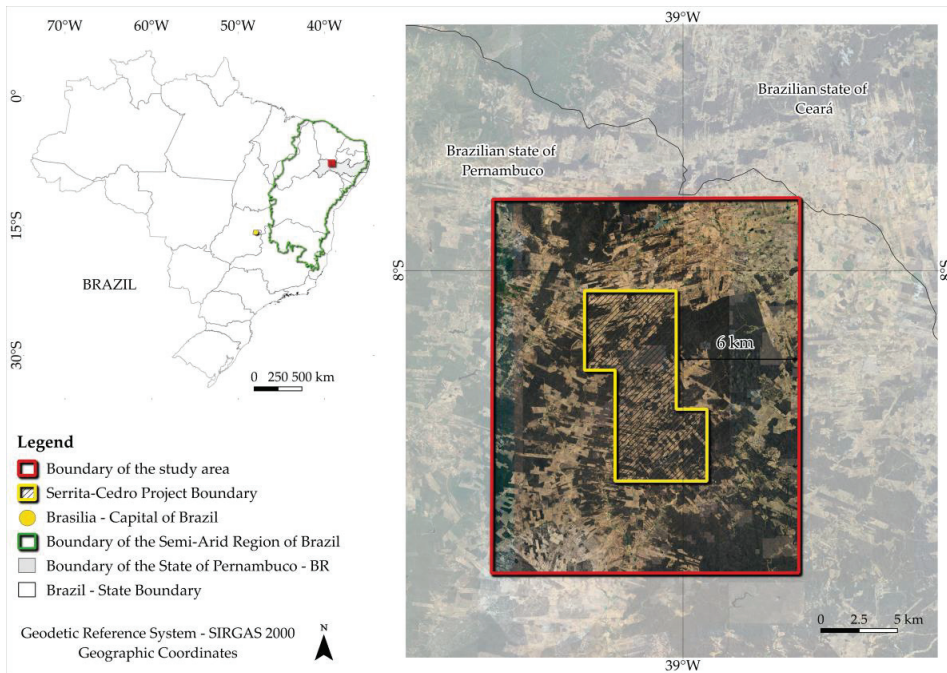


Figure 2. Map of the study area. The investigated region, designated for gold mining activities, is outlined by a red rectangle, and encompasses 459.33 km², including a 6 km buffer zone around the Serrita-Cedro Project. The boundary of the Serrita-Cedro Project, part of the National Program for the Study of Mining Districts conducted by the National Department of Mineral Production (DNPM), is indicated by a yellow line. The area is located in the semi-arid region of Pernambuco, Brazil.

Gold mining in the semi-arid region of Pernambuco, Brazil, is predominantly conducted by corporate companies, such as the Serrita-Cedro Project, managed by Trilha Gold Capital. Despite these regulations, mining activities continue to be associated with environmental degradation, such as deforestation and significant land use changes. The mining sector faces the challenge of aligning its production processes with environmental and social sustainability requirements. As noted by IBRAM [47], incorporating responsible practices is increasingly essential for maintaining competitiveness in the market, given the growing environmental and social demands from investors and consumers.

In this context, the use of satellite images combined with machine learning models presents a valuable tool for better understanding landscape changes in areas associated with gold mining practices [13].

2.2. Materials

2.2.1. Satellite Data

Two scenes of orbital images from the PlanetScope Instruments mission, from 2018 and 2023, were used, both acquired in October, a period of low rainfall in the region [49]. The analysis of the Caatinga's vegetation cover is more effective during the dry season, as the vegetation is sensitive to minimal moisture, which can cause false positives during rainy periods [45,50]. The PlanetScope constellation, managed by Planet Labs, consists of over 130 satellites that offer daily global coverage [51]. The images provided by PlanetScope

(PS) include four spectral bands: blue, green, red, and near-infrared (NIR), with a spatial resolution of 3 m and a radiometric resolution of 16 bits [52]. The images from PSB.SD and PS2 sensors used in this study, along with their characteristics and acquisition dates (<https://www.planet.com/>, accessed on 4 March 2024), are presented in Table 1.

Table 1. Technical specifications of PlanetScope images.

Image ID	Acquisition Date	Sensor	Spectral Range
120231031_120836_24_24a1	31 October 2023	PSB.SD	Blue: 465–515 nm Green: 547–585 nm Red: 650–680 nm NIR: 845–885 nm
220181020_122327_0e0e	20 October 2018	PS2	Blue: 455–515 nm Green: 500–590 nm Red: 590–670 nm NIR: 780–860 nm

Iqbal et al. [53], using the kNN model with PlanetScope images to map native and invasive species distributions in two forest reserves in Pakistan, highlighted the images' good performance in identifying targets compared to the Sentinel-2 MSI sensor.

2.2.2. Hydrological Data

The Caatinga vegetation has shown sensitivity to available rainfall [45,50,54]. In this context, analyzing the relationship between the Caatinga vegetation cover and precipitation becomes a key element for the accuracy of the results obtained when mapping land use and occupation in the study region. During October 2018, two rainy days were recorded (17 October 2018 and 18 October 2018), totaling 69.9 mm for the month and 818.9 mm for the year. In 2023, there were no rainy days, with monthly rainfall of 0 mm and 733 mm annually [55].

2.3. Methods

2.3.1. Spectral Indices

After pre-processing the PlanetScope satellite images, the NDVI and NDWI spectral indices were calculated based on their respective operations, and the results were analyzed using the Jeffries–Matusita distance (JMD) [56].

NDVI serves as an effective indicator of active plant biomass or, otherwise, vegetation vitality. Developed by Rouse et al. [31], the NDVI ranges from -1 to 1 , obtained using Equation (1):

$$\text{NDVI} = \frac{(\text{NIR} - \text{RED})}{(\text{NIR} + \text{RED})} \quad (1)$$

where NIR is the reflectance in the near-infrared band, and RED is the reflectance in the visible red band.

This index helps differentiate vegetated areas from other land covers, such as artificial ones, and allows for the assessment of the overall vegetation condition [57]. Additionally, NDVI enables the demarcation and monitoring of vegetation zones, as well as the recognition of any anomalies or changes in the observed area. This indicator is useful for monitoring seasonal variations in vegetation, though its effectiveness depends on surface reflection characteristics [58].

NDWI, using the green and near-infrared bands, is an efficient indicator for monitoring the presence and distribution of water in terrestrial and aquatic surfaces. This index is particularly effective in identifying water bodies and assessing moisture in vegetation,

contributing to irrigation and water resource management studies [59]. NDWI is also helpful in detecting flooded areas and analyzing soil water saturation, making it a valuable tool for environmental and agricultural planning [32]. The NDWI ranges from -1 to 1 and is calculated using Equation (2):

$$\text{NDWI} = \frac{(\text{Green} - \text{NIR})}{(\text{Green} + \text{NIR})} \quad (2)$$

where NIR is the reflectance in the near-infrared band, and Green is the reflectance in the visible green band.

2.3.2. Jeffries–Matusita Distance

JMD is a statistical metric used to evaluate the separability between classes in RS data. JMD is particularly useful for quantifying the distinction between probability distributions of classes, which is critical in multispectral image classification [60]. JMD is based on Bhattacharyya distance, which measures the overlap between two statistical distributions, and is transformed to the range $[0, 2]$ [56]. The formula for calculating JMD between two classes is given by Equation (3):

$$\text{JMD} = 2\sqrt{1 - e^{-B}} \quad (3)$$

where B is the Bhattacharyya index (measure) that quantifies the overlap between two probability distributions. This measure is based on the means and variances of the characteristics of each class given by Equation (4).

$$B = \frac{1}{8}(\mu_1 - \mu_2)^T \Sigma^{-1}(\mu_1 - \mu_2) + \frac{1}{2} \ln \left(\frac{|\Sigma|}{\sqrt{|\Sigma_1||\Sigma_2|}} \right) \quad (4)$$

where μ represents the mean, Σ the average covariance matrix, and $|\Sigma|$ the determinant of the covariance matrix for each class. High JMD values indicate greater separability between classes, while lower values suggest significant overlap, making it difficult to distinguish between them [60].

2.3.3. k-Nearest Neighbors (kNN) Classification

The kNN classification algorithm is a simple yet powerful method used for classification and regression. Introduced by Cover and Hart [61], kNN operates on the principle that similar samples tend to be close to each other in feature space, as highlighted by James et al. [62]. This algorithm identifies the k nearest neighbors of an unknown sample within the training set, assigning the sample to the most common class (or the average of the responses) among these neighbors.

The distance between samples, fundamental to the operation of kNN, can be calculated in several ways. The most common is the Euclidean distance, given by Equation (5):

$$d(p, q) = \sqrt{\sum_{i=1}^m (p_i - q_i)^2} \quad (5)$$

Equation (5) calculates the distance between two samples, p and q , each with m features, illustrating how the algorithm navigates the multidimensional space. The choice of k is a critical aspect that directly influences the algorithm's performance. A very small k may make the model overly sensitive to data noise, while a very large k may cause it to overlook class distribution nuances. It is recommended to experiment with various k

values and potentially use validation methods, such as cross-validation, to determine the optimal k .

Cross-validation, as described by Kohavi [63], is a technique used to assess a statistical model's generalization ability and to tune hyperparameters, such as k in kNN. The most common cross-validation method is k -fold, which divides the dataset into k subsets. The model is trained k times, each time using $k-1$ subsets for training and the remaining subset for testing. The model's performance is then evaluated by averaging the results obtained in each of the k iterations.

kNN, along with cross-validation, offers a robust approach to data classification, leveraging the algorithm's simplicity and the efficacy of cross-validation to adjust hyperparameters and assessing the model's generalization ability for new data.

The choice of the kNN algorithm over the previously mentioned models (ANN, DT, RF, and SVM) was based on its simplicity of implementation, high accuracy in scenarios with balanced data, and results previously reported in the literature [61–63]. Recent studies [40,64–66] have demonstrated that in land use and land cover analyses in mining regions, kNN achieves comparable or superior performance in Overall Accuracy and Kappa when compared to more complex methods, particularly when applied to datasets with a limited number of training samples, as in this study. Furthermore, the interpretative nature of kNN enables a more direct analysis of the impact of spectral distance on results, facilitating the identification of specific challenges, such as separability between classes with similar spectral characteristics, for example, vegetation and urban area.

2.3.4. Samples and Training

The training samples were extracted from both 2018 and 2023 images, generating two training sets, each representing four classes of interest: water, urban area, vegetation, and bare soil. For this initial process, the open-source software QGIS, version 3.34.2-Prizren [67], was used, where the training preparation involved collecting several sample polygons for each class. The selection was made through the manual analysis of composite images (RGBs). After visual interpretation, the masks were saved in shapefile format, allowing them to be accessed and processed in the subsequent stage.

The definition of land use and land cover classes (water, urban area, vegetation, and bare soil) was based on the main features observed in the study area, which is characterized by mining activities in semi-arid regions [47]. Although other categories, such as croplands, may be common in some semi-arid regions, they did not stand out significantly in the investigated area, as they were often confused with native vegetation or bare soil due to spectral similarity. Moreover, the spatial resolution of the images used (3 m) limited the ability to identify subtle differences between small-scale croplands and the herbaceous or shrub vegetation of the Caatinga.

In this study, the data were partitioned for training and testing the kNN model, with 80% of the data used for training and 20% for testing. This partitioning ratio was selected considering the moderate size of the dataset, enabling the model to effectively learn the class characteristics while ensuring a robust evaluation of its performance. The achieved accuracy of 0.99 was based on this partition, which may be influenced by the size and quality of the data. However, this division is considered appropriate for the context of the study.

Training was conducted using the R programming 4.4.2 language through the RStudio software 2024.04.7 [68]. The two sets of samples for the four classes were used with cross-validation, where the dataset was randomly divided into 10 subsets (or "folds"), and the model was trained 10 times, each time using 9 of the subsets for training and the remaining subset for testing, for each sample set.

2.3.5. Accuracy Analysis of the Classification

The use of CE and OE metrics is essential for evaluating model errors in RS systems, allowing for a more detailed and precise analysis of the model's ability to correctly identify positive cases and avoid incorrectly classifying positives. The CE metric is calculated by the proportion of false positives relative to the total number of events classified as positive, while the OE metric is calculated by the proportion of false negatives relative to the total number of actual positive events. OE can be calculated by Equation (6):

$$OE = \frac{\text{False Negatives(FN)}}{\text{True Positives(TP)} + \text{False Negatives(FN)}} \quad (6)$$

Subsequently, CE can be calculated by Equation (7):

$$CE = \frac{\text{False Positives(FP)}}{\text{True Positives(TP)} + \text{False Positives(FP)}} \quad (7)$$

These parameters allow monitoring of prediction accuracy and are widely used in RS literature, as highlighted by Sano et al. [69] and Tejado-Ramos et al. [70].

The Overall Accuracy (OA) and the Kappa Index were also used as parameters for analyzing the thematic accuracy of the mapping.

OA is used to measure the model's prediction accuracy and is the ratio of correctly classified samples to the total number of samples [71]. The OA can be calculated using Equation (8):

$$OA = \frac{\sum_{i=1}^n x_{ii}}{N} \quad (8)$$

where x_{ii} represents the number of correctly classified samples along the diagonal, and N is the total number of samples. The higher the OA value, the better the overall prediction accuracy of the model.

The Kappa Coefficient is used to measure classification accuracy and is calculated according to Equation (9).

$$\text{Kappa} = \frac{P_0 - P_C}{P_p - P_C} \quad (9)$$

where P_0 is the proportion of correctly simulated pixels, P_p is the proportion of correctly predicted pixels in an ideal situation, and P_C is the proportion of correctly predicted pixels in a random situation. The closer the kappa coefficient is to 1, the better the classification result matches the actual situation [71].

2.3.6. Quantitative Analysis of Classified Areas

After the image classification process, each pixel was assigned a value to one of the four predefined classes, where the value 1 corresponds to water, 2 to urban area, 3 to bare soil, and 4 to vegetation. The quantitative analysis was conducted by summing the pixels of each class for the analyzed years. The PlanetScope satellite images have a spatial resolution of 3×3 m, which implies an area of 9 m^2 per pixel. To facilitate quantitative analysis, the total area of each class was converted from m^2 to km^2 , allowing for a more accessible comparison of classified areas between the years 2018 and 2023.

3. Results

3.1. Monitoring of Land Use and Occupation

Thematic land use and occupation maps (Figure 3) were generated through classification using the kNN algorithm. The classes analyzed were water, urban area, bare soil, and vegetation, allowing the identification of landscape changes between 2018 and 2023.

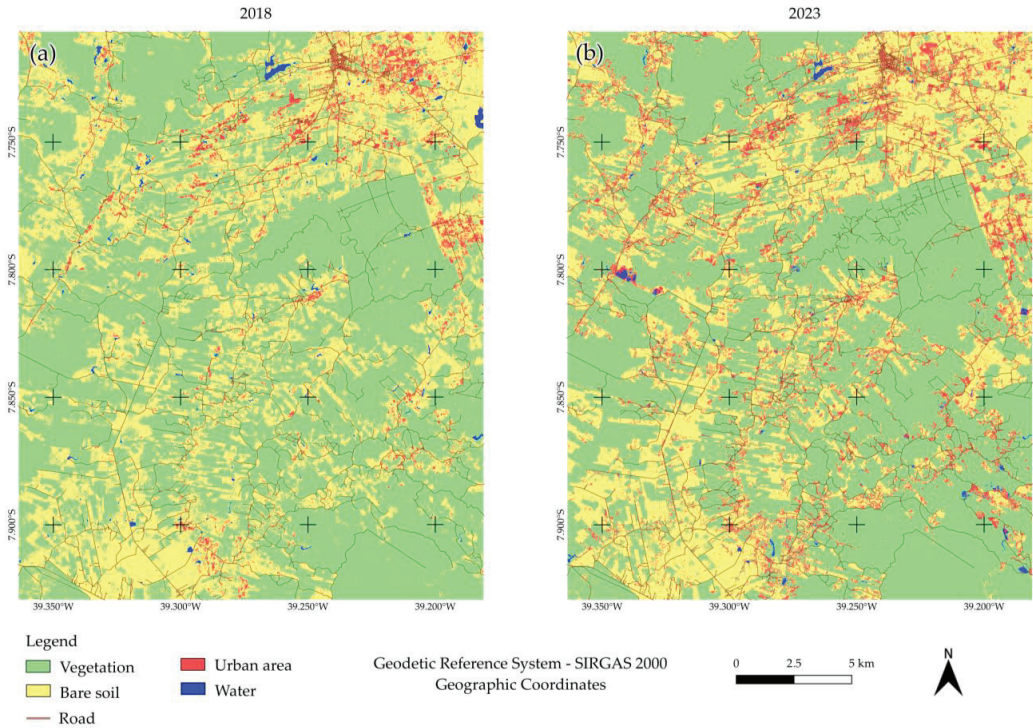


Figure 3. Thematic land use and occupation maps for 2018 and 2023: (a) classified image for 2018 and (b) classified image for 2023, generated using the kNN algorithm. The maps highlight four classes: water, urban area, bare soil, and vegetation. The comparison reveals a noticeable increase in built-up areas and a proportional reduction in vegetated areas, particularly near natural water resources, indicating accelerated loss of riparian forests. Bare soil areas remained largely unchanged over the five-year period.

In Figure 3, there is a noticeable increase in built-up areas proportional to a reduction in vegetated areas, especially in regions near natural water resources, indicating accelerated loss of riparian forests. On the other hand, bare soil areas did not show significant visible changes. The “urban area” class includes roofs of structures such as houses, warehouses, sports courts (with ceramic or metallic coverings), and paved roads like asphalt or cobblestone streets. The cartographic conventions for linear features such as roads were incorporated into the maps using the photointerpretation method on PlanetScope images, complemented by data from the Brazilian National Department of Transport Infrastructure (DNIT) (<https://servicos.dnit.gov.br/vgeo/>, accessed on 4 April 2024). This approach allowed for the identification of roads in the study area with high precision, considering the 3 m spatial resolution of the analyzed images. The analysis revealed that several roads are closely related to mining areas, indicating a possible correlation between the expansion of road infrastructure and increased productive activities. This methodology revealed a significant expansion of the road network during the analyzed period, contributing directly to the growth of the built-up area identified in the maps. The inclusion of these features highlights the essential role of roads and other constructions in shaping the landscape, thereby explaining the changes observed in the urban class from 2018 to 2023.

By comparing the classifications from 2018 and 2023, a reduction of approximately 2.10% in vegetation over the five years was identified, as shown in Figure 4.

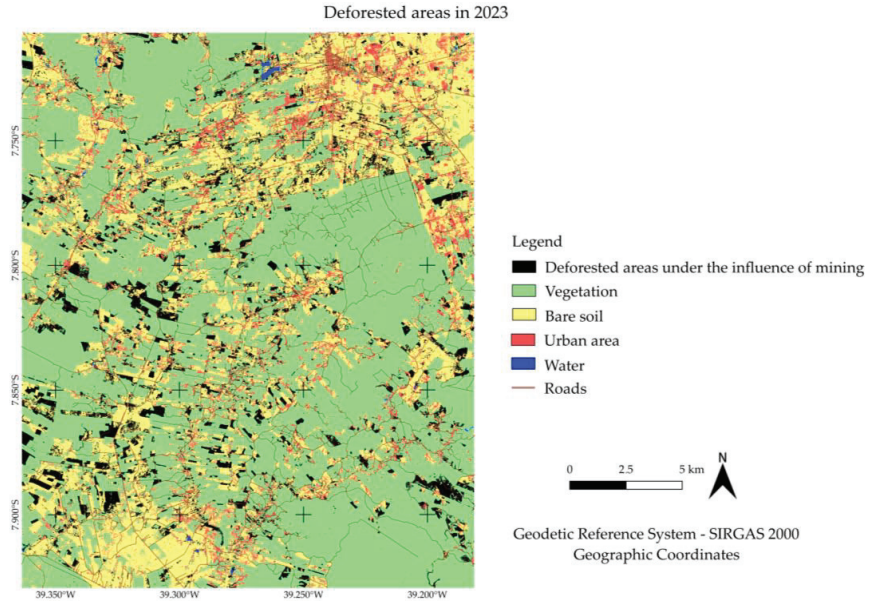


Figure 4. Thematic land use map highlighting deforested areas between 2018 and 2023. This map emphasizes the reduction of approximately 2.10% in vegetation during the five-year period, particularly in regions adjacent to water resources, reflecting the extent of deforestation.

Data extraction enabled the quantification of land use and occupation classes, as shown in Figure 5.

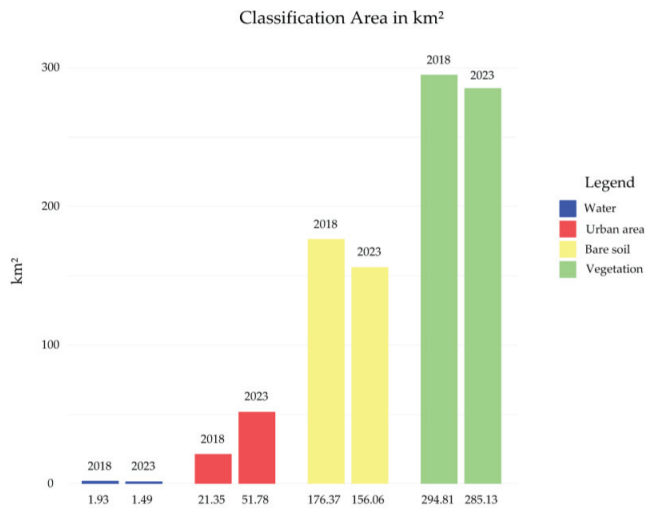


Figure 5. Quantification of land use and occupation classes (in km²) for 2018 and 2023. The graph highlights significant changes in land use over the five-year period, including a 9.68 km² (3.28%) decrease in vegetation cover, a 0.44 km² (22.80%) reduction in water areas, and a 20.31 km² (11.52%) decrease in bare soil. Conversely, built-up areas increased by 30.43 km² (142.53%), reflecting urban expansion. The percentages are relative to the total study area of 459.33 km².

In 2023, vegetation cover decreased by 9.68 km², which is equivalent to 3.28% compared to the vegetation area in 2018 and 2.11% of the total area of 459.33 km². Rainfall over

the period studied fell considerably, which may have influenced changes in the Caatinga vegetation. This decrease was particularly noticeable in October 2023, when there was no precipitation. The lower availability of water may have reduced the natural regeneration capacity of vegetation, contributing to the decrease in vegetation cover, between 2018 and 2023. If the downward trend in precipitation continues, it is possible that the impact on vegetation will intensify, exacerbating the effects of anthropogenic activities, such as mining, and affecting the long-term health of vegetation.

Water areas also decreased by 0.44 km², representing a 22.80% reduction compared to the area in 2018 and 0.09% of the total area. Bare soil areas showed a decrease of 20.31 km², which corresponds to an 11.52% reduction compared to 2018 and 4.42% of the total area. Conversely, built-up areas increased by 30.43 km², representing a 142.53% increase compared to 2018 and 6.62% of the total area.

Some areas classified as deforested under the influence of mining were identified as artisanal gold mining activities through Google Earth validation, supporting the accuracy of the classification results. In these regions, it was observed that farmers converted areas originally designated for agriculture and grazed into clear-cut zones with extensive excavations in search of gold. These actions are directly linked to the presence of the Serrita-Cedro Project in the region, which has drawn significant attention from informal gold miners. The conversion of agricultural and pastureland into mining sites has caused significant impacts on land use and land cover, along with environmental and social consequences, highlighting the need for continuous monitoring and proper regulation.

3.2. Separability Analysis

The separability between the land use and cover classes mapped by kNN was evaluated using the JMD. Tables 2 and 3 show the JMD values for the years 2018 and 2023.

Table 2. JMD for the year 2018.

Class 1	Class 2	Blue	Green	Red	NIR	NDVI	NDWI
Water	Urban area	0.819	0.719	1.187	1.993	1.144	1.435
Water	Bare soil	0.983	0.819	1.022	1.992	1.452	1.770
Urban area	Bare soil	0.165	0.108	0.116	0.024	0.273	0.330
Water	Vegetation	0.408	0.570	0.528	1.980	1.827	1.953
Urban area	Vegetation	1.317	1.410	1.690	1.628	1.710	0.904
Bare soil	Vegetation	1.521	1.612	1.649	1.551	1.529	1.398

Table 3. JMD for the year 2023.

Class 1	Class 2	Blue	Green	Red	NIR	NDVI	NDWI
Water	Urban area	1.478	1.545	1.987	2.000	1.276	1.909
Water	Bare soil	1.911	1.880	1.991	1.999	1.591	1.957
Urban area	Bare soil	0.154	0.129	0.053	0.262	0.213	0.245
Water	Vegetation	0.644	0.060	1.408	1.980	1.948	1.996
Urban area	Vegetation	1.324	1.622	1.900	1.815	1.816	1.178
Bare soil	Vegetation	1.824	1.910	1.936	1.839	1.867	1.840

In 2018, the separability between water and vegetation, with NDVI (1.827), NDWI (1.953), and the NIR band (1.980), was high, indicating a good distinction between these classes. However, the separability between urban area and vegetation showed values below 1 for NDWI, suggesting less consistency in distinguishing these classes. Following the same evaluation pattern used for 2018, the separability between the classes for 2023 was assessed (Table 3).

In 2023, the JMD values also indicated good separability for the water vs. vegetation classes, with an emphasis on NDWI (1.996). For urban area vs. vegetation, the separability was effective, with high values in the red band (1.900), NIR (1.815), NDVI (1.816), and NDWI (1.178). The separability between bare soil and vegetation remained high for all variables, with values above 1.823.

3.3. Accuracy of kNN Classification

The classification was evaluated using the accuracy parameters OA, Kappa index, OE, CE, and cross-validation, as shown in Figure 6.

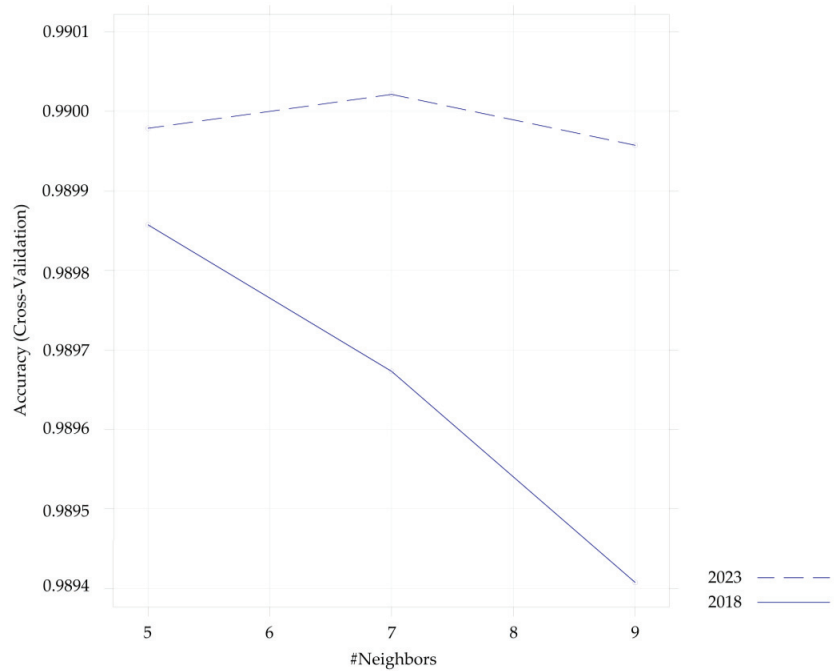


Figure 6. Comparison between accuracy (cross-validation) and the number of the training neighbors (k) for the years 2018 and 2023.

In 2018, the accuracy decreases continuously as k increases, going from approximately 0.9889 with k = 5 to 0.9894 with k = 9. This indicates that in 2018, the increase in the number of neighbors had a negative impact on the model's performance, with k = 5 being the best performer. In 2023, there is a different trend, the accuracy peaks at k = 7, reaching approximately 0.9900, and then starts to decrease for higher values of k. This indicates that the choice of k = 7 was optimal in the 2023 scenario. Based on the classification defined by Landis and Koch [72], these results suggest that the classification was not only accurate, but also consistent and reliable.

These results indicate good precision and agreement between the classification and the actual landscape. In this context, it is demonstrated that the model has precise classification potential, producing results that are very close to the actual or expected values. The narrow confidence interval suggests a high probability that the model's actual accuracy is within this range, which is indicative of consistent results [73]. Figure 7 presents a comparison between the classification using the kNN algorithm and an RGB composite, with the PlanetScope bands.

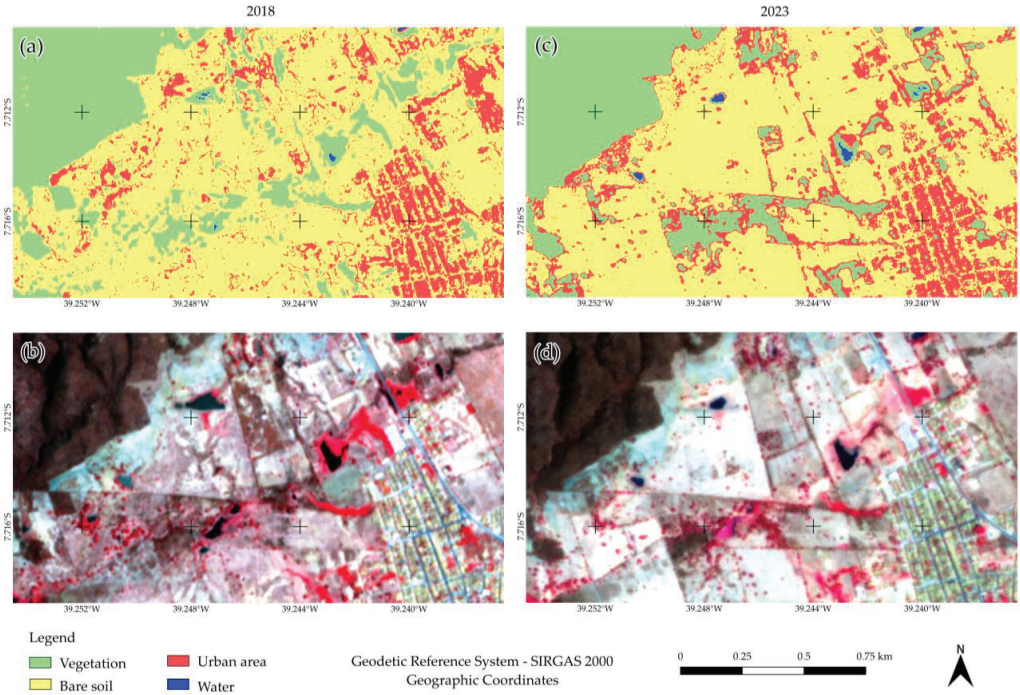


Figure 7. Comparison between the classification using the kNN algorithm and an RGB composite, with the PlanetScope bands for the years 2018 and 2023: (a) sample area of the classified image for 2018; (b) sample area of the PlanetScope image (RGB) for the classified area in 2018; (c) sample area of the classified image for 2023; (d) sample area of the PlanetScope image (RGB) for the classified area in 2023.

Through Figure 7, it is possible to spatially identify the results obtained with the OA and Kappa index parameters; however, an analysis of OE and CE is necessary, as conducted in this study, to identify the presence of false positives and false negatives. Table 4 presents the verification results of these parameters.

Table 4. Omission Errors (OEs) and Commission Errors (CEs) for the years 2018 and 2023.

Classes	2018		2023	
	OE	CE	OE	CE
Water	0	0	0	0
Urban area	22.10%	6.18%	24.67%	2.57%
Bare soil	0.6%	2.53%	0.37%	2.02%
Vegetation	0.01%	0	0.29%	0.19%

It can be observed in Table 4 that, in the “Vegetation” class, there was a slight improvement over time, with low commission and omission errors reflecting a high accuracy in detecting this class. In contrast, the omission and commission errors for “Bare soil” increased from 2018 to 2023, indicating a slight decline in detection accuracy and a moderate tendency toward overclassification. However, as with “Vegetation”, the errors remained low. These results are consistent with previous studies [33], which suggest that soil and vegetation classes in the Caatinga tend to vary little compared to reference products. This behavior is associated with the consolidated use of these areas and the low anthropogenic interference in the Caatinga biome landscape [11].

The “Urban area” class showed the highest error values, though with an improvement in omission error, suggesting greater effectiveness in detecting urban area over time (Table 4). On the other hand, the commission error increased considerably, indicating a greater tendency to misclassify other classes as urban area in 2023. The spectral similarity between urban soil and bare soil classes, which share spectral characteristics, may have contributed to the significant omission and commission errors in this category, as illustrated in Table 4 and discussed by [10].

For the “Water” class, the omission error remained at 0% from 2018 to 2023, indicating high accuracy in identifying this class in both years. However, the commission error increased slightly from 0% to 0.07%, suggesting a slight tendency to overestimate the area of water bodies in 2023. These results also corroborate previous studies [22], which highlight the high detection quality of water bodies, attributed to their high spectral absorption characteristics compared to general soil and vegetation classes.

The water bodies identified in the study area, primarily small lakes and intermittent ponds, reflect the typical seasonal dynamics of the semi-arid region of Pernambuco, influenced by variations in precipitation and evapotranspiration patterns. This characteristic directly impacts local gold mining practices, which are not exclusively reliant on perennial water bodies such as streams. Instead, mining operations frequently occur in dry areas or near intermittent water bodies, often utilizing artificial systems for ore washing. This reality was incorporated into the revised maps, which now more accurately highlight the spatial distribution of these water resources in the context of mining activities, providing a more robust foundation for environmental impact analysis.

The high OE in the Constructions class reveals that the model failed to correctly identify many true positive cases, while the high CE indicates that the model mistakenly classified some cases as belonging to the class when they did not. These results highlight the need for improvements or adjustments in the model to increase both sensitivity and specificity, reducing the rates of false negatives and false positives (Figure 8).

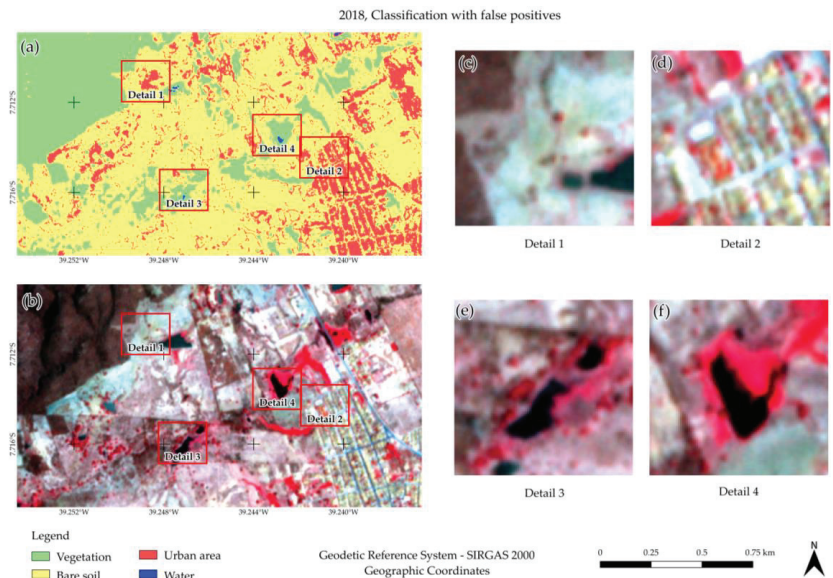


Figure 8. Classification analysis with false positives in 2018 northwest of Cedro-PE city: (a) samples indicated in the classified image; (b) samples indicated in the PlanetScope image (RGB); (c) false positives in the bare soil area; (d) false positives in the bare soil area; (e,f) false positives in the water target.

Figure 8 shows areas that, although devoid of constructions, were erroneously classified as such. These false positives generated in the classification can be attributed to the characteristics of the materials used in the construction roofs, which are predominantly clay. In Figure 9, a visualization of the coverage of a constructed area in the study region is presented, comparing PlanetScope images and the Google Earth platform.

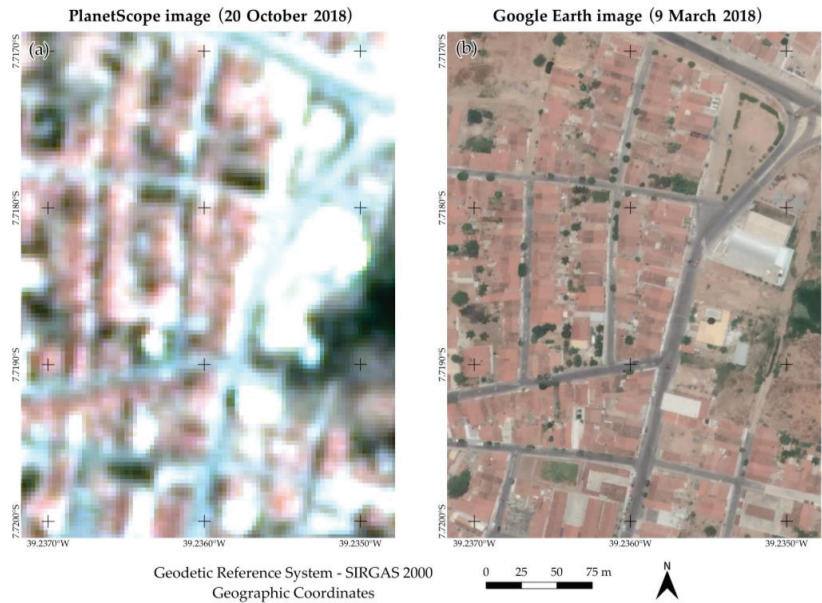


Figure 9. Example of a constructed area in the study region: (a) sample built-up area (PlanetScope scene) and (b) sample built-up area (Google Earth image base).

Due to the satellite's spatial resolution, the lot boundaries are not well-defined, and non-ceramic roofs are merged with areas of bare soil. Additionally, the area features frequent arborization between lots, which can also result in spectral mixing for the construction target.

4. Discussion

The experimental results revealed significant changes in land use and land cover between 2018 and 2023, with a 3.28% decrease in vegetation cover and a 6.62% increase in urbanized areas. These figures highlight the accelerated impact of mining activities, especially in the direct influence area along water bodies, where an increase in riparian vegetation loss was observed. The effectiveness of the kNN algorithm, demonstrated by an Overall Accuracy above 99% and a Kappa index of 0.98, reinforces its applicability in mining-impacted scenarios. However, the identified challenges, such as spectral overlap between urban area and exposed soil, reflect the need for complementary methods, such as textural variables or images with higher spatial resolution.

The reduction in the "water" class may be related to the decrease in precipitation recorded in October 2023, a month with little or no rain in the region. However, data variations may also be attributed to possible classification errors between bare soil and constructions, caused by the spectral similarity of the objects due to the sensor's spatial resolution. According to Novo et al. [74], different types of land cover have distinct spectral signatures, but the similarity of these signatures under certain conditions can result in classification errors. This phenomenon is particularly challenging in RS, demanding refined techniques to ensure greater accuracy.

The separability analysis between land use and land cover classes, using JMD associated with the NDVI and NDWI spectral indices, demonstrated high effectiveness, especially in distinguishing between Water and Vegetation classes. The results corroborate studies such as those by Shikhov et al. [7], who also observed a strong correlation between mining activities and their influence on the environmental degradation process. However, while other studies often report difficulties in detecting water in mined areas, the use of the NDWI in this work ensured clear separability for the water class, as evidenced by the high Jeffries–Matusita distance values (>1.95). This result is consistent with the findings of Foody [75], who emphasized the importance of vegetation indices like NDVI in improving the separation of classes with distinct spectral characteristics, such as dense vegetation and water bodies.

Another relevant point is the high separability observed for the Bare soil vs. Vegetation class, particularly with the Red and NIR bands. Xie et al. [76] point out that the use of these bands, associated with vegetation indices, significantly improves the discrimination of bare soil due to the high reflectance in the red and near-infrared bands. These authors also suggest that the combination of spectral indices and specific bands can improve the accuracy of classification in mined and deforested areas, as observed in their study.

However, the low separability between Constructions and Vegetation, especially for NDWI, reflects a frequent challenge in using spectral indices in urban areas. Yang et al. [77] identify similar limitations when using spectral indices to separate urban areas from vegetation, pointing to the need for post-processing techniques, such as the integration of textural variables, to overcome spectral mixing problems. Additionally, Pal and Foody [78] also discuss how the spectral similarity between construction materials and bare soil can complicate classification, requiring more refined adjustments to the classification algorithm.

The use of multiple spectral bands in combination with NDVI and NDWI indices, as evaluated through JMD, proved to be an effective strategy for improving class separability. Camps-Valls et al. [79] highlight that the use of machine learning techniques, such as kNN, in combination with spectral bands and derived indices, can maximize classification accuracy, especially in areas where the distinction between classes is difficult due to complex spectral signatures.

The accuracy of kNN in the years 2018 and 2023, with values above 99% and a Kappa index over 0.98, indicates excellent performance of the machine learning model in land use and cover classification. These results are consistent with the study by Zaki et al. [39], who also achieved high precision using machine learning algorithms to predict mineralization in mined areas. The robustness of the Kappa index in both studies demonstrates that, even in complex scenarios such as mining environments, kNN can provide consistent and reliable classifications.

The precision of kNN in this study highlights the efficiency of combining NDVI and NDWI spectral indices with the machine learning algorithm, something also supported by Fonseca et al. [10]. They pointed out that the integration of temporal spectral indices, such as NDVI, substantially improves the detection of changes in artisanal and small-scale mining areas. The high global accuracy values observed for 2018 and 2023 suggest that kNN can be a reliable alternative for monitoring land use changes, especially in regions with mining activities.

However, OE and CE identified, particularly in the Constructions class, indicate room for improvement, especially in differentiating between urban areas and bare soil, as also reported by Shikhov et al. [7]. The errors observed in this study may be related to the spatial resolution of the PlanetScope sensor and the spectral similarity between construction materials and bare soil, as discussed by Isidro et al. [40]. Improvements in

spectral segmentation techniques or the use of sensors with higher spatial resolution could potentially reduce these errors.

These results reinforce the relevance of using robust machine learning methodologies, such as kNN, for monitoring land use and cover in mining areas, but also point to the need for model adjustments to improve its sensitivity in certain classes, such as built-up areas and bare soil. The difficulties encountered in distinguishing between urban soil and bare soil classes are largely due to their spectral similarity and the sensor's spatial resolution. To overcome these limitations, future studies could explore integrating textural variables derived from high-resolution imagery or employing hybrid classifiers that combine machine learning with texture analysis. This approach could improve the accuracy of class separation in complex urban environments.

The selection of land use and land cover classes was a critical step in the methodology. The delineation of categories was based on predominant features that were most relevant to the study's objectives, considering the spectral and spatial limitations of PlanetScope images. The integration of categories such as croplands was considered but proved unfeasible in the study area due to the low expressiveness of this class and the difficulty in distinguishing cultivated lands from native vegetation or bare soil. Future research could explore the use of sensors with higher spectral resolution or complementary techniques to enhance the detail of the classes.

Evaluating surface mining areas through high spatial resolution satellite images is an efficient tool for monitoring and assessing land cover and use changes in mining complexes. It is important to highlight that high spatial resolution satellite images from the PlanetScope constellation have been freely available since 2017, making them an important data source for land use and cover monitoring in general.

The analysis based on PlanetScope images, combined with visual validation through Google Earth, has proven to be a powerful tool for monitoring land use and land cover changes in areas affected by mining. PlanetScope's ability to provide daily high-resolution images, coupled with the use of machine learning algorithms such as kNN, allows for the rapid identification of impacted areas and the prioritization of mitigation actions. This approach can also be integrated into public management systems, enabling regulatory bodies such as the National Mining Agency (ANM) to use updated data to monitor mining activities in near real time. This integration provides a solid foundation for monitoring illegal activities, planning environmental recovery strategies, and promoting more sustainable use of mineral resources.

This technical association allows for spatial and temporal validation of the obtained data, especially in areas where the 3 m spatial resolution of PlanetScope may generate uncertainties due to spectral similarities between classes, such as urban area and exposed soil. Additionally, the use of historical images from Google Earth enables a retrospective analysis of environmental transformations, enriching the understanding of spatial dynamics and providing a visual history to support strategic decisions in environmental and mining management. This integrated approach demonstrates considerable potential for future applications in continuous monitoring and environmental oversight, contributing to greater accuracy in identifying environmental impacts in mining-affected areas.

Other methodological advances should focus on recognizing and distinguishing different stages of rehabilitation in mining areas (e.g., herbaceous, shrub, and forest cover) from high-resolution satellite systems and unmanned aerial vehicles to remotely track the environmental progress of revegetation areas [33].

According to Tang et al. [80], environmental changes caused by human factors, such as industrialization, urbanization, economy, and technology, surpass even those caused by natural factors in intensity and have a decisive impact on short-term land cover changes in

mining areas, where social and economic factors are more important. As a result, the traditional farming mode may be affected, leading to the destruction of the ecological environment.

The expansion of mining activities and the associated vegetation degradation in the Serrita-Cedro Project region have caused significant environmental and socioeconomic impacts. From an environmental perspective, extensive vegetation removal has led to a loss of biodiversity and a decline in ecosystem services. This degradation has disrupted the local hydrological cycle, increasing erosion risks and reducing soil infiltration. Furthermore, waste generated by mining activities has polluted soil and water resources, compromising the quality of essential water supplies for local communities. These environmental challenges have heightened the region's ecological vulnerabilities, threatening long-term sustainability [81].

From a socioeconomic perspective, mining activities in the Serrita-Cedro Project and other areas in Brazil have provided immediate economic opportunities, such as job creation and increased local income. However, economic dependence on mining has left communities vulnerable, particularly as mines near resource depletion. Additionally, the displacement of local populations and territorial conflicts have impacted traditional communities, exacerbating social inequalities. Atmospheric pollution from mining activities has further contributed to a rise in respiratory diseases, highlighting the need for more robust strategies to mitigate these damages [82].

RS monitoring and evaluation of the effects of mining on long-term changes can provide a solid understanding to guide mine ecological restoration and local ecosystem sustainability [83], despite some limitations of this technology. However, in the future, with the development of new sensors and satellites with better resolutions, integrated with new methodological processes, RS monitoring of mining areas will become more efficient.

5. Conclusions

The spatiotemporal analysis of mining areas in the semi-arid region of Pernambuco, utilizing high-resolution images from 2018 and 2023 and machine learning techniques, highlighted the magnitude of the environmental transformations occurring in the region. The data revealed a reduction in vegetation cover and a significant increase in urban areas and bare soil, which are direct reflections of the expansion of mining activities. These results underscore the continuous pressure that these activities exert on local ecosystems, especially in sensitive regions like the Caatinga, where biodiversity is already naturally adapted to extreme climate and soil conditions.

The applied methodology, which combined the kNN algorithm and the NDVI and NDWI spectral indices, demonstrated accuracy in image classification and landscape change identification. With an accuracy exceeding 99% and a Kappa index above 0.98, the methodology was effective in detecting impacted areas, confirming the potential of these tools in environmental monitoring in mining areas. However, some challenges were observed, such as the separability between the classes of urban area and bare soil, suggesting that future adjustments in modeling may further increase the precision of the results.

The findings indicate that between 2018 and 2023, there was a marked degradation of vegetation and a significant increase in built areas, especially near water bodies. This trend reflects the intense human intervention in the region and reinforces the need for public policies aimed at mitigating these impacts, as well as promoting environmental recovery in affected areas.

The uncontrolled expansion of mining poses a threat to environmental sustainability, endangering local communities that rely on natural resources for their livelihoods. The results obtained in this study demonstrated that mining activities significantly influenced

changes in land use and cover in the analyzed region. However, this study reaffirms the importance of using RS and machine learning technologies in environmental monitoring, especially in vulnerable areas like the Brazilian semi-arid region. Furthermore, it highlights the need for regulation and responsible management of mining activities, to adopt more sustainable practices that balance economic development and environmental preservation.

This work provided an in-depth understanding of spatiotemporal changes in land cover, emphasizing the importance of RS and spatial data analysis in environmental monitoring. The classification system adopted in this study was suitable for representing the main land use and land cover transformations in the mining area under investigation. However, we acknowledge that the inclusion of additional categories, such as croplands, could enrich the analysis in regions where such features are more prominent, especially using higher-resolution images and refined methodologies.

For future research, it is suggested to expand the training dataset and explore other machine learning techniques to enhance classification. Additionally, it is recommended to conduct further studies to investigate the impact of land use policies and climate change on vegetation dynamics in mining areas, aiming to contribute to conservation strategies and sustainable development.

It is also noted that the methodology tested in this study could be implemented to assess the spatiotemporal behavior of land cover in other mining regions with arid and/or semi-arid climatic characteristics.

Author Contributions: Conceptualization, A.d.P.P., J.A.S.d.N., A.M.R.-A., U.J.d.S.J., S.M.d.S., F.D.R.F. and C.A.P.M.G.; Data curation, A.d.P.P., J.A.S.d.N., A.M.R.-A., U.J.d.S.J., S.M.d.S., F.D.R.F. and C.A.P.M.G.; Formal analysis, A.d.P.P., J.A.S.d.N., A.M.R.-A., U.J.d.S.J., J.A.d.S.J., L.M.M.d.O., S.M.d.S., F.D.R.F. and C.A.P.M.G.; investigation, A.d.P.P., J.A.S.d.N., A.M.R.-A., U.J.d.S.J., J.A.d.S.J., L.M.M.d.O., S.M.d.S., F.D.R.F. and C.A.P.M.G.; Methodology, A.d.P.P., J.A.S.d.N., A.M.R.-A., U.J.d.S.J., J.A.d.S.J., L.M.M.d.O., S.M.d.S., F.D.R.F. and C.A.P.M.G.; Supervision A.d.P.P., J.A.S.d.N., A.M.R.-A., U.J.d.S.J., J.A.d.S.J., L.M.M.d.O., S.M.d.S., F.D.R.F. and C.A.P.M.G.; Validation, A.d.P.P., J.A.S.d.N., A.M.R.-A., U.J.d.S.J., J.A.d.S.J., L.M.M.d.O., S.M.d.S., F.D.R.F. and C.A.P.M.G.; Writing—original draft, A.d.P.P., J.A.S.d.N., A.M.R.-A., U.J.d.S.J., J.A.d.S.J., L.M.M.d.O., S.M.d.S., F.D.R.F. and C.A.P.M.G.; Writing—review and editing, A.d.P.P., J.A.S.d.N., A.M.R.-A., U.J.d.S.J., J.A.d.S.J., L.M.M.d.O., S.M.d.S., F.D.R.F. and C.A.P.M.G. All authors have read and agreed to the published version of the manuscript.

Funding: This research was funded by the project “Geophysical and Geodetic Studies for Monitoring of Hydrographic Basins and Dams”, grant No. UFPE/0311662.

Data Availability Statement: The data presented in this study are available on request from the corresponding author.

Acknowledgments: Research was supported by PAIUIJA-2023/2024 and CEACTEMA from University of Jaén (Spain), and RNM-282 research group from the Junta de Andalucía (Spain).

Conflicts of Interest: The authors declare no conflicts of interest.

References

1. Song, W.; Gu, H.H.; Song, W.; Li, F.P.; Cheng, S.P.; Zhang, Y.X.; Ai, Y.J. Environmental assessments in dense mining areas using remote sensing information over Qian'an and Qianxi regions China. *Ecol. Ind.* **2023**, *146*, 109814–109835. [CrossRef]
2. Buczyńska, A.; Blachowski, J.; Bugajska-Jędraszek, N. Analysis of Post-Mining Vegetation Development Using Remote Sensing and Spatial Regression Approach: A Case Study of Former Babina Mine (Western Poland). *Remote Sens.* **2023**, *15*, 719. [CrossRef]
3. Ern, A.M.L.E.; Arts, D.; Crawford, D.; Bonifacio, V.; Labatos, B.V., Jr.; Ngo, K.D.; John, R.; Owen, J.R.; Gibbins, C.; Lechner, A.M. Socio-environmental land cover time-series analysis of mining landscapes using Google Earth Engine and web-based mapping. *Remote Sens. Appl. Soc. Environ.* **2021**, *21*, 100458–100460. [CrossRef]
4. Hook, R.L.; Martín-Duque, J.F.; Pedraza, J. Land transformation by humans: A review. In *GSA Today*, 12th ed.; Housen, B., Ed.; Geological Society of America Today: Boulder, CO, USA, 2012; Volume 22, pp. 1–10.

5. Keenan, R.J.; Reams, G.A.; Achard, F.; De Freitas, J.V.; Grainger, A.; Lindquist, E. Dynamics of global forest area: Results from the FAO Global Forest Resources Assessment 2015. *For. Ecol. Manag.* **2015**, *352*, 9–20. [CrossRef]
6. Chetty, S.; Pillay, L.; Humphries, M.S. Gold mining's toxic legacy: Pollutant transport and accumulation in the Klip River catchment, Johannesburg. *S. Afr. J. Sci.* **2021**, *117*, 8668–8678. [CrossRef]
7. Shikhov, A.; Ilyushina, P.; Makarieva, O.; Zemlianskova, A.; Mozgina, M. Satellite-Based Mapping of Gold-Mining-Related Land-Cover Changes in the Magadan Region, Northeast Russia. *Remote Sens.* **2023**, *15*, 3564. [CrossRef]
8. Alessi, M.A.; Chirico, P.G.; Millones, M. Artisanal Mining River Dredge Detection Using SAR: A Method Comparison. *Remote Sens.* **2023**, *15*, 5701. [CrossRef]
9. Akbar, S.; Abdolmaleki, M.; Ghadernejad, S.; Esmaeili, K. Applying Knowledge-Based and Data-Driven Methods to Improve Ore Grade Control of Blast Hole Drill Cuttings Using Hyperspectral Imaging. *Remote Sens.* **2024**, *16*, 2823. [CrossRef]
10. Fonseca, A.; Marshall, M.T.; Salama, S. Enhanced Detection of Artisanal Small-Scale Mining with Spectral and Textural Segmentation of Landsat Time Series. *Remote Sens.* **2024**, *16*, 1749. [CrossRef]
11. Silva, N.L.; Fonseca, B.M. Spatio-temporal land use landandcover changesanalysis in the São Thomé das Letras municipality. *Cad. Geogr.* **2016**, *26*, 45. [CrossRef]
12. Bezerra, J.J.L.; Lira, W.B.; Silva, T.d.C. Impactos ambientais causados pela mineração: Uma análise da percepção de pequenos mineradores do município de Frei Martinho—PB. *Rev. Monogr. Ambient.* **2020**, *19*, 75–95. [CrossRef]
13. Lobo, F.; Costa, M.; Novo, E.; Telmer, K. Distribution of Artisanal and Small-Scale Gold Mining in the Tapajós River Basin (Brazilian Amazon) over the Past 40 Years and Relationship with Water Siltation. *Remote Sens.* **2016**, *8*, 579. [CrossRef]
14. Corbett, T.; O'Faircheallaigh, C.; Regan, A. 'Designated areas' and the regulation of artisanal and small-scale mining. *Land Use Policy* **2017**, *68*, 393–401. [CrossRef]
15. Fritz, M.; Mcquiklen, J.; Collins, N.; Weldegiorgis, F. Global Trends in Artisanal and Small-Scale Mining (ASM): A Review of Key Numbers and Issues. International Institute for Sustainable Development (IISD). 2022. Available online: <https://www.iisd.org/publications/report/global-trends-artisanal-and-small-scale-mining-asm-review-key-numbers-and> (accessed on 8 August 2024).
16. Bansah, K.J.; Dumakor-Dupey, N.K.; Kansake, B.A.; Assan, E.; Bekui, P. Socioeconomic and environmental assessment of informal artisanal and small-scale mining in Ghana. *J. Clean. Prod.* **2018**, *202*, 465–475. [CrossRef]
17. BRAZIL. Lei nº 6.938, de 31 de Agosto de 1981. Dispõe Sobre a Política Nacional do Meio Ambiente, Seus fins e Mecanismos de Formulação e Aplicação, e dá Outras Providências. Diário Oficial [da] República Federativa do Brasil, Brasília, DF, 02 set. 1981. 2024. Available online: https://www.planalto.gov.br/ccivil_03/Leis/L6938.htm (accessed on 19 September 2024).
18. Acharya, P.; Fangzhou Liu, F. Mining, Minerals, and Sustainable Development: A Review of Key Social and Environmental Issues. Available online: <https://open.library.ubc.ca/soa/cIRcle/collections/59368/items/1.0438161> (accessed on 25 October 2024). [CrossRef]
19. Michałowska, K.; Pirowski, T.; Głowienka, E.; Szypuła, B.; Malinverni, E.S. Sustainable Monitoring of Mining Activities: Decision-Making Model Using Spectral Indexes. *Remote Sens.* **2024**, *16*, 388. [CrossRef]
20. Camalan, S.; Cui, K.; Pauca, V.P.; Alqahtani, S.; Silman, M.; Chan, R.; Plemmons, R.J.; Dethier, E.N.; Fernandez, L.E.; Lutz, D.A. Change Detection of Amazonian Alluvial Gold Mining Using Deep Learning and Sentinel-2 Imagery. *Remote Sens.* **2022**, *14*, 1746. [CrossRef]
21. Li, Y.; Zhao, H.; Fan, J. Application of Remote Sensing Technology in Mine Environment Monitoring. *MATEC Web Conf.* **2015**, *22*, 04008. [CrossRef]
22. Song, W.; Song, W.; Gu, H.; Li, F. Progress in the Remote Sensing Monitoring of the Ecological Environment in Mining Areas. *Int. J. Environ. Res. Public Health* **2020**, *17*, 1846. [CrossRef]
23. Gallwey, J.; Robiati, C.; Coggan, J.; Vogt, D.; Eyre, M. A Sentinel-2 based multispectral convolutional neural network for detecting artisanal small-scale mining in Ghana: Applying deep learning to shallow mining. *Remote Sens. Environ.* **2020**, *248*, 111970. [CrossRef]
24. Kimijima, S.; Sakakibara, M.; Nagai, M. Detection of Artisanal and Small-Scale Gold Mining Activities and Their Transformation Using Earth Observation, Nighttime Light, and Precipitation Data. *Int. J. Environ. Res. Public Health* **2021**, *18*, 10954. [CrossRef]
25. Kimijima, S.; Sakakibara, M.; Nagai, M. Characterizing Time-Series Roving Artisanal and Small-Scale Gold Mining Activities in Indonesia Using Sentinel-1 Data. *Int. J. Environ. Res. Public Health* **2022**, *19*, 6266. [CrossRef] [PubMed]
26. Alarcon-Aguirre, G.; Mamani, M.M.; Canahuire-Robles, R.R.; Zavaleta, T.V.; Valdeiglesias, J.P.; Revoredo, J.D.; Achata, L.R.; Enciso, D.R.; Garate-Quispe, J. Forest Loss Related to Brazil Nut Production in Non-Timber Forest Product Concessions in a Micro-Watershed in the Peruvian Amazon. *Remote Sens.* **2023**, *15*, 5438. [CrossRef]
27. Werner, T.T.; Mudd, G.M.; Schipper, A.M.; Huijbregts, M.A.J.; Taneja, L.; Northey, S.A. Global-scale remote sensing of mine areas and analysis of factors explaining their extent. *Glob. Environ. Chang.* **2020**, *60*, 102007. [CrossRef]

28. Ilyushina, P.G.; Shikhov, A.N. Makarieva, Satellite-Based Mapping of the Negative Impact of Gold Mining Enterprises on the Natural Environment of the Cryolithozone (Using the Example of Magadan Oblast). *Izv. Atmos. Ocean. Phys.* **2023**, *59*, 1093–1102. [CrossRef]
29. Kimijima, S.; Nagai, M.; Sakakibara, M. Distribution of Enhanced Potentially Toxic Element Contaminations Due to Natural and Coexisting Gold Mining Activities Using Planet Smallsat Constellations. *Remote Sens.* **2023**, *15*, 861. [CrossRef]
30. PLANET LABS a. Planet Imagery Product Specifications. 2024. Available online: <https://www.planet.com/products/> (accessed on 9 May 2024).
31. Rouse, J.W.; Haas, R.H.; Schell, J.A.; Deering, D.W. Monitoring Vegetation Systems in the Great Plains with ERTS. NASA. Goddard Space Flight Center 3d ERTS-1 Symp.; Volume 1, Sect. A 1974. Available online: <https://ntrs.nasa.gov/citations/19740022614> (accessed on 25 October 2024).
32. Gao, B.C. NDWI-A normalized difference water index for remote sensing of vegetation liquid water from spac. *Remote Sens. Environ.* **1996**, *58*, 257–266. [CrossRef]
33. Padró, J.-C.; Carabassa, V.; Balagué, J.; Brotons, L.; Alcañiz, J.M.; Pons, X. Monitoring Open-cast Mine Restorations Using Unmanned Aerial System (UAS) Imagery. *Sci. Total Environ.* **2019**, *657*, 1602–1614. [CrossRef]
34. Nascimento, F.S.; Gastauer, M.; Souza-Filho, P.W.M.; Nascimento, W.R., Jr.; Santos, D.C.; Costa, M.F. Land Cover Changes in Open-Cast Mining Complexes Based on High-Resolution Remote Sensing Data. *Remote Sens.* **2020**, *12*, 611. [CrossRef]
35. Stančić, L.; Oštir, K.; Kokalj, Ž. Fluvial gravel bar mapping with spectral signal mixture analysis. *Eur. J. Remote Sens.* **2021**, *54*, 31–46. [CrossRef]
36. McKenna, P.B.; Lechner, A.M.; Phinn, S.; Erskine, P.D. Remote Sensing of Mine Site Rehabilitation for Ecological Outcomes: A Global Systematic Review. *Remote Sens.* **2020**, *12*, 3535. [CrossRef]
37. Caballero Espejo, J.; Messinger, M.; Román-Dañobeytia, F.; Ascorra, C.; Fernandez, L.E.; Silman, M. Deforestation and Forest Degradation Due to Gold Mining in the Peruvian Amazon: A 34-year Perspective. *Remote Sens.* **2018**, *10*, 1903. [CrossRef]
38. Dethier, E.N.; Sartain, S.L.; Lutz, D.A. Heightened Levels and Seasonal Inversion of Riverine Suspended Sediment in a Tropical Biodiversity Hot Spot Due to Artisanal Gold Mining. *Proc. Natl. Acad. Sci. USA* **2019**, *116*, 23936–23941. [CrossRef] [PubMed]
39. Malik, K.; Robertson, C.; Braun, D.; Greig, C. U-Net convolutional neural network models for detecting and quantifying placer mining disturbances at watershed scales. *Int. J. Appl. Earth Obs. Geoinf.* **2021**, *104*, 102510. [CrossRef]
40. Zaki, M.M.; Chen, S.; Zhang, J.; Feng, F.; Qi, L.; Mahdy, M.A.; Jin, L. Optimized Weighted Ensemble Approach for Enhancing Gold Mineralization Prediction. *Appl. Sci.* **2023**, *13*, 7622. [CrossRef]
41. Isidro, C.M.; McIntyre, N.; Lechner, A.M.; Callow, I. Applicability of Earth Observation for Identifying Small-Scale Mining Footprints in a Wet Tropical Region. *Remote Sens.* **2017**, *9*, 945. [CrossRef]
42. Alba, E.; de Souza Alexandre, M.L.; Marchesan, J.; de Souza, L.S.B.; Bezerra, A.C.; Silva, E.A. Comparação entre algoritmos de aprendizado de máquina para a identificação de floresta tropical sazonalmente seca. *Anuário Inst. Geociências—UFRJ* **2022**, *45*, 75–95. [CrossRef]
43. da Penha Pacheco, A.; Da Silva Junior, A.J.; Ruiz-Armenteros, M.A.; Henriques, F.F.R. Assessment of k-Nearest Neighbor and Random Forest Classifiers for Mapping Forest Fire Areas in Central Portugal Using Landsat-8, Sentinel-2, and Terra Imagery. *Remote Sens.* **2021**, *13*, 1345. [CrossRef]
44. Noi, P.T.; Kappas, M. Comparison of Random Forest, k-Nearest Neighbor, and Support Vector Machine Classifiers for Land Cover Classification Using Sentinel-2 Imagery. *Sensors* **2017**, *18*, 18. [CrossRef]
45. Barbosa, H.A.; Kumar, T.V.L.; Paredes, F.; Elliott, S.; Ayuga, J.G. Assessment of Caatinga response to drought using Meteosat-SEVIRI Normalized Difference Vegetation Index (2008–2016). *ISPRS J. Photogramm. Remote Sens.* **2019**, *148*, 235–252. [CrossRef]
46. DNPM. *National Department of Mineral Production. Serrita-Cedro Project: Phase I*, 2nd ed.; DNPM: Recife, Brazil, 1995; Available online: https://www.dnpm-pe.gov.br/Trabalhos/Projeto_Serrita_I.pdf (accessed on 15 June 2023).
47. IBRAM. *Informações Sobre a Economia Mineral Brasileira 2020—Ano Base 2019*, 1st ed.; Instituto Brasileiro de Mineração: Brasília, Brazil, 2020; pp. 1–84.
48. Schueler, T.A.; de Aguiar, P.F.; Yagmurlu, B.; Goldmann, D. Removal of Base Metals from Mine Tailings in Chloride- and Seawater-Based Media Followed by Solvent Extraction. *Sustainability* **2023**, *15*, 15515. [CrossRef]
49. Da Silva Junior, U.J.; Gonçalves, R.M.; de Oliveira, L.M.M.; da Silva Júnior, J.A. Sensibilidade Espectral dos Índices de Vegetação: GNDVI, NDVI e EVI na Mata Ciliar do Reservatório de Serrinha II—PE, Brasil. *Rev. Bras. Cartogr.* **2021**, *73*, 17–35. [CrossRef]
50. Da Silva Junior, U.J.; Da Fonseca, R.C.; Da Silva Júnior, J.A. Mapeamento da vegetação do Bioma Caatinga por meio de séries temporais MODIS NDVI e ALBEDO, na Bacia Hidrográfica do Rio Pajeú—PE, BR. *Caminhos Geogr.* **2022**, *23*, 75–89. [CrossRef]
51. Marta, S. Planet Planet Imagery Product Specification. 2018. Available online: <https://assets.planet.com/docs/Combined-Imagery-Product-Spec-Dec-2018.pdf> (accessed on 25 March 2023).
52. Dos Reis, A.A.; Werner, J.P.S.; Silva, B.C.; Figueiredo, G.K.D.A.; Antunes, J.F.G.; Esquerdo, J.C.D.M.; Coutinho, A.C.; Lamparelli, R.A.C.; Rocha, J.V.; Magalhães, P.S.G. Monitoring Pasture Aboveground Biomass and Canopy Height in an Integrated Crop–Livestock System Using Textural Information from PlanetScope Imagery. *Remote Sens.* **2020**, *12*, 2534. [CrossRef]

53. Iqbal, I.M.; Balzter, H.; Firdaus-e-Bareen; Shabbir, A. Mapping Lantana camara and Leucaena leucocephala in Protected Areas of Pakistan: A Geo-Spatial Approach. *Remote Sens.* **2023**, *15*, 1020. [CrossRef]
54. de B. M. Trovão, D.M.; Fernandes, P.D.; de Andrade, L.A.; Dantas Neto, J. Variações sazonais de aspectos fisiológicos de espécies da Caatinga. *Rev. Bras. Eng. Agrícola E Ambient.* **2007**, *11*, 307–311. [CrossRef]
55. APAC. AGÊNCIA PERNAMBUCANA DE ÁGUAS E CLIMA. Monitoramento Pluviométrico. 2023. Available online: <https://www.apac.pe.gov.br/> (accessed on 4 April 2024).
56. Padma, S.; Sanjeevi, S. Jeffries Matusita Based Mixed-Measure for Improved Spectral Matching in Hyperspectral Image Analysis. *Int. J. Appl. Earth Obs. Geoinf.* **2014**, *32*, 138–151. [CrossRef]
57. EOS Data Analytics. NDVI: Frequently Asked Questions to Understand the Index. 2020. EOS Data Analytics, 25 Set. 2020. Available online: <http://eos.com/pt/blog/ndvi-faq/> (accessed on 4 July 2023).
58. Teodoro, A.; Amaral, A. A Statistical and Spatial Analysis of Portuguese Forest Fires in Summer 2016 Considering Landsat 8 and Sentinel 2A Data. *Environments* **2019**, *6*, 36. [CrossRef]
59. McFEETERS, S.K. The Use of the Normalized Difference Water Index (NDWI) in the Delineation of Open Water Features. *Int. J. Remote Sens.* **1996**, *17*, 1425–1432. [CrossRef]
60. Richards, J.A.; Jia, X. *Remote Sensing Digital Image Analysis: An Introduction*, 3rd ed.; Springer: Berlin/Heidelberg, Germany, 2013; p. 363.
61. Cover, T.; Hart, P. Nearest neighbor pattern classification. *IEEE Trans. Inf. Theory* **1967**, *13*, 21–27. [CrossRef]
62. James, G.; Witten, D.; Hastie, T.; Tibshirani, R. *An Introduction to Statistical Learning*, 2nd ed.; Springer: New York, NY, USA, 2013; pp. 1–545. [CrossRef]
63. Kohavi, R. The Power of Decision Tables. *Lect. Notes Comput. Sci.* **1995**, *912*, 174–189. [CrossRef]
64. Manjate, E.P.A.; Okada, N.; Ohtomo, Y.; Adachi, T.; Bene, B.M.; Arima, T.; Kawamura, Y. An AI-Based Approach for Developing a Recommendation System for Underground Mining Methods Pre-Selection. *Mining* **2024**, *4*, 747–765. [CrossRef]
65. Farahnakian, F.; Luodes, N.; Karlsson, T. Machine Learning Algorithms for Acid Mine Drainage Mapping Using Sentinel-2 and Worldview-3. *Remote Sens.* **2024**, *16*, 4680. [CrossRef]
66. He, Y.; Lai, Y.; Chen, B.; Chen, Y.; Xie, Z.; Yu, X.; Luo, M. An Open-Pit Mines Land Use Classification Method Based on Random Forest Using UAV: A case study of a ceramic clay mine. *Minerals* **2024**, *14*, 1282. [CrossRef]
67. QGIS Development Team. Geographic Information System. QGIS Development Team, 2023: Open-Source Geospatial Foundation Project. Available online: https://qgis.org/pt_BR/site/ (accessed on 4 July 2023).
68. R Core Team. *A Language and Environment for Statistical Computing*; R Foundation for Statistical Computing: Vienna, Austria, 2023; Available online: <https://posit.co/download/rstudio-desktop/> (accessed on 8 May 2023).
69. Sano, E.E.; Rosa, R.; Brito, J.L.S.; Ferreira, L.G. Land cover mapping of the tropical savanna region in Brazil. *Environ. Monit. Assess.* **2010**, *166*, 113–124. [CrossRef]
70. Tejado-Ramos, J.J.; Chocarro-León, M.; Barrero-Béjar, I.; Valverde-Calvo, A.; Ferreras-Moreno, M.; Giraldo-Pavón, F.; Tarragona-Pérez, C. Enhancement of the sustainability of wolfram mining using drone remote sensing technology. *Remote Sens. Appl. Soc. Environ.* **2021**, *23*, 100542. [CrossRef]
71. Zheng, Z.; Wang, J.; Ni, J.; Cui, Y.; Zhu, Q. Lacustrine Wetlands Landscape Simulation and Multi-Scenario Prediction Based on the Patch-Generating Land-Use Simulation Model: A case study on shengjin lake reserve, china. *Remote Sens.* **2024**, *16*, 4169. [CrossRef]
72. Landis, J.R.; Kock, G.G. The measurement of observer agreement for categorical data. *Biometrics* **1977**, *33*, 159–174. Available online: <https://pubmed.ncbi.nlm.nih.gov/843571/> (accessed on 4 July 2023). [CrossRef]
73. Manolakis, D.; Marden, D.; Shaw, G.A. Hyperspectral image processing for automatic target detection applications. *Linc. Lab. J.* **2003**, *14*, 79–116.
74. Novo, E.M.L.M.; Ferreira, L.G.; Barbosa, C.; Carvalho, C.; Sano, E.E.; Shimabukuro, Y.; Huete, A.; Potter, C.; Roberts, A.; Hess, L.L.; et al. Técnicas avançadas de sensoriamento remoto aplicadas ao estudo de mudanças climáticas e ao funcionamento dos ecossistemas amazônicos. *Rev. Bras. Cartogr.* **2005**, *35*, 259–272. [CrossRef]
75. Foody, G.M. Thematic map comparison: Evaluating the statistical significance of differences in classification accuracy. *Photogramm. Eng. Remote Sens.* **2004**, *70*, 627–633. [CrossRef]
76. Xie, Y.; Sha, Z.; Yu, M. Remote sensing imagery in vegetation mapping: A review. *J. Plant Ecol.* **2008**, *1*, 9–23. [CrossRef]
77. Yang, X.; Zhao, S.; Qin, X.; Zhao, N.; Liang, L. Mapping of urban surface water bodies from Sentinel-2 MSI imagery at 10 m resolution via NDWI-based image sharpening. *Remote Sens.* **2013**, *9*, 595. [CrossRef]
78. Pal, M.; Foody, G.M. Feature selection for classification of hyperspectral data by SVM. *IEEE Trans. Geosci. Remote Sens.* **2010**, *48*, 2297–2307. [CrossRef]
79. Camps-Valls, G.; Tuia, D.; Bruzzone, L.; Benediktsson, J.A. Advances in hyperspectral image classification: Earth monitoring with statistical learning methods. *IEEE Signal Process. Mag.* **2014**, *31*, 45–54. [CrossRef]

80. Tang, H.; Fang, J.; Xie, R.; Ji, X.; Li, D.; Yuan, J. Impact of Land Cover Change on a Typical Mining Region and Its Ecological Environment Quality Evaluation Using Remote Sensing Based Ecological Index (RSEI). *Sustainability* **2022**, *14*, 12694. [CrossRef]
81. Rezende, V.L. A mineração em Minas Gerais: Uma análise de sua expansão e os impactos ambientais e sociais causados por décadas de exploração. *Soc. Nat.* **2016**, *28*, 375–384. [CrossRef]
82. Silva, M.G.; ARAÚJO, N.M.S.; SILVA, P.G. Conflitos socioambientais envolvendo água e mineração no Brasil: Sujeitos políticos e suas lutas. *Libertas* **2023**, *23*, 521–538. [CrossRef]
83. Meng, D.; Bao, N.; Tayier, K.; Li, Q.; Yang, T. A remote sensing based index for assessing long-term ecological impact in arid mined land. *Environ. Sustain. Indic.* **2024**, *22*, 100364. [CrossRef]

Disclaimer/Publisher’s Note: The statements, opinions and data contained in all publications are solely those of the individual author(s) and contributor(s) and not of MDPI and/or the editor(s). MDPI and/or the editor(s) disclaim responsibility for any injury to people or property resulting from any ideas, methods, instructions or products referred to in the content.

MDPI AG
Grosspeteranlage 5
4052 Basel
Switzerland
Tel.: +41 61 683 77 34

Land Editorial Office
E-mail: land@mdpi.com
www.mdpi.com/journal/land



Disclaimer/Publisher's Note: The title and front matter of this reprint are at the discretion of the Guest Editors. The publisher is not responsible for their content or any associated concerns. The statements, opinions and data contained in all individual articles are solely those of the individual Editors and contributors and not of MDPI. MDPI disclaims responsibility for any injury to people or property resulting from any ideas, methods, instructions or products referred to in the content.



Academic Open
Access Publishing

[mdpi.com](https://www.mdpi.com)

ISBN 978-3-7258-3848-6